Design of robot end-effector for collaborative robot works

Wanda Zhao

To cite this version:

Wanda Zhao. Design of robot end-effector for collaborative robot works. Automatic. École centrale de Nantes, 2021. English. NNT : 2021ECDN0042 . tel-04700359

HAL Id: tel-04700359
https://theses.hal.science/tel-04700359

Submitted on 17 Sep 2024

THESE DE DOCTORAT DE

L'ÉCOLE CENTRALE DE NANTES

ECOLE DOCTORALE N° 602
Sciences pour l'Ingénieur
Spécialité : Robotique-Mécanique

Par
Wanda ZHAO

Design of Robot End-Effector for Collaborative Robot Works

Thèse présentée et soutenue à Nantes, le 02/12/2021
Unité de recherche : UMR 6004, Laboratoire des Sciences du Numérique de Nantes (LS2N)

Rapporteurs avant soutenance :

Marc GOUTTEFARDE	Directeur de recherche CNRS, Université de Montpellier
David DANEY	Chargé de recherche HDR, INRIA, Talence

Composition du Jury :

Président :	Christian DURIEZ	Directeur de recherche, INRIA, Villeneuve d'Ascq
Examinatrice :	Margot VULLIEZ	Maître de conférences, Université de Poitiers
Dir. de thèse :	Damien CHABLAT	Directeur de recherche CNRS, Ecole Centrale de Nantes
Co-dir. de thèse:	Anatol PASHKEVICH	Professeur, IMT Atlantique Nantes

ACKNOWLEDGMENT

When I am looking at this thesis and thinking back on my three years of Ph.D. study, I feel that time is so short and so fast, every day is so clear in my remember just like yesterday. I still remember when I first came into contact with my research topic，I felt both very interesting and confused because I didn't know what techniques I need to use. But now I have already learned this knowledge and used them to complete this scientific research.

First of all, I want to sincerely thank my supervisor Damien Chablat, who gave me this precious opportunity to study here three years ago, helped me find this interesting research topic, and gave me support not only in my works but also in life. No matter how busy he is，he always tries his best to help me in time. Every time we met he treated me as a good friend, made me feel relaxed when I met problems with his light and humorous words.

I should also give my great gratitude to my Co-supervisor Anatol Pashkevich, the guide on my scientific research road. He let me know how important patience and seriousness are in scientific research. He taught me all the knowledge hardly and carefully, working with me together day by day with full passion. He verified every task of us personally and did it with me together again with full patience to make sure accuracy. He gave me encouragement and enough time to think when I encountered difficulties and lost patience. He taught me how to write scientific articles word by word, told me to check the papers we finished over and over again before submission. These valuable scientific research qualities have greatly touched me and inspired me to be an excellent scientific researcher

Besides, I would like to thank our cooperator professor Alexandr Klimchic, who gave so much help for our works and papers. I would also like to thank my friends, my workmates who have spent the lunchtime and coffee break time with me in Ecole Centrale Nantes and IMT Atlantique Nante, brought me happiness, and helped me to solve difficulties.

I really appreciate the understanding of my parents, because of Covid19 I cannot come back home and stay with them, but they always give me courage and care without any complaints.

Finally, I want to thank the Chinese Scholarship Council, my funding supporter. This work is supported by the China State Scholarship Fund (No. 201801810036) of the project “CSC-Centrale Schools Program”.

ABSTRACT

This thesis focuses on the design of new versatile and compliant end-effectors for collaborative robot works, which are based on multi-segment dual-triangle tensegrity mechanisms that can be actuated independently to achieve the desired configuration with the required stiffness properties. Different with the conventional rigid robot end-effectors, it was demonstrated from the stiffness analysis that such type of mechanism can achieve high flexibility, designers can evaluate the stiffness sensitivity of this mechanism with respect to an arbitrary initial configuration for different combination of the geometric parameters, external loading and the springs pre-stresses. Besides, the buckling and quasi-buckling phenomenon of this serial mechanism under the loading were detected. And an analytical method allowing to compute the critical force causing the buckling for this serial structure with an arbitrary number of segments was proposed, which is based on the eigenvalue analysis of the some special matrix depending on both geometric and elastostatic parameters. This allows designers to predict or avoid the dangerous states of this mechanism by properly changing the geometric parameters and control inputs. Furthermore, the optimization-based kinematic control strategies were proposed in this thesis, which allow this redundant multi-segment mechanism to achieve the target endpoint location and avoid collisions between not only the mechanism end-point but also the mechanism body and the workspace obstacles. The advantages of the developed technique are confirmed via the computing simulation, and the results show that this redundant serial mechanism has a very flexible shape changing capacity while passing through the task space.

Keywords: Robot end-effector, compliant manipulator, tensegrity mechanism, stiffness analysis, kinematic control.

CONTENTS

LIST OF FIGURES

LIST OF TABLES

LIST OF SYMBOLS

$\boldsymbol{\Lambda}^{r}$	Diagonal matrix describing the boundary conditions of the rigid connections
$\boldsymbol{\Lambda}^{p}$	Diagonal matrix describing the boundary conditions of the passive connections
$(\mathbf{J}^{\mathrm{T}})^{\dagger}$, $\mathbf{J}^{\dagger}$	Pseudo-inverse matrices of the considered matrices
$[\mathbf{L}\times]$	Skew-symmetric matrix derived from the length vector **L**
Aj	matrix, composed of inequality constraints
A_eq	3×*n* Jacobian matrix related to **J**, equality constraints parameters
A_Neq	Matrix, inequality constraints parameters
$\mathbf{A}_i$, $\mathbf{B}_i$, $\mathbf{C}_i$, $\mathbf{D}_i$	Block matrices that are obtained using MSA technique
bj	Vector, composed of the minimum safe distance *dmin_ij*
b_eq	Vector, related to **dp** and manipulator orientation angles, equality constraints
b_Neq	Vector, inequality constraints
$\mathbf{B}(i,j)$	$m\times n$ binary matrix describing the obstacle locations: $\mathrm{B}(i,j)=1$ denotes the point $\mathbf{L}(i,j)$ inside of the obstacle
$\mathbf{C}_0$	Unloaded compliance matrix
$\mathbf{C}_{\mathrm{F}}$	Loaded compliance matrix
$\mathbf{C}_q$	Compliance matrix of the mechanisms/manipulator
Delt_L0	Vector, configuration control inputs of each segment of the manipulator
dst(i)	Vector containing the lengths of the shortest sub-paths connecting the initial point $\mathbf{L}(i_0,0)$ and an arbitrary intermediate target point $\mathbf{L}(i,j)$
Dst(i)	Internal vector containing the lengths for all possible sub-paths between the initial point $\mathbf{L}(i_0,0)$ and an arbitrary intermediate target point $\mathbf{L}(i,j)$
dp	Current end-effector deflection (between the current and the desired locations)
dq	Current joint increment corresponding to **dp**
$\mathbf{e}_{ij}$	Unit vector with the direction from joint $\mathbf{p}_i$ to obstacle ${}^{0}\mathbf{p}_j$
$\mathbf{F}$, $\mathbf{F}_i$	Vector, external force applied to the mechanism/manipulator ends
$\mathbf{F}^{0}$	Vector, initial external loading applied to the mechanism end
I	Identity matrix

$\mathbf{ind}(i,j)$	$m \times n$ Matrix of the previous row indices for the optimal sub-paths connecting the initial point $\mathbf{L}(i_0,0)$ and an arbitrary point $\mathbf{L}(i,j)$
$\mathbf{indP}(j)$	Vector of optimal row indices $\{i_0,i_1,...,i_n\}$ describing the collision-free shortest path between the initial point $\mathbf{L}(i_0,0)$ and the target point $\mathbf{L}(i_n,n)$
$\mathbf{J}$	Kinematic Jacobian matrix of the mechanical system/manipulator
$\mathbf{J}_a$	Composed of element $\mathbf{e}_{ij}^T \cdot \mathbf{J}_i$ corresponding to the active constraints in collision-free kinematic optimization algorithms
$\mathbf{J}_e$	Composed of all elements $\mathbf{e}_{ij}^T \cdot \mathbf{J}_i$ from the inequality constraints in collision-free kinematic optimization algorithms
$\mathbf{J}_0$	Kinematic Jacobian matrix related to the unloaded initial configurations $\mathbf{q}^0$
$\mathbf{J}_{aggr}$	Aggregating Jacobian matrix corresponding to the deflection $\mathbf{\Delta\Theta}$
$\mathbf{J}_\mathrm{i}$	Manipulator partial Jacobian matrix with respect to the ith joint
$\mathbf{J}_\mathbf{q}$	Kinematic Jacobian matrix related to the angle q
$\mathbf{J}_{\boldsymbol{\theta}}$	Kinematic Jacobian matrix related to the angle θ of the passive joint
$\mathbf{K}$, $\mathbf{K}_{ij}$	Square matrix, stiffness matrix of the mechanism
$\mathbf{K}_{aggr}$	Aggregate stiffness matrices composed of $\mathbf{K}_q$ and $\mathbf{K}_{link}$
$\mathbf{K}_\mathrm{C}$	Stiffness matrix of the considered system/manipulator
$\mathbf{K}_F$	Loaded stiffness matrix
$\mathbf{K}_g$	Partial stiffness matrix that is related to the external loading $\mathbf{F}$
$\mathbf{K}_{link}$	Stiffness matrix of the beam/link material
$\mathbf{K}_q$	Diagonal matrix composed of the joint stiffness coefficients of the manipulators
$\mathbf{L}$	Vector, lengths of each links of the mechanisms/manipulators
$\mathbf{L0}$	Matrix, symmetrically distributed linear springs initial lengths of manipulators
$\mathbf{L}(i,j)$	$m \times n$ Matrix of point locations in task space
$\mathbf{M}$	Vector, external torque applied to the mechanism/manipulator ends
$\mathbf{Me}$, $\mathbf{M}_\mathrm{q}$	Torques generated be springs on each joints of the manipulator
$\mathbf{p}$	Vector, end-point location of the mechanisms or manipulators
$\mathbf{pt}$	Points locating on the path between the initial and target end-effector location
$\mathbf{pc}$	Current endpoint location of the manipulator
$\mathbf{P}^0$, $\mathbf{P0}$	Initial point location in the manipulator task space (x, y)

$\mathbf{Path}(i,j)$	$m\times n$ Matrix of the minimum lengths of the optimal sub-paths connecting the initial point $\mathbf{L}(i_0,0)$ and an arbitrary intermediate target point $\mathbf{L}(i,j)$
Path	Matrix, the obtained point locations on the path from the initial to target point**.**
$\mathbf{P}^{g}$, **Pg**	Target point location in the manipulator task space (x, y)
$\mathbf{P}ij$	Vector, from the ith joint to the jth obstacle
pob	Matrix, location of the obstacles in workspace
${}^{0}\mathbf{p}_j$	Location of obstacle central point
rob	Vector, effective radius of the obstacles
$\mathbf{p}_i$	Vector, locations of joint q_i
q	Vector, joint configuration angles of the mechanisms or manipulators
$\mathbf{q}^0$, **q0**	Vector, mechanism/manipulator unloaded initial configurations
qc	Vector, current joint configuration angles
$\mathbf{S}_0$	Vector, related to the links lengths of manipulator
$\mathbf{S}_1$	Matrices related to the links lengths of manipulator
$\mathbf{S}(u, v)$	Matrix composed of points locations describing several big areas in task space
Set_Qout	Matrix, joint configuration angles corresponding to all the manipulator current motion
Set_Delt	Matrix, configuration control inputs of each segment corresponding to all the manipulator current motion
T	Vector, the manipulator joint torques;
$\mathbf{T}_z$	Diagonal matrix describing the rotation transformation around z-axis by angle π
$\boldsymbol{v}$	Eigenvector
W, $\mathbf{W}_i$	Vector, external wrench (force/torque) applied to the mechanism/manipulator ends
$\Delta\boldsymbol{\Theta}$	Vector, rotation, translation and joint angle deflection of the mechanism system
$\Delta\boldsymbol{\varphi}$	Vector, rotation deflection of the mechanism ends
$\delta\mathbf{F}$	Increment of the external loading applied to the mechanism end
$\Delta\mathbf{p}$	Vector, translation deflection of the mechanism or manipulator ends
$\delta\mathbf{p}$	Vector, end-point translation deflection caused by the loading increment $\delta\mathbf{F}$
$\Delta\mathbf{p}^0$	Vector, end-point translation deflection caused by the initial loading $\mathbf{F}^0$
$\Delta\mathbf{q}$	Vector, joint angle deflections of the mechanisms or manipulators

$\delta\mathbf{q}$	Vector, joint angle deflections caused by the loading increment $\delta\mathbf{F}$
$\Delta\mathbf{q}^*$	Optimal solution for avoiding collisions between the manipulator body and the obstacles in task space
$\Delta\mathbf{t}$, $\Delta\mathbf{t}_i$	Vector, deflection of the mechanism or manipulator ends
$M'(q_i), K(q_i)$	Stiffness coefficients of the joint q_i
φ	Manipulator joint angle parameter
λ	Parameters describing the mechanism-manipulator shape (obtained by computing the critical force causing the buckling)
μ	Parameters describing the mechanism-manipulator shape (obtained by computing the critical force causing the buckling)
$\nabla(\bullet)$	Gradient function
μ_{eq}	Energy factor describing the mechanism-manipulator shape (obtained by computing the critical force causing the buckling) for $q_i \to 0$
(x_0, y_0)	Initial end-point location of the mechanism/manipulator
a_i, b_i	Geometric parameters of the tensegrity mechanisms
C_i, C_{ijk}	Describing cos(q_i) of angle q_i and cos(q_i+ q_j+ q_k) of angle q_i, q_j and q_k respectively
C_{yy}	Beam/link/manipulator compliance coefficient in the lateral deflection y
$C_{\theta y}$	Beam/link compliance coefficient related to the bending angle θ (around z-axis) while deflection is in the lateral deflection y
delta	Distance increment between the points $\mathbf{L}(i, j)$ and $\mathbf{L}(i', j+1)$ computed using the function $dist(\_\,,\_\,)$
$det(\bullet)$	Determinant of matrix
d_{ij}	Distance between the ith joint and the jth obstacle
d_j^0	Allowable minimum value for avoiding collision to the jth obstacle
dmin_ij	The minimum safe distance between the ith joint and the jth obstacle
E	Young's modules of the beams
$E(\Delta)$, $E(q_i)$	Mechanism/manipulator strain energy
F	Force generated by the springs
F_C, F_{Ci}	Critical force causing the buckling phenomenon
F_e	External force applied to the mechanism/manipulator end-point
$f_x(\bullet)$, $f_y(\bullet)$	Forward kinematic functions in x- and y-direction respectively

F_x, F_y	External force applied to the end-point in x- and y-direction respectively
F_x^0, F_y^0	Critical force causing the buckling in x- and y-direction respectively
G	Coulomb’s modules of the beams
I	Minimum area moment of the column/beam cross section
i_0	Row index defining the initial point location $\mathbf{L}(i_0, 0)$
ind_optPij	Element of $\mathbf{ind}(i, j)$
I_y	Second moments of the beams respect to the direction of y
I_z	Second moments of the beams respect to the direction of z
J	Polar moment of the beams
j_0	Row index defining the target point location $\mathbf{L}(i_n, n)$
k, k_i	Springs stiffness coefficients
k_i	Stiffness coefficients of joint q_i
K_{xx}	Beam/link/manipulator stiffness coefficient in the x-deflection
K_{yy}	Beam/link/manipulator stiffness coefficient in the lateral deflection y
L, L_i	Length of the beams or links of the mechanisms/manipulators
L^0, L_{ij}^0	Free length of the springs that applying pre-stress to the tensegrity mechanisms
M_{ext}, M_{e}	External torque applied to the mechanisms
M_i, $M_i(q_i)$	Internal torques generated by the elastic joint q_i
$optP$	Length of the shortest collision-free path connecting the initial point $\mathbf{L}(i_0, 0)$ and the target point $\mathbf{L}(i_n, n)$
$optPij$	Element of $\mathbf{Path}(i, j)$
phi	Manipulator orientation angle
q_C	Mechanism configuration angle corresponding to the buckling phenomenon
q_{crit}	Critical values of configuration angles obtained from $K(q_i)=0$
q_e	Configuration angle corresponding to the equilibriums
q_i	Mechanism configuration angle
q_i^0	Mechanism initial unloaded configuration angle
$q_i^{\max}$	Limited values of joint angles
r_j	Obstacle radius
S	Cross-section area of the beams

S_i, S_{ijk}	Describing sine(q_i) of angle q_i and sine(q_i+ q_j+ q_k) of angle q_i, q_j and q_k respectively
S_w	Workspace area of manipulators
T_i	External torque acting on the joint q_i
U	Strain energy stored in the springs
V	Mechanism system potential energy
var	Variables
w, $w(x)$	Lateral deflection of the column/beam
$x(t_j)$, $y(t_j)$	Current location of the end-point while moving
α, α_i	Mechanism joint angle parameter
Δ	Mechanism translation deflection
$\Delta(q)$, $\Delta(q_i)$	Control inputs for adjusting the pre-stress of the tensegrity mechanisms
$\Delta(x)$, $\Delta(y)$	End-point increments in Cartesian system
Δ_C	Mechanism translation deflection corresponding to the buckling phenomenon
Δq_i	Angle deflections of joint q_i
δx, δy	Deflections of the mechanism/manipulator end-point

INTRODUCTION

Motivation

Nowadays, robots are used in many fields for complicated non-conventional tasks, such as helping with surgery operations, exploring the environment or repairing fiber optic cables in the deep ocean, working in extreme environment (high temperature, radiation, etc.), most of which require *interacting and collaborating* with humans. For this reason, the *end-effectors*, as the most important part of the robots that actively interacting with the environment, are required to execute rather *complicated motions* and to be more *flexible* than the other parts of the robotic manipulators. Consequently, the problem of designing more maneuverable end-effectors are getting more and more attention from robotic engineers.

In practice, the robot end-effectors essentially differ in their designs, which depend on both the executed task and the robot architecture. In manufacturing industry the robot end-effectors are usually equipped with specific tools for welding, machining, laser or plasma cutting, etc. There are also some other types of end-effectors in this area that are allow to grasp, hold or move the target objects. The latter are usually equipped with some gripper mechanisms that can physically grasp by direct impact upon the object, or penetrate the surface of the object. Besides, in the precision machinery or semiconductor industry, in order to avoid damage to the objects, the more popular approach is to use some devices that can generate the attractive or adhesion forces applying to the objects surface, like vacuum. However, there are a number of modern applications where the users are not satisfied with the traditional rigid end-effectors; so they tried to design different kinds of soft grippers that can collaborate with humans and handle fragile objects, like glass, bakery items. But as follows from the relevant studies, the pure soft end-effectors usually cannot provide great output forces, so they are not very attractive in many application fields. On the other hand, combining rigid and elastic or soft components often allows to achieve desired properties and to find reasonable compromise between the end-effector compliance and its ability to generate desired force applied to the object.

One of the promising approaches to obtain the desired end-effector properties is using *small serial manipulators* composed of large number similar segments possessing large or even infinite degree of kinematic redundancy. From the point of view of bioinspired robotics, they are very close to an elephant trunk or snake robots, which can achieve complex motions with high flexibility, and are long and large enough to fit the desired work environment. These advantages are quite important especially for designing the collaborative robots, as they can ensure the safe contact between the robot end-effectors and humans. These motivate us to use the compliant multi-segment serial manipulator as the end-effector rather than conventional simple ones. And to the best of our knowledge, *the tensegrity* *mechanisms*, which are assembly of compressive parts and tensile parts that can change not only their stiffness but also their shapes and sizes in any constrained environment, are very promising for the above mentioned applications. They allow designers to use simultaneously advantages of rigid and elastic or soft components, and to obtain properties required in many fields, such as medical, underwater and aerospace. Their high flexibility and compliances also let them being quite “soft” for using as the robot end-effectors, which allow to avoid the traditional collision problem that is critical for conventional rigid robots. For these reasons, this thesis focuses on the *compliant serial structures composed of a number of similar modules or segments*, each of which is based on the tensegrity mechanisms. Particular attention will be payed to their elastostatic properties and static stability with respect to the external loading. Also, the kinematic control issues for such redundant architectures will be considered.

The practical importance of these problems is also confirmed by financial support provided by the China State Scholarship Fund (No. 201801810036) of the project “CSC-Centrale Schools Program” founded by the China Scholarship Council.

Thesis goal and research problems

This thesis focuses on the design of *new versatile and compliant end-effectors* for collaborative robot works, which are *based on multi-segment planar tensegrity mechanisms* that can be actuated independently to achieve the desired configuration with the required stiffness properties. To achieve this goal, the following problems should be solved:

Problem 1:

Comparison study of different tensegrity mechanisms and *selection of the best architecture* for design of multi-segment robot end-effectors.

Problem 2:

Stiffness analysis of the multi-segment dual-triangle mechanism for both unloaded and loaded modes and detection of possible *nonlinear behaviour* under the loading as well as the *buckling* phenomenon.

Problem 3:

Development of the *kinematic control* strategies for redundant multi-segment mechanism based on dual-triangles allowing to achieve the target endpoint location and avoid collisions with the workspace obstacles.

Thesis structure

To address the above defined problems, the thesis is organized as follows.

Chapter 1:

This part is devoted to the state of art and literature review on the flexible mechanisms or compliant manipulators as the robotic end-effectors for collaborative robots. It includes a review of the conventional and current novel trends in designing the robotic end-effectors, and a review of the tensegrity mechanisms and their applications in robotics. That allows us to choose the dual-triangle tensegrity mechanisms as the base segment of the compliant robot end-effector in this thesis. Three typical stiffness analysis techniques are presented here, from which the VJM technique is chosen as the best for the mechanism stiffness analysis in this work. In addition, the buckling phenomenon in both the traditional mechanical systems and the robotic manipulators were analyzed and compared in this part, which provided us with theoretical base for analysis of nonlinear stiffness behavior in the following chapters. In general, this chapter allowed us to define the goal and the problems studied in this thesis

Chapter 2*:*

This part deals with the stiffness analysis and stability study of two potential tensegrity architectures (X-shape and dual-triangles), which are both actuated by adjusting the pre-stress of the springs located on two sides of the mechanisms, and selection the best of them as the base segment for the compliant serial manipulator end-effector proposed in this thesis. It was demonstrated for the dual-triangle mechanisms that for different combinations of the geometric parameters, the force-deflection relation curves may be either monotonic (a single equilibrium) or non-monotonic (one stable and two unstable equilibriums). While for the X-shape mechanisms, the force-deflection relation curve is always non-monotonic with one stable and two unstable equilibriums. Corresponding stability conditions for both X-shape and dual-triangle mechanisms were presented, and the control strategy for changing the mechanism configuration through adjusting the pre-stress of the springs (for both loaded and unloaded model) was also proposed in this chapter. This allowed to choose appropriate geometric parameters and springs pre-stresses ensuring the mechanism controllability. These results were confirmed by relevant simulation analysis.

Chapter 3*:*

This part is devoted to the stiffness analysis of the two-segment serial structure based on the dual-triangle tensegrity mechanism for both straight and non-straight initial configurations.

For this manipulator, the stiffness matrix was obtained through the VJM technique, and the conventional inverse kinematic transformation for two-link serial manipulator was used straightforwardly. The particularity of this serial mechanism is that, for the initial straight configuration, the buckling phenomenon was detected, and the critical force causing the buckling was obtained analytically. The control strategy presented in chapter 2 was also enhanced. The simulation results confirmed the efficiency of the developed technique.

***Chapter 4**:*

This part is devoted to the analysis of the redundant three-segment serial structure composed of the dual-triangles. Both the analytical and numerical methods were used to find the stable and unstable equilibrium configurations, and to predict the corresponding manipulator shapes. Similar to the previous chapter, it was demonstrated that either buckling or quasi-buckling phenomenon may occur under the loading if the manipulator initial configuration is straight or non-straight one, and the critical force was obtained analytically. Further, the stiffness analysis was carried on for both loaded and unloaded modes, the stiffness matrices were computed using the VJM technique. At last, some useful optimization techniques were applied to solve the geometric redundancy problem, and to ensure the stability of the manipulator configurations with respect to the external forces/torques applied to the end-effector. Relevant kinematics control strategies based on these techniques were proposed, the efficiency and accuracy of which were confirmed by the simulation results.

***Chapter 5**:*

This part is focusing on the general case, dealing with the analysis of the redundant multi-segment serial structure composed of the dual-triangles. For practical convenience, the four-segment manipulator is considered as the basic illustrated example. It was discovered that under the external loading such manipulator may have six equilibrium configurations but only two of them are stable. In the neighborhood of these configurations, the manipulator behavior was analyzed using the VJM technique. This approach allowed us to propose an analytical technique for computing the critical force causing the buckling and evaluate the manipulator shape under the loading. Further, the redundancy resolution in kinematic control of such mechanism while moving in a multi-obstacle environment was considered. The general problem was decomposed into two sub-problems, which deal consequently with the collision-free path planning for the mechanism end-point and the collision-free motion planning for the mechanism body. The first of them was solved via discrete dynamic programming, the second one was solved using quadratic programming with mixed linear equality/inequality constraints. Relevant simulation studies confirmed the efficiency of the proposed technique.

Main contributions

This thesis focuses on the design of new versatile and compliant end-effectors for collaborative work of robots and human operators, which are based on multi-segment planar tensegrity mechanisms that can be actuated independently to achieve the desired configuration with the required stiffness properties. To achieve this goal, three main problems were considered, which were solved gradually by increasing number of segments in the considered compliant mechanism. The main results and contributions of this thesis can be summarized as follows.

For the ***Problem #1***, dealing with the *comparison study* of different mechanisms that can be used for designing compliant end-effectors, two potential tensegrity architectures (*X-shape* and *dual-triangles*) were considered. For both of them, configuration can be adjusted by means of the controllable elastic springs locating on the two edges. It was shown that both of these two options ensure high flexibility and may be potentially used for designing soft robot end-effectors. For practical reasons, the main attention was paid to the symmetrical structure and to the case of equal spring pre-stress, for which the *analytical condition of equilibrium stability* was derived. Also, the relation between the external torque and the deflection was obtained which showed that the X-shape mechanism has always non-monotonic force-deflection relation, while for the dual-triangle one it is possible to achieve the monotonic force-deflection curve. The latter allowed us to conclude that the dual-triangle tensegrity mechanism has essential advantages for the considered application, and it was chosen as the basic structure for the compliant serial manipulator considered in this thesis.

The main results and contributions related to the ***problem* #1** include the following issues.

(i) There were obtained analytical *stability conditions* and *equilibrium configurations* (stable and unstable) for both X-shape and dual-triangle tensegrity mechanisms for unloaded and loaded modes, which allow user to select the mechanical architecture ensuring the controllability of the manipulator based on such segments.

(ii) It was shown that for different combinations of the geometric parameters for the *dual-triangle mechanisms*, the force-deflection relation curves may be either monotonic (a single stable equilibrium) or non-monotonic (one stable and two unstable equilibriums). While for the *X-shape mechanisms*, the force-deflection relation curve is always non-monotonic with one stable and two unstable equilibriums.

For the ***Problem #2,*** dealing with the *stiffness analysis* of the multi-segment dual-triangle mechanism, both unloaded and loaded modes were considered, and specific mechanical properties were analysed in detail. Particular attention was paid to the mechanism stiffness behaviour for the straight and non-straight initial configurations. In this study, the *analytical stiffness/compliance matrices* were derived using the VJM technique that allow designers to evaluate the stiffness sensitivity of this structure with respect to an arbitrary initial configuration for different geometric parameters, external loading and the springs pre-stresses. Besides, the *force-deflection relations* were obtained, which allowed us to detect the *buckling and quasi-buckling phenomenon* in this serial mechanism under the loading. The main theoretical contribution is *an analytical method allowing to compute the critical force* causing the buckling for the serial structure with an arbitrary number of segments, which is based on the eigenvalue analysis of the some special matrix depending on both geometric and elastostatic parameters. This allows designers to predict or avoid the dangerous states of this mechanism by properly changing the geometric parameters and control inputs.

The main results and contributions related to the ***problem* #2** include the following issues

(i) The *stiffness/compliance matrices* of this mechanism for both unloaded and loaded mode, which were obtained using the VJM technique, as well as the mechanism *force-deflection curves*.

(ii) *Mechanism equilibrium configurations* (both stable and unstable ones) and their classification, which were obtained using the energy method.

(iii) Detection of specific mechanical property of this mechanism i.e. the *buckling phenomenon*, which can be observed for the straight initial configuration if the external loading exceeds certain critical value.

(iv) Detection of the *quasi-buckling phenomenon* for the non-straight configuration, when the mechanism resistance in certain direction may be suddenly lost under the loading, while the resistance in other directions still exists.

(v) Analytical technique for *computing the critical force* causing the buckling, which is based on the eigenvalues analysis applied to some special matrix. This technique is rather general and can be applied to other serial manipulators of similar structure.

For the ***Problem #3***, dealing with the *kinematic control* of considered redundant multi-segment mechanism, the optimization-based control strategies were proposed allowing to achieve the target endpoint location and avoid collisions to the workspace obstacles. To generate the desired motions, it is proposed to decompose the general control problem in three separate ones. *The first* of them focuses on the separate segments and is targeting on achieving the desired joint angles of the dual-triangle mechanisms via adjusting the spring pre-stresses. *The second* sub-problem concentrates on the redundancy resolution for the multi-segment manipulator ensuring the end-point displacement to the desired location using minimal joint motion increments. *The third* sub-problem deals with the obstacle-avoidance kinematic control ensuring safe distances between the manipulator segments and some objects located inside of the manipulator workspace. Because of computation of complexity, the last sub-problem was further divided in two sequential steps: (a) *collision-free path planning for the manipulator end-effector*; (b) *collision-free path planning for the manipulator body*, i.e. including intermediate segments. The proposed kinematic control strategy was carefully verified via the computing simulation, which confirmed its advantages and abilities in achieving of the desired manipulator flexibility and shape changing capacity.

The main results and contributions related to the ***problem* #3** include the following issues

(i) *The kinematic control technique for a single segment*, which allows to achieve the desired joint angles of the dual-triangle tensegrity mechanism via anti-symmetrical adjusting the spring pre-stresses (for both loaded and unloaded modes).

(ii) *The collision-free path planning technique for the mechanism end-point*, which is based on discrete dynamic programming that provides the shortest path for reaching the desired target point avoiding the workspace obstacles.

(iii) *The minimum joint motion control technique,* which is based on the quadratic optimization with linear equality constraints that ensures the redundancy resolution and the manipulator end-point displacement to the desired location with minimal joint increments.

(iv) *The obstacle-avoidance kinematic control technique for the manipulator body*, which is based on quadratic programming with mixed linear equality and inequality constraints, allowing to pass through the multi-obstacle environment without collisions while implementing the desired end-point path.

In general, combination of all results related to the problems 1, 2, 3 allow to achieve the desired goal, i.e. to develop a new robot end-effectors based on compliant serial structures composed of a number of similar modules or segments, each of which contains a *tensegrity mechanism*.

Publications and conference presentations

The main results obtained in this thesis have been published in 9 works. Among them, there are two papers in international journals (*Journal of Mechanisms and Robotics*; *International Journal of Mechanical Engineering and Robotics Research*), a book chapter (In: *Lecture Notes in Electrical Engineering*), proceedings of six international conferences (*ICINCO, International Conference on Informatics in Control, Automation and Robotics*; *IDETC, International Design Engineering Technical Conferences and Computers and Information in Engineering Conference; ICCCR, International Conference on Computer, Control and Robotics; CASE, International Conference on Automation Science and Engineering; APMS Advances in production management systems*).

CHAPTER 1
FLEXIBLE SERIAL MANIPULATORS AS END-EFFECTORS FOR COLLABORATIVE ROBOTS

This chapter is devoted to the state of art and literature review on the flexible mechanisms or compliant manipulators as the robotic end-effectors for collaborative robots. It includes a review of the conventional and current novel trends in designing the robotic end-effectors, and a review of the tensegrity mechanisms and their applications in robotics. That allows us to choose the dual-triangle tensegrity mechanisms as the base segment of the compliant robot end-effector in this thesis. Three typical stiffness analysis techniques are presented here, from which the VJM technique is chosen as the best for the mechanism stiffness analysis in this work. In addition, the buckling phenomenon in both the traditional mechanical systems and the robotic manipulators were analyzed and compared in this part, which provided us with theoretical base for analysis of nonlinear stiffness behavior in the following chapters. In general, this chapter allowed us to define the goal and the problems studied in this thesis

1.1 Robot end-effector design: conventional approaches and current trends

In robotics, the end-effector is the end part of the robotic manipulators that interacting with the environment. For achieving the complicated movements, the end-effector should be usually more maneuverable than the other parts of the robots. In practice, the robot end-effectors essentially differ in their designs, which depend on both the executed task and the robot architecture (Lan et al., 2010; Ma and Yang, 2016; Mohammad et al., 2018; Pedersen et al., 2005; Tavakoli et al., 2005). In the first industrial robots, the end-effectors were usually composed of the gripper mechanisms, which can hold or grasp the target objects (Becedas et al., 2011; Bicchi, 2000; Gilardi and Sharf, 2002; King et al., 2009; Singh et al., n.d.; Yang and Wang, 2008). For example, in **Fig. 1. 1a** it is shown a typical end-effector of a serial industrial manipulator, which has two rotational degree of freedoms and where a two-finger device can close and grasp objects (Haugaløkken et al., 2018). Sometimes such manipulators are equipped with a 3-d.o.f. grippers, and the number of fingers may be three or more. In contrast, the famous Delta parallel manipulators, which are very maneuverable because of the parallel architecture, are often equipped with a simple vacuum gripper mechanism as shown in **Fig. 1. 1b** (Nordin et al., 2016).

The above two types of end-effectors are simple and generally used in industry. Nowadays, there are a number of non-industrial applications, especially with collaborative robot work, that require more sophisticated end-effectors. For instance, the Shadow Dexterous Hand shown in **Fig. 1. 1c** is equipped with a multi-finger gripper, which can achieve 24 movements and owns 20 degrees of freedom, allowing increased flexibility in grasping and manipulating a range of objects (Li et al., 2019). Moreover, there are a number of modern applications where the users are not satisfied with the rigid end-effectors; so they tried to design different kinds of soft grippers that can handle fragile objects, like glass, bakery items, etc. One of such examples is shown in **Fig. 1. 1d**, which presents the pneumatically powered mGrip gripper that is made of soft elastomers. At present, there are also some new types of the end-effectors that can achieve the similar tasks but are based on new principles rather than the traditional mechanisms. For example, the end-effectors that are composed of magnetic devices, or some electronic devices (Kim et al., 1992; Tsui et al., 2004). It is worth mentioning that there are a number of other type robot end-effectors that are used for specific industrial tasks, different from the above mentioned grasping and object manipulation (such as welding, machining, laser or plasma cutting, composite fibber placement, etc.) (Abele et al., 2007; Fang et al., 2013; Groppe, 2007; Guo et al., 2015; Kordi et al., 2007; Liang and Bi, 2010; Zhang et al., 2005), but they are out of scope of this thesis.

This work concentrates mainly on the robot end-effectors employed for object grasping and manipulation. Depending on the gripping type, such devices can be classified into four following groups.

- *Impactive*: jaws or claws that physically grasp by direct impact upon the object (used in assembling, packaging, etc.);
- *Ingressive*: pins, needles or hackles that physically penetrate the surface of the object (used in textile, carbon and glass fiber handling);
- *Astrictive*: attractive forces applied to the objects surface (whether by vacuum, magneto- or electro adhesion);
- *Contigutive*: requiring direct contact for adhesion to take place (such as glue, surface tension or freezing).

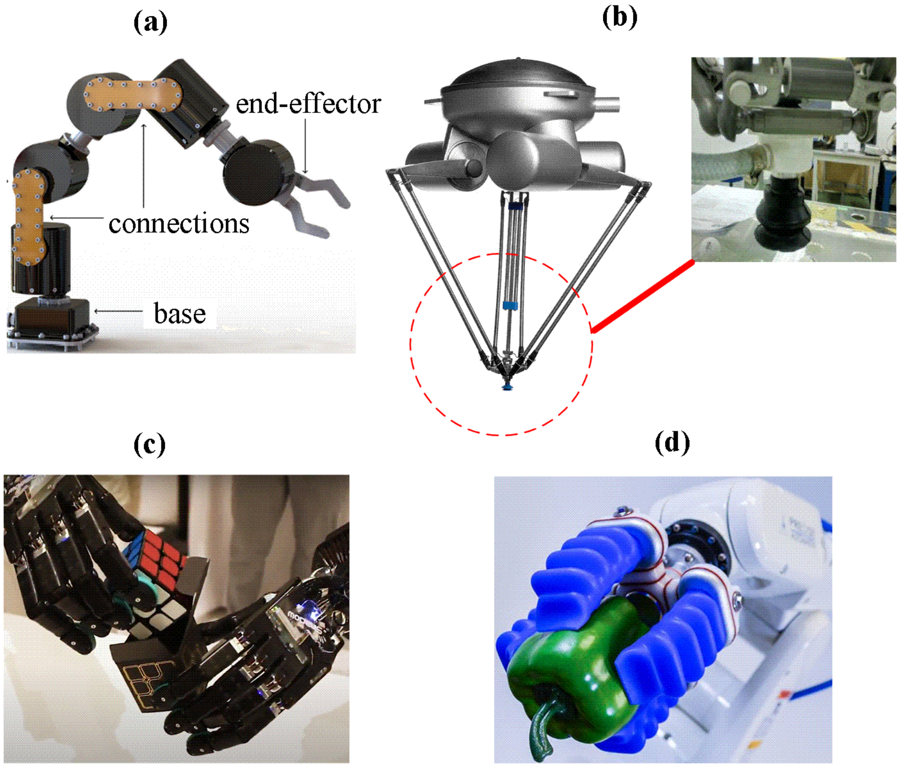

Fig. 1. 1: Different types of robot end-effector: (a) two-finger gripper of a serial industrial manipulator (Haugaløkken et al., 2018); (b): vacuum gripper of Delta parallel robot (Nordin et al., 2016); (c): multi-finger gripper of Shadow Dexterous Hand (Li et al., 2019); (d): soft gripper of mGrip made of elastomers ("Soft Robotics mGrip Circular kit," n.d.).

In designing conventional robot end-effectors, only rigid parts are usually used for connecting articulating joints (such as hinges, axles, or bearings), while elastic deformation of links/joints are considered undesirable. However, there are a growing number of applications that require compliant mechanisms that contain passive or active elastic members such as springs or motors, and can gain their motions from the constrained bending of flexible parts. This allows users to increase the flexibilities of devices and achieve complex motions in very constraint environment. (Albu-Schaffer et al., 2008; Frecker et al., 1997; Howell, 2013; Leidner, 2019; Pan et al., 2018; Wang and Chen, 2009)

A new trend in robotics is to use some flexible continuum compliant devices as the end-effector rather than conventional simple ones. Designers choose the soft flexible mechanisms as the end-effector, such as the total compliant manipulator body (Camarillo et al., 2009, 2009; Gravagne and Walker, 2002; Kang et al., 2013; Konishi et al., 2001; Kumar et al., 2017; McMahan et al., 2006, 2005; Trivedi et al., 2008). Because sometimes the end-effector should be long or large enough so that it can fit the desired work environment and achieve the complicated movements. Two examples of such design are shown in **Fig. 1. 2** . The first of them presented in **Fig. 1. 2a** is the snake robots used for rescuing. Here, the robot itself can be treated as an end-effector, which is composed of similar modular parts that can be added or subtracted to change its length. It can move rapidly through unstructured environments and avoid obstacles by going around or over them, or through small holes in the obstacle, such as a rock pile (Wright et al., 2012). Another example is the robotic elephant trunk of Festo Company (**Fig. 1. 2b**) (Müller et al., 2020). In this case, the small pure soft end-effector is connected with the large soft body, which are all activated by pneumatic. In both examples, the compliance allows robots working safety with human and also achieving complicated movements that traditional rigid manipulators cannot. In the field of modern robotics, there are also some new kinds of manipulators appeared, with multi-d.o.f., and a large or even infinite degree of kinematic redundancy, which may be used for the end-effectors design (Chirikjian, 1993; Huang et al., 2010; Marchese et al., 2014a; Rolf and Steil, 2012; Wang et al., 2013; Webster and Jones, 2010).

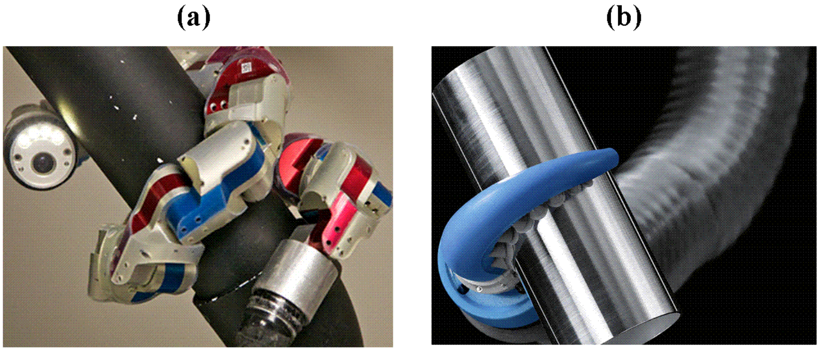

Fig. 1. 2: Examples of soft compliant robot end-effectors: (a) Snake Robots (Wright et al., 2012); (b): Soft Tentacle Gripper of Fest Company (Müller et al., 2020);

For designing the flexible robot end-effectors, similar principles as robotic manipulators can be referred. Generally, the robotic manipulators can be classified into three types, conventional discrete, serpentine, and continuum robots (Robinson and Davies, 1999). The first one is made of traditional rigid components, such design is usually used in industry. The second type, the serpentine robots, uses discrete joints but combine very short rigid links with a large density joints, which produce smooth curves and make the robot similar to a snake or elephant trunk (Chirikjian and Burdick, 1995). And finally the third type, the continuum robots are different with the serpentine robots, they do not contain any rigid links or joints, they are very smooth and soft, bending continuously when working (Yang et al., 2006). Both the serpentine and continuum robots received very great attention in the recent years, their highly articulated structures make them well suited for many applications, such as inspection and operation in highly constrained environments (Chirikjian and Burdick, 1994). But the pure soft continuum robot cannot provide great output force, and considering at the application field, difficulties of design and analysis, the research of it is not so more as the serpentine robots. Thus, combining rigid and elastic or soft components to make part of robot manipulator becomes a popular and useful practice. The typical earlier hyper-redundant robot designs and implementations can be date to 1970s, (Anderson, V. C., & Horn, R. C., 1970), which includes a series of plates interconnected by universal joint and elastic control components for pivotable action with respect to one another, through adjusting the elastic control components, it can be pivoted to desired positions resulting in a snake-like movement of the entire arm assembly (Cieślak and Morecki, 1999; Gravagne and Walker, 2000a, 2000b; Morecki et al., 1988; Rolf and Steil, 2012; Yang and Zhang, 2015).

Recently, robotic engineers started intensively use new types of mechanical structures in compliant robot design. One of the promising trends is employing the *tensegrity mechanisms as the robot end-effectors*. This approach allows efficiently combine useful properties of rigid and elastic or soft components and achieve high flexibility similar to an elephant trunk or snake robot (Gravagne et al., 2003; Grzesiak et al., 2011; Hannan and Walker, 2003; Rolf and Steil, 2014; Tanaka and Matsuno, 2014; Webster and Jones, 2010; Wright et al., 2012; Yang and Zhang, 2015). For these reasons, this thesis focuses on the *compliant serial structures composed of a number of similar modules or segments*, each of which is based on the tensegrity mechanisms. Particular attention will be payed to their elastostatic properties and static stability with respect to the external loading. Also, the kinematic control issues for such redundant architectures will be considered.

1.2 Tensegrity mechanisms and their application in robotics

Recently, robotic engineers started intensively use **new types of manipulator mechanisms** based on **tensegrity structures**, which are assembly of compressive parts and tensile parts held together in equilibrium. Because of their numerous advantages, such structures look very promising for robot end-effector design. Let us consider them in detail.

1.2.1 Definition and history of tensegrity structures

In literature, the word *tensegrity* appeared several decades ago as a conjunction of the two words, *tension* and *integrity* (Fuller, 1962; Snelson, 1965), (Motro, 1990; Motro and Raducanu, 2003; Pugh, 2020; Skelton and Oliveira, 2009). It is usually used to describe the mechanical structures belonging to the class of *prestressable* ones, which should stay at the equilibrium state with the preload inside of the tensile parts. Such structures have some important particularities separating them from the normal pre-stressable structures that have been studied by mechanical engineers for many years. Usually, the compressive parts of tensegrity structures are *rigid bodies or bars*, and the tensile parts are created from *strings or cables* connected to each other and to the rigid bodies end by end. This kind of structures is able to keep its original form (i.e. statically stable) and have many special advantages, like low weight and high flexibility, that attracted attention of many researchers (Bel Hadj Ali and Smith, 2010; Jáuregui, 2020; Schenk et al., 2007; Skelton et al., 2001, 2002; Snelson, 2012; Tran and Lee, 2010; Wang et al., 2020; Wenger and Chablat, 2018, 2019a; P. Zhang et al., 2014).

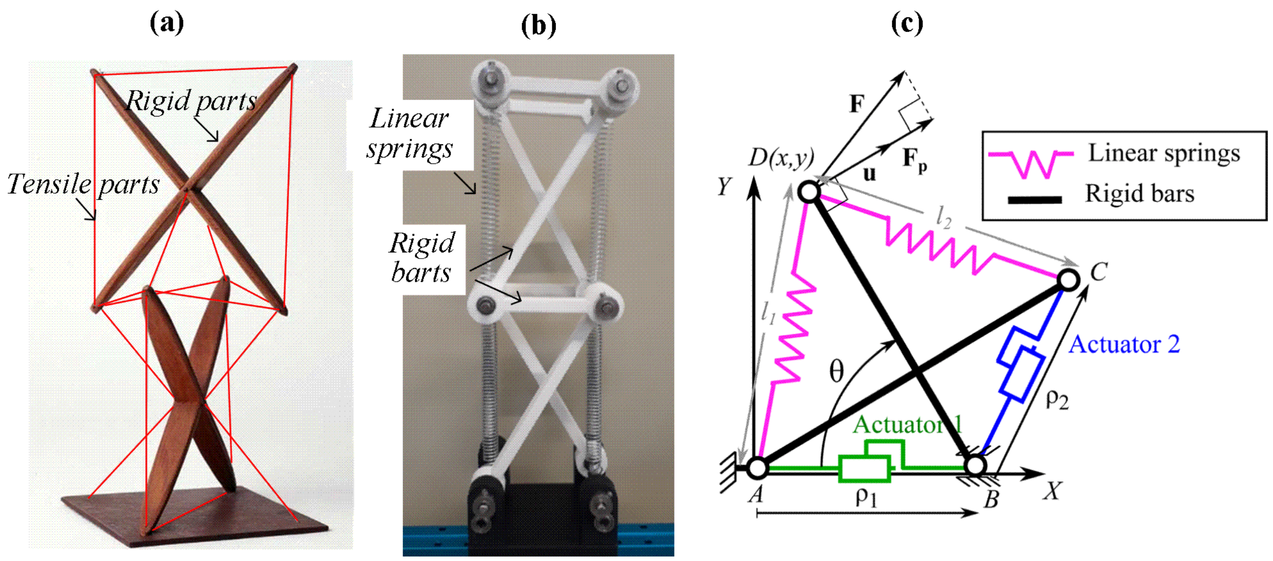

Fig. 1. 3: Typical stable tensegrity structures composed of rigid bodies connected by tensile parts: (a) Snelson's 3DOF X-piece, 1948 (Skelton and Oliveira, 2009). (b): 2-segment serial tensegrity mechanism (Furet and Wenger, 2019a). (c): 2DOF planar tensegrity mechanism (Boehler et al., 2015).

One of the first tensegrity structures widely described in literatures is the famous "X-piece" of Kenneth Snelson proposed in 1948 (Skelton and Oliveira, 2009). This three-dimensional structure is composed of two rigid wooden "X" pieces made up by rigid bars and cables as shown in Fig. 1a. One can change the shape of this art as they wish through adjusting the tensile cables, and also maintain the same shape but increase or decrease the internal force of the tensile cables. It is worth mentioning that, this structure may achieve multiple equilibrium configurations, both stable and unstable ones. Also, this "X-piece" can be considered as a basic module of more complicated structures, created by increasing the number of the pieces in serial or parallel.

Classification for the tensegrity structures is usually based on the number of independent rigid bodies and tensile parts. In particular, in literature can be found numerous examples of tensegrity structures of class 1 (with a single rigid body and a single cable), class 2 (with two rigid bodies and two cables), and so on (Motro and Raducanu, 2003; Skelton and Oliveira, 2009). It should be noted that this classification can be easily applied for the simple structures only, because there are a number of cases when the definition of this classification is not evident. For instance, this two X-piece structure from **Fig. 1**. **3a** composed of 2 rigid bodies and many tensile cables cannot be named through the above classification.

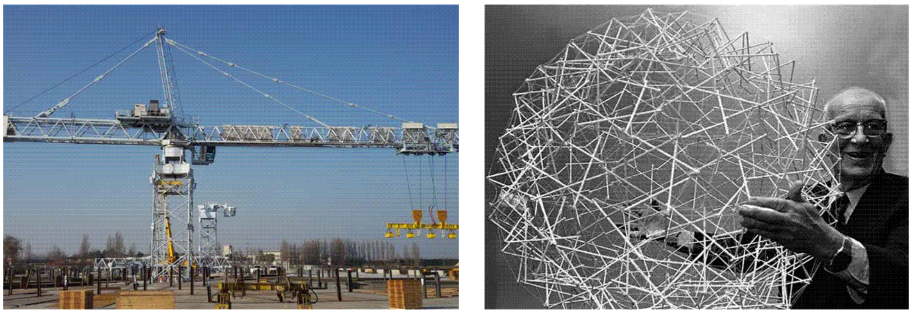

(a) tower crane **(b)** tensegrity spherical architecture

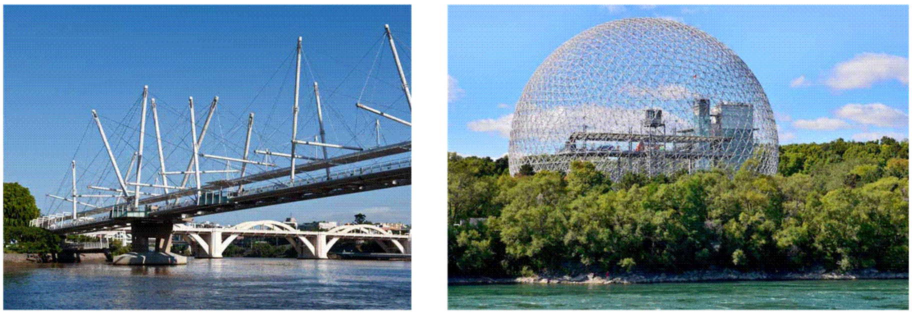

(c) Kurilpa Bridge **(d)** geodesic dome

Fig. 1. 4: Examples of tensegrity structures in engineering, art and architecture (a): the tensegrity tower crane (b) model of the tensegrity spherical architecture designed by R. Buckminster Fuller, 1979; (c): the Kurilpa Bridge based on tensegrity structure in Australia designed by Baulderstone, 2007; (d): the tensegrity geodesic dome of the Montreal Biosphère in Canada designed by R. Buckminster Fuller, 1967 (these images are from Wikipedia).

Besides of the X-piece, there are a number of other interesting tensegrity structures that attracted attention of mechanical engineers. For instance, a planar tensegrity manipulator made of two similar segments in series, which are composed of two rigid bars and linear springs held together was studied by Philippe Wenger et al (Fasquelle et al., 2022; Furet et al., 2019a, 2019b; Furet and Wenger, 2019a, 2019b, n.d.; Muralidharan et al., 2020; Wenger and Chablat, 2019b; Wenger and Furet, 2021). Here, there are four bars for each segment (two on bottom and top and other two crossed inside) and two linear elastic springs on two side of the segment. They form an hourglass shape or X shape, as shown in **Fig. 1**. **3b**. By adjusting the springs the segment can change its shape and stiffness as desired. While different with the Snelson's X-piece, here the two crossed bars inside do not contact each other, they are two independent parts that allows this mechanism achieving more complicated motions. Another mechanism based on X-piece architecture is presented in **Fig. 1**. **3c** (Boehler et al., 2015). Here the tensegrity structure has two inside crossed bars only, but it includes four adjustable tensile parts. There are two linear springs on the top and left, and two adjustable tensile cables or strings with actuators on the bottom and right. Such design allows this type of tensegrity mechanism having larger workspace compared with other ones, and also let the mechanism being more flexible allowing implementing more complicated tasks. In literature, there are a number of other examples, where the tensegrity structures demonstrated very promising properties and unique advantages compared to totally rigid mechanisms (Booth et al., 2020; Furet et al., 2019b; Skelton and Oliveira, 2009).

Tensegrity structures are used in many fields, for example in engineering, arts architecture and medical (Fu, 2005; Levin, 2002), where they are integrated in design of the plane wings, antenna, steel cable bridge and some towers, as shown in **Fig. 1. 4**. The simplest of them is a well-known *tower crane* shown in **Fig. 1. 4a**, where the steel trusses are connected with wire ropes, and the crane can keep balance in stable way for different working conditions by using suitable numbers and types of wire ropes through computing the limit force of it. Another familiar example of tensegrity structure is the *bicycle wheels*. The wheels are connected with a lot of adjustable metal tension-spoke, such design allows the bicycle wheels being light and stable. While here the rigid body is a circle rather as the normal straight one, which means it is no need to consider the stable equilibrium here without any external load, as all the forces focusing on the central point are already stable themselves.

More interesting and attractive tensegrity structures can be found *in architecture*. In particular, R. Buckminster Fuller designed many architectures based on tensegrity structures, which are quite stable and light, and also very beautiful. Some examples are shown in **Fig. 1. 4b** and **Fig. 1. 4d**, where the spherical and shell tensegrity structures can achieve the largest internal space and ultimate load by using the least materials. For this application area, the tensegrity structures allow designers to fix or improve the partial objects rather than to change the whole structure body. Plenty of similar tensile and compressive parts held together also maintaining the structure steadier than the other types. Another famous architecture application of tensegrity structures is the Kurilpa Bridge (**Fig. 1. 4c**), where the straight bridge body is held by many tensile steels along it, which are connected with the columns locating on the bridge. It is similar to a mechanical chain, and it is not hard to imagine that if the tensile steels can be adjusted and the bridge body can be also bended or rotated, this structure will be flexible and controllable. In fact, this excellent properties give very interesting prospective for new designs in mechanisms and robotics, which are considered in detail below.

1.2.2 Mechanical properties of tensegrity structures

In general, the tensegrity mechanisms exhibit high flexibilities with lower weight, but their design requires careful investigation of *static equilibrium configurations and their stability*. For a tensegrity mechanism of equilibrium state, while there is no external forces, the connections between each strings and rigid bars are torqueless (e.g. via frictionless ball-joints or so-called passive joint), if there is a way to let the structure be stable equilibrium through the internal force generated by the internal tensile members, then we say the structure have a *tensegrity configuration*. If no tensile strings are required and/or no set of tensile strings exist to let the structure be stable equilibrium, then it is not a tensegrity configuration. (Bing, 2019; Deng and Kwan, 2005; Masic et al., 2005; Tibert and Pellegrino, 2003; Vassart and Motro, 1999; Zhang and Ohsaki, 2006, n.d.)

It is quite different with the structures that stabilized by the *external forces*, as any stable or unstable equilibriums may occur under the external forces. Actually, to verify if the equilibrium configuration is stable or not, one should do the stiffness analysis of the mechanism, i.e. in practice it means if the structure can return to the original given configuration after the application of arbitrarily small perturbations anywhere within the configuration, it is stable equilibrium, otherwise, it is not. As an example in **Fig. 1. 3b**, the cable-driven X-shape tensegrity structures were considered in (Furet, M., et al. 2018), where each section was composed of four fixed-length rigid bars and two springs. For this mechanism, the authors investigated influence on the cable lengths on the mechanism equilibrium configurations, which maybe both *stable and unstable*.

There is also a very important and useful property that let the tensegrity mechanism being favorite to designers, it is the *variable stiffness*. Because of the elastic strings or cables of the tensegrity mechanisms, one can change the stiffness by using different pre-stress generated by the elastic components without changing its shape. Of course, by suitable design of the geometric structure, one can get the same stiffness from different structure shape. This quite special property gives the tensegrity mechanism a very flexible structure. Besides, it allows to get the desired configuration or the same stiffness either applying the external force or not, through the rule to choose the magnitude of the pre-stress in practical designs. Also, comparing to other mechanism structures, the tensegrity mechanisms can provide rather large stiffness. It means that to generate a same force the tensegrity mechanism may just need a very small "motion" and also a very light weight, which is very attractive in robotics (Amendola et al., 2018; Crane et al., 2005; Guest, 2011; Li et al., 2010; Murakami, 2001; Tran and Lee, 2010; L.-Y. Zhang et al., 2014; Zhang et al., 2012).

Further, designers can also do some optimization to *reduce the weight* of the tensegrity mechanism. One of the possible approaches is based on the well-known buckling formula, which considers the moment when the rigid bars are buckling under the pre-stress. It is possible to combine the Euler's formula with the mass-density formula together, then get the relationship between the geometric parameters of the rigid bars and the critical force causing the buckling, and at last to get the minimal mass of the bars (Carpentieri et al., 2017; Chen and Skelton, 2020; Fraternali et al., 2015; Ma et al., 2020; Nagase and Skelton, 2014; Skelton et al., 2016, 2014). Additionally, one can also use the same method to compute the largest critical force by changing the geometric shape without changing the mechanism mass, which just need to do the optimization of the geometric parameters of the structure.

In literature, there are already some research focusing on the geometric buckling phenomenon in tensegrity mechanisms, with special attention to the work space and singularities analysis (Goyal et al., 2020; Masic et al., 2006; Murakami, 2001; Rimoli, 2018, n.d.; Rimoli and Pal, 2017; Shekastehband et al., 2012; Stamenovic´ and Coughlin, 1999; Volokh et al., 2000). One group of related works (Arsenault and Gosselin, 2006) deals with the mechanism composed of two springs and two length-changeable bars. The authors analysed the mechanism stiffness using the energy method, and demonstrated that the stiffness of this mechanism always decreases when it is subjected to external loads with the actuators locked, which may lead to "buckling". Some other research in this area (Wenger and Chablat, 2018) focus on the three-spring mechanisms, for which the equilibrium configurations stability and singularity were analysed. Using these results the authors obtained conditions under which the mechanism can work continuously, without the "buckling" or "jump" phenomenon.

It is worth mentioning that majority of works dealing with the stiffness analysis of tensegrity structures assume that the primary source of the mechanism flexibility is stiffness of tensile parts while there remaining ones are considered as absolutely rigid. Thus, the material deformation is not usually presented in the model and the force that will buckle a bar is not accurately predicted. However, if one want to know the behavior of this mechanism under large stress (when the bars are bending), or high accuracy is required, then the beam stiffness must be also taken into account.

1.2.3 Tensegrity structures in robotics

Recently, a number of researchers combined the tensegrity mechanism with the robots, which allowed to design excellent novel manipulators that can change not only their stiffness but also their shapes and sizes. This yielded many useful examples of the tensegrity robots that are used in medical, domestic and military applications, such as underwater, aerospace, for inspecting pipelines, patrolling or maintaining tortuous plumbing, for exploring complex underwater structures, or for search and rescue missions (Aldrich et al., 2003; Arsenault and Gosselin, 2008; Booth et al., 2020; Caluwaerts et al., 2014; Graells Rovira and Mirats Tur, 2009; Masic and Skelton, 2004; Paul et al., 2005; Rieffel and Mouret, 2018; Shibata et al., 2009; Zappetti et al., 2020). Their primary advantages are caused by the variable stiffness allowing the tensegrity robots to have high flexibility and compliances, and consequently easily changing their shapes to satisfy any constrained workspace. The high compliances also let the tensegrity robots being quite "soft", which allowed to avoid the traditional collision problem that is critical for convergent rigid manipulators (Chen et al., 2017; Chung et al., 2019; Gravish and Lauder, 2018; Koizumi et al., 2012; Marchese et al., 2014b, 2013; Mintchev et al., 2018, 2018; Roper et al., 2011; Sfakiotakis et al., 1999; Wen et al., 2020). Additionally, as combining with more advanced novel materials and control algorithms, the tensegrity robots become more and more closed to biological structures, which motivate designers to use them in robot end-effectors (replacing operator hands) that is the primary goal of this thesis.

One of the most famous tensegrity robots is the Spherical Under actuated Planetary Exploration Robot ball (SUPERball) of NASA, which is shown in **Fig. 1. 5a**. It is an all-in-one landing and mobility platform based on tensegrity structures, which is designed to explore other planets in the future. It is a collapsible, terrestrial robot based on a tensegrity toy. Before working, the shape of SUPERball is just like a bunch of sticks, every rigid sticks are held together in the smallest volume, while after unfolding, all the sticks acted by the cables build up a big cube. The sphere-like matrix of cables and joints give the robot the ability to withstand being dropped from a spacecraft high above a planetary surface and hit the ground with a bounce. While it is not possible for a traditional robot without buffer device facing to the same substantial impact. Another advantage is that the joints could adjust to roll the SUPERbot in any direction quickly without limited by the obstacles on the ground, unlike the wheeled robots, which must move very slowly and carefully to avoid damage. Also, here this tensegrity structure reduce the robot weight as much as possible, and improve its maneuverability greatly.

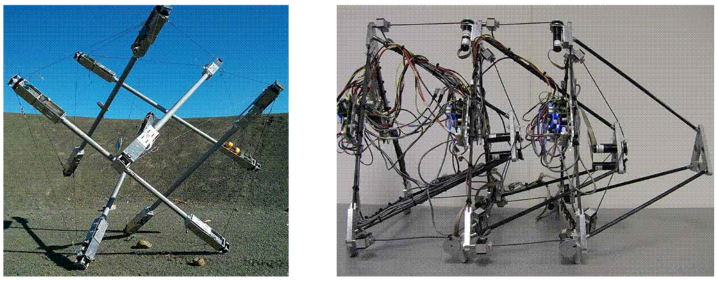

(a) NASA's Super Ball Bot **(b)** spine-like robot

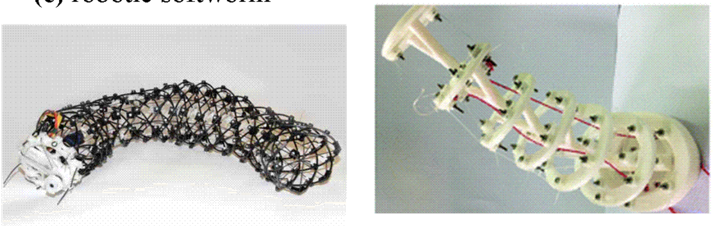

(c) robotic softworm **(d)** robotic fish

Fig. 1. 5: Examples of tensegrity structures in robotic mechanisms: (a) SUPERball of NASA, 2015 (Sabelhaus et al., 2015); (b) the tunably compliant spine-like tensegrity robots of NASA (Mirletz et al., n.d.); (c) CMMWorm of the Case Western Reserve University, 2012 (Kernbaum et al., 2009); (d) the continuous compliant robotic fish by Harbin Institute of Technology, 2019 (Chen and Jiang, 2019).

Another interesting example is the spine-like robot (**Fig. 1. 5b**) that was also designed by NASA. It is composed of similar rigid parts and tensile cables, and is inspired from the biological spine. The goal is to let the spine-like robot being flexible as spine and also can be made up by similar independent modular tensegrity parts. This type of robots have the excellent ability to achieve complicated and difficult manipulation tasks through demonstration of simulations and experiments.

In bio-inspired robotics, the biologically inspired Compliant Modular Mesh Worm robot (CMMWorm) shown in **Fig. 1. 5c** is one of the famous and outstanding works. Miniaturized versions of worm-like robots could find multiple applications in medicine, such as endoscopy or angioplasty. Instead of the traditional design of soft-bodied worm-like robot, they improved the structure and peristaltic motion by adding the hoop actuators that are made of steel cable wrapped around the robot. That change the typical structure of the soft body, which is developed using long braided pneumatic actuators (artificial muscles), into a tensegrity structure. Different is that here the force inside of the tensile cables are activated by the internal fluid pressure inside of the shape memory alloy (details are in reference), not as the other tensegrity structures that directly generate the forces inside of the tensile cables. This robot shows quite outstanding performances, it can imitate the peristaltic motion of worms perfectly and go through very small gap easily.

Another similar example is the tensegrity continuous compliant robotic fish designed by Harbin Institute Technology University (see **Fig. 1. 5d**), the main flexible structure of the robotic fish body was composed with a series of rigid segments linked with tensegrity joints by means of tension elements, and each rigid segment can rotate around tensegrity-compliant joint and have no direct contact with each other. It is a serial-parallel structure that can both have the variable stiffness of serial compliance tensegrity mechanism and the stability of the parallel mechanism. This tensegrity robotic fish can swimming like a fish underwater by controlling the vibrational mode of desired kinematics of locomotion. They had improved the structure compared to the other compliant robotic fish, avoided the energy loses of friction and increased the flexibility through their control algorithm.

The tensegrity structures have also been used for some other soft bio-robots or robotic manipulators, such as the elephant trunk robot, octopus robot, artificial arm and shoulder et al, due to their compliant and flexible capabilities. They are designed for many different purpose, include replacing the human beings or the traditional robots to work in the dangerous or limited space, avoiding the undesired problems caused by people (like the surgery in medicine), and helping people with mobility impairments to work (Fasquelle et al., 2022; Feng et al., 2021; Hustig-Schultz et al., 2016; Levin, 2002; Mirletz et al., 2015; Moored et al., 2006; Sun et al., 2019; Venkateswaran et al., 2021, 2020). All these application requiring the robots to move exactly accurate as people wish, by means that the robots can achieve a serious of continuous motions with high accuracy while working in an environment with obstacles. That needs not only an excellent tensegrity structure, but also an efficient kinematic control strategy, so the controllable tensegrity robots are still in focus of many researchers. As there may be many stable or unstable equilibrium configurations for tensegrity mechanisms, the variable stiffness control for tensegrity mechanisms are quite complicated, which let the stiffness analysis for tensegrity robots be so important. The robots may work without any external load or with quit large external load, a simple stiffness model describing the robots as in traditional mechanics is not enough at all, some accuracy stiffness analysis method concerning both loaded, unloaded and the buckling phenomenon should be taken into account.

1.3 Stiffness of flexible manipulators and existing modelling techniques

It is natural that for the flexible manipulators considered in this thesis, the stiffness is the primary property to be analyzed. It is usually evaluated via stiffness/compliance matrices showing reaction of the robot end-effector location and its shape to the external force/torque. Currently, there are three popular methods for computing these matrices: the Finite Element Analysis (FEA), the Virtual Joint Method (VJM) and the Matrix Structural Analysis (MSA) (Alexandr Klimchik et al., 2019b; Anatol Pashkevich et al., 2011), which are considered in detail below.

1.3.1 Finite Element Analysis

The main idea of FEA is to decompose the physical model of the mechanical structure on a number of rather small (finite) elements and to introduce compliant relations between adjacent nods described by relevant stiffness matrices (Borst et al., 2012; Hrennikoff, 2021; Hughes, 2012; Ramm et al., 2003; Stein, 2014). Then, a number of simple equations describing relations between the element deformations and the corresponding forces/torques are introduced, which are further assembled into a larger system of equations that describes the entire structure. It is worth mentioning that FEA is a rather modern stiffness modelling technique that requires essential computation efforts, but its background can be dated back to the 18th century, when Leonhard Euler presented the famous Euler-Bernoulli beam theory. Further, several investigations related to Finite Element Analysis were developed in the next century (Bathe and Dvorkin, 1986; Courant, 1943, 1943; Hughes and Hulbert, 1988; Jirouseka and Guex, 1986; LANGEFORS, 1952; Melenk and Babuška, 1996; Schellbach, 1851; Simo and Rifai, 1990; Zienkiewicz and Cheung, 1971). FEA is widely used in mechanics and is included in most of 3D modelling software packages.

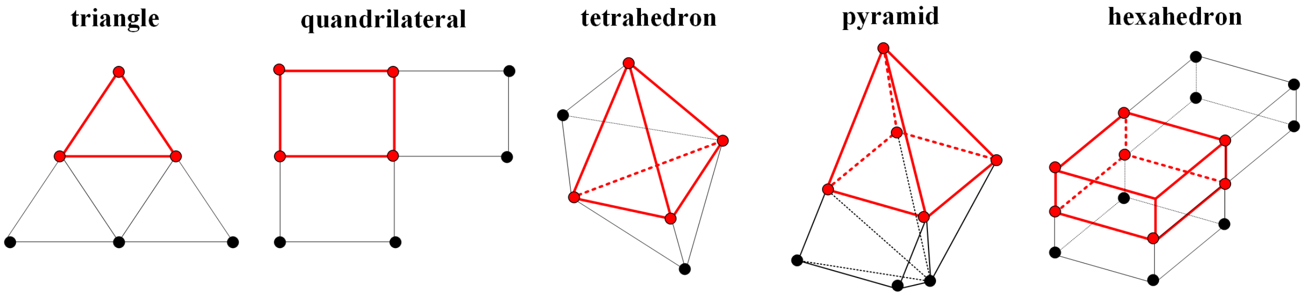

Fig. 1. 6: Typical geometric elements in FEA.

During the FEA-based simulation process, there are usually six steps, which are supported by corresponding software tools:

(1) *Creation of 3D model*: a proper 3D model of the designed mechanical structure is built using a computer, which contains the accurate geometric parameters of the important parts, but ignores the geometric features of the unimportant parts. The reason for such simplification is that the complicated 3D model will increase the calculation time and difficulty, especially the parts that give insignificant or no influence on the stiffness of the total structure.

(2) *Material definition*: for an obtained 3D model, the material properties should also be defined, which include some parameters describing the material resistance under external loading, such as the Elastic Modulus. These parameters are usually known, they will be used to compute the deformation of each small element in step (4).

(3) *Definition of loads and boundary conditions*: at this step the external loads (or sometime internal loads for close-loop structure) and the boundary conditions describing connections of the mechanical structure are defined. This step allows to obtain some additional equations that are further used to compute the forces and torques applied to each parts.

(4) *Meshing*: it is the most important step in the FEA modelling, which essentially influences the modelling accuracy and simulation time. Here, the 3D model is divided into many small elastic elements that are further presented as a set of discrete nodes with flexible connections between them. There are many types of geometric element used in FEA, for example the two-dimensional triangle and quadrilateral, and the three-dimensional tetrahedron, pyramid and hexahedron, which are shown in **Fig. 1. 6**. In practice, selection of the FEA element may influence the simulation results. So, to choose the better one, some other methods or comparative experiments are usually carried on. It should be mentioned that to decrease the computation time, suitable number and geometric size of the finite elements should be defined for each parts of the mechanism structure.

(5) *Simulation*: it is the step that consumes the most of the total FEA modelling time. The computer takes into account all the finite elements obtained above, derives the stiffness models for all of these elements, and then assembles them in the global system of equations describing the force-deflection relations for the total mechanism. Then, after solving these systems, the desired deflections are computed for each node showing the mechanism reaction to the given loads. Besides, the global stiffness matrix for the considered

mechanism structure is computed.

(6) *Post-processing and visualization*: in this step, some additional computations are executed allowing to present the simulation results in a better way. Usually, the 3D model of the mechanism is used with different colors showing the stress distribution as shown in Fig. 5. Also, the contour plots or animations of the force-deflection for the considered mechanism structure may be obtained. These allow directly to find the mechanism weak parts, and also detect some special phenomenon in mechanism stiffness behavior.

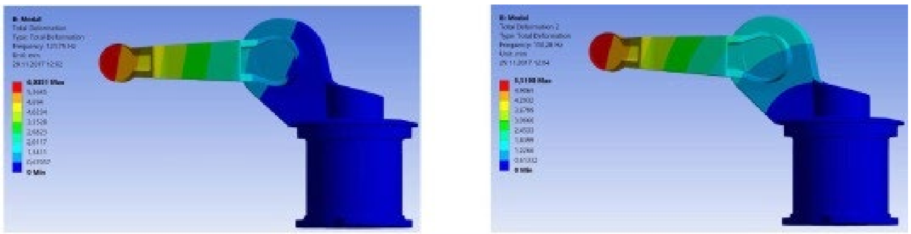

(a) Mode 1 *(twisting)* (b) Mode 2 *(deflection)*

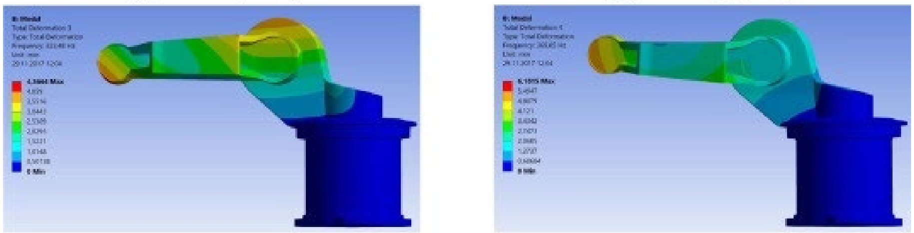

(c) Mode 3 *(twisting)* (d) Mode 4 *(deflection)*

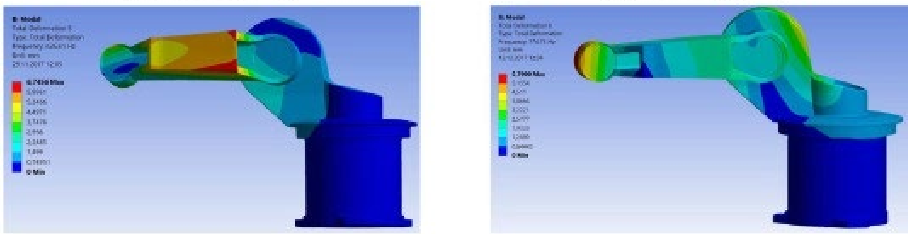

(e) Mode 5 *(twisting)* (f) Mode 6 *(twisting)*

Fig. 1. 7: Example of FEA applications to the design optimization of industrial robotic manipulator (Bugday and Karali, 2019).

An evident advantage of the FEA method is that it can describe the structure deformation and its corresponding stress using the obtained approximated stiffness function continually. Every rather small part of the structure is taken into account and its partial stiffness of each direction in the space can be obtained, an example of the simulation of the steel beam based on FEA is shown in **Fig. 1. 7** (Bugday and Karali, 2019). However, the accuracy of FEA and the number of the discretization step while calculation are not related directly. It means that although FEA requires a large numbers of finite elements, but the round-off errors due to the excessive meshing may reduce the accuracy. Besides, the problem of limited computer memory and the difficulty of the high-dimension matrix inversion is rather critical.

In the frame of the FEA technique, the robotic manipulator can be described in many details with the real shape of its components, allowing to compute the deformation and stress distribution along the links. However, since the manipulator structure becomes more and more complicated, it may contains both serial and parallel components, the FEA technique causes rather high computational expenses for the repeated re-meshing and re-computing. Besides, the manipulator may contains both active and passive joints also, which are quite difficult to be described in the FEA model. So in robotics, this method is usually applied at the final design stage only, or for some robots made of novel materials. For this reason, the FEA technique is not very attractive for the stiffness analysis of the tensegrity mechanisms. In contrast, the Virtual Joint Method (VJM) method and the Matrix Structural Analysis (MSA) method considered below look more suitable for the tensegrity structures studied in this thesis.

1.3.2 Matrix Structural Analysis method (MSA)

This method incorporates the main ideas of FEA but operates with rather large compliant elements such as beams, arcs, cables, etc. This obviously leads to the reduction of the computational expenses and, in some cases, allows us to obtain an analytical stiffness matrix for the specific task (Clinton et al., 1997; D'Altri et al., 2019; Deblaise et al., 2006; Gallagher, 2014; Ghali et al., 2017; Huang et al., 2002; Alexandr Klimchik et al., 2019b; Li et al., 2002; McGuire et al., 2000; Papadrakakis and Sapountzakis, 2018; Pashkevich et al., 2009). Similar to the FEA-modeling the MSA method gives forces/torques and displacements for each node, but here it has a clear physical interpretation (manipulator active or passive joint), which can be useful for some tasks. For parallel robots, this method has been developed in works (A. Klimchik et al., 2018; Alexandr Klimchik et al., 2018a, 2018b, 2019a), where a general technique for stiffness modeling of the manipulator with rigid/flexible links and passive joints was proposed. It has been illustrated by stiffness analysis of parallel manipulator of Delta architecture where the links were approximated by regular beams. The latter causes some doubts in the model accuracy compared to the combination of the FEA and VJM techniques that are being developed here. Besides, this result was obtained under the assumption that the external forces/torques are relatively small (i.e. for the unloaded mode), and it is unlikely that such approach can be enhanced to take into account particularities of manipulator behavior in loaded mode. In addition, here there exists a problem of the stiffness matrix computation for the manipulator singular configurations.

From a computational point of view, the MSA method is less complicated than the FEA-based one. In spite of the fact that MSA still involves matrix operations of rather high-dimension, it gives a reasonable trade-off between the accuracy and computational time, provided that links approximations by the beam elements are realistic. It should be also noted that, in their general formulations, the FEA and MSA methods are closed: both of them interpret physical system as a set of nodes with mutual flexible connections. The main difference is that the MSA operates with true physical objects (like beams, arcs and others), while the FEA decomposes them into small finite elements. So, the MSA can be treated as a special case of the FEA that has already found its application in robotics.

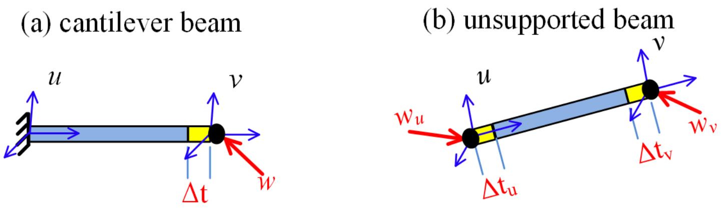

Fig. 1. 8: MSA modeling of cantilever and unsupported beams: nodes, deflections and wrenches(Alexandr Klimchik et al., 2019b).

To introduce the basic principle of the MSA technique, let us apply it first to the simplest mechanical systems, such as the cantilever and unsupported beams. In classical mechanics, the stiffness properties of the *cantilever beam* (fixed at one side, see **Fig. 1. 8a**) are described by the Hook's law that defines a linear relationship between the applied external wrench (force/torque) **W** and corresponding deflection **Δt** at the free-end.

$$\mathbf{W} = \mathbf{K} \cdot \mathbf{\Delta t} \tag{1. 1}$$

where **K** is 6×6 stiffness matrix. It should be mentioned that here **Δt** is a 6-dimensional deflection vector that includes both translational $\mathbf{\Delta p} = [\Delta p_x, \Delta p_y, \Delta p_z]^T$ and rotation $\boldsymbol{\Delta\varphi} = [\Delta\varphi_x, \Delta\varphi_y, \Delta\varphi_z]^T$ components. Similarly, the wrench vector **W** is also 6-dimensional and contains both the force $\mathbf{F} = [F_x, F_y, F_z]^T$ and torque $\mathbf{M} = [M_x, M_y, M_z]^T$ components. In general case, the stiffness matrix **K** from the Hook's law is symmetric and positive definite but may include a number of off-diagonal elements (Alexandr Klimchik et al., 2019b). *For typical beams* commonly used in practice (with regular cross-section) the stiffness matrix can be computed analytically as the formula shown in (1.2) in below, where *L* is the beam length, *S* is the beam cross-section area, *Iy, Iz* are the second moments, *J* is the polar moment, *E* and *G* are Young's and Coulomb's modules of the beam material, respectively. *For more complicated beam shapes*, the above matrix can be obtained numerically by means of the FEA method using technique proposed in (Borst et al., 2012; Hughes, 2012; Kim et al., 2018).

$$\mathbf{K}=\begin{bmatrix} E\cdot S/L & 0 & 0 & 0 & 0 & 0 \\ 0 & 12E\cdot I_z/L^3 & 0 & 0 & 0 & \\ 0 & 0 & 12E\cdot I_y/L^3 & 0 & 6E\cdot I_y/L^2 & 0 \\ 0 & 0 & 0 & G\cdot J/L & 0 & 0 \\ 0 & 0 & 6E\cdot I_y/L^2 & 0 & 4E\cdot I_y/L & 0 \\ 0 & -6E\cdot I_z/L^2 & 0 & 0 & 0 & 4E\cdot I_z/L \end{bmatrix} \tag{1. 2}$$

For the *unsupported beam* (with two non-fixed ends, see **Fig. 1. 8b**) that are used in MSA as principal components, it is necessary to define the deflections and wrenches for both sides. The latter will be further referred to as "*u* "and "*v* "or "1"and "2". In this case, the stiffness model is presented in an extended form

$$\begin{bmatrix} \mathbf{W}_1 \\ \mathbf{W}_2 \end{bmatrix}=\begin{bmatrix} \mathbf{K}_{11} & \mathbf{K}_{12} \\ \mathbf{K}_{21} & \mathbf{K}_{22} \end{bmatrix}_{12\times12}\cdot\begin{bmatrix} \Delta\mathbf{t}_1 \\ \Delta\mathbf{t}_2 \end{bmatrix} \tag{1. 3}$$

that relates the deflections on both sides $\Delta\mathbf{t}_1$, $\Delta\mathbf{t}_2$ and corresponding wrenches $\mathbf{W}_1$, $\mathbf{W}_2$ by means of 12×12 extended stiffness matrix composed of four 6×6 blocks $\mathbf{K}_{11}$, $\mathbf{K}_{12}$, $\mathbf{K}_{21}$, $\mathbf{K}_{22}$. It is clear that this 12×12 matrix is rank deficient since the wrenches $\mathbf{W}_1$, $\mathbf{W}_2$ should satisfy the static equilibrium equation that defines linear dependence between the matrix rows in (1.3). To find the submatrices $\mathbf{K}_{11}$, $\mathbf{K}_{22}$, the boundary conditions should be taken into account, which describes the deflection and force at the beam endpoints. In this case, it is easily to assume that either $\Delta\mathbf{t}_1=0$ or $\Delta\mathbf{t}_2=0$, then by taking it into (1.3), one can get the desired 6×6 blocks, which can be expressed via the classical 6×6 matrix **K** from equation (1.1) in the following way

$$\begin{aligned} &\mathbf{K}_{11}=\mathbf{T}_z^T\cdot\mathbf{K}\cdot\mathbf{T}_z; && \mathbf{K}_{22}=\mathbf{K}; \\ &\mathbf{K}_{12}=-\begin{bmatrix} \mathbf{I}_{3\times3} & \mathbf{0}_{3\times3} \\ [\mathbf{L}\times]^T & \mathbf{I}_{3\times3} \end{bmatrix}\cdot\mathbf{K}_{22}; && \mathbf{K}_{21}=-\begin{bmatrix} \mathbf{I}_{3\times3} & \mathbf{0}_{3\times3} \\ [\mathbf{L}\times] & \mathbf{I}_{3\times3} \end{bmatrix}\cdot\mathbf{K}_{11}=\mathbf{K}_{21}^T \end{aligned} \tag{1. 4}$$

where $[\mathbf{L}\times]$ is the 3×3 skew-symmetric matrix derived from the beam length vector **L** and **I** is the identity matrix, $\mathbf{T}_z$ is the 6×6 diagonal matrix describing the rotation around *z*-axis by angle *π*.

For more complicated mechanical systems, which are composed of several beams with different connections, the desired MSA-based stiffness model can be derived by aggregating the MSA models of separate beams taking into account relations describing the connections. For example, *for the two-link system with rigid connection* (as in **Fig. 1. 9a**), the force deflection relations for the first link can be written using the formula in (1.5) in the below, where nodes numbers 0, 1 denote the coordinate system locating on the endpoints.

$$\begin{bmatrix}\mathbf{W}_0\\ \mathbf{W}_1\end{bmatrix}=\begin{bmatrix}\mathbf{K}_{11}^1 & \mathbf{K}_{12}^1\\ \mathbf{K}_{21}^1 & \mathbf{K}_{22}^1\end{bmatrix}\cdot\begin{bmatrix}\Delta\mathbf{t}_0\\ \Delta\mathbf{t}_1\end{bmatrix} \tag{1. 5}$$

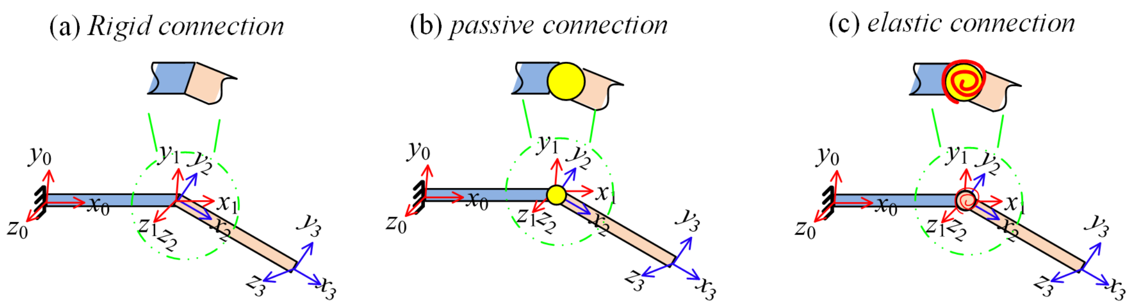
(a) *Rigid connection*
(b) *passive connection*
(c) *elastic connection*

Fig. 1. 9: MSA modeling of two-link systems with different connections

Similarly, for the second link, the MSA-model relation can be obtained using the coordinate transformation of the basic expression, which yields

$$\begin{bmatrix}\mathbf{W}_2\\ \mathbf{W}_3\end{bmatrix}=\begin{bmatrix}\mathbf{T}_z\cdot\mathbf{K}_{11}^2\cdot\mathbf{T}_z^T & \mathbf{T}_z\cdot\mathbf{K}_{12}^2\cdot\mathbf{T}_z^T\\ \mathbf{T}_z\cdot\mathbf{K}_{21}^2\cdot\mathbf{T}_z^T & \mathbf{T}_z\cdot\mathbf{K}_{22}^2\cdot\mathbf{T}_z^T\end{bmatrix}\cdot\begin{bmatrix}\Delta\mathbf{t}_2\\ \Delta\mathbf{t}_3\end{bmatrix} \tag{1. 6}$$

where $\mathbf{T}_z$ is the 6×6 matrix describing the rotation around *z*-axis allowing to transform the frame (x_1, y_1, z_1) to (x_2, y_2, z_2). Then, by combing (1.4), (1.5) and taking into account the boundary conditions describing connections of the link ends,

$$\Delta\mathbf{t}_0=\mathbf{0};\qquad \Delta\mathbf{t}_1=\Delta\mathbf{t}_2;\qquad \mathbf{W}_1=-\mathbf{W}_2 \tag{1. 7}$$

where the first expression describes the left fixed end (node 0) and the remaining ones define the rigid connection between the two links, one can get the desired MSA-based model of the considered two-link system with the rigid connection,

$$\begin{bmatrix}\mathbf{0}\\ \mathbf{W}_3\end{bmatrix}_{12\times1}=\begin{bmatrix}\mathbf{K}_{22}^1+\mathbf{T}_z\cdot\mathbf{K}_{11}^2\cdot\mathbf{T}_z^T & \mathbf{T}_z\cdot\mathbf{K}_{12}^2\cdot\mathbf{T}_z^T\\ \mathbf{T}_z\cdot\mathbf{K}_{21}^2\cdot\mathbf{T}_z^T & \mathbf{T}_z\cdot\mathbf{K}_{22}^2\cdot\mathbf{T}_z^T\end{bmatrix}_{12\times12}\cdot\begin{bmatrix}\Delta\mathbf{t}_2\\ \Delta\mathbf{t}_3\end{bmatrix}_{12\times1} \tag{1. 8}$$

which allows us to compute the deflections $\Delta\mathbf{t}_2$, $\Delta\mathbf{t}_3$ corresponding to the wrench $\mathbf{W}_3$ applied at the right endpoint (node 3). It can be proved that elimination of $\Delta\mathbf{t}_2$ leads to the following expression

$$\mathbf{W}_3=\mathbf{K}_C\cdot\Delta\mathbf{t}_3 \tag{1. 9}$$

where $\mathbf{K}_C$ is the desired stiffness matrix of this two-link system that is related with the stiffness matrices of the separated beams in the following way

$$\mathbf{K}_C = \mathbf{T}_z \cdot \mathbf{K}_{22}^2 \cdot \mathbf{T}_z^T - \mathbf{T}_z \cdot \mathbf{K}_{21}^2 \cdot \mathbf{T}_z^T \cdot (\mathbf{K}_{22}^1 + \mathbf{T}_z \cdot \mathbf{K}_{11}^2 \cdot \mathbf{T}_z^T)^{-1} \cdot \mathbf{T}_z \cdot \mathbf{K}_{12}^2 \cdot \mathbf{T}_z^T \tag{1. 10}$$

It should be mentioned that here the matrix $\mathbf{K}_C$ is non-singular and invertible.

For the two-link system with passive connection (as in **Fig. 1. 9b**), the problem cannot be solved in a straightforward way as above. Here, the force deflection relations for the separate beams can be also written as (1.4) and (1.5). However, the boundary conditions for this case are different and may be presented as follows

$$\begin{array}{lll} \Delta\mathbf{t}_0 = \mathbf{0}; & \boldsymbol{\Lambda}^r \cdot (\Delta\mathbf{t}_1 - \Delta\mathbf{t}_2) = \mathbf{0}; & \\ \boldsymbol{\Lambda}^r \cdot (\mathbf{W}_1 + \mathbf{W}_2) = \mathbf{0}; & \boldsymbol{\Lambda}^p \cdot \mathbf{W}_1 = \mathbf{0}; & \boldsymbol{\Lambda}^p \cdot \mathbf{W}_2 = \mathbf{0} \end{array} \tag{1. 11}$$

where the subscripts “r” and “p” denote the rigid and passive connections, and the corresponding matrices $\boldsymbol{\Lambda}^r$, $\boldsymbol{\Lambda}^p$ describing the passive joint are $\boldsymbol{\Lambda}^r = diag(1,1,1,1,1,0)$, $\boldsymbol{\Lambda}^p = diag(0,0,0,0,0,1)$. The first of them $\boldsymbol{\Lambda}^r$ ensures that the angle deflection in the direction of *z*-axis is not taken into account, as well as that the 3-rd Newton’s law is not applied to the corresponding wrench components. The second matrix $\boldsymbol{\Lambda}^p$ is used to ensure that these wrench components (torques with respect to the *z*-axis) are equal to zero. It should be mentioned that here both $\boldsymbol{\Lambda}^r$ and $\boldsymbol{\Lambda}^p$ are diagonal matrices but in the general case, for arbitrary direction of the passive joint axis, they can be non-diagonal.

Using such boundary conditions (1.10) and combining them with the link MSA models (1.4) and (1.5), one can obtain the following linear system with 12 zero rows

$$\begin{bmatrix} \mathbf{0} \\ \mathbf{0} \\ \mathbf{0} \\ \mathbf{0} \\ \mathbf{W}_3 \end{bmatrix}_{30\times1} = \begin{bmatrix} \boldsymbol{\Lambda}^r & -\boldsymbol{\Lambda}^r & \mathbf{0}_{6\times6} \\ \boldsymbol{\Lambda}^p \cdot \mathbf{K}_{22}^1 & \mathbf{0}_{6\times6} & \mathbf{0}_{6\times6} \\ \mathbf{0}_{6\times6} & \boldsymbol{\Lambda}^p \cdot \mathbf{T}_z \cdot \mathbf{K}_{11}^2 \cdot \mathbf{T}_z^T & \boldsymbol{\Lambda}^p \cdot \mathbf{T}_z \cdot \mathbf{K}_{12}^2 \cdot \mathbf{T}_z^T \\ \boldsymbol{\Lambda}^r \cdot \mathbf{K}_{22}^1 & \boldsymbol{\Lambda}^r \cdot \mathbf{T}_z \cdot \mathbf{K}_{11}^2 \cdot \mathbf{T}_z^T & \boldsymbol{\Lambda}^r \cdot \mathbf{T}_z \cdot \mathbf{K}_{12}^2 \cdot \mathbf{T}_z^T \\ \mathbf{0}_{6\times6} & \mathbf{T}_z \cdot \mathbf{K}_{21}^2 \cdot \mathbf{T}_z^T & \mathbf{T}_z \cdot \mathbf{K}_{22}^2 \cdot \mathbf{T}_z^T \end{bmatrix}_{30\times18} \cdot \begin{bmatrix} \Delta\mathbf{t}_1 \\ \Delta\mathbf{t}_2 \\ \Delta\mathbf{t}_3 \end{bmatrix}_{18\times1} \tag{1. 12}$$

that can be further presented in a more compact way as follows

$$\begin{bmatrix} \mathbf{0}_{12\times1} \\ \mathbf{W}_3 \end{bmatrix}_{18\times1} = \begin{bmatrix} \mathbf{A}_1 & \mathbf{B}_1 \\ \mathbf{C}_1 & \mathbf{D}_1 \end{bmatrix}_{18\times18} \cdot \begin{bmatrix} \Delta\mathbf{t}_1 \\ \Delta\mathbf{t}_2 \\ \Delta\mathbf{t}_3 \end{bmatrix}_{18\times1} \tag{1. 13}$$

where the detailed expressions for the block matrices $\mathbf{A}_1, \mathbf{B}_1, \mathbf{C}_1, \mathbf{D}_1$ can be found in (A. Klimchik et al., 2019b). Further, similar to the above case, expression (1.12) can be simplified by eliminating $\Delta\mathbf{t}_1$, $\Delta\mathbf{t}_2$, which yields the desired stiffness model

$$\mathbf{W}_3 = \mathbf{K}_C \cdot \Delta\mathbf{t}_3$$

with the stiffness matrix

$$\mathbf{K}_C = \mathbf{D}_1 - \mathbf{C}_1 \cdot \mathbf{A}_1^{-1} \cdot \mathbf{B}_1 \tag{1. 14}$$

which should be obviously rank-deficient because of the passive joint.

For the two-link system with elastic connection (as in **Fig. 1. 9c**), the general force deflection relations of the separate links (1.4) and (1.5) should be considered together with the boundary conditions describing the elastic connections that are presented as follows

$$\begin{aligned} &\Delta\mathbf{t}_0 = \mathbf{0}; && \mathbf{W}_1 = -\mathbf{W}_2; \\ &\mathbf{\Lambda}^r \cdot (\Delta\mathbf{t}_1 - \Delta\mathbf{t}_2) = \mathbf{0}; && \mathbf{\Lambda}^e \cdot \mathbf{W}_2 = K_q \cdot \mathbf{\Lambda}^e \cdot (\Delta\mathbf{t}_2 - \Delta\mathbf{t}_1) \end{aligned} \tag{1. 15}$$

where K_q is the stiffness coefficient of the elastic connection, the subscripts "r" and "e" denote the rigid and elastic connections, and the corresponding diagonal matrices are $\mathbf{\Lambda}^r = diag(1,1,1,1,1,0)$, $\mathbf{\Lambda}^e = diag(0,0,0,0,0,1)$. Here the matrix $\mathbf{\Lambda}^r$ also ensures that the angle deflection in the direction of *z*-axis is not taken into account. However, the second matrix $\mathbf{\Lambda}^e$ is used here to describe the Hook's law which is applied to the rotation around *z*-axis. Similar to the previous case, the equations (1.4), (1.5) and (1.11) can be also presented in a more compact way as

$$\begin{bmatrix} \mathbf{0}_{12\times1} \\ \mathbf{W}_3 \end{bmatrix}_{18\times1} = \begin{bmatrix} \mathbf{A}_2 & \mathbf{B}_2 \\ \mathbf{C}_2 & \mathbf{D}_2 \end{bmatrix}_{18\times18} \cdot \begin{bmatrix} \Delta\mathbf{t}_1 \\ \Delta\mathbf{t}_2 \\ \Delta\mathbf{t}_3 \end{bmatrix}_{18\times1} \tag{1. 16}$$

with the slightly different block matrices $\mathbf{A}_2, \mathbf{B}_2, \mathbf{C}_2, \mathbf{D}_2$ that can be found in (A. Klimchik et al., 2019b). Further, the above expression (1.12) can also be simplified by eliminating $\Delta\mathbf{t}_1$, $\Delta\mathbf{t}_2$ and that yields the desired stiffness model

$$\mathbf{W}_3 = \mathbf{K}_C \cdot \Delta\mathbf{t}_3$$

with the full-rank stiffness matrix (1.17) that depends on both the stiffness properties of the beams and the stiffness coefficient of the elastic connection.

$$\mathbf{K}_C = \mathbf{D}_2 - \mathbf{C}_2 \cdot \mathbf{A}_2^{-1} \cdot \mathbf{B}_2 \tag{1. 17}$$

Hence, as follows from the above presented case studies, the MSA technique allows us to compute the system stiffness matrix quite easy compared to the FEA technique. It is obviously that this approach can be straightforwardly used for the multi-link system with the given different types of connections. For the MSA, the final expression is simpler and includes the matrices of lower dimensions than FEA method. For example, in (A. Klimchik et al., 2019; Alexandr Klimchik et al., 2018b) the authors used the MSA technique to study the NAVARO robot, which is a 3-d.o.f. planar parallel manipulator with variable actuation schemes. By combining all equations describing the constraints and boundary conditions, they first expressed the stiffness model of the separate manipulator legs using 120×120 matrices for each of them, which were further simplified to the form with a matrix of size 42×42. So, in spite of evident advantage compared to the FEA method, the MSA technique still requires numerical inversion of matrices of rather high dimension. The later motivates us to investigate another stiffness modeling approach, the VJM method, which is computationally simpler especially for the serial mechanical structures.

1.3.3 Virtual Joint Method (VJM)

This method was first introduced by Salisbury and Gosselin (Gosselin, 1990; Majou et al., 2007; Salisbury, 1980) who assumed that all flexibilities of the multilink robot are located in the connection joints that are presented as one-dimensional springs with corresponding stiffness coefficient, which are combined together using the kinematic Jacobian. This allows to obtain the robot stiffness/compliance matrix of a rather simple form, which is widely used in many research works devoted to the manipulator stiffness analysis. The main idea of this technique is an extension of the conventional rigid-body model of the robotic manipulator, where the links are treated as rigid but the joints are assumed to be compliant (in order to accumulate all types of existing flexibilities in the joints only) (Alici and Shirinzadeh, 2005; Alexandr Klimchik et al., 2012; Klimchik et al., 2014; Pashkevich et al., 2009; Sun et al., 2016; Taghvaeipour et al., 2012; Wang et al., 2017; Zhang, 2005). To introduce the VJM technique in detail, let us consider a planar two-link manipulator as a simple example, which is shown in **Fig. 1. 10**.

For this manipulator, the relation between the joint angle deflections $\Delta\mathbf{q} = [\Delta q_1, \Delta q_2]^T$ and the end-defector deflections $\Delta\mathbf{p} = \left[\Delta x, \Delta y\right]^T$ can be obtained from the differential geometric model as shown in (1.18) in below,

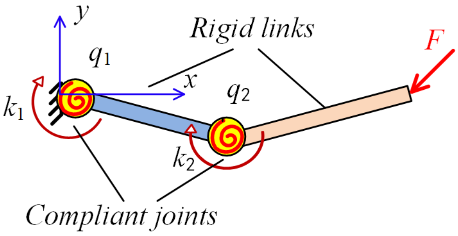

Fig. 1. 10: VJM modeling of two-link manipulator: rigid links and compliant joints

$$\Delta\mathbf{p} = \mathbf{J}_q \cdot \Delta\mathbf{q} \tag{1. 18}$$

where   is the kinematic Jacobian matrix of this manipulator that is written here in the following way

$$\mathbf{J}_q = \begin{bmatrix} -L_1S_1 - L_2S_{12} & -L_2S_{12} \\ L_1C_1 + L_2C_{12} & L_2C_{12} \end{bmatrix} \mathbf{J}_q \tag{1. 19}$$

and depends both on the link lengths L_1 , L_2 and the manipulator joint angles $\mathbf{q} = (q_1, q_2)$ included in expressions $C_1 = \cos q_1$, $S_1 = \sin q_1$, $C_{12} = \cos(q_1 + q_2)$, $S_{12} = \sin(q_1 + q_2)$. Besides, from the static equilibrium condition, the manipulator joint torques $\mathbf{T} = [T_1, T_2]^T$ and the external force $\mathbf{F} = [F_x, F_y]^T$ applied to the end-effector are related by the equation

$$\mathbf{T} + \mathbf{J}_q^T \cdot \mathbf{F} = \mathbf{0} \tag{1. 20}$$

where **T** can be computed using the Hook's law and expressed via the joint deflections $\Delta\mathbf{q}$ and the diagonal matrix $\mathbf{K}_q = diag(k_1, k_2)$ of the joint stiffness coefficients as follows

$$\mathbf{T} = \mathbf{K}_q \cdot \Delta\mathbf{q} \tag{1. 21}$$

After combining these geometric and static equations, one can obtain the linearized force-deflection relation

$$\Delta\mathbf{p} = -\left(\mathbf{J}_q \cdot \mathbf{K}_q^{-1} \cdot \mathbf{J}_q^T\right) \cdot \mathbf{F} \tag{1. 22}$$

allowing us to compute the manipulator reaction $\Delta\mathbf{p}$ to the external force **F**. Thus we obtain the desired compliance matrix $\mathbf{C}_q$ of this manipulator

$$\mathbf{C}_q = \mathbf{J}_q \cdot \mathbf{K}_q^{-1} \cdot \mathbf{J}_q^T \tag{1. 23}$$

and its Cartesian stiffness matrix, which is the inverse of $\mathbf{C}_q$

$$\mathbf{K}_C = \left(\mathbf{J}_q \cdot \mathbf{K}_q^{-1} \cdot \mathbf{J}_q^T\right)^{-1} \tag{1. 24}$$

It should be mentioned that here the compliance matrix $\mathbf{C}_q$ is usually invertible, except of some singular configurations with $q_2 = 0$ or $q_2 = \pm\pi$.

Geometrically, the VJM technique is equivalent to adding to the joints some auxiliary virtual joints, such as the rotational springs in the above presented case. For some other cases, the links can also be considered as elastic, whose stiffness may be described as the stiffness coefficient or beam matrix, then combined with the corresponding Jacobian matrix one can also obtain the similar results. Corresponding extension of this method is known as an *enhanced VJM technique* (A. Klimchik et al., 2012; Anatol Pashkevich et al., 2011). Let us present it for the same two-link planar manipulator shown in Fig. 8 for which the elasticity of each link can be described by a 3×3 matrix derived directly from the 6×6 matrix (1.2) describing a three-dimensional beam

$$\mathbf{K}_{link} = \begin{bmatrix} E \cdot S/L & 0 & 6E \cdot I_z/L^2 \\ 0 & 12E \cdot I_z/L^3 & 0 \\ 0 & -6E \cdot I_z/L^2 & 4E \cdot I_z/L \end{bmatrix} \tag{1. 25}$$

It should be mentioned that such presentation deals with additional elastic deflections $(\Delta x, \Delta y, \Delta\varphi_z)$. So totally, the extended VJM model includes eight deflections where six of them are related with the link elasticities and the remaining two $(\Delta q_1, \Delta q_2)$ describe the joint flexibilities. After combining these deflections in a single vector

$$\Delta\mathbf{\Theta} = [\Delta q_1, \Delta q_2, \Delta x_1, \Delta y_1, \Delta\varphi_{z1}, \Delta x_2, \Delta y_2, \Delta\varphi_{z2}] \tag{1. 26}$$

and aggregating the joint/link stiffness matrices in a single one

$$\mathbf{K}_{aggr} = \left[\begin{array}{c:cc} \mathbf{K}_q & & \\ \hdashline & \mathbf{K}_{link}^{(1)} & \\ & & \mathbf{K}_{link}^{(2)} \end{array}\right]_{8\times 8} \tag{1. 27}$$

we can obtain the desired expression for the compliance matrix

$$\mathbf{C}_q = \mathbf{J}_{aggr} \cdot \mathbf{K}_{aggr}^{-1} \cdot \mathbf{J}_{aggr}^T \tag{1. 28}$$

which includes the aggregating Jacobian $\mathbf{J}_{aggr}$ of size 2×8 corresponding to the deflection vector $\Delta\mathbf{\Theta}$:

$$\mathbf{J}_{aggr} = \left[\begin{array}{cc|ccc|ccc} -L_1S_1 - L_2S_{12} & -L_2S_{12} & C_1 & -S_1 & -L_2S_{12} & C_{12} & -S_{12} & 0 \\ L_1C_1 + L_2C_{12} & L_2C_{12} & S_1 & C_1 & L_2C_{12} & S_{12} & C_{12} & 0 \end{array}\right]_{2\times 8} \tag{1. 29}$$

It is obvious that, compared to the MSA method, such technique essentially simplifies the robot stiffness analysis and it can also be used for the multi-link serial manipulator. So, at present it is the most popular stiffness analysis method in robotics.

The VJM technique is also useful for the stiffness analysis of the *parallel manipulators*, relevant case studies can be found in (Gosselin, 1990; A. Klimchik et al., 2012; Wang et al., 2017). The simplest parallel manipulator considered here has several separate serial chains that are connected to each other at the end-effector only. Physically, each serial chains has the same end-defector deflection $\Delta\mathbf{p}$, but the external loading $\mathbf{F}$ is distributed between the chains in such a way that $\mathbf{F} = \mathbf{F}_1 + \mathbf{F}_2 + \ldots$ where $\mathbf{F}_i = \mathbf{K}_C^{(i)} \cdot \Delta\mathbf{p}$. Thus the total Cartesian stiffness matrix for this manipulator is the sum of partial ones of each chain and the linearized force-deflection relation is expressed as follows

$$\mathbf{F} = \sum_{i=1}^{n} \mathbf{K}_C^{(i)} \cdot \Delta\mathbf{p} \tag{1. 30}$$

It should be noted that in literature (A. Klimchik et al., 2012; Klimchik et al., 2014) there are a number of examples where the partial stiffness matrix of the chains are rank-deficient but the total Cartesian stiffness matrix is non-singular. And this technique was also extended for parallel manipulators with more complicated geometry where the serial chains are not connected in a single point but are linked to a rigid or flexible platform. However, for some parallel manipulators of complicated architectures (with internal close-loops or parallelogram-based links), this formula cannot be used straightforwardly, some essential modifications are required.

Another important extension of the VJM method is related to taking into account the influence of the *passive joints*. For serial kinematic chains with passive joints the problem has been studied in detail in (Anatol Pashkevich et al., 2011). Let us illustrate this approach for a simple two-link manipulator with the passive connection between the first and second links and the elastic connection between the first link and the base as shown in **Fig. 1. 11**. For this manipulator, the end-effector deflection can be expressed from the geometry as

$$\Delta\mathbf{p} = \mathbf{J}_q \cdot \Delta q + \mathbf{J}_\theta \cdot \Delta\theta \tag{1. 31}$$

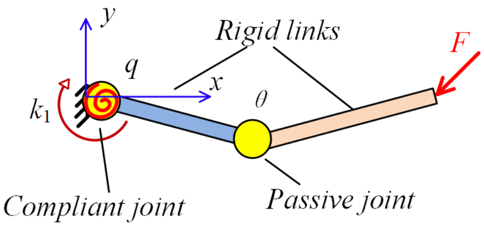

Fig. 1. 11: VJM modeling of two-link manipulator with an elastic and a passive joint.

where $\mathbf{J}_q$ is the kinematic Jacobian matrix of this manipulator related to the angle q of the elastic joint, $\mathbf{J}_\theta$ is the Jacobian matrix related to the angle θ of the passive joint. As the second joint is the passive one, it does not generate the internal torque, so here $T_2 = 0$ while the torque for the first joint is computed similar to the above case, i.e. $T_1 = k_1 \cdot \Delta q$. Then from the static equilibrium condition we can rewrite the equation $T_2 = 0$ as

$$\mathbf{J}_\theta^T \cdot \mathbf{F} = 0 \tag{1. 32}$$

For the elastic joint, the force-deflection relation can also be expressed similarly as the above

$$\mathbf{J}_q \cdot \Delta q = -\mathbf{J}_q \cdot k_1^{-1} \cdot \mathbf{J}_q^T \cdot \mathbf{F} \tag{1. 33}$$

Further, by combining (1.31) and (1.32) we can get the redundant system of equations describing the relation between the external force $\mathbf{F}$ and end-effector deflection $\Delta\mathbf{p}$

$$\begin{pmatrix} \Delta\mathbf{p} \\ 0 \end{pmatrix} = \begin{pmatrix} \mathbf{J}_q k_1^{-1} \mathbf{J}_q^T & \mathbf{J}_\theta \\ \mathbf{J}_\theta^T & 0 \end{pmatrix}_{3\times3} \cdot \begin{pmatrix} \mathbf{F} \\ \theta \end{pmatrix} \tag{1. 34}$$

where the passive joint angle θ is treated as the redundant variable. From this system, the desired force-deflection relation $\mathbf{F} = \mathbf{K}_C \cdot \Delta\mathbf{p}$ can be found either numerically or analytically. The first approach is based on the direct inversion of the relevant 3×3 matrix in (1.33) and extracting from it the 2×2 sub-matrix corresponding to $\mathbf{J}_q k_1^{-1} \mathbf{J}_q^T$. The second approach yields the following expression for the

Cartesian stiffness matrix

$$\mathbf{K}_C = \mathbf{C}^{-1} - \mathbf{C}^{-1}\mathbf{J}_\theta\left(\mathbf{J}_\theta^T\mathbf{C}^{-1}\mathbf{J}_\theta\right)^{-1}\mathbf{J}_\theta^T\mathbf{C}^{-1} \tag{1. 35}$$

where $\mathbf{C} = \mathbf{J}_q k_1^{-1}\mathbf{J}_q^T$ is the compliance matrix .

It is worth mentioning that here the 3×3 matrix in (1.33) is invertible but its inversion reduces the 2×2 stiffness matrix $\mathbf{K}_c$ which is rank-deficient. Hence, it is not impossible to compute the compliance matrix for this manipulator, it does not exist for the serial chain with a passive joint from the point of view of mechanics. This method was also generalized for the serial chains with an arbitrary number of flexible links and an arbitrary number of passive and/or elastic connections (Anatol Pashkevich et al., 2011). Its main advantage is the computational simplicity, since the number of the virtual springs does not influence on the size of matrix to be inverted. Besides, the method does not require manual elimination of the redundant variables corresponding to the passive joints, since this operation is inherently included in the numerical algorithm.

The VJM technique was also extended to the case when the manipulator is subject of essential loading (both internal and external). In contrast to the unloaded case, where the external force $\mathbf{F} = \delta\mathbf{F}$ is assumed to be very small, here the force $\mathbf{F} = \mathbf{F}^0 + \delta\mathbf{F}$ is rather large. So, the derivatives included in Jacobian must be computed for another configuration variable $(\mathbf{q} + \Delta\mathbf{q})$ where $\mathbf{q}$ corresponds to the unloaded case, and $\Delta\mathbf{q}$ denotes the joint deflection caused by the loading $\mathbf{F}^0$. Nevertheless, the static equilibrium condition is also written here using (1.19) and (1.20) that yields the basic equation for the loaded equilibrium

$$\mathbf{J}_q^T \cdot \mathbf{F} + \mathbf{K}_q \cdot \Delta\mathbf{q} = \mathbf{0} \tag{1. 36}$$

where Jacobian $\mathbf{J}_q$ is computed for $(\mathbf{q} + \Delta\mathbf{q})$ and $\mathbf{K}_q$ denotes the virtual joint stiffness coefficients. Within this technique, the total end-effector deflection $\Delta\mathbf{p} = \Delta\mathbf{p}^0 + \delta\mathbf{p}$ is also presented as a sum of two components where $\Delta\mathbf{p}^0$ is caused by the loading $\mathbf{F}^0$ and $\delta\mathbf{p}$ corresponds to $\delta\mathbf{F}$. Application of the above equation for the loading $\mathbf{F} = \mathbf{F}^0 + \delta\mathbf{F}$ and computing relevant differentials yields

$$\delta\left(\mathbf{J}_q^T \cdot \mathbf{F}\right) + \delta\left(\mathbf{K}_q \cdot \Delta\mathbf{q}\right) = \mathbf{0} \tag{1. 37}$$

that can be further rewritten as follows

$$\left(\frac{d\mathbf{J}_q^T}{d\mathbf{q}}\delta\mathbf{q}\right) \cdot \mathbf{F} + \mathbf{J}_q^T \cdot \delta\mathbf{F} + \mathbf{K}_q \cdot \delta\mathbf{q} = \mathbf{0} \tag{1. 38}$$

where the part including the Jacobian derivative $d\mathbf{J}_q^T / d\mathbf{q}$ can be presented as $\mathbf{K}_g \cdot \delta\mathbf{q}$ with

$$\mathbf{K}_g = \frac{\partial \mathbf{J}^{\mathrm{T}}}{\partial q_i}\mathbf{F} = \left[\frac{\partial \mathbf{J}^{\mathrm{T}}\mathbf{F}}{\partial q_1}, \ldots, \frac{\partial \mathbf{J}^{\mathrm{T}}\mathbf{F}}{\partial q_n} \right]_{n\times n} \tag{1. 39}$$

Details concerning such presentation can be found in (Chen and Kao, 2000). Further, after combining (1.36) with the linearized geometric model $\delta\mathbf{p} = \mathbf{J}_q \cdot \delta\mathbf{q}$ and some simplifications, the desired force-deflection relation for this loaded mode can be written as

$$\delta\mathbf{p} = \mathbf{J}_q \cdot \left(\mathbf{K}_q - \mathbf{K}_g\right)^{-1} \cdot \mathbf{J}_q^T \cdot \delta\mathbf{F} \tag{1. 40}$$

The latter also allows us to obtain the loaded stiffness matrix of the manipulator

$$\mathbf{K}_C = \left[\mathbf{J}_q \cdot \left(\mathbf{K}_q - \mathbf{K}_g\right)^{-1} \cdot \mathbf{J}_q^T \right]^{-1} \tag{1. 41}$$

which depends on both the virtual joint stiffness coefficients included in $\mathbf{K}_q$ and also the loading amplitude included in $\mathbf{K}_g$. It should be mentioned that here the Cartesian stiffness matrix $\mathbf{K}_C$ is related to rather small displacement $\delta\mathbf{p}$ caused by the force deviation $\delta\mathbf{F}$ with respect to the loading **F**. At the same time, the deflection $\Delta\mathbf{p}$ corresponding to the large force **F** as well as the corresponding deflection of the configuration angles $\Delta\mathbf{q}$ should be computed from the basic static equilibrium equation (1.35). It is also worth mentioning that in literature can be also found some modifications of the above method allowing to compute the Cartesian stiffness matrix for other types of external loading and internal loads (Alici and Shirinzadeh, 2005; Chen and Kao, 2000; Merlet et al., 2016) (Quennouelle and Gosselin, 2009a, 2009b).

The latest developments in the VJM-based modeling operate with 6-dimensinal virtual springs describing the link elasticities that are identified using the FEA-based technique (Anatol Pashkevich et al., 2011). This leads to essential increasing of the VJM method accuracy that becomes comparable with the accuracy of the FEA method, but with much lower computational expenses. History of the VJM method development and some important contributions are presented in **Table 1**.

Table 1 History of the VJM method development and some important contributions (Anatol Pashkevich et al., 2011)

Publications	Model & assumptions	Stiffness matrix
(Salisbury, 1980)	Serial manipulator,	$\mathbf{K}_C = \mathbf{J}_\theta^{-T}\mathbf{K}_\theta\mathbf{J}_\theta^{-1}$

	elasticity in actuator	
(Ciblak and Lipkin, 2021, 1999; Gosselin, 1990; Pigoski et al., 1998)	Parallel manipulator elasticity in actuators for non-overconstrained	$\mathbf{K}_C = \mathbf{J}_\theta^{-T}\mathbf{K}_\theta\mathbf{J}_\theta^{-1}$
(Xi et al., 2004; Zhang et al., 2004)	Serial kinematic chain without passive joints, elasticity in virtual joints	$\mathbf{K}_C = \sum_i \left(\mathbf{J}_{\theta i}\mathbf{K}_{\theta i}^{-1}\mathbf{J}_{\theta i}^T\right)^{-1}$
(A. Pashkevich et al., 2011; Pashkevich et al., 2010)	Serial kinematic chain with passive joints, elasticity in virtual joints	$\begin{bmatrix} \mathbf{K}_C & * \\ * & * \end{bmatrix} = \begin{pmatrix} \mathbf{J}_\theta\mathbf{K}_\theta^{-1}\mathbf{J}_\theta^T & \mathbf{J}_q \\ \mathbf{J}_q^T & 0 \end{pmatrix}^{-1}$
(Zhang and Gosselin, 2002)	Parallel manipulator without cross-linking between kinematic chains	$\mathbf{K}_C = \sum_i \mathbf{K}_C^{(i)};\ \mathbf{K}_C^{(i)} = \left(\sum_j \mathbf{J}_{\theta j}\mathbf{K}_{\theta j}^{-1}\mathbf{J}_{\theta j}^T\right)^{-1}$
(Alexandr Klimchik et al., 2012; Anatol Pashkevich et al., 2011)	Parallel manipulator without cross-linking between kinematic chains	$\mathbf{K}_C = \sum_i \mathbf{K}_C^{(i)}$ $\begin{bmatrix} \mathbf{K}_C^{(i)} & * \\ * & * \end{bmatrix} = \begin{pmatrix} \mathbf{J}_{\theta i}\mathbf{K}_{\theta i}^{-1}\mathbf{J}_{\theta i}^T & \mathbf{J}_{qi} \\ \mathbf{J}_{qi}^T & 0 \end{pmatrix}^{-1}$
(Alici and Shirinzadeh, 2005; Chen and Kao, 2000; Merlet et al., 2016)	Serial or parallel manipulator with external loading (non over-constrained)	$\mathbf{K}_C = \mathbf{J}_\theta^{-T}\left(\mathbf{K}_\theta - \mathbf{K}_g\right)\mathbf{J}_\theta^{-1}$
(Quennouelle and Gosselin, 2009a, 2009b)	Parallel manipulator with external loading and supplementary geometric constraints (cross-linkings)	$\mathbf{K}_C = \mathbf{J}_\theta^{-T}\left(\mathbf{K}_\theta - \mathbf{K}_g + \mathbf{K}_I\right)\mathbf{J}_\theta^{-1}$
(Yi and Freeman, 1992)	Parallel manipulator with external loading, inertia and gravity loads, joint stiffness actuation redundancy	$\mathbf{K}_C = \mathbf{J}_\theta^{-T}\mathbf{K}_u\mathbf{J}_\theta^{-1}$

Summarizing advantages of the VJM-based technique for the manipulator stiffness analysis, it is worth mentioning its simplicity compared to the FEA and the MSA approaches because of lower dimensions of the matrices, especially for the multi-link serial manipulator that composed of the similar parts. For this particular case, which is in the focus of this thesis, the above presented expressions allow us to obtain the manipulator stiffness matrix rather straightforwardly. Besides, the VJM approach is very promising for investigating some specific phenomenon in the stiffness behavior of the manipulators based on the tensegrity structures studied in this work. Some examples of such nonlinear analysis for the simple manipulators are presented in the next section.

1.4 Non-linear stiffness behaviour of flexible robotic manipulators

1.4.1 Buckling phenomenon in continuous mechanical systems

In mechanics, buckling is mainly known from Euler-Bernoulli theory (Jones, 2006; Khang et al., 2009, 2009; Muvdi and McNabb, 2012; Trahair, 2019) of a slender column acted by an axial compressive load. Under the small loading, the column keeps its initial straight shape, but if this load is larger than some critical value, the column suddenly bends or buckle. This phenomenon can be explained using the column bending equation

$$EI\frac{d^2w}{dx^2}+Fw=0 \tag{1. 42}$$

which allows to compute the column lateral deflection $w(x)$ caused by the axial compressive load F as shown in **Fig. 1. 12**. In this equation, x denotes the distance from the column fixed end, E is the Young's modulus of the material, and I is the minimum area moment the column cross section. It is also assumed that here $0 \le x \le L$, where L is the column length. As known from mathematics, the general solution of this equation can be expressed as

$$w(x)=A\sin(\lambda x)+B\cos(\lambda x) \tag{1. 43}$$

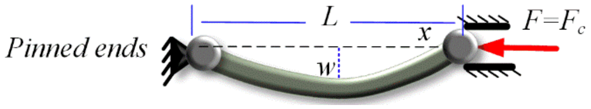

Fig. 1. 12: Deformation of the Euler column under an axial compressive load.

Where $\lambda^2 = F/EI$ and A, B are some constants computed from the boundary conditions $w(0)=0$ and $w(L)=0$. It can be easily seen that the left-end boundary condition $w(0)=0$ yields the second constant $B = 0$, while the right-end one $w(L) = 0$ leads to the equation $A\sin(\lambda L) = 0$, from which one can get that either A=0 or $\sin(\lambda L) = 0$.

The first case produces the trivial solution $w(x) = 0$ corresponding to the straight column shape (without bending). However, the second case yields a number of non-trivial solutions with different parameter λ

$$\lambda_n = \frac{n\pi}{L}; \quad n = 0,1,\ldots,n \tag{1. 44}$$

which for $n \neq 0$ describes different bending shapes presented in **Fig. 1. 13**. It is clear that such λ must also satisfy the above equation $\lambda^2 = F/EI$, which leads to the following expression of the so-called critical loads

$$F_{cn} = n^2 \frac{\pi^2 EI}{L^2}; \quad n = 0,1,\ldots,n \tag{1. 45}$$

corresponding to different bended shapes. In engineering, these loads are usually treated as the critical ones causing the column buckling. From mechanical point of view, each critical load corresponds to the static equilibrium with different column shape, different endpoint displacement and different strain energy caused by elastic deformation. It is clear that some of these equilibriums cannot be observed in practice. In particular, for the load $F < F_1$ only the trivial solution $w(x) = 0$ corresponding to the straight column shape exists and is stable, while for $F = F_1$ the solution $w(x) = 0$ becomes unstable and the non-trivial solution $w(x) = A\sin(\pi x/L)$ appears, which corresponds to the bended column shape described by 1/2 of sine function (see **Fig. 1. 13**, n=1). It is also clear that $F_1 < F_2 < F_3\ldots$, so the non-trivial solutions with n>1 cannot be observed in practice. (In some cases, the shapes with n>1 can be observed if bracing is placed at the points where w=0 to prevent buckling at lower loads). It is also worth mentioning that the constant A cannot be determined from the considered boundary conditions, it is simply assumed that A is very small.

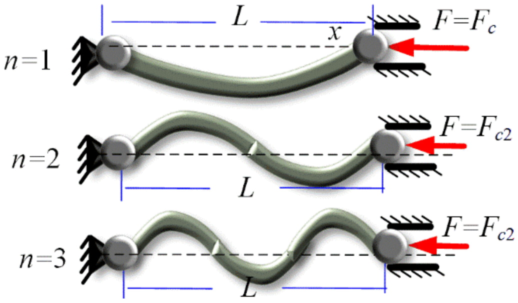

Fig. 1. 13: Possible shapes of beam after buckling (pinned ends)

It should be noted that the above results corresponds to the case to so-called pin-ended column with perfect passive joints (with zero torques) at the both ends. For the general case dealing with more other types of column fixing, it is necessary to use the forth-order differential equation

$$\frac{d^4w}{dx^4}+EI\frac{d^2w}{dx^2}=0 \tag{1. 46}$$

with greater number of boundary conditions depending on the column fixing. In particular, there are three cases here (Leipholz, 2013; Timoshenko and Gere, 2009a):

(a)pined end: $w(x)=0$ and $\dfrac{d^2w}{dx^2}=0$

(b)fixed end: $w(x)=0$ and $\dfrac{d^2w}{dx^2}=0$

(c)free end: $\dfrac{d^2w}{dx^2}=0$ and $\dfrac{d^3w}{dx^3}+EI\dfrac{dw}{dx}=0$

In any of these cases, the general solution of the differential equation (1.46) is

$$w(x)=A\sin(\lambda x)+B\cos(\lambda x)+Cx+D \tag{1. 47}$$

Here A, B, C, D are some constants computed from the above the boundary conditions. In literature (Lee, 2001; Muvdi and McNabb, 2012; Zahavi et al., 2001), there is detailed analysis of all possible cases with different combination of boundary conditions, for which there were obtained expressions for the column shapes $w(x)$ and corresponding the critical forces F_i. Relevant results are presented in **Fig. 1. 14**， where the efficient length L_e involved in the critical force computing is also shown.

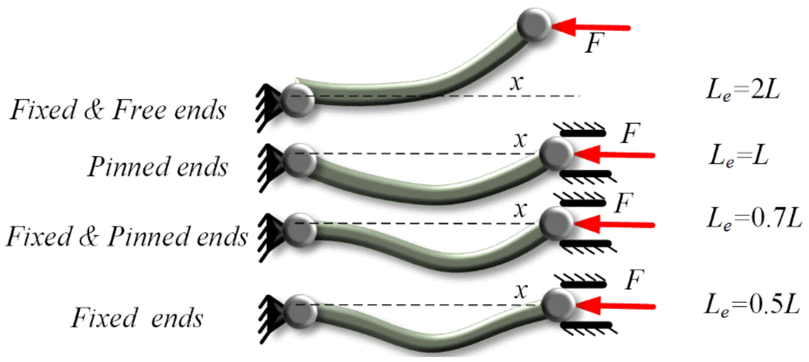

Fig. 1. 14: The shape of the compressed beam for different end conditions (L_e is efficient length for critical force computing $F_c = \pi^2 EI/L_e^2$).

Summarizing the above classical results dealing with the column buckling, it worth mentioning that the problem is usually treated in a pure mathematical way, where the eigenvalues λ_i and Eigen functions $w(x)$ are obtained for certain differential operators. Then the critical forces F_i are computed via the eigenvalues λ_i. However, the weak point of the classical approach is that the usual right-end boundary condition $w(L)=0$ neglects the axial deflection caused by changing of the column shape. Besides, at least one of the constants *A*, *B, C*, *D* cannot be found from the given data. The later does not allows us to obtain the force-deflection relation after buckling and evaluate stability of possible equilibriums.

The above presented Euler-Bernoulli theory allows also to predict buckling in other mechanical structures composed of flexible **beams**, which can be found in robotics. In particular for a single beam this theory can be applied almost the straightforward way assuming that after the buckling, the beam is bended and their right-end boundary condition is written as $w(L-\Delta)=0$, where Δ denotes the axial deflection under the load. Also, as follows from the beam bending theory, the shape of the bended beam in the equilibrium state is described by one of the possible expressions

$$w(x) = A\sin(\frac{n\pi}{d}x);\quad d = L-\Delta,\ n = 1,2,..,\tag{1. 48}$$

and the corresponding axial load is

$$F = n^2\frac{\pi^2 EI}{d^2};\quad n = 1,2,...\tag{1. 49}$$

The latter allows us to easily obtain a number of force-deflection relations describing the beam evolution after the buckling

$$F(\Delta) = n^2\frac{\pi^2 EI}{(L-\Delta)^2};\quad n = 1,2,...\tag{1. 50}$$

that correspond to different beam shapes (1/2 of sine, full sine 3/2 of sine, etc.). It is clear that $F(\Delta)$ is a monotonically increasing function as shown in **Fig. 1. 15**. So, after the buckling the beam behavior is continuous, i.e. the axial force increasing and leads to progressive increasing of the sine amplitude A in expression (1.48). It can be proved that for relatively small deflection Δ, this amplitude can be estimated from expression

$$A \approx \frac{2}{\pi n}\sqrt{\left(L-d\right)d};\quad n = 1,2,...\tag{1. 51}$$

derived from the geometric assumption that the curved beam length is also equal to the original length

L. The open question however is related to the stability of the possible equilibrium shapes (1.48), which differ in parameter n. To answer this question let us compare the potential energy stored in the beam for different shapes. It is clear that this energy can be evaluated as the work of the force $F(\Delta)$ on the interval $[0,\Delta]$

$$E = \int_0^{\Delta} F(\Delta) d\Delta = n^2 \frac{\pi^2 \Delta}{L(L-\Delta)} EI; \quad n = 1,2,... \tag{1. 52}$$

So the potential energy for the half-sine shape is the smallest of all possible ones and only this shape can be observed in practice. In the following sections these half-sine shapes of the loaded beam will be compared with the minimum-energy shape of the loaded serial manipulator.

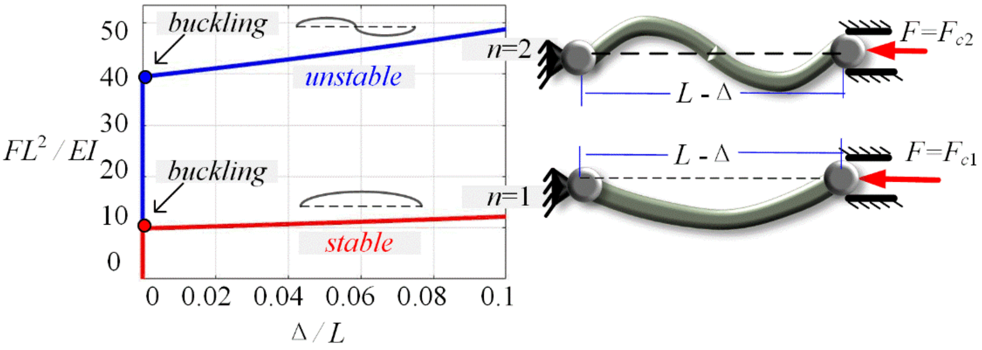

Fig. 1. 15: Force-deflection relations for different beam bending shapes under axial load

Another conclusion from the classical theory, which will be useful further for robotics, is related to computation of the critical force using some elements of the beam stiffness matrix. As known from the literature (Muvdi and McNabb, 2012), the stiffness properties of the beam in the lateral direction can be expressed in the following way

$$K_{yy} = \frac{12EI}{L^3}; \quad C_{yy} = \frac{L^3}{3EI}; \quad C_{\theta y} = \frac{L^2}{2EI} \tag{1. 53}$$

where K_{yy} and C_{yy} denote the beam stiffness and compliance in the lateral direction, L is the beam length and E is the Young's modulus of the material, I is the corresponding area moment the cross section. The latter allows us to rewrite the primary expression for the critical force in the following way

$$F_{c1} = \frac{\pi^2}{12} K_{yy} L \quad \text{or} \quad F_{c1} = \frac{\pi^2}{3} \frac{L}{C_{yy}}; \quad F_{c1} = \frac{\pi^2}{2} \frac{1}{C_{\theta y}} \tag{1. 54}$$

which allows user easily estimate the critical force using data obtained from very simple experiments giving either stiffness K_{yy} or compliance coefficient C_{yy} of the beam. In the following sections this approach will be also verified for the multi-link robotic manipulators whose stiffness behavior can be roughly approximated by the beam model.

Finally, it worth mentioning that the buckling phenomenon can be also observed for the 3-dimensional plates, which are subject to compressive loads. In particular, for the case of the one-directional compressive loading shown in **Fig. 1. 15**, there are infinite number of possible equilibrium shapes with n=1, 2, … waves but only the shape with n=1 is stable and is really seen in practice (as for the flexible beam studied above). Similar phenomenon can be also observed for two-dimensional compressive loadings when possible equilibrium shapes include multiple peaks/hollows as shown in **Fig. 1. 16** and **Fig. 1. 17**, but only the single-peak shape is stable. From intuitive point of view, such buckling phenomenon may be also detected for parallel robotic manipulators that are subject to compressive loading.

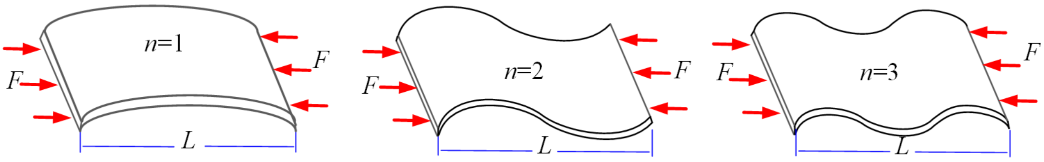

Fig. 1. 16: Possible equilibrium shapes of a thin plate under one-directional compressive loading.

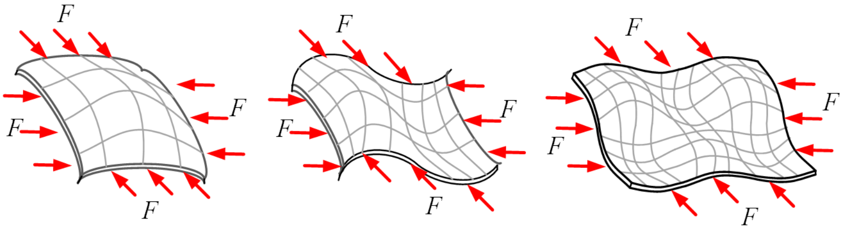

Fig. 1. 17: Possible equilibrium shapes of a thin plate under two-directional compressive loading.

1.4.2 Buckling in discrete mechanical systems and robotics

In additional to continuous systems, buckling phenomenon was also detected in a number of mechanisms composed of rigid/flexible links and springs, which are connected by passive or elastic joints. Several examples of such mechanisms with one degree of freedom are presented in **Fig. 1. 18**. Let us consider them in detail.

Case (a): two-bar mechanism with internal linear spring. For this mechanism, the static equilibrium equation can be written as follows

$$\frac{F}{2\sin(\alpha-q)}=\frac{F_{spring}}{\cos(\alpha-q)} \tag{1. 55}$$

where F is the external force, F_{spring} is the force generated by the spring, q is the mechanism configuration angle, α is an angle defining the mechanism initial shape as shown in **Fig. 1. 18a**. Using these definitions, the elastic force of the spring F_{spring} and the deflection Δ of the force application point can be expressed as

$$\begin{aligned} F_{spring} &= 2kL\left(\cos(\alpha-q)-\cos(\alpha)\right) \\ \Delta &= L\left(\sin\alpha-\sin(\alpha-q)\right) \end{aligned} \tag{1. 56}$$

where k is the stiffness coefficient of the spring and L is the length of the links. These allows us to get the desired force-deflection relation $F(\Delta)$ of the considered mechanism and present it in the following parameter form.

$$\begin{aligned} F(\varphi) &= 4kL\frac{\cos\varphi-\cos\alpha}{\cos\varphi}\sin\varphi \\ \Delta(\varphi) &= L\left(\sin\alpha-\sin\varphi\right) \end{aligned} \tag{1. 57}$$

where $\varphi=\alpha-q$. An example of the obtained force-deflection curve for $\alpha=\pi/3$ is presented in **Fig. 1. 19a**, which clearly shows that the function $F(\Delta)$ is not a monotonic one and has both a local minimum and a local maximum. In practice, this property causes very specific (discontinuous) mechanism behavior under the loading. In particular, when the force is small and increasing gradually from zero value, the configuration angle is also increasing slowly. So, the mechanism shape and the configuration angle q are changing continuously. However, when the force reaches some critical values F_C defined by the local maximum of $F(\Delta)$, the mechanism suddenly changes its shape and both the configuration angle q and the deflection Δ essentially increase demonstrating the buckling phenomenon similar to the Euler's column. Further, when the external force F is greater than F_C, the mechanism reaction to the external loading for this new shape remains continuous.

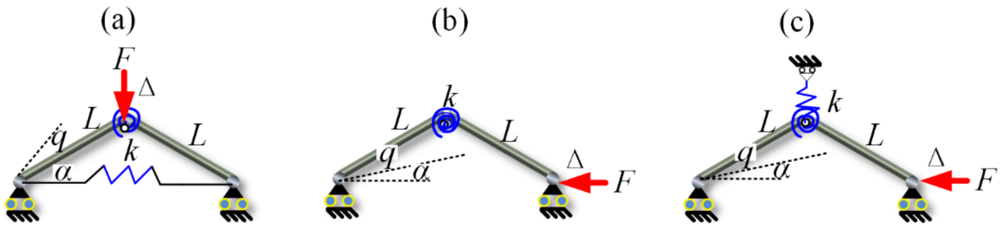

Fig. 1. 18: Examples of two-bar mechanisms where the buckling phenomenon is observed.

It is worth mentioning that in theory of the elastic stability (Timoshenko and Gere, 2009a), the above described phenomenon is also called “snap-through buckling” which is typical for the curved arch with transverse loading. As follows from **Fig. 1. 20** showing possible equilibrium configurations for relatively small load $F<F_C$, the snap-through buckling is also observed in the considered mechanism, which snaps from one stable configuration to another stable configuration when the load reaches the critical value $F=F_C$. It is clear that for such critical loading the configuration ① and ② are merged, the stability is lost and the mechanism snaps into stable configuration ③ (see **Fig. 1. 19** and **Fig. 1. 20**).

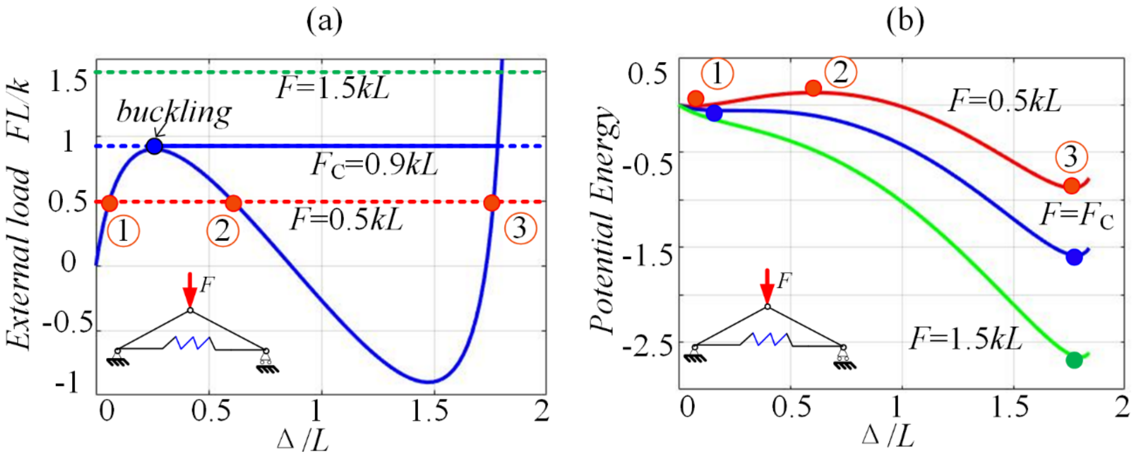

Fig. 1. 19: The load-deflection and energy curves for two-link mechanism with internal linear spring ($\alpha=\pi/3$).

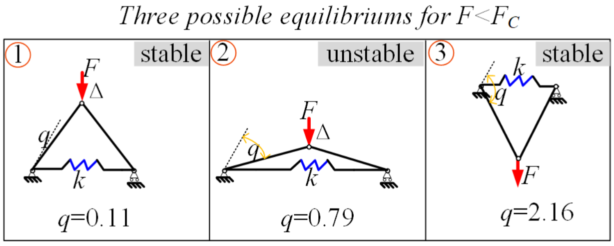

Fig. 1. 20: Mechanism shapes in equilibrium configurations for the loading F_C=0.5kL, which is lower than F_C=0.9kL (case $\alpha=\pi/3$).

The above buckling phenomenon can be also explained using the energy method, by considering maximums and minimums of the potential energy curves corresponding to the stable and unstable equilibriums respectively (Timoshenko and Gere, 2009b). As known from the general theory, the potential energy V of the considered mechanism can be expressed as follows

$$V(q)=U(q)-F\cdot\Delta(q) \tag{1. 58}$$

where U is the strain energy stored in the spring, F is the applied conservative load and deflection Δ is the distance moved by F in its direction. It can be easily proved that for the considered mechanism the strain energy can be expressed as follows

$$U = 2kL^2(\cos\alpha - \cos\varphi)^2 \tag{1. 59}$$

where $\varphi=\alpha-q$. So, using expression for the deflection $\Delta(q)$ from (17), one can get the final expression for the potential energy

$$V(q) = 2kL^2(\cos\alpha - \cos\varphi)^2 - F \cdot L\left(\sin\alpha - \sin\varphi\right) \tag{1. 60}$$

which obviously includes the force F as a parameter. The examples of the energy curves on the plane (V, Δ) are presented in **Fig. 1. 19b**, which clearly show that for $F<F_C$ the energy curve has two local minimums and a single local maximum. For $F=F_C$, there are two stationary points: a saddle point obtained by max/min merging and a local minimum. Further, for $F>F_C$, a single local minimum exists only. Obviously, it is in good correspondence with the force-deflection curves $F(\Delta)$ presented in **Fig. 1. 19a** showing that the equation $F(\Delta)=C$ may have different number of roots (one, two or three). Using the static equilibrium conditions (1.58) the critical force for this mechanism can be computed from the equation $dF(q)/dq=0$, which yields $\cos\alpha - \cos^3\varphi = 0$ leading to the final expressions for the force

$$F_C = 4kL\frac{\sqrt[3]{\cos\alpha} - \cos\alpha}{\sqrt[3]{\cos\alpha}}\sqrt{1-\cos^{2/3}\alpha} \tag{1. 61}$$

and corresponding configuration angle and deflection

$$\begin{aligned} q_C &= \alpha - \mathrm{acos}(\sqrt[3]{\cos\alpha}) \\ \Delta_C &= L(\sin\alpha - \sqrt{1-\cos^{2/3}\alpha}) \end{aligned} \tag{1. 62}$$

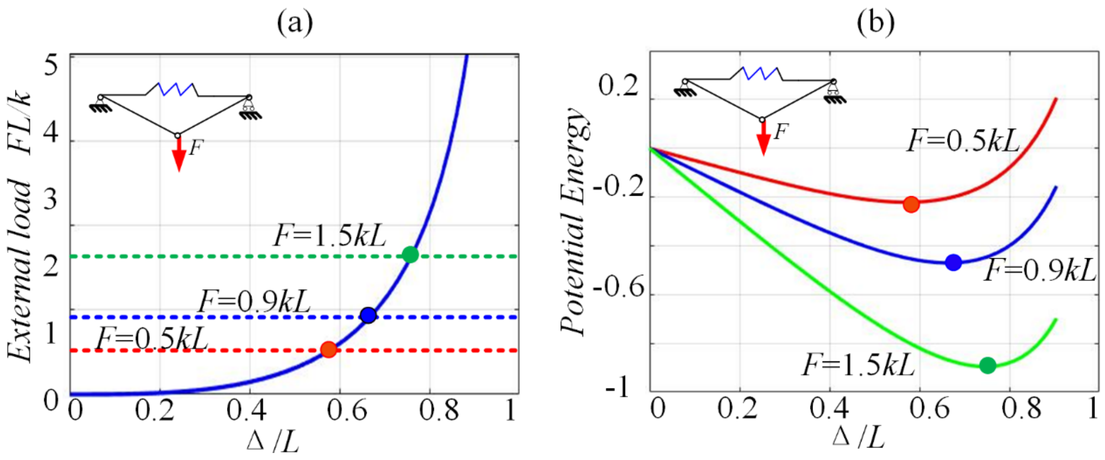

Fig. 1. 21: The load-deflection and energy curves for two-bar mechanism with internal linear spring (case α=0, i.e. straight initial configuration).

In the case of α=0 corresponding to the straight initial configuration, the above equations produce continuously monotonic force-deflection curves passing through the zero point $F(\Delta)=(0, 0)$ as shown in **Fig. 1. 21a**. So, the mechanism always resist to the external loading. Corresponding energy curves are shown in **Fig. 1. 21b**, all of them have a single minimum defining stable equilibriums with different $\Delta\neq0$ depending on the external loading F. Hence, the considered 1-d.o.f. two-link mechanism with the internal linear spring may demonstrate the snap-through buckling behavior that may be found in some robotic manipulators.

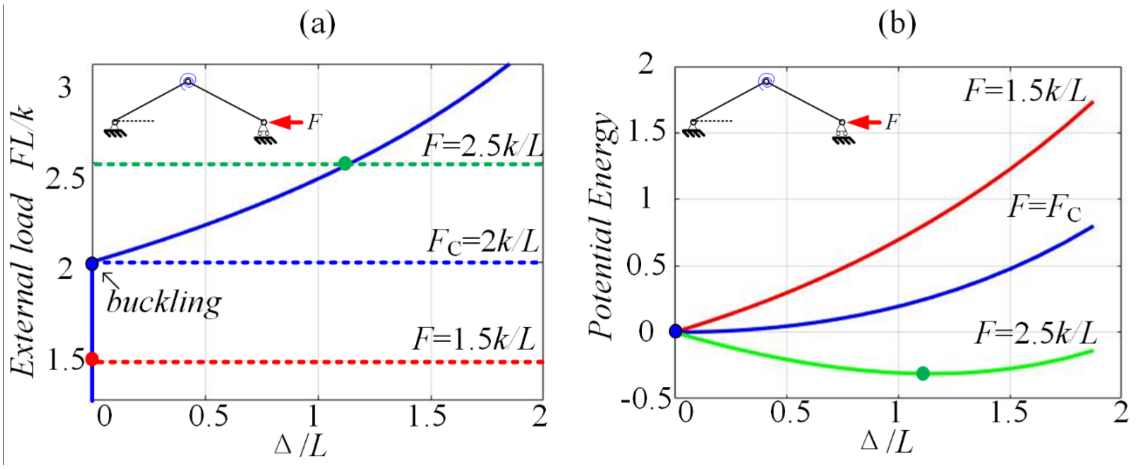

Fig. 1. 22: The load-deflection and energy curves for two-bar mechanism with internal rotational spring (case α=0, i.e. straight initial configuration).

Case (b): two-bar mechanism with internal rotational spring. For this mechanism, the static equilibrium equation is $FL\sin(\alpha+q)=2kq$, which allows us to get the desired force-deflection relation $F(\Delta)$ in the following form.

$$\begin{aligned} F(q) &= \frac{2kq}{L\sin(\alpha+q)} \\ \Delta(q) &= 2L\left(\cos\alpha-\cos(\alpha+q)\right) \end{aligned} \tag{1. 63}$$

where F is the external force, q is the mechanism configuration angle, α is an angle defining the mechanism initial shape, k is the stiffness coefficient of the rotational spring and L is the length of the links. An example of this force-deflection curve for the case α=0 (i.e. for the straight initial configuration) is presented in **Fig. 1. 22a**, which shows that at first the function $F(\Delta)$ goes from the zero to a non-zero value without changing the deflection Δ until achieving the critical force causes the buckling. Then it increases monotonically as the deflection increasing. Clearly, this is very similar to the Euler's column behavior but here only a single equilibrium configuration is possible corresponding to n=1 in (1.49). Exact value of the critical force for the considered 1-d.o.f mechanism in the straight configuration (α=0) can be found by computing the limit of $F(q)$ for q=0:

$$F_C = \lim_{q\to 0} F(q) = \frac{2k}{L}; \quad \text{for } \alpha = 0 \tag{1.64}$$

The above buckling phenomenon can be also explained using the energy curves defined by general expression (1.58). Here the strain energy stored in the rotational spring is $U = 2kq^2$ and the potential energy of this mechanism can be expressed as

$$V(q) = 2kq^2 - 2FL\left(\cos\alpha - \cos(\alpha + q)\right) \tag{1.65}$$

For the case α=0 the energy curves on the plane (V, Δ) are presented in **Fig. 1. 22b**, which show that for $F \le F_C$ the energy minimum is achieved when Δ=0 and the equilibrium is stable and corresponds to the straight shape of the mechanism (q=0). In contrast, for $F > F_C$ the energy minimum is achieved when Δ≠0, which corresponds to the non-straight mechanism shape in the stable equilibrium state. It is clear that this shape depends on the external force F.

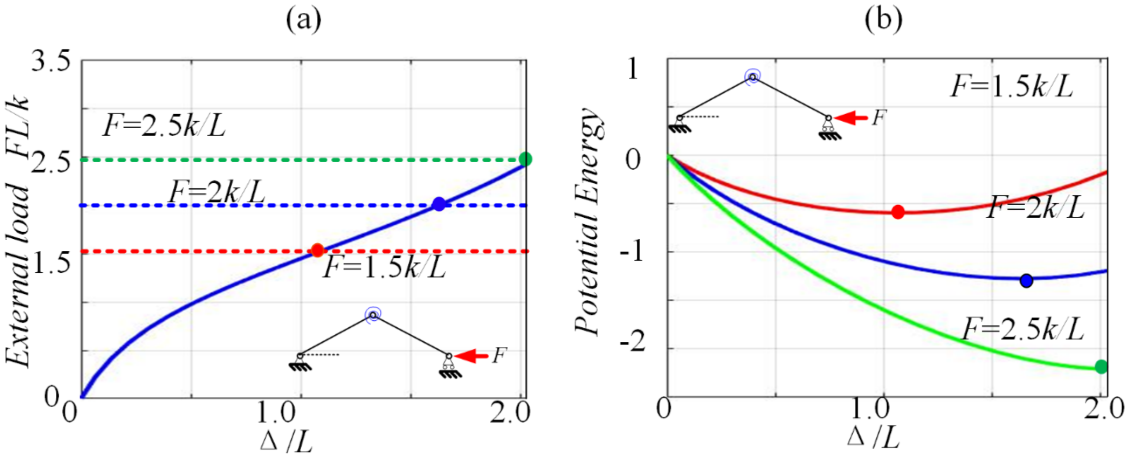

Fig. 1. 23: The load-deflection and energy curves for two-bar mechanism with internal rotational spring (case α=π/6, i.e. non-straight initial configuration).

In the case of α≠0 corresponding to the non-straight initial configuration, the above equations produce continuously monotonic force-deflection curves passing through the zero point F(Δ)=(0, 0) as shown in **Fig. 1. 23a**. So, the mechanism behavior is similar to a simple non-linear spring that always resist to the external loading (providing that the geometric constraint $\Delta \le 2L\cos\alpha$ is not violated). Corresponding energy curves are shown in **Fig. 1. 23b,** all of them have a single minimum defining stable equilibrium with different Δ≠0 depending on the external loading F.

Hence, the considered 1-d.o.f. two-link mechanism with the rotational spring may demonstrate the so called “bifurcation” buckling similar to the Euler’s column which is quite different from the “snap-through” buckling considered above (compare **Fig. 1. 21** and **Fig. 1. 23**).

Case (c): two-bar mechanism with external linear spring. For this mechanism, we can get the force $F(q)$ and the deflection $\Delta(q)$ from the static equilibrium equation $2F\tan(\alpha+q)=kL\left(\sin(\alpha+q)-\sin\alpha\right)$ and from the geometry in the following way

$$\begin{aligned} F(q) &= \frac{kL}{2}\frac{\sin(\alpha+q)-\sin\alpha}{\sin(\alpha+q)}\cos(\alpha+q) \\ \Delta(q) &= 2L\left(\cos\alpha-\cos(\alpha+q)\right) \end{aligned} \tag{1. 66}$$

where F is the external force, q is the mechanism configuration angle, k is the stiffness coefficient of the external linear spring and L is the length of the rigid links. It is clear that here similar to the above case (b) the shape of the force-deflection curve $F(\Delta)$ essentially depends on the initial configuration angle α. In particular, for $\alpha=0$ corresponding to the straight initial configuration, this curve is discontinuous at the point $\Delta=0$ as shown in **Fig. 1. 24a**. Also, similar to the case (b), at first the function $F(\Delta)$ goes from the zero to a non-zero value without changing the deflection Δ until achieving the critical force causes the buckling. However, after the buckling, the force F decreases linearly as the deflection Δ is increasing, which corresponds to the negative stiffness and mechanism instability after the buckling. The latter shows quite different performance of the mechanism (c) under the loading compared to the previous cases (a) and (b). Using the above equations the critical force causing the buckling can be found by computing the limit of $F(q)$ for $q=0$, which gives us

$$F_C = \lim_{q\to 0} F(q) = \frac{kL}{2}; \qquad \text{for } \alpha = 0 \tag{1. 67}$$

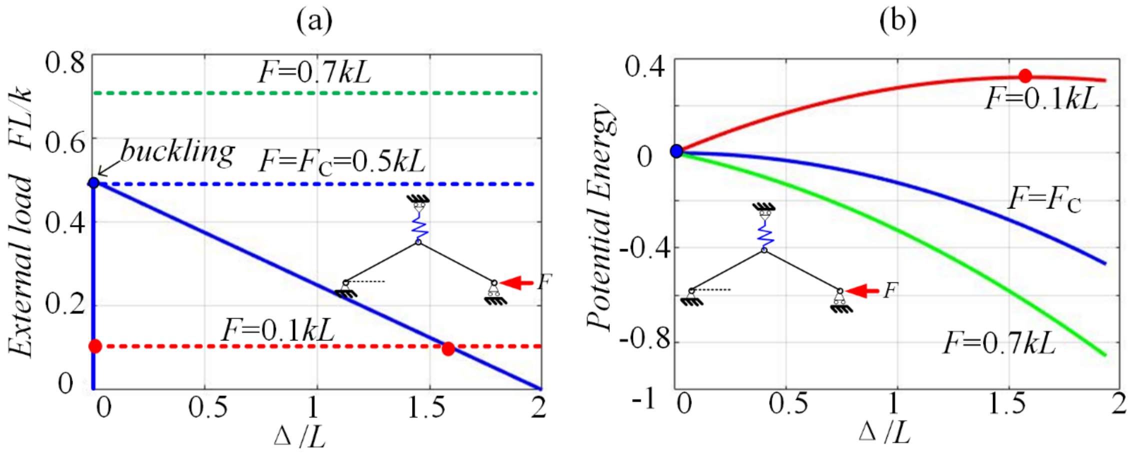

Fig. 1. 24: The load-deflection and energy curves for two-bar mechanism with external linear spring (case α=0, i.e. straight initial configuration).

To analyze the above buckling phenomenon using the energy method, let us express first the strain energy stored in the external linear spring as

$$U = \frac{1}{2}kL^2\left(\sin(\alpha+q)-\sin\alpha\right)^2 . \tag{1. 68}$$

This allows us to get the following expression for the full potential energy of this mechanism

$$V(q) = \frac{1}{2}kL^2\left(\sin(\alpha+q)-\sin\alpha\right)^2 - 2FL\left(\cos\alpha-\cos(\alpha+q)\right) \tag{1. 69}$$

and find its equilibrium configurations via the maximums/minimums of $V(q)$ with respect to q. For the case $\alpha=0$, several energy curves on the plane (V, Δ) are presented in **Fig. 1. 24b**. As follows from this figure, for $F<F_C$ there is a minimum point at $\Delta=0$ and a maximum point at $\Delta=0$, which are corresponding to the stable and unstable equilibriums respectively. It is clear that in practice, only the stable equilibrium is observed. Further, for $F=F_C$, there is only a maximum point on the energy curve, where the buckling is happened and the corresponding equilibrium is unstable. And finally, for $F>F_C$, there is only maximum point on the energy curve at $\Delta=0$, so the stable equilibrium configurations for such large force do not exist.

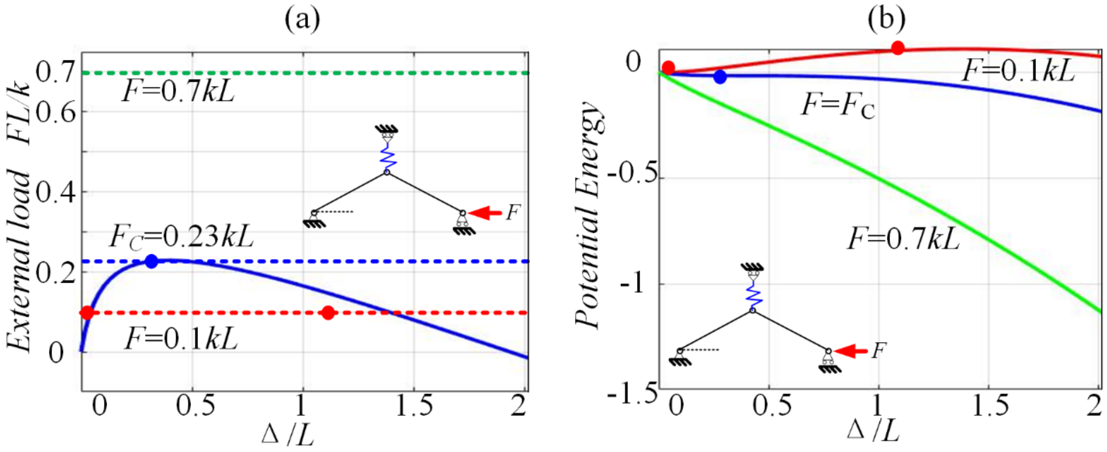

Fig. 1. 25: The load-deflection and energy curves for two-bar mechanism with external linear spring (case $\alpha=\pi/12$, i.e. non-straight initial configuration).

In the case of $\alpha\neq0$ corresponding to the non-straight initial configuration, the above equations produce continuous and non-monotonic force-deflection curve passing through the zero point (F, Δ)=(0, 0) as shown in **Fig. 1. 25a**. So, the mechanism behavior is similar to the case (a), where at the beginning the mechanism resists to the external force and takes a stable equilibrium configuration. However, later when the external force reaches its critical value, the mechanism loses its resistance and moves until stopped by its geometric constraints ($\Delta \le 2L\cos\alpha$) because of its negative stiffness. Corresponding energy curves are shown in **Fig. 1. 25b**, which also confirms the described mechanism behavior.

Table 2 Examples of two-bar mechanisms where the buckling phenomenon are observed

	Rigid links & Internal linear spring	Rigid links & Internal rotational spring	Rigid links & External linear spring
Mechanism structure	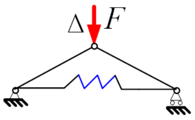	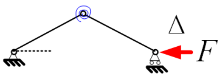	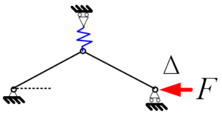
Force-deflection curve α =0	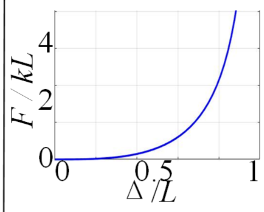	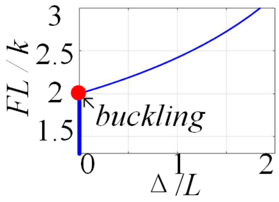	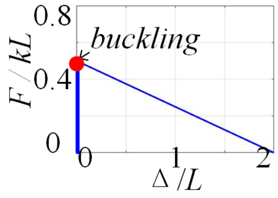
Force-deflection curve α ≠ 0	α = π /3 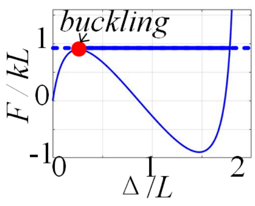	α = π /6 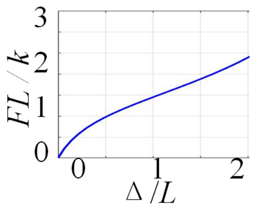	α = π /12 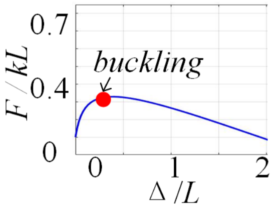

The critical force for this case $\alpha \neq 0$ can be computed straightforwardly from the equation $dF(q)/dq = 0$, which yields $\sin\alpha - \sin^3(\alpha + q) = 0$ leading to the final expression for the force

$$F_C = \frac{kL}{2}\frac{\sqrt[3]{\sin\alpha} - \sin\alpha}{\sqrt[3]{\sin\alpha}}\sqrt{1-\sin^{2/3}\alpha} \qquad (1.\,70)$$

and corresponding configuration angle and deflection

$$q_C = \mathrm{acos}\sqrt{1-\sin^{2/3}\alpha} - \alpha\,; \qquad \Delta_C = 2L\left(\cos\alpha - \sqrt{1-\sin^{2/3}\alpha}\right) \qquad (1.\,71)$$

Hence, the considered 1-d.o.f. two-link mechanism with the external linear spring may demonstrate the “quasi-snap-through” buckling behavior which is quite different from the “snap-through” buckling and “bifurcation” buckling considered above for the case (a) and (b). Summary of the stiffness properties for all considered 1-d.o.f mechanism (a), (b), (c) is given in **Table 2**.

Case (d): three-bar mechanism with internal rotational springs. For this mechanism, the buckling phenomenon was also described in literature (Rimoli, 2018). Let us consider it in detail assuming that it is composed of three similar rigid links of the same length L and two rotational linear springs with stiffness coefficient k, as shown in **Fig. 1. 26**. The left end point of this mechanism is connected to the base by a passive joint, there are two linear springs located on the second and the third joints, the right end point is also equipped with a passive joint and is moved horizontally by the external force F.

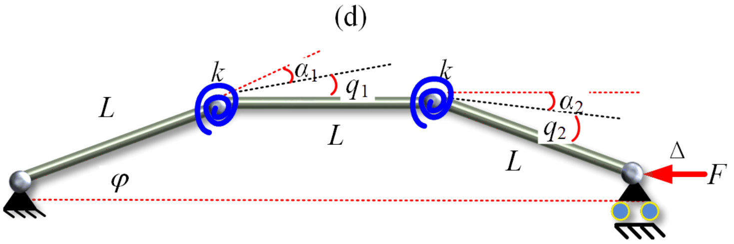

Fig. 1. 26: Example of three-bar mechanisms with the buckling phenomenon.

It is also assumed that the orientation angle of the first link is denoted as φ, and the initial values of the second and the third angles are α_1 and α_2 respectively. Under the loading F the right end point is moved to the left, which is described by the deflection Δ and corresponding orientation angles α_1+q_1 and α_2+q_2. Using these notations, the end-point coordinates for the initial configuration can be expressed as

$$\begin{aligned} x_0 &= L\cos\varphi + L\cos(\varphi+\alpha_1) + L\cos(\varphi+\alpha_1+\alpha_2) \\ y_0 &= L\sin\varphi + L\sin(\varphi+\alpha_1) + L\sin(\varphi+\alpha_1+\alpha_2) \end{aligned} \tag{1. 72}$$

Under the loading, the end-point moves to a new position

$$\begin{aligned} x &= L\cos\varphi + L\cos(\varphi+\alpha_1+q_1) + L\cos(\varphi+\alpha_1+q_1+\alpha_2+q_2) \\ y &= L\sin\varphi + L\sin(\varphi+\alpha_1+q_1) + L\sin(\varphi+\alpha_1+q_1+\alpha_2+q_2) \end{aligned} \tag{1. 73}$$

that can be also expressed as via the deflection Δ as

$$x = x_0 - \Delta\,; \qquad y = 0 \tag{1. 74}$$

It should be noted that here, because of the geometric constraints $y_0=y=0$. To find the angles q_1, q_2 corresponding to the external force F, it is necessary to consider the static equilibrium equation that generally is written as follows

$$\mathbf{J}^{\mathrm{T}}\mathbf{F} + \mathbf{M} = \mathbf{0} \tag{1. 75}$$

where $\mathbf{F}=[F_x\ F_y]$ is the external force, $\mathbf{M}$ is the internal torques in the joints that can be computed via the angles q_1, q_2 as $\mathbf{M}=[0\ kq_1\ kq_2]^{\mathrm{T}}$ and $\mathbf{J}$ is the Jacobian matrix of size 2×3 that is expressed as follows

$$\mathbf{J} = L \cdot \left[\begin{array}{c:c:c} -S_0 - S_{01} - S_{012} & -S_{01} - S_{012} & -S_{012} \\ C_0 + C_{01} + C_{012} & C_{01} + C_{012} & C_{012} \end{array} \right]. \tag{1. 76}$$

Here S_0=sinφ, C_0=cosφ, S_{01}=sin(φ+α_1+q_1), C_{01}=cos(φ+α_1+q_1), and S_{02}=sin(φ+α_1+q_1+α_2+q_2), C_{02}=cos(φ+α_1+q_1+α_2+q_2). Taking into account that the static equilibrium corresponds to minimum of the potential energy, for known equilibrium configuration described by the angles (φ, q_1, q_2), the external force can be obtained from (1.75) by using the Moore-Penrose pseudo inverse

$$\mathbf{F}(\mathbf{q}) = -\left[\mathbf{J}^{\mathrm{T}}(\mathbf{q})\right]^{\dagger} \cdot \mathbf{M}(\mathbf{q}) \tag{1. 77}$$

where $(\mathbf{J}^{\mathrm{T}})^{\dagger} = \mathbf{J}(\mathbf{J}^{\mathrm{T}}\mathbf{J})^{-1}$, and $\mathbf{q}$=(φ, q_1, q_2). It is clear that for such equilibrium configuration the corresponding end-effector deflection $\Delta(\mathbf{q})$ can be straightforwardly computed from equation (1.74).

It should be noted that the above equations operate with three variables (φ, q_1, q_2), but the problem dimension can be easily reduced using the analytical solution of the geometric equations (1.73) for the end-effector location (x, y)=(x_0–Δ, 0). The latter allows us to replace the initial configuration space (φ, q_1, q_2) by a reduced space (Δ, φ), which is more convenient for the stiffness analysis. This reduction can be easily executed by applying the inverse-kinematics of a 2-link manipulator that yields the following expressions for the angles q_1, q_2.

$$\begin{aligned} q_2 &= \operatorname{atan2}\left(S_2, C_2\right) - \alpha_2 \\ q_1 &= \operatorname{atan2}(y_0 - L\sin\varphi, x_0 - \Delta - L\cos\varphi) - \operatorname{atan2}\left(LS_2, L + LC_2\right) - \varphi - \alpha_1 \end{aligned} \tag{1. 78}$$

where $C_2 = \left[\left(x_0 - \Delta - L\cos\varphi\right)^2 + \left(y_0 - L\sin\varphi\right)^2 - 2L^2\right] \big/ 2L^2$, $S_2 = \pm\sqrt{1 - C_2^2}$. Hence, using the above transformation, a single redundant variable φ corresponding to the equilibrium configuration can be found from the given Δ using condition of the min/max of the spring strain energy, i.e. $\varphi = \arg\min\limits_{\varphi} E(\Delta, \varphi)$ for stable equilibrium and $\varphi = \arg\max\limits_{\varphi} E(\Delta, \varphi)$ for unstable one, where the strain energy of this mechanism can be expressed as

$$E(\Delta, \varphi) = \frac{k}{2} q_1(\Delta, \varphi)^2 + \frac{k}{2} q_2(\Delta, \varphi)^2 \tag{1. 79}$$

It should be mentioned that here, assuming that Δ is given, minimization of the full potential energy

$$V(\Delta, \varphi) = E(\Delta, \varphi) - F_x \cdot \Delta \tag{1. 80}$$

is not necessary for computing the redundant variable φ.

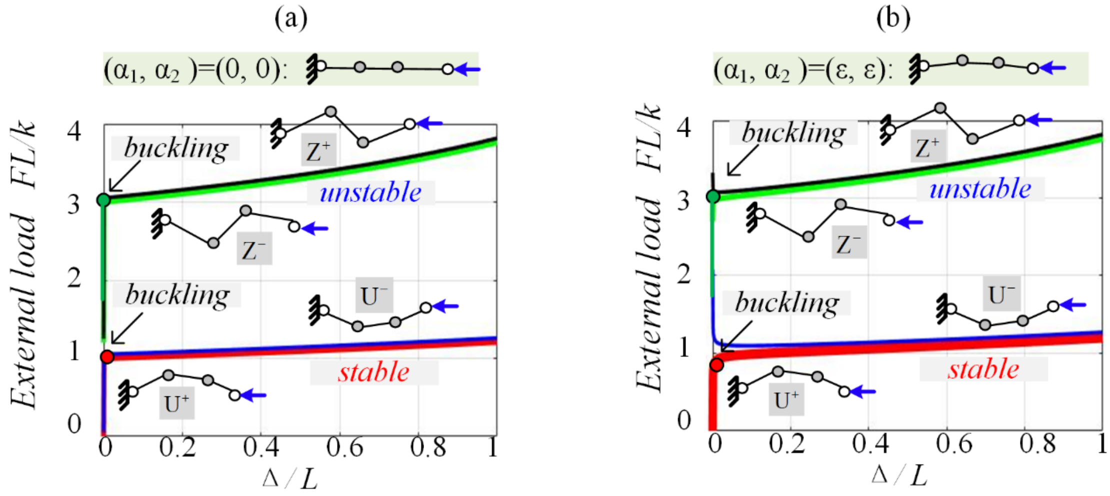

Fig. 1. 27: Force-deflection curves for the initial "straight" and "quasi-straight" configurations and four possible equilibriums with the stable shapes (U^+, U^-) and unstable shapes (Z^+, Z^-).

Some simulation results based on the above expressions are presented in **Figs 1.27**, **1.28, 1.29, 1.30**. They include the force-deflection curves describing the manipulator resistance to the external loading for different initial configurations defined by the parameters α_1 and α_2. As follows from them, for the initial straight or quasi-straight configuration (see **Fig. 1. 26**) the manipulator stiffness behavior is similar to the behavior of the compressed Euler's column considered above (**Fig. 1. 15**). In particular, there are also here four equilibriums (U^+, U^-) and (Z^+, Z^-) corresponding to the half-sine-shape and sine-shape of the compressed column. However, only (U^+, U^-) are stable and either U^+ or U^- equilibriums can be observed in practice that depending on small initial perturbations of (α_1, α_2). For example, as shown in **Figs 1.27b**, for relatively small (α_1, α_2)= (ε, ε) the initial U^+ configuration is the only stable one that can be observed.

To compute the critical force for the initial "straight" configuration (see **Fig. 1. 27**), let us use the geometric approach allowing to assume that after the buckling the manipulator takes either "U" or "Z" shape with small angle φ as shown in **Fig. 1. 28**, where the configuration angles are correspondingly (φ, -φ, -φ) or (φ, -3φ, 3φ). In the first case (U-shape), the kinematic Jacobian can be expressed as

$$\mathbf{J} = L \cdot \begin{bmatrix} 0 & \sin\varphi & \sin\varphi \\ 1+2\cos\varphi & 1+\cos\varphi & \cos\varphi \end{bmatrix} \tag{1. 81}$$

giving the following solution of the static equilibrium equation $\mathbf{J}^{\mathrm{T}}\mathbf{F} + \mathbf{M} = \mathbf{0}$

$$F_x = k\varphi / L\sin\varphi; \qquad F_y = 0 \tag{1. 82}$$

that yields the first critical force

$$F_x^C = \lim_{\varphi \to 0} \frac{k\varphi}{L \sin\varphi} = \frac{k}{L}\,. \tag{1. 83}$$

Similarly, in the second case (Z-shape), for small $\varphi = \varepsilon$ the kinematic Jacobian is

$$\mathbf{J} = L \cdot \begin{bmatrix} 0 & \varepsilon & -\varepsilon \\ 3 & 2 & 1 \end{bmatrix} \tag{1. 84}$$

for which the static equilibrium equation gives the following value of the critical force

$$F_x^C = \frac{3k}{L} \tag{1. 85}$$

As follows from **Fig. 1. 27**, the obtained expressions for the critical force are in good correspondence with the simulation results.

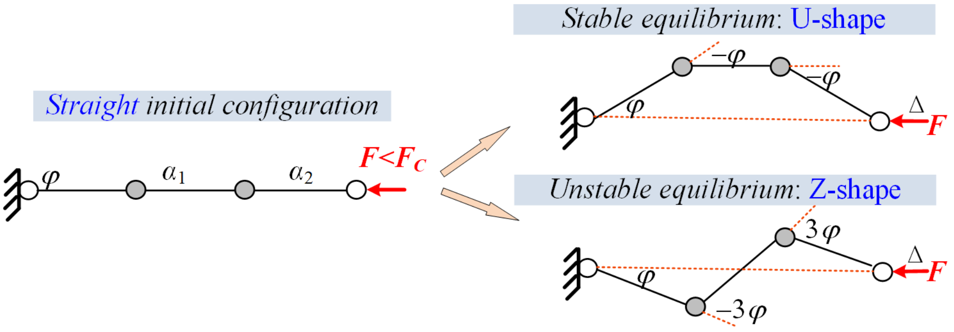

Fig. 1. 28: Evolution of the initial straight mechanism shape after the buckling: two possible equilibriums with U-shape and Z-shape.

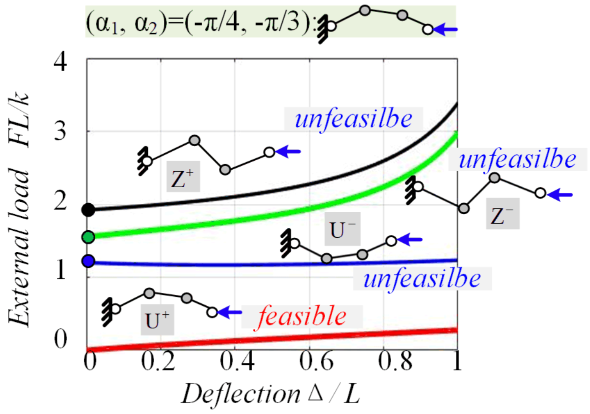

Fig. 1. 29: Force-deflection curves for the initial “U-configuration” and four possible equilibriums with the stable shapes (U^+, U^-) and unstable shapes (Z^+, Z^-).

In contrast to the previous case, for the initial U^+*-configuration* with rather large initial angles (α_1, α_2)=(–π/4, –π/3) there are four different equilibriums corresponding to four different force-deflection curves, which are shown in **Fig. 1. 29**. For the U^+ configuration that is continuously changed from the initial configuration, there is no buckling phenomenon happened. While for the other three U^- and (Z^+, Z^-) configurations that are totally different from the initial one, there are the buckling phenomenon caused by the suddenly change of the mechanism shape under the large enough critical force, which can be also treated as the jumping of the configuration. It is quite hard for this jumping to happen, so in practice only the stable U^+ equilibrium can be observed instead of these three equilibriums.

And finally, for the initial Z^-*-configuration* with (α_1, α_2)=(π/10, –π/10), the manipulator stiffness behavior has some particularities compared with the cases described above. In particular, the force-deflection curve for this manipulator shown in **Fig. 1. 30** is not smooth, and there is here the buckling phenomenon happened. It is worth mentioning that, similar to the above cases, here there are also four different equilibriums (two stable and two unstable ones). Nevertheless, in this case for the detail analysis, only a single stable configuration is taken into account, which corresponds to the continuous change of the mechanism stable shape under the loading. This evolution can be also illustrated by the energy curves on the (E, φ) plane as shown in **Fig. 1. 31**.

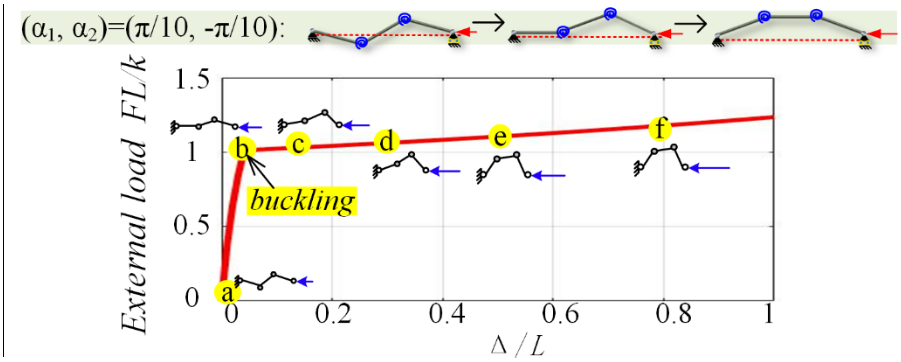

Fig. 1. 30: Force-deflection curves for the initial "Z-configuration"

As follows the obtained figures, at the beginning, the mechanism keeps the initial configuration with negative $\varphi<0$ and changes continuously its shape (as shown in **Fig. 1. 31a**), then, after the force F reaches some critical value, the angle φ becomes equal to zero $\varphi=0$ (as shown in **Fig. 1. 31b**), and the mechanism stiffness essentially reduces and the buckling is occurring. Further, for the higher loading, this angle is positive $\varphi>0$, the mechanism maintains the stable equilibriums configuration (corresponding to the minimum potential energy) and the deflection changing under the external force is monotonic (see **Fig. 1. 31c, d**). It is worth mentioning that for some configurations the observed manipulator shape does not correspond to the global minimum of the potential energy (as in **Fig. 1. 31e**), but the mechanism is not able to jump to this new configuration, instead it keeps maintaining the configuration of the local minimum of the potential energy (see **Fig. 1. 31f**).

Summarizing all the above case studies dealing with the discrete mechanical system, we can conclude that some mechanical structures can demonstrate the non-linear stiffness behavior with sudden change of the mechanism geometric configuration and its stiffness coefficient. Usually, such behavior is typical for initial straight configurations that under the loading can be suddenly replaced by a curved one, similar to the half-sine shape of the compressed Euler's column. However, the buckling phenomenon where also detected for some other initial configurations (non-straight ones) that were not studied in Euler's column theory. For instance, under the loading the three-bar serial mechanism can suddenly change its configuration from the so-called "Z-shape" to "U-shape" and essentially reduce the stiffness coefficients. So, it is quite possible that similar phenomenon can be observed in multi-link tensegrity mechanisms studied in the following chapters of this thesis.

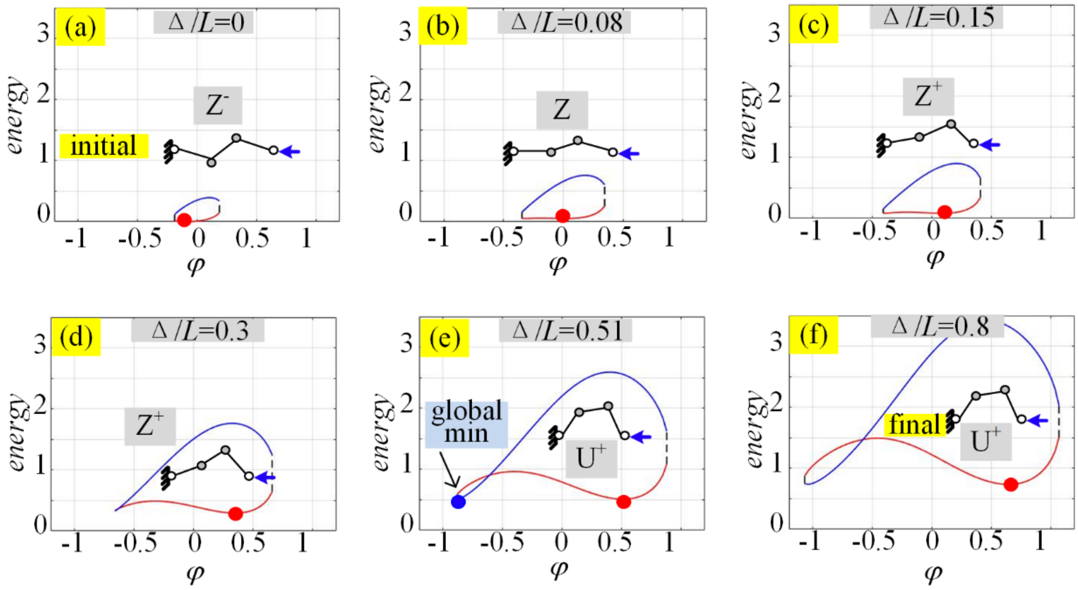

Fig. 1. 31: Evolution of energy-φ curves for stable configuration for the initial "Z-configuration.

1.4.3 Summary: thesis goal and principle tasks (research problems)

As follows from the presented review, collaborative robots involved in complicated tasks require *new types of the soft end-effectors* that possess high compliance and good manoeuvrability. The traditional industrial robots are usually equipped with rigid end-effectors, which cannot execute complicated motions in constraints environment and ensure safe collaboration with human operators. This motivates development of new compliant mechanisms that are used as the robot end-effectors, which replace traditional rigid devices. They should be much longer but lighter than the conventional ones, and also have excellent deformation capacities in very limited workspace. One of possible approaches in designing such mechanisms is using artificial muscles as the actuating components.

However, this approach is not very attractive in industrial robotics because it usually requires additional source of energy for actuation (pneumatic or hydraulic). Another difficulty is associated with the control complexity and low manipulation accuracy. These issues motivate designers to *create new soft serial mechanisms using tensegrity structures* that are proved to be very efficient in other applications such as civil engineering, architecture and art. In these structures, it is possible to combine useful properties of rigid, elastic or soft components and achieve high flexibility similar to an elephant trunk or snake robot.

The above mentioned issues motivate the primary **goal** of this thesis, which focuses on development of new robot end-effectors based on compliant serial structures composed of a number of similar modules or segments, each of which contains a *tensegrity mechanism*. Because of industrial applications and assumed human-robot collaboration, particular attention should be payed to the mechanism elastostatic properties as well as the static stability with respect to the external loading.

To achieve this goal, the following problems should be solved:

***Problem 1*:**

> ***Comparison study*** of different tensegrity mechanisms that can be potentially employed in considered applications and *selection of the best architecture* for design of multi-segment robot end-effectors.

***Problem 2*:**

> ***Stiffness analysis*** of the multi-segment dual-triangle tensegrity mechanism (that was selected as the best architecture for the end-effector) for both unloaded and loaded modes and detection of possible nonlinear behaviour under the loading as well as the *buckling* phenomenon.

***Problem 3*:**

> Development of the ***kinematic control*** strategies for redundant multi-segment mechanism based on dual-triangle tensegrity mechanisms allowing to achieve the target endpoint location and avoid collisions with the workspace obstacles.

To address these problems, the remainder of the work is organized as it follows. Chapter 2 deals with the statics and stiffness analysis of two potential tensegrity architectures (X-shape and dual-triangles) and selection the best of them for the robot end-effector base segment. Chapter 3 focuses on the stiffness analysis and control of the two-link serial chains composed of the dual-triangles for both loaded and unloaded mode. Chapter 4 concentrates on the mechanical properties and kinematic control of the three-link serial chains based on dual-triangle tensegrity segments. In Chapter 5, the stiffness analysis and the kinematic control strategies are extended for the case of multi-link redundant serial manipulator composed of the dual-triangles. And finally, Conclusion summarizes the main results and contributions, and also gives prospective for future research.

CHAPTER 2

COMPARISON OF TENSEGRITY MECHANISMS FOR DESIGN OF MULTI-SEGMENT ROBOT END-EFFECTORS

This chapter is devoted to the stiffness analysis and stability study of two potential tensegrity architectures (X-shape and dual-triangles), which are both actuated by adjusting the pre-stress of the springs located on two sides of the mechanisms, and selection the best of them as the base segment for the compliant serial manipulator end-effector proposed in this thesis. It was demonstrated for the dual-triangle mechanisms that for different combinations of the geometric parameters, the force-deflection relation curves may be either monotonic (a single equilibrium) or non-monotonic (one stable and two unstable equilibriums). While for the X-shape mechanisms, the force-deflection relation curve is always non-monotonic with one stable and two unstable equilibriums. Corresponding stability conditions for both X-shape and dual-triangle mechanisms were presented, and the control strategy for changing the mechanism configuration through adjusting the pre-stress of the springs (for both loaded and unloaded model) was also proposed in this chapter. This allowed to choose appropriate geometric parameters and springs pre-stresses ensuring the mechanism controllability. These results were confirmed by relevant simulation analysis.

2.1 Possible architectures of manipulating mechanisms for robot end-effectors

In this work we aim to develop the design methodology for *serial redundant soft mechanisms which are used as the robot end-effectors*. One of possible choices for such applications is the artificial muscle actuated manipulator, which is composed of similar segments that are adjusted by controlling the artificial muscles located symmetrically around of its geometrical central axis. An excellent example of such mechanisms is the famous McKibben Artificial Muscle (Ganguly et al., 2012; Mori et al., 2010; Tondu et al., 1994; Tondu and Lopez, 2000; Wickramatunge and Leephakpreeda, 2010), which is composed of two main parts, an inner elastomeric rubber tube surrounded by a braided sheath as shown in **Fig. 2. 1**. The artificial muscles can change their shape by controlling the pressure of the fluid medium inside of the rubber tube. When the injected pressure of the fluid is increasing, the tube will expand radially but compress axially because the materials of the braid sheath are non-elastic soft, and the axial tension force occurs correspondingly. In contrast, when the internal pressure is decreasing, the tension force becomes smaller. It is similar to the elastic springs or hydraulic cylinders but the artificial muscles are lighter and softer, especially for the robotic manipulators composed of them. For example, **Fig. 2. 2a** shows a serial manipulator composed of three similar segments, each of which is based on three parallel artificial muscles. Each artificial muscle is adjusted independently by controlling their internal pressure, so when the internal pressure are different the muscles will be compressed to different lengths and then the manipulator will bend to the desired direction. In **Fig. 2. 2b**, the robot-arm is composed of the pneumatic artificial muscles, here there are some additional mechanisms to help increasing the stability and the accuracy of this arm.

Fig. 2. 1: Mechanical design of McKibben Artificial Muscles: (a) basic components of the muscle (Zhao et al., 2018); (b) state of the muscle before and after compression (Zhao et al., 2017);

However, one of the *disadvantages* of the artificial muscles is that the f*orce-deflection relations of them are highly nonlinear*, not as simple as for the classical elastic springs, there is no accurate formulas. So, the related research is usually based on the practical experiments. Another disadvantage is that the axial deflections of the artificial muscles cannot be controlled accurately, which means that when the injected pressure of the fluid is increasing the muscles may compress to the shortest length straightforwardly, because the internal rubber tube and the outside braided sheath are both too soft so that they tend to become the largest volume under the internal pressure. Besides, as the artificial muscle is similar to the springs that can only generate/resist the axial force, the manipulator composed of them should be combined with some rigid components or structures to increase the stability, such as the example in **Fig. 2. 2b** Moreover, because the artificial muscles are made up of rather soft materials that are not as stable as the rigid mechanisms, it should be mentioned in practice to avoid the external collision to damage the muscles. So the artificial muscle actuated manipulators are still not possible to achieve the desired configuration or bending angle in practice. While this type of architecture is still interesting if the artificial muscles are replaced by some other elastic mechanisms, like springs or hydraulic cylinders, with which the manipulators can be still adjusted in the similar way to the ones actuated by the artificial muscle. And the manipulators may maintain their flexibility and soft features but their motions can be achieved more accurately. This motivates us *to achieve the desired soft properties for serial soft robot end-effectors using another design, which are based on the tensegrity mechanisms* that potentially allows us to eliminated the disadvantages of the artificial muscles. In the frame of this thesis, only planar tensegrity mechanisms are considered, but the obtained results are easily generalized for the three-dimensional case.

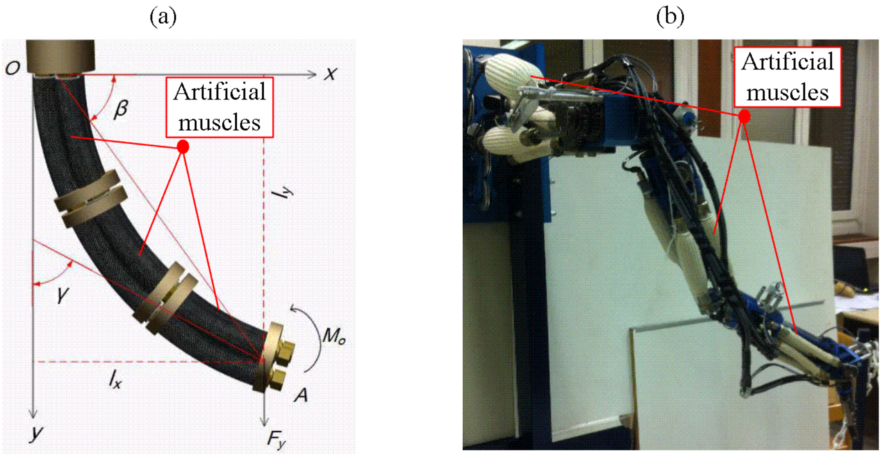
(a) (b)

Fig. 2. 2: Examples of serial-parallel manipulators actuated the artificial muscles (Kumar Hari Shankar Lal Das et al., 2016; Zhao et al., 2017).

As follows from the previous chapter there are some tensegrity mechanisms showing excellent abilities in flexible operations and load capacity, and in addition, they are more lighter than the traditional mechanisms. One of the most promising tensegrity structures for our application (soft robot end-effectors) is the *X-shape* tensegrity mechanism, which is considered in detail in the previous chapter (see **Fig. 1.3b**). This mechanism is composed of four rigid bars (two crossed ones) and two adjustable edges controlled by cables or springs. Similar to the artificial muscle actuated manipulator, each of the edges can be controlled independently, this tensegrity mechanism was demonstrated that can achieve the desired configuration and can be controlled accurately in a large workspace (Fasquelle et al., 2022). It is clear that the serial manipulators composed of this type of tensegrity mechanisms (see **Fig. 2. 3**) are highly compliant and they may be as soft as the artificial muscle actuated manipulator.

So, based on these advantages, we will consider the tensegrity mechanisms as the basic segment for the serial redundant soft robot end-effectors in this thesis. This design is inspired by the artificial muscles that are actuated by the internal fluid press. Here we consider the pre-stress springs as the actuating components and their original lengths as control inputs. In this way, one can change the control inputs of the pre-stress springs to generate the desired torque, which allows the mechanism to achieve the desired configurations in stable equilibriums.

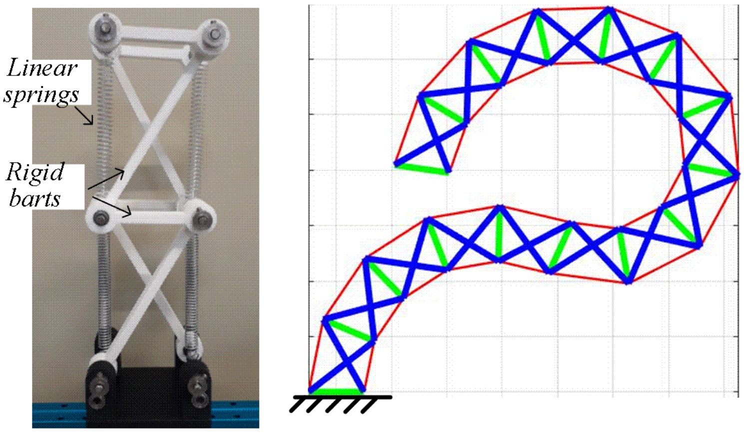

Fig. 2. 3: Examples of serial-parallel manipulators based on the X-shape tensegrity mechanisms (Wenger and Chablat, 2019c).

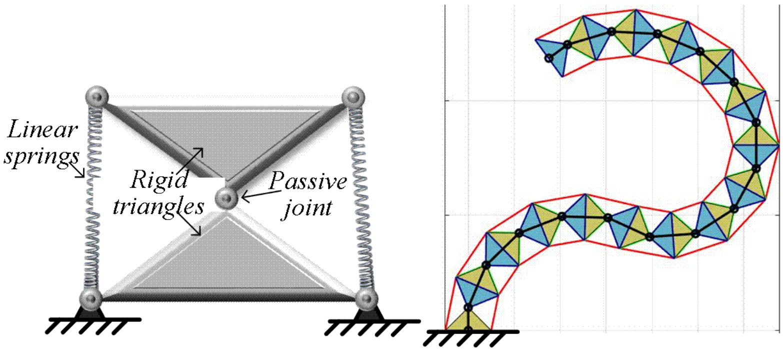

Fig. 2. 4: Proposed architecture of serial-parallel manipulators based on the dual-triangle tensegrity mechanisms

For comparison study, in this chapter we will not only consider the X-shape tensegrity mechanisms, but also propose a new design of soft serial manipulator based on the *dual-triangle* tensegrity mechanisms (see **Fig. 2. 4**). In this case, each manipulator segment is composed of two rigid triangles connected by a passive joint, and two elastic edges. And this mechanism is also adjusted by the pre-stress springs locating on the two sides. The adjusting ways of the pre-stress springs and the artificial muscles are similar, it is clear that they are almost equivalent from this point of view. However, the manipulators based on the dual-triangle mechanisms have some potential advantages that are very important for manipulator control. For this reason, the following sections focus on elastostatic analysis of the one-degree-of-freedom tensegrity mechanisms that are treated in this thesis as the basic element of the soft serial manipulator, which is used as a robot end-effector.

2.2 Stiffness properties of the dual-triangle tensegrity mechanism

2.2.1 Geometrical model and static equilibrium equation

Let us consider first a 1-d.o.f. segment of the total flexible structure to be studied, which consists of two rigid triangles connected by a passive joint whose rotation is constrained by two linear springs as shown in **Fig. 2. 5**. It is assumed that the mechanism geometry is described by the triangle parameters (a_1, b_1) and (a_2, b_2) , and the mechanism shape is defined by the angle that can be adjusted by means of two control inputs influencing on the spring lengths L_1 and L_2. Let us denote the spring lengths in the non-stress state as L_1^0 and L_2^0, and the springs stiffness coefficients k_1 and k_2.

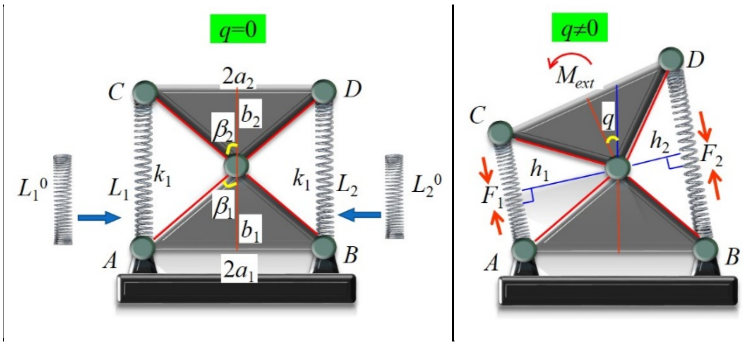

Fig. 2. 5: Geometry of a single segment mechanism.

To find the mechanism configuration angle q corresponding to given control inputs L_1^0 and L_2^0, let us derive first the static equilibrium equation. Here, the forces F_1, F_2 generated by the springs can be obtained from Hook's law as follows.

$$F_1 = k_1\,(L_1 - L_1^0); \quad F_2 = k_2\,(L_2 - L_2^0) \tag{2. 1}$$

where $L^1$and L^2 are the spring lengths $|AD|$, $|BC|$ corresponding to the current value of the angle q. These values can be computed from the triangles ΔAOD and ΔBOC using the formulas

$$\begin{aligned} L_1(\theta_1) &= \sqrt{c_1^2 + c_2^2 + 2c_1c_2\cos(\theta_1)} \\ L_2(\theta_2) &= \sqrt{c_1^2 + c_2^2 + 2c_1c_2\cos(\theta_2)} \end{aligned} \tag{2. 2}$$

where $c_1 = \sqrt{a_1^2 + b_1^2}$, $c_2 = \sqrt{a_2^2 + b_2^2}$ and the angles θ_1, θ_2 are expressed via the mechanism parameters as follows

$$\theta_1 = \beta_{12} + q, \quad \theta_2 = \beta_{12} - q, \quad \beta_{12} = \mathrm{atan}(a_1 / b_1) + \mathrm{atan}(a_2 / b_2) \tag{2. 3}$$

The torques $M_1 = F_1 \cdot h_1$, $M_2 = F_1 \cdot h_1$ created by the forces F_1, F_2 in the passive joint O can be computed using the triangle area relations $L_1 h_1 = c_1 c_2 \sin(\theta_1)$, $L_2 h_2 = c_1 c_2 \sin(\theta_2)$ of ΔAOD and ΔBOC, which yield the following expressions

$$\begin{aligned} M_1(q) &= +k_1\,(1 - L_1^0 / L_1(\theta_1))\; c_1 c_2 \sin(\theta_1) \\ M_2(q) &= -k_2\,(1 - L_2^0 / L_2(\theta_2))\; c_1 c_2 \sin(\theta_2) \end{aligned} \tag{2. 4}$$

where the difference in signs is caused by the different direction of the torques generated by the forces F_1, F_2 with respect to the passive joint.

Further, taking into account the external torque M_{ext} applied to the moving platform, the static equilibrium equation for the considered mechanism can be written as follows

$$M_1(q) + M_2(q) + M_{ext} = 0 \tag{2. 5}$$

Solving this equation we can get the rotation angle q defining the mechanism equilibrium configuration and corresponding to the control inputs L_1^0, L_2^0 and the external torque M_{ext} applied to the moving platform. This equation is highly nonlinear and cannot be solved analytically, so it is reasonable to apply the numerical Newton technique, which leads to the iterative scheme

$$q^{k+1} = q^k - \left(M(q^k) + M_{ext}\right) / M'(q^k) \tag{2. 6}$$

where $M(q) = M_1(q) + M_2(q)$, and the derivative $M'(q) = dM(q)/dq$ can be computed analytically, in order to speed up the computations.

2.2.2 Equilibrium configurations and their stability

Let us now evaluate the stability of the mechanism under consideration, which shows its resistance against the external disturbances. In general, this property highly depends on the equilibrium configuration defined by the angle *q*, which satisfies the equilibrium equation $M(q) + M_{ext} = 0$. As follows from the relevant analysis, the function $M(q)$ can be either monotonic or non-monotonic one, so the single-segment mechanism under study may have multiple stable and unstable equilibriums, which are studied in detail below.

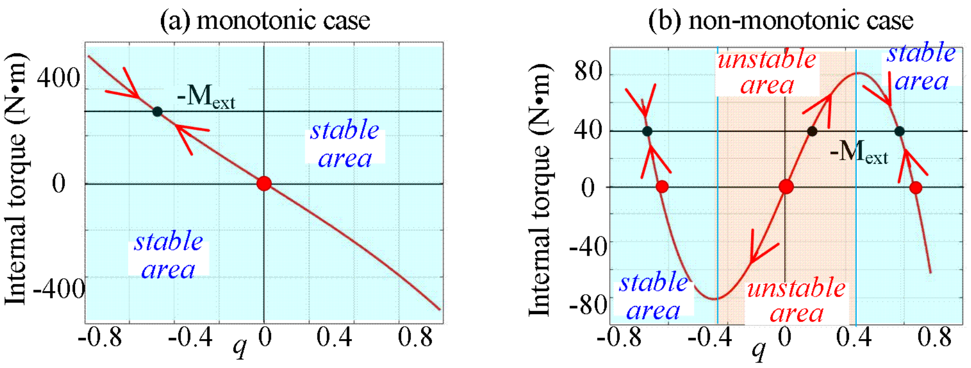

Fig. 2. 6: The torque-angle curves and static equilibriums for $L_1^0 = L_2^0$ (q_0=0).

To analyze the mechanism equilibriums, let us consider the torque-angle curves $M(q) = M_1(q) + M_2(q)$ defined by (2.3) and presented in **Fig. 2. 6**. It is clear that for the monotonic function $M(q)$ with negative derivative (see **Fig. 2. 6a**) increase of the external loading M_{ext} always leads to higher mechanism resistance, so the equilibrium is unique and stable. However, in the non-monotonic case, while increasing the external loading, it is possible to achieve a point where the mechanism does not resist any more and suddenly changes its configuration as shown in **Fig. 2. 6b**. It is worth mentioning that similar phenomenon can be observed in other mechanism and is known in mechanics as “buckling”. Hence, in the non-monotonic case, there maybe three solutions of the equilibrium equation (two stables and one unstable).

As follows from the above presented figures, the static equilibrium defined by angle q is stable if and only if the corresponding derivative $M'(q)$ is negative. However, taking into account possible shapes of the torque-angle curves $M(q)$ that can be either monotonic or two-model one, the considered stability condition can be simplified and reduced to the derivative sign verification at the zero point only, i.e.

$$M'(q)\big|_{q=0} < 0 \tag{2.7}$$

which is easy to verify in practice. It should be noted that here the derivative $M'(q)$ represents the equivalent rotational stiffness of the mechanism for the unloaded configuration with q=0.

To express the above derivative $M'(q)$ analytically, let us represent the function $M(q)$ in the following way

$$M(q) = c_1 c_2 k_1 \left(1 - \frac{L_1^0}{L_1(\theta_1)}\right) \cdot \sin\theta_1 - c_1 c_2 k_2 \left(1 - \frac{L_2^0}{L_2(\theta_2)}\right) \cdot \sin\theta_2 \tag{2.8}$$

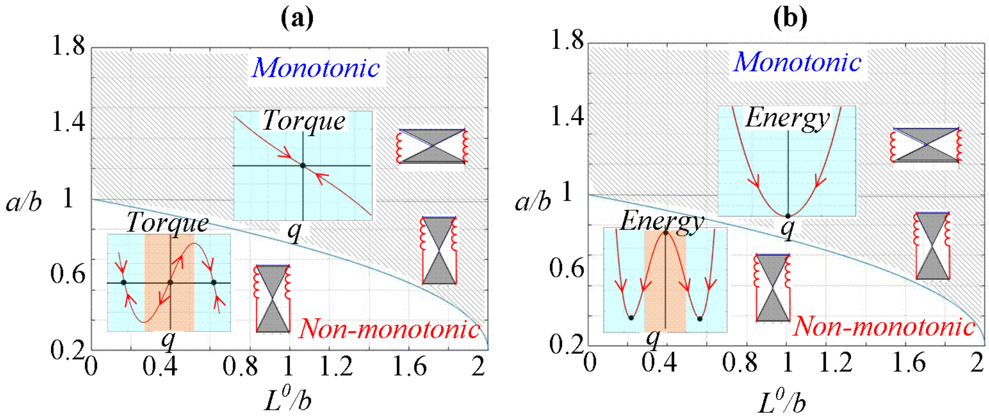

Fig. 2. 7: Monotonic and non-monotonic regions of the parameter plane for $L_1^0 = L_2^0$

This allows us to express the mechanism stiffness in general case as follows

$$M'(q) = c_1c_2k_1\left(1-\frac{L_1^0}{L_1(\theta_1)}\right)cos\theta_1 + c_1c_2k_2\left(1-\frac{L_2^0}{L_2(\theta_2)}\right)cos\theta_2 - \frac{c_1^2c_2^2k_1L_1^0}{\left(L_1(\theta_1)\right)^3}sin^2\theta_1 - \frac{c_1^2c_2^2k_2L_2^0}{\left(L_2(\theta_2)\right)^3}sin^2\theta_2 \quad (2.9)$$

For the special cases $q=0$ and $q=\pm\beta_{12}$, which are needed for further analysis, the above expression is simplified respectively to

$$M'(q)\,\big|_{q=0} = -c_1^2c_2^2\left(k_1L_1^0+k_2L_2^0\right)\frac{sin^2\beta_{12}}{\left(L\,(\beta_{12})\right)^3} + c_1c_2cos\beta_{12}\left(k_1+k_2-\frac{k_1L_1^0+k_2L_2^0}{L\,(\beta_{12})}\right) \quad (2.10)$$

$$M'(q)\,\big|_{q_0=\beta_{12}} = c_1c_2k_1cos2\beta_{12}\left(1-\frac{L_1^0}{L\,(2\beta_{12})}\right) + c_1c_2k_2\left(1-\frac{L_2^0}{c_1+c_2}\right) - c_1^2c_2^2k_1L_1^0\frac{sin^2 2\beta_{12}}{\left(L\,(2\beta_{12})\right)^3} \quad (2.11)$$

where

$$L\,(\beta_{12}) = \sqrt{c_1^2+c_2^2+2c_1c_2\cos\beta_{12}} \quad \text{and} \quad L\,(2\beta_{12}) = \sqrt{c_1^2+c_2^2+2c_1c_2\cos2\beta_{12}}$$

Here the geometry constrain is taken into account which making sure that triangles ΔAOD and ΔBOC (See **Fig. 2. 7**) exist at the same time.

Let us also consider in detail the symmetrical case, for which $a_1 = a_2$, $b_1 = b_2$, $c_1 = c_2$, $k_1 = k_2$, $L_1^o = L_2^o$. In this case, we can omit some indices and present the torque-angle relationship as well as the stiffness expression in the more compact forms:

$$M(q) = 2ck\left(c\cos\beta_{12}\sin q - L^0\cos\frac{\beta_{12}}{2}\sin\frac{q}{2}\right) \quad (2.12)$$

$$M'(q) = ck\left(2c\cos\beta_{12}\cos q - L^0\cos\frac{\beta_{12}}{2}\cos\frac{q}{2}\right) \tag{2. 13}$$

where the control input L^0 must satisfy the condition $0 < L^o < 2b$, as follows from the mechanism geometry (see **Fig. 2. 5**). To distinguish the monotonic and non-monotonic cases presented in **Fig. 2. 7**, it is also necessary to compute the derivative $M'(q)$ for the unloaded equilibrium configuration $q = 0$, which after simplification can be expressed in the following way

$$M'(q)\,\big|_{q=0} = k\left(2\left(b^2 - a^2\right) - L^o b\right) \tag{2. 14}$$

The latter allows us to present the condition (2.5) of torque-angle curve monotonicity as

$$\frac{L^0}{b} > 2\left(1 - \left(\frac{a}{b}\right)^2\right) \tag{2. 15}$$

and separate the parameter plane in two regions, monotonic and non-monotonic ones as shown in **Fig. 2. 7**. As follows from **Fig. 2. 7a**, the unloaded equilibrium is always stable if $a > b$. Otherwise, to have stable unloaded equilibrium, the control inputs $L_1^o = L_2^o$ should be higher than certain value.

$$L_i^o > 2b\left[1 - \left(a/b\right)^2\right];\quad i = 1, 2 \tag{2. 16}$$

The monotonic and non-monotonic cases are also illustrated by **Fig. 2. 7b**, which includes the energy curves

$$E(q) = \frac{1}{2}\sum\nolimits_{i=1}^{2} k\left(L_i(q) - L^0\right)^2 \tag{2. 17}$$

as the function of the rotation angle q. As follows from this figure, the energy $E(q)$ has either a single minimum $q = 0$ corresponding to a stable equilibrium, or two symmetrical minima

$$q_e = \pm\, 2\arccos\left(\frac{L^0 b}{2\left(b^2 - a^2\right)}\right) \tag{2. 18}$$

and a local maximum $q = 0$ corresponding to two stable equilibriums and one unstable equilibrium.

For the symmetrical case with equal control inputs $L_1^0 = L_2^0$, let us also compute the torques (2.8) at the boundary points $q = \pm\beta_{12}$.

$$M(q)\Big|_{q=\pm\beta_{12}} = \pm\frac{2abk}{a^2+b^2}\left(2\left(b^2-a^2\right)-L^0\sqrt{a^2+b^2}\right) \tag{2. 19}$$

which allows us to decide if the stable equilibriums in the non-monotonic case are located inside of the interval of feasible rotation angles $q\in\left[-\beta_{12},+\beta_{12}\right]$. It can be proved that the relevant condition can be expressed as follows

$$L^0 > \frac{2\left(b^2-a^2\right)}{\sqrt{b^2+a^2}} \tag{2. 20}$$

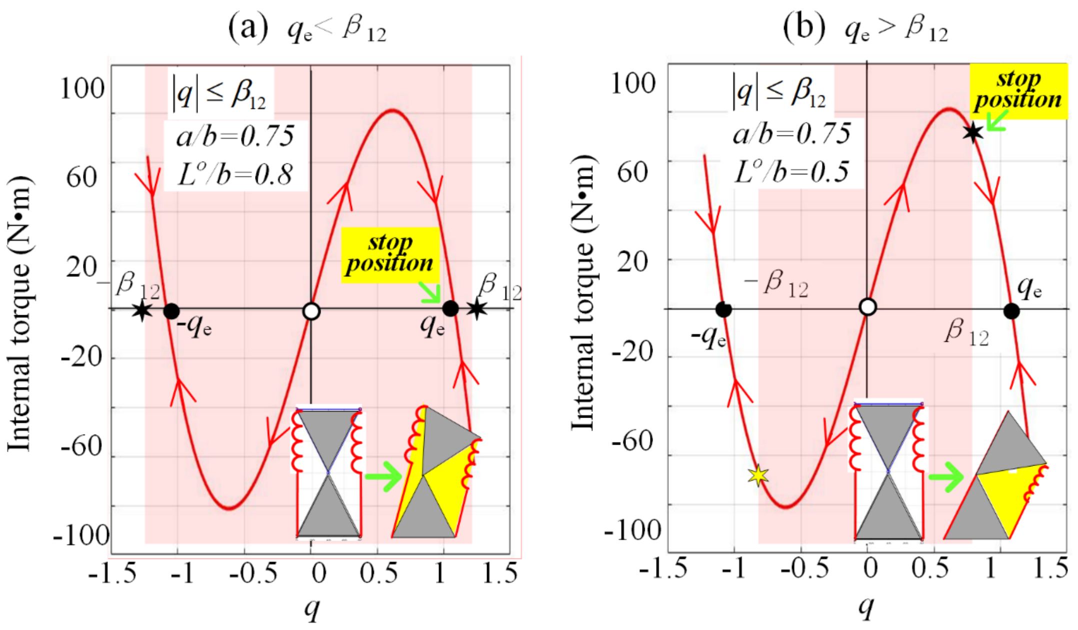

Fig. 2. 8: Location of stable “●” and unstable “o” equilibriums with respect to geometric boundary [-β_{12}, -β_{12}].

and allows user to estimate if the energy minimum is achieved inside or on the border of the feasible region of q. A physical interpretation of this inequality is shown in **Fig. 2. 8**, where two cases are presented. In the first case, the mechanism is unstable in the desired configuration q=0 and jumps to one of two possible stable configurations $q=\pm q_e$ that are located inside of mechanical limits. In the second case, the mechanism is also unstable in the equilibrium configuration q=0 but it jumps to one of the mechanical limits $q=\pm\beta_{12}$ (because the stable configurations are out of the limits). So, a static error appears in both cases, whose value is equal to either $\pm\beta_{12}$ or $\pm q_e$. For this reason, it is necessary to avoid in practice the parameters combinations producing non-monotonic torque-angle curves.

It is also useful to investigate the case when the control inputs are not equal, i.e. $L_1^0 \neq L_2^0$, assuming that they produce the desired stable configuration with the output angle $q \neq 0$. In this case, the torque and its derivative can be presented as follows.

$$M\left(q\right)=2c^2k\cos\beta_{12}\sin q-ck\left(L_1^0\sin\frac{\beta_{12}+q}{2}-L_2^0\sin\frac{\beta_{12}-q}{2}\right) \tag{2. 21}$$

$$M'(q)=2k\left(b^2-a^2\right)\cos q-k\left(\frac{L_1^0+L_2^0}{2}b\cos\frac{q}{2}-\frac{L_1^0-L_2^0}{2}a\sin\frac{q}{2}\right) \tag{2. 22}$$

where all notations are the same as in the above expressions (2.7) and (2.8). It is clear that to implement such control, the desired configuration must correspond to stable equilibrium for which $M(q)=0$, $M'(q)<0$. It is also obvious that for $L_1^0<L_2^0$ the equilibrium correspond to positive angle $q>0$, and vice versa.

It can be proved from the equilibrium equation that the control inputs L_1^0, L_2^0 insuring the desired output angle q must satisfy the linear relation

$$L_1^0\sin\frac{\beta_{12}+q}{2}-L_2^0\sin\frac{\beta_{12}-q}{2}=2c\cos\beta_{12}\sin q \tag{2. 23}$$

which gives infinite set of control variables $\left(L_1^0,L_2^0\right)$, which may correspond either to a stable or unstable equilibrium, depending on the derivative $M'(q)$. To analyze sign of the derivative, let us consider separately two cases: $a>b$ and $a<b$. In the first case, when $a>b$ and mechanism geometry imposes the constrain $\left|q\right|<\pi/2$, so all three terms of (2.22) are negative, and the desired equilibrium configuration q is stable. In the second case, when $a<b$ and the angle q maybe out of the range $\left[-\pi/2,\pi/2\right]$, and the equilibrium maybe unstable. Corresponding separation curves can be found from the conditions $M(q)=0$ and $dM(q)/dq=0$, which yield the following system of linear equations with respect to the control variables L_1^0, L_2^0.

$$\left(\sin\frac{\beta_{12}+q}{2}\right)L_1^0-\left(\sin\frac{\beta_{12}-q}{2}\right)L_2^0=2c\cos\beta_{12}\sin q \tag{2. 24}$$

$$\left(\frac{a}{2}\sin\frac{q}{2}-\frac{b}{2}\cos\frac{q}{2}\right)L_1^0-\left(\frac{a}{2}\sin\frac{q}{2}+\frac{b}{2}\cos\frac{q}{2}\right)L_2^0=-2\left(b^2-a^2\right)\cos q \tag{2. 25}$$

whose solution allows us to present the stability condition in the following form

$$\frac{L_1^0}{b}>2\left(\frac{b}{a}-\frac{a}{b}\right)\left(\frac{a}{b}\cos^3\frac{q}{2}+\sin^3\frac{q}{2}\right) \tag{2. 26}$$

$$\frac{L_2^0}{b} > 2\left(\frac{b}{a}-\frac{a}{b}\right)\left(\frac{a}{b}\cos^3\frac{q}{2}-\sin^3\frac{q}{2}\right) \tag{2.27}$$

(a) *a*/*b*=0.5 **(b)** *a*/*b*=0.75

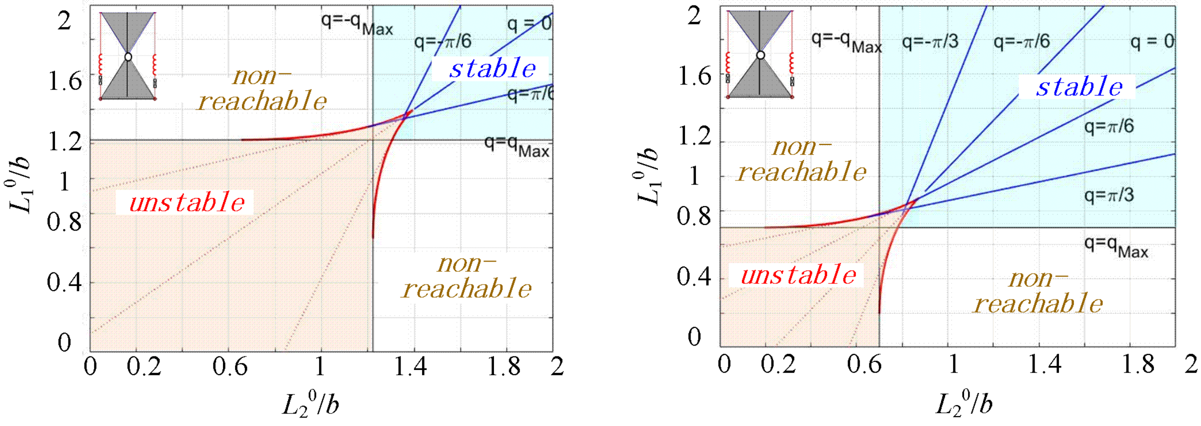

(c) *a*/*b*=1.0 **(d)** *a*/*b*=1.5

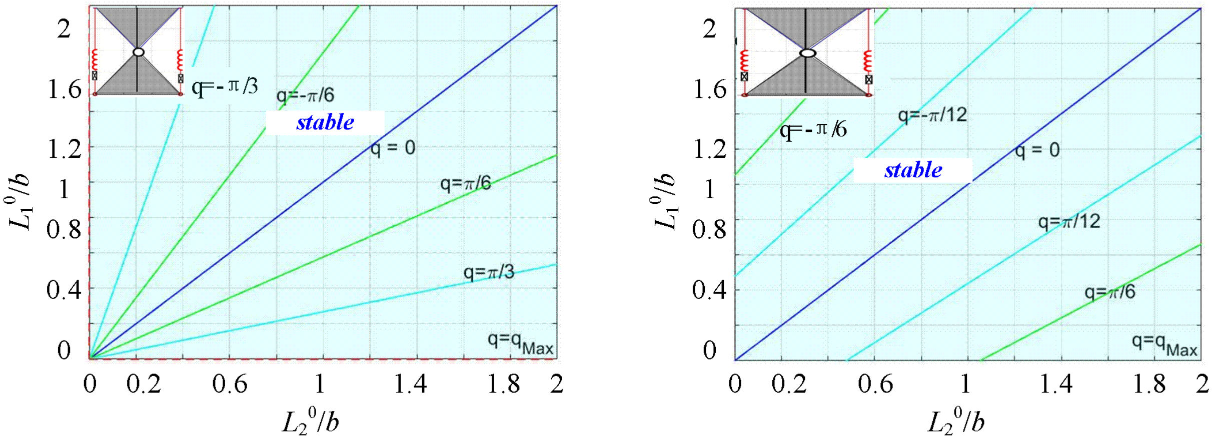

Fig. 2. 9: Regions of equilibrium stability for different inputs L_1^0, L_2^0.

It is worth mentioning that in the case of q=0 the above expressions give the stability condition (2.24). Hence, to achieve the desired configuration q it is necessary to apply the control inputs L_1^0, L_2^0 satisfying both the equilibrium condition (2.22) and the stability conditions (2.23). Corresponding regions of L_1^0, L_2^0 are presented in **Fig. 2. 9**, which clearly shows for which combination of control inputs the desired configuration q can be reached geometrically and it is statically stable. This results are also confirmed by the case study presented in **Fig. 2. 10** that demonstrate the monotonic and non-monotonic torque-angle curves for the parameters a/b=0.75, and control inputs (a) $L_1^0 = 0.88b$, $L_2^0 = 0.92b$, and (b) $L_1^0 = 0.75b$, $L_2^0 = 0.65b$, which produce the unloaded equilibrium configurations with the same angle $q_0 = \pi/6$ (but with different stability properties). It should be also noted that here there are only two equilibriums in the non-monotonic case presented in **Fig. 2. 8b**, while normally three equilibriums exist for equal control inputs as shown in **Fig. 2. 10b**. The latter is caused by the geometric constrains which eliminate the third equilibrium for non-equal control inputs.

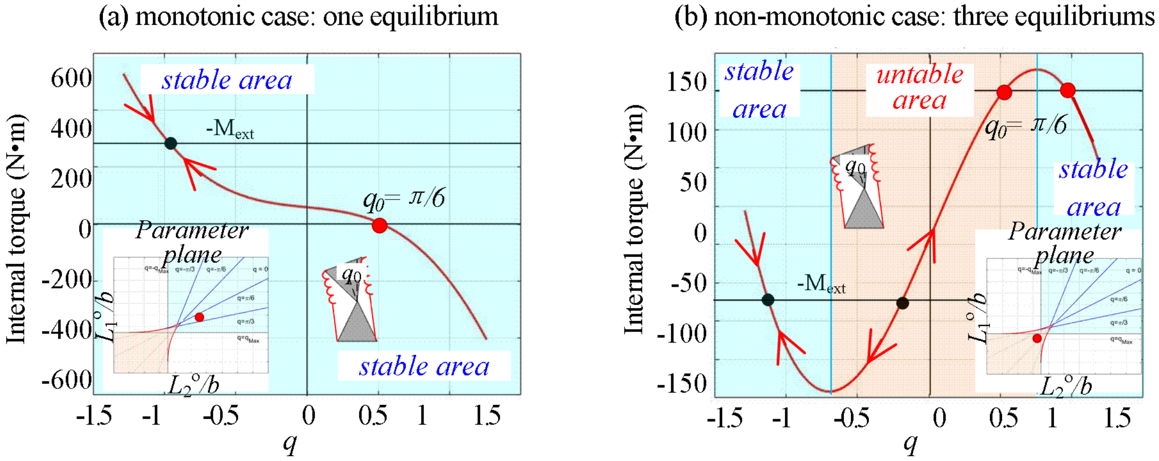
(a) monotonic case: one equilibrium

(b) non-monotonic case: three equilibriums

Fig. 2. 10: The torque-angle curves and static equilibriums for $L_1^0 \neq L_2^0$ ($q0 = \pi/6$).

2.2.3 Controlling mechanism configurations

As follows from the mechanism structure (see **Fig. 2. 5**), the desired configuration is defined by single variable *q* which is adjusted by two control variables L_1^0 and L_2^0. The latter creates redundancy and ambiguity in control inputs selection. To eliminate this difficulty, it is reasonable to define L_1^0 and L_2^0 in a symmetrical way, i.e. as $L_1^0 = L^0 - \Delta$ and $L_2^0 = L^0 + \Delta$. This allows us to rewrite (2.19) as follows

$$M_q = 2k\left[(b^2 - a^2)\sin(q) - L^0 b \cdot \sin(\frac{q}{2}) + \Delta \cdot a \cdot \cos(\frac{q}{2})\right] \qquad (2.\ 28)$$

and present the control law $\Delta(q)$ for the unloaded case ($M_{ext} = 0$) in the following way

$$\Delta(q) = \frac{L^0 b \sin(q/2) - (b^2 - a^2)\sin(q)}{a\cos(q/2)} \qquad (2.\ 29)$$

It should be noted that the desired configuration defined by the angle *q* should always satisfy the geometric constrains

$$\begin{aligned} |q| &< 2\text{atan}(a/b), & a \le b \\ |q| &< \pi - 2\text{atan}(a/b), & a > b \end{aligned} \qquad (2.\ 30)$$

that can be easily obtained from the geometry analysis. The obtained control law $\Delta(q)$ as well as the corresponding sensitivity and stiffness coefficient are presented in **Fig. 2. 11**. As follows from these figures, for the proposed control strategy it is necessary carefully select initial values of control inputs $L_1^0 = L_2^0$, in order to avoid the negative equivalent rotational stiffness causing instability of the desired configuration of the mechanism.

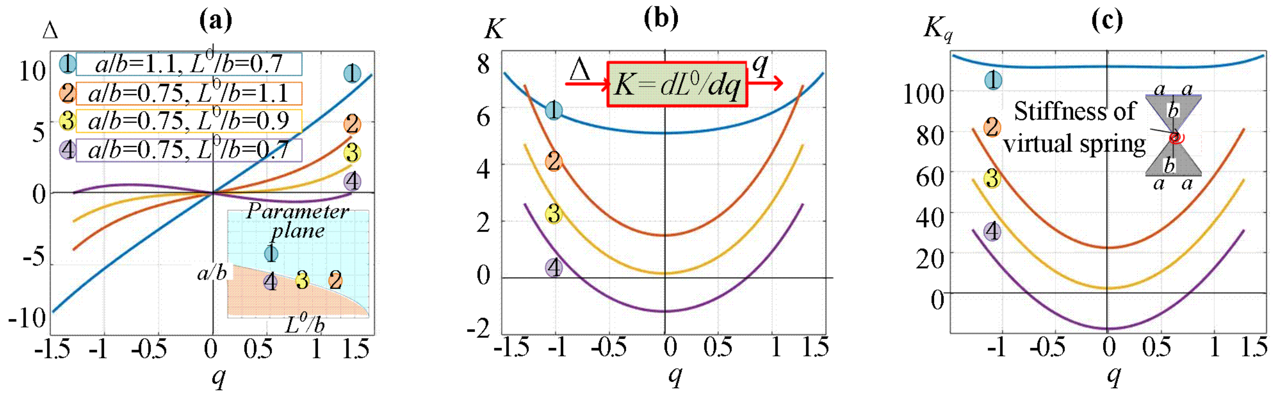

Fig. 2. 11: Relations between the control input Δ, sensitivity coefficient K, stiffness coefficient K_q and the desired configuration angle q (unloaded case $M_{\text{ext}}=0$).

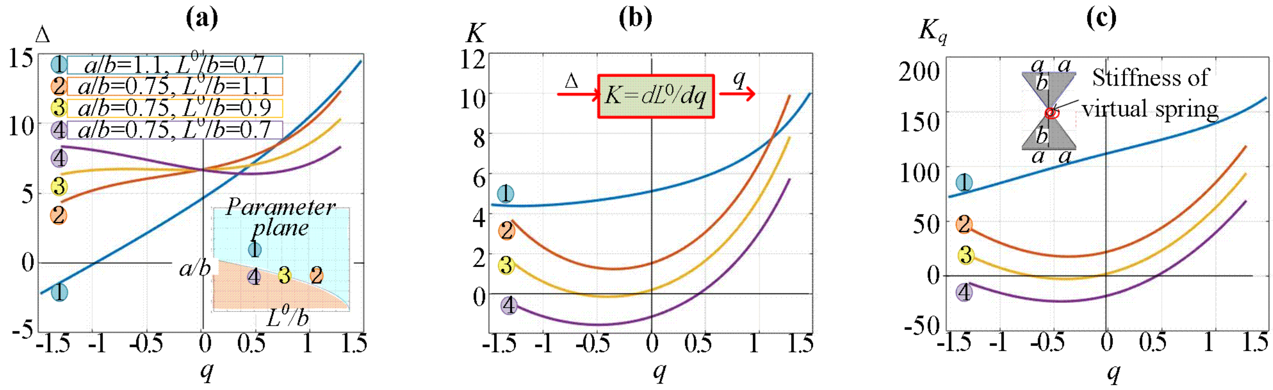

Fig. 2. 12: Relations between the control input Δ, sensitivity coefficient K, stiffness coefficient K_q and the desired configuration angle q (loaded case $M_{\text{ext}}\neq 0$).

It is worth mentioning that the above equations were derived assuming that the external loading M_{ext} is equal to zero. So, in more general case when $M_{ext} \neq 0$, the control law must be revised. It can be proved that to achieve the desired configuration with the angle q and the external loading M_{ext}, the control input Δ should be computed using an expression

$$\Delta(q, M_{ext}) = \frac{M_{ext}/2k + L^0 b \cdot \sin(q/2) - (b^2 - a^2)\sin(q)}{a \cdot \cos(q/2)} \tag{2. 31}$$

which shows that in the loaded case, the symmetrical configuration with q_0=0 is achieved by applying a non-zero control input that compensate the external loading. Relevant simulation results are shown in **Fig. 2. 12**. However, it is necessary to be careful about selection of the parameter L^0 which in some cases can cause negative stiffness leading to the buckling phenomenon.

2.3 Stiffness properties of the X-shape tensegrity mechanism

2.3.1 Geometrical model and static equilibrium equation

Let us consider now an X-shape tensegrity mechanism, which consists of four rigid links and two elastic edges, where there are two linear springs located as shown in **Fig. 2. 13**. For this mechanism all the links and springs are connected by passive joints and it is assumed that the initial orientation angles are β_1^0 and β_2^0, and the primary geometric parameters are (a_1, b_1) and (a_2, b_2), where $a_i \le b_i \;\; (i=1,2)$. Here, the mechanism shape is defined by the lengths of the elastic edges AD and BC, which are denoted as L_1 and L_2. It is also assumed that the stiffness coefficients of the springs incorporated in the elastic edges are k_1 and k_2, while their initial unstressed lengths are L_1^0 and L_2^0. Similar to the previous section, the later are considered as the control inputs influencing on the mechanism shape. More details of such type of tensegrity mechanisms were presented in (Furet and Wenger, 2019a), while in this work we concentrate mainly on the comparison analysis with the dual-triangle mechanism considered above.

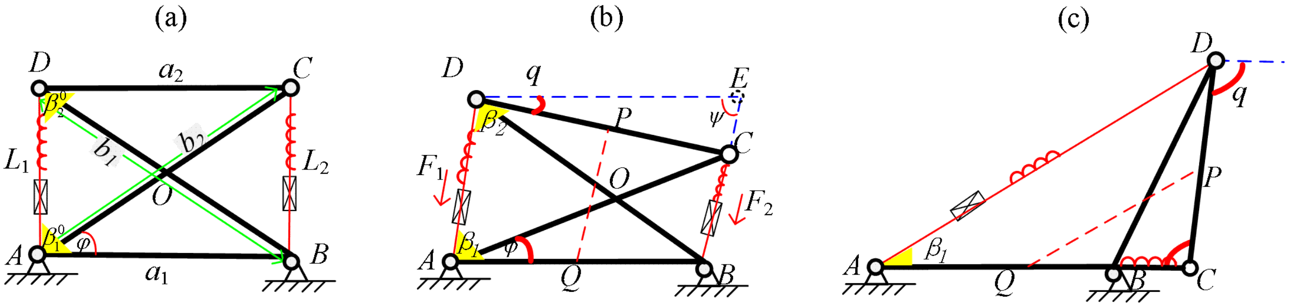

Fig. 2. 13: Geometry of an X-shape tensegrity mechanism for three typical configurations: (a) initial configuration with q=0; (b) intermediate configuration; (c) extreme configuration with q=$q_{\max}$.

To find the mechanism equilibrium condition, let us first assume that the orientation angle q is known and it is defined as shown in **Fig. 2. 13b**. Also let us define the unknown variables β_1 and β_2 as the values of the angle $\angle$BAD and $\angle$ADC respectively. It is clear that here the angle β_1 can be expressed as $\beta_1 = \pi - \beta_2 - q$. Besides, as follows from the cosine theorem, apply to the triangles ΔABD and ΔACD, the considered variable are related in the following way

$$\begin{aligned} & L_1^2 + a_1^2 + 2a_1 L_1 \cos(\beta_2 + q) = b_1^2 \\ & L_1^2 + a_2^2 - 2a_2 L_1 \cos\beta_2 = b_2^2 \end{aligned} \tag{2. 32}$$

which gives us two independent equations with respect to two variables β_2 and L_1. By solving these equations one can obtain the values of $L_1(q)$ and $\beta_2(q)$ with respect to angle q. Then, similar technique can be also applied to the triangle $\Delta \mathrm{ACD}$, for which one can get the angle $\angle \mathrm{DAC}$ if L_1 is obtained already. That gives us the following expression

$$\angle \mathrm{DAC} = \mathrm{acos} \frac{L_1^2(q) + b_2^2 - a_2^2}{2b_2 L_1(q)} \tag{2. 33}$$

So, the angle φ in triangle $\Delta \mathrm{ABC}$ can be obtained as $\varphi = \beta_1 - \angle \mathrm{DAC}$, from which one can get the length of the other elastic edge L_2 from the cosine theorem as follows

$$L_2(q) = \sqrt{a_1^2 + b_2^2 - 2a_1 b_2 \cos\varphi} \tag{2. 34}$$

Thus, the configuration of this mechanism corresponding to the orientation angle q is obtained.

Further, it is necessary to take into account that the forces F_1, F_2 generated by the springs can be obtained from Hook's law as follows

$$F_1 = k_1 (L_1 - L_1^0); \quad F_2 = k_2 (L_2 - L_2^0) \tag{2. 35}$$

Further, the torques created by the forces F_1, F_2 in the virtual passive joint O can be computed from the geometric and physic analysis, from which the static equilibrium condition can be obtained. However, it should be stressed that in this case (in contrast to the dual-triangle mechanism) the virtual passive joint O is not fixed and such computation is complex. For this reason, more convenient and universal way for getting the static equilibrium condition is using the energy method. It can be proved that the total potential energy U of this mechanism can be expressed using (2.36) as shown in below, where $\Delta L_1(q)$ and $\Delta L_2(q)$ are the elastic edge deflections that are computed from the expressions $\Delta L_1(q) = L_1(q) - \sqrt{b^2 - a^2}$ and $\Delta L_2(q) = -L_2(q) + \sqrt{b^2 - a^2}$.

$$U(q) = -F_1 \cdot \Delta L_1(q) + F_2 \cdot \Delta L_2(q) \tag{2. 36}$$

It is worth mentioning that in the above expression the minus sign shows that the work generated by the force F_1 is negative, because the angle deflection caused by it is in the different direction with the current increment of the angle q. Finally, after some simplifications, the mechanism total energy with respect to the angle q is expressed as follows

$$U(q)=-k_1L_1^2(q)-k_2L_2^2(q)+k_1L_1(q)L_1^0+k_2L_2(q)L_2^0+\left(k_1L_1(q)+k_2L_2(q)-k_1L_1^0-k_2L_2^0\right)\sqrt{b^2-a^2} \quad (2.37)$$

Using this expression, the total torque applying to the end platform CD can be computed as the derivative of the energy function $U(q)$ with respect to the orientation angle q. So, for the unloaded case, the desired static equilibrium configuration of this mechanism can be obtained from the minimum energy condition, which yields

$$\frac{dU(q)}{dq}=0 \quad (2.38)$$

For the loaded case, taking into account the external torque M_{ext} applied to the end platform, the static equilibrium equation for the considered mechanism can be written as follows

$$\frac{dU(q)}{dq}+M_{ext}=0 \quad (2.39)$$

It should mentioned that for this X-shape mechanism, the obtained static equilibrium equation is highly nonlinear and cannot be solved analytically, but the derivative $dU(q)/dq$ can be easily obtained from (2.37) analytically. Hence, in the general case, numerical computing of equilibrium configuration corresponding to the external torque M_{ext} does not create particular difficulties. However, in practice, non-symmetrical architecture of such type of mechanisms is not attractive for designers, because multi-segment serial manipulators composed of such non-symmetrical sections are difficult to control (computations are rather complex).

Let us now evaluate the stability of the mechanism under consideration and concentrate on the symmetrical case, for which $a_1=a_2=a$ and $b_1=b_2=b$. In this case, $|\text{DE}|=|\text{DC}|=a$ and $\beta_1=\beta_2=\psi$, where β_1 can be expressed via the angle q as follows

$$\beta_1=\beta_2=\frac{\pi-q}{2} \quad (2.40)$$

Thus the length $L_1(q)$ of (2.32) can be found analytically as

$$L_1(q)=a\sin\frac{q}{2}+\sqrt{b^2-a^2\cos^2\frac{q}{2}} \quad (2.41)$$

Besides, here $\angle\text{BCD}=\pi-\beta_1$, so the length L_2 can be computed use the cosine theorem for the triangle

ΔBCD, i.e.

$$L_2^2 + a^2 + 2aL_2\cos\beta_1 = b^2 \tag{2. 42}$$

which allows to present the function of $L_2(q)$ in the following way

$$L_2(q) = -a\sin\frac{q}{2} + \sqrt{b^2 - a^2\cos^2\frac{q}{2}} \tag{2. 43}$$

The above expressions also allow us to find the length of midline PQ, which is considered as the distance between the platform and the base of this mechanism

$$L_{PQ}(q) = \sqrt{b^2 - a^2\cos^2\frac{q}{2}} \tag{2. 44}$$

So, for the symmetrical architecture, the derivative of the potential energy with respect to q from (2. 37) can be written as

$$\frac{dU}{dq} = k_1\left(-2L_1(q) + L_1^0 + \sqrt{b^2 - a^2}\right)\cdot\frac{dL_1(q)}{dq} + k_2\left(-2L_2(q) + L_2^0 + \sqrt{b^2 - a^2}\right)\cdot\frac{dL_2(q)}{dq} \tag{2. 45}$$

where the derivatives of the lengths $L_1(q)$, $L_2(q)$ are

$$\begin{aligned} \frac{dL_1(q)}{dq} &= \frac{1}{2}a\cos\frac{q}{2} + \frac{1}{4}\frac{a^2\sin q}{\sqrt{b^2 - a^2\cos^2\frac{q}{2}}} \\ \frac{dL_2(q)}{dq} &= -\frac{1}{2}a\cos\frac{q}{2} + \frac{1}{4}\frac{a^2\sin q}{\sqrt{b^2 - a^2\cos^2\frac{q}{2}}} \end{aligned} \tag{2. 46}$$

These allow us to rewrite the static equilibrium condition $dU(q)/dq + M_{ext} = 0$ in a simplified form and easily find the orientation angle q for given control inputs L_1^0, L_1^0 parameters a, b and external load M_{ext}.

It should be mentioned that the maximum/minimum values for the variable q can be found from the geometric analysis, which shows that when the links AC and AB are parallel, this mechanism will achieve the limited configuration as shown in **Fig. 2. 13c**. In this case $q_{\lim} = \angle\text{BCD}$, which can be computed from the cosine theorem applied to the triangle ΔBCD, which yields

$$q_{\lim} = \operatorname{acos}\frac{a_2^2 + (b_2 - a_1)^2 - b_1^2}{2a_2(b_2 - a_1)} \tag{2. 47}$$

and allows us to present the geometric constraints for angle q in the following form $q \in [-q_{\lim},\ q_{\lim}]$

2.3.2 Equilibrium configurations and their stability

To analyze stability of the equilibrium configurations, let us consider the second derivative of the potential energy $U(q)$ with respect to q, which for symmetrical case can be expressed as follows

$$\begin{aligned}\frac{d^2U}{dq^2} = &-2k_1\left(\frac{dL_1(q)}{dq}\right)^2 + k_1\left(-2L_1(q) + L_1^0 + \sqrt{b^2-a^2}\right)\frac{dL_1^2(q)}{dq^2} - \\ &-2k_2\left(\frac{dL_2(q)}{dq}\right)^2 + k_2\left(-2L_2(q) + L_2^0 + \sqrt{b^2-a^2}\right)\frac{dL_2^2(q)}{dq^2}\end{aligned} \tag{2. 48}$$

where the second order derivatives of $L_1(q), L_2(q)$ are

$$\begin{aligned}\frac{dL_1^2(q)}{dq^2} &= -\frac{1}{4}a\sin\frac{q}{2} + \frac{1}{4}\left(\frac{a^2\cos q}{\sqrt{b^2 - a^2\cos^2\frac{q}{2}}} - \frac{(a^2\sin q)^2}{4\sqrt{b^2 - a^2\cos^2\frac{q}{2}}^{\,3}}\right) \\ \frac{dL_2^2(q)}{dq^2} &= \frac{1}{4}a\sin\frac{q}{2} + \frac{1}{4}\left(\frac{a^2\cos q}{\sqrt{b^2 - a^2\cos^2\frac{q}{2}}} - \frac{(a^2\sin q)^2}{4\sqrt{b^2 - a^2\cos^2\frac{q}{2}}^{\,3}}\right)\end{aligned} \tag{2. 49}$$

First, let us assume that the stiffness coefficient of the springs are equal, i.e. $k_1 = k_2 = k$, as well as the values of two control inputs, i.e. $L_1^0 = L_2^0 = L^0$. That allows us to rewrite the above formulas in a more compact way and the internal torque computed for the mechanism midpoint P can be derived from $M(q) = dU(q)/dq$ and rewritten as

$$M(q) = ka^2\sin q \cdot \left(\frac{L^0 + \sqrt{b^2-a^2}}{2\sqrt{b^2 - a^2\cos^2\frac{q}{2}}} - 2\right) \tag{2. 50}$$

It should be noted that here by solving the unloaded equilibrium condition $M(q) = 0$, we can get more than one solutions that describe both stable and unstable equilibriums of this mechanism:

$$q_1 = 0; \qquad q_{2,3} = \pm\pi; \qquad q_{4,5} = \pm \mathrm{acos}\left(\frac{2b^2}{a^2} - \frac{\left(L^0+\sqrt{b^2-a^2}\right)^2}{8a^2} - 1 \right) \tag{2. 51}$$

The first group of these solutions $q_1 = 0$ or $q_{2,3} = \pm\pi$ do not violate any geometric constraints (i.e. exist mathematically), while the existence of $q_{4,5}$ depends on the value of the spring pre-stress L^0. According to the cosine value range [-1, 1], we can get the following condition for existence of $q_{4,5}$

$$3\sqrt{b^2-a^2} \le L^0 \le 4b \tag{2. 52}$$

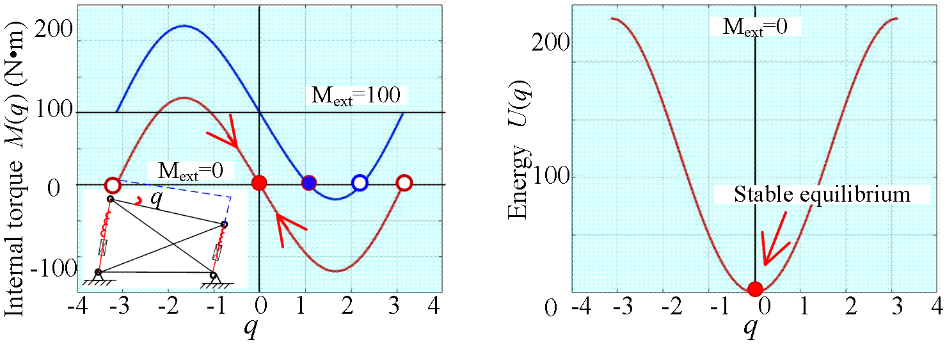

Fig. 2. 14: The torque-angle curves and static equilibriums for X-shape mechanism ($L_1{}^0 = L_2{}^0$).

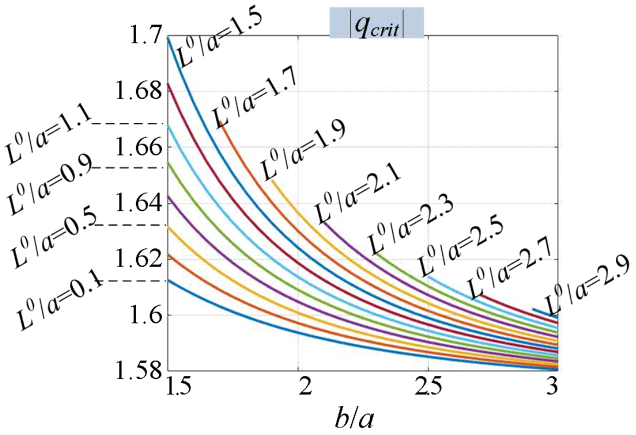

Fig. 2. 15: The critical value of configuration angle q for different combination of the control input L^0 and the parameters a, b.

It is sure that for the symmetric architecture ($a_1 = a_2 = a$ and $b_1 = b_2 = b$,), from the geometry the relation between the parameters is $b>a$, and the control inputs should be less than the length of the edge, i.e. $L^0 < \sqrt{b^2-a^2}$. So the above two solutions of (2. 51) do not exist at all. It means that for this X-shape tensegrity mechanism, there is only one stable equilibrium configuration q=0 for the unloaded mode.

To evaluate the mechanism stability for the obtained equilibrium configurations defined by the angle *q*, let us compute the corresponding stiffness coefficients that can be found from the second derivative of the energy $K(q) = dU''(q)/dq^2$. Relevant computations yield the following analytical expression

$$K(q) = ka^2 \cos q \left(\frac{L^0 + \sqrt{b^2 - a^2}}{2\sqrt{b^2 - a^2 \cos^2 \frac{q}{2}}} - 2 \right) - ka^4 \sin^2 q \frac{L^0 + \sqrt{b^2 - a^2}}{8\sqrt{b^2 - a^2 \cos^2 \frac{q}{2}}^{3}} \qquad (2.\ 53)$$

It is clear that the static equilibrium defined by angle *q* is stable if and only if there is the resistance for the external load, i.e. the corresponding stiffness coefficient *K*(*q*) is negative. Taking into account the shape of the curve *M*(*q*) shown in **Fig. 2. 14**, the desired stability condition can be simplified and reduced to the derivative sign verification at the zero point only, i.e.

$$K(q)\big|_{q=0} < 0 \qquad (2.\ 54)$$

So, it is necessary to compute the derivative *K*(*q*) for the unloaded equilibrium configuration $q = 0$, which after simplification can be expressed in the following way

$$K(q)\,\big|_{q=0} = ka^2 \left(\frac{L^0 + \sqrt{b^2 - a^2}}{2\sqrt{b^2 - a^2}} - 2 \right) \qquad (2.\ 55)$$

The latter allows us to present the stability condition of the unloaded mechanism as

$$L^0 < 3\sqrt{b^2 - a^2} \qquad (2.\ 56)$$

Since for this mechanism, it is assumed that *a*<*b*, for the case of equal control inputs $L_1^0 = L_2^0$ it is obviously from the geometry that $L^0 < \sqrt{b^2 - a^2}$. So, this mechanism has stable equilibrium for unloaded mode. The latter is also confirmed by the energy-*q* curve shown in the right-hand part of **Fig.** , which shows that for $M_{ext} = 0$ there is a single stable equilibrium configuration corresponding to the minimum of energy. However, as also follows from this figure, under the loading ($M_{ext} \neq 0$) the mechanism stability is ensured only for some limited values of the configuration angle $q \in [-q_{cri}, q_{cri}]$, where the stiffness coefficient is negative. If the angle *q* is outside of this range, the stiffness coefficient is positive and the mechanism is unstable and does not resist to the external loading. The critical values of q_{cri} can be computed from the condition $K(q_{crit}) = 0$, they are presented in **Fig. 2. 15** as functions of geometric parameters *a, b* and the spring pre-stress L^0. As follows from this figure, to achieve the stable state of this mechanism, the desired configuration angle *q* and the corresponding *a, b* and L^0

should be selected from the area below the presented curves.

If the mechanism control inputs are not equal, i.e. $L_1^0 \neq L_2^0$, the angle q corresponding to the unloaded equilibrium configuration is not equal to zero $q \neq 0$. In this case, the torque and its derivative functions can be rewritten as follows.

$$
\begin{aligned}
M(q) &= ka^2 \sin q \left(\frac{2\sqrt{b^2-a^2} + L_1^0 + L_2^0}{4\sqrt{b^2 - a^2\cos^2\frac{q}{2}}} - 2 \right) + \frac{ka}{2}\cos\frac{q}{2}\left(L_1^0 - L_2^0\right) \\
K(q) &= -2ka^2\cos q + ka^2 \frac{-a^2(1+\cos q)^2 + 4b^2\cos q}{16\sqrt{b^2 - a^2\cos^2\frac{q}{2}}^{\,3}}\left(2\sqrt{b^2-a^2} + L_1^0 + L_2^0\right) - \frac{ka}{4}\sin\frac{q}{2}\left(L_1^0 - L_2^0\right)
\end{aligned}
\tag{2.57}
$$

Similarly to the above case, the equilibrium condition for the unloaded mode may be presented as $M(q) = 0$, which yields the following equation for computing the configuration angle q

$$
2a\sin\frac{q}{2}\left(\frac{2\sqrt{b^2-a^2} + L_1^0 + L_2^0}{2\sqrt{b^2 - a^2\cos^2\frac{q}{2}}} - 4 \right) + \left(L_1^0 - L_2^0\right) = 0 \tag{2. 58}
$$

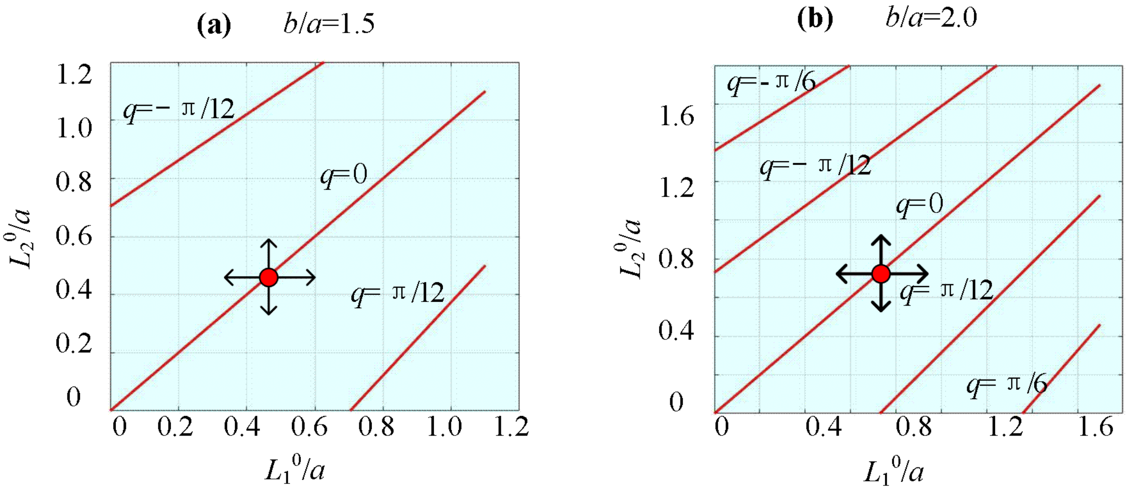

Fig. 2. 16: Regions of equilibrium stability for different inputs L_1^0, L_2^0 for X-shape tensegrity mechanism.

It is clear that the above equation may have multiple solutions but the equilibrium stability condition can be also expressed as $K(q) < 0$, which leads to the following inequality

$$-8a\cos q + a\left(2\sqrt{b^2-a^2}+\left(L_1^0+L_2^0\right)\right)\left(\frac{\cos q}{\sqrt{b^2-a^2\cos^2\frac{q}{2}}}-\frac{a^2\sin^2 q}{4\sqrt{b^2-a^2\cos^2\frac{q}{2}}^{\,3}}\right)-\sin\frac{q}{2}\left(L_1^0-L_2^0\right)<0 \quad (2.59)$$

Relevant computation results are presented in **Fig. 2. 16**, which allows to choose the control inputs L_1^0, L_2^0 corresponding to the desired equilibrium configuration *q*. It is worth mentioning that the mapping $q \to \left(L_1^0, L_2^0\right)$, i.e. there exist infinite number of control inputs L_1^0, L_2^0 corresponding to the desired angle *q*.

2.3.3 Controlling mechanism configurations

As follows from the mechanism structure (see **Fig. 2. 13**), the desired configuration is defined by a single variable *q* which is adjusted by two control variables L_1^0, L_2^0. The latter creates redundancy and ambiguity in control inputs selection. To eliminate this difficulty, it is reasonable to define L_1^0, L_2^0 in a symmetrical way, i.e. as $L_1^0 = L^0 - \Delta$ and $L_2^0 = L^0 + \Delta$. This allows us to rewrite (2.27) as follows

$$M(q) = ka^2\sin q\left(\frac{\sqrt{b^2-a^2}}{2\sqrt{b^2-a^2\cos^2\frac{q}{2}}}-2\right)+\frac{ka^2\sin q}{2\sqrt{b^2-a^2\cos^2\frac{q}{2}}}L^0 - ka\cos\frac{q}{2}\Delta \qquad (2.\ 60)$$

and present the control law $\Delta(q)$ for the unloaded case ($M_{ext}=0$) in the following way

$$\Delta(q) = \frac{a\sin\frac{q}{2}}{\sqrt{b^2-a^2\cos^2\frac{q}{2}}}\left(\sqrt{b^2-a^2}-4\sqrt{b^2-a^2\cos^2\frac{q}{2}}+L^0\right) \qquad (2.\ 61)$$

It should be noted that the desired configuration defined by the angle *q* should always satisfy the geometric constrains (2.47) ensuring that the unloaded equilibrium is stable. The obtained control law $\Delta(q)$ is presented in **Fig. 2. 17a**.

It is worth mentioning that the above equations were derived assuming that the external loading M_{ext} is equal to zero. So, in more general case when $M_{ext} \neq 0$, the control law must be revised. It can be proved that to achieve the desired configuration with the angle *q* and the external loading M_{ext}, the control input Δ should be computed using an modified expression

$$\Delta(q,M_{ext}) = \frac{M_{ext}}{ka\cos\frac{q}{2}} + \frac{a\sin\frac{q}{2}}{\sqrt{b^2-a^2\cos^2\frac{q}{2}}}\left(\sqrt{b^2-a^2} - 4\sqrt{b^2-a^2\cos^2\frac{q}{2}} + L^0\right) \tag{2. 62}$$

which shows that in the loaded case, the symmetrical configuration with $q_0=0$ is achieved by applying a non-zero control input that compensate the external loading, as shown in **Fig. 2. 17b**.

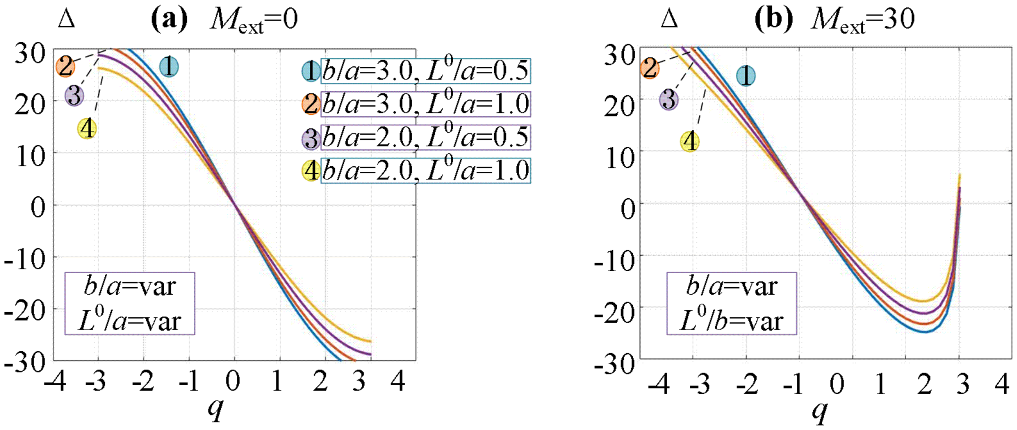

Fig. 2. 17: Relations between the control input Δ and the desired configuration angle q ($a=10$).

2.4 Comparison of the dual-triangle and X-shape tensegrity mechanisms

In the previous sub-sections, we have considered *two types of tensegrity mechanisms,* both of which can be a candidate for designing a multi-segment compliant serial chain that is in the focus of this thesis. The first of these mechanisms (see **Fig. 2. 5**) is composed of two rigid triangles connected in a passive joint and two elastic edges. The second mechanism (called here as an X-shape one) consists of four rigid links and two elastic edges as shown in **Fig. 2. 13**. In both cases the mechanism configuration is adjusted by pre-stressing the springs located on the elastic edges, which are treated as the control inputs.

For the dual-triangle mechanism, the configuration angle q limits are caused by the geometric issues. It was proved that for the symmetrical architecture the configuration angle may achieve a quite big range, such as $[-\pi/2, \pi/2]$. It means that a serial manipulator composed of the dual-triangle mechanisms may provide a *large workspace* by choosing suitable combination of the geometric parameters a, b and control input L^0. It is also worth mentioning that such type of tensegrity mechanisms may have either *monotonic or non-monotonic force-deflection* relation with either stable or unstable equilibrium configuration. This property depends on the geometric parameters a, b and spring pre-stress L^0 that must satisfy certain constraints obtained in sub-section 1.2. It is clear that for the monotonic case the mechanism always have a single stable equilibrium when the configuration angle q is inside of the geometric constraints. However, for the non-monotonic case, the mechanism has an unstable equilibrium when the configuration angle q is smaller than some critical value q_{crit} or larger than $-q_{crit}$, but when the configuration angle q is outside of this range the mechanism may have two symmetrical stable equilibriums (the existence of them is depending on the geometric constraints). From engineering point of view the monotonic force-deflection relation is an *essential advantage* of the dual-triangle mechanism, which ensures stability of the desired configuration and the mechanism resistance to the external loading.

For the X-shape tensegrity mechanism, it was proved that the geometric constraints are not so hard as above. Potentially, this may provide a rather *large range for the configuration angle q* and a quite large workspace. However, this large range of q cannot be achieved in practice because of the equilibrium stability issues. In particular, the force-deflection relation for this mechanism *is always non-monotonic*, so the configuration angle q should be inside of the smaller range $q \in [-q_{crit}, q_{crit}]$ ensuring the mechanism stability (out of this range there may exist two unstable equilibriums). It means that practical workspace is essentially smaller than the geometric limits. More details on this issue are given in section 2.3.3, where the critical values q_{crit} was obtained for different combination of the geometric parameters a, b and the spring pre-stress L^0, it was shown that the critical value q_{crit} is usually smaller than $\pi/2$.

From point of view of stiffness properties, the dual-triangle and X-shape mechanisms are quite similar, except of the high loading case when the X-shape mechanism may demonstrate buckling because of non-monotonicity of the force-deflection relation. However, for the dual-triangle mechanism the stiffness coefficient on the joint with respect to the configuration angle *q can be presented analytically*, which allows potential user to control the manipulator stiffness in real time. Besides, the direct/inverse kinematic relations for the dual-triangle mechanisms are also simpler because there is a fixed passive joint here. In particular, for the manipulator composed of such mechanisms, the lengths of each links are constant, so the kinematics is similar to the typical serial manipulator and the computations are simpler and faster. In contrast, for the X-shape tensegrity mechanism, there is no fixed joint thus the lengths of the two elastic edges L_1, L_2 are nonlinearly related to the configuration angle q and they cannot be expressed via q straightforwardly. Also, it is not possible to express analytically the stiffness coefficient with respect to q. Hence, for the manipulator composed of such mechanisms, the kinematic and elastostatic computations are rather difficult and do not well suit to the real-time implementation.

Hence, *the dual-triangle tensegrity mechanism has essential advantages for the considered applications compared to the X-shape ones.* In particular, the dual-triangle structure can always have the stable equilibrium if suitable parameters a, b and spring pre-stress L^0 are chosen. On the other hand, for the X-shape tensegrity mechanism the stable equilibrium can only be achieved when the absolute value of the configuration angle q is smaller than the certain critical value depending on the geometric parameters. So, in this thesis, we will consider the serial manipulator composed of the dual-triangle tensegrity mechanisms, relevant results are presented in the following chapters.

2.5 Summary

This part deals with the stiffness analysis and stability study of two potential tensegrity architectures (X-shape and dual-triangles), each of which can be used in design of compliant robot end-effectors.

*The **main contributions*** are related to the comparison analysis of the mechanical properties of these mechanisms and the control strategy for changing the mechanism configurations. The two length-controllable elastic edges of these mechanisms can generate internal preloading, which is a very promising design and very convenient for constructing of a multi-section serial structures with high flexibility that are needed in many modern robotic applications. For practical reasons, the main attention is paid to the symmetrical structure. In particular, the case of equal spring pre-stress was investigated in detail and analytical condition of equilibrium stability is obtained. The relation between the external torque and the deflection is also obtained allowing to find loaded equilibriums.

It is demonstrated *for the **dual-triangle mechanisms*** that for different combinations of the geometric parameters, the force-deflection relation curves may be *either monotonic (a single equilibrium) or non-monotonic (one stable and two unstable equilibriums)*. While *for the **X-shape mechanisms***, the force-deflection relation curve *is always non-monotonic* with one stable and two unstable equilibriums. It was proved for the dual-triangle mechanisms that depending on parameters combinations, the actuation can lead to either the desired mechanism configuration (corresponding to a stable equilibrium) or undesired configuration corresponding to shifted stable equilibrium or joint limits. In the following chapters, these results will be used for the stiffness analysis of multi-section mechanisms that may demonstrate unusual behavior under static load and suddenly change its configuration.

In more details, new results and contributions of Chapter 2 include the following issues

(i) ***Stiffness analysis*** of the *X-shape* and *dual-triangle* tensegrity mechanism based on the VJM technique, which allows to easily obtain the lower dimensional stiffness matrices compared to other methods, and get the mechanism stability condition analytically.

(ii) The mechanism ***stability conditions*** are presented analytically and different equilibriums of these two types of mechanisms are obtained, which allows user to select the mechanical architecture ensuring the mechanism controllability.

(iii) The proposed ***control strategy*** allows to achieve the desired mechanism configuration through anti-symmetrical adjusting the pre-stress of the springs (for both loaded and unloaded model).

It should mentioning that for both symmetrical and non-symmetrical architectures, the stiffness models and the stability conditions of these mechanisms are presented. Although the main attention in this thesis is only paid to the symmetrical one, relevant results for the non-symmetrical one can also be obtained in a similar way.

The main results of Chapter 2 are published in the following works: (Zhao et al., 2021a, 2020).

CHAPTER 3

ANALYSIS OF A TWO-SEGMENT MECHANISM COMPOSED OF DUAL-TRIANGLES

This chapter is devoted to the stiffness analysis of the two-segment serial structure based on the dual-triangle tensegrity mechanism for both straight and non-straight initial configurations. For this manipulator, the stiffness matrix was obtained through the VJM technique, and the conventional inverse kinematic transformation for two-link serial manipulator was used straightforwardly. The particularity of this serial mechanism is that, for the initial straight configuration, the buckling phenomenon was detected, and the critical force causing the buckling was obtained analytically. The control strategy presented in chapter 2 was also enhanced. The simulation results confirmed the efficiency of the developed technique.

3.1 Stiffness analysis of a straight configuration

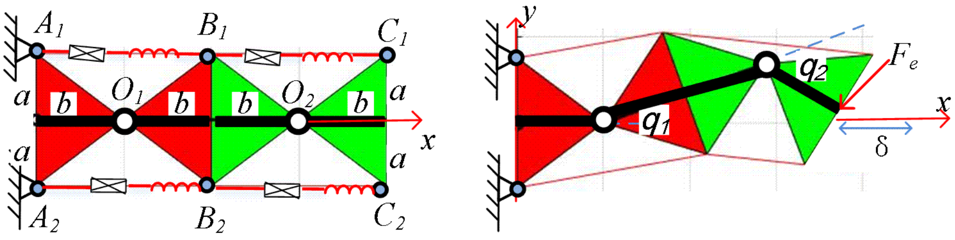

Fig. 3. 1: The two segment mechanism in the “straight” and “non-straight” configurations.

Let us consider first an aggregated mechanism presented in **Fig. 3. 1**, which is composed of two segments considered in the previous section. It is assumed that the left hand-side of the mechanism is fixed and the desired configuration corresponds to the "straight" shape with $q_1 = q_2 = 0$ that is achieved by applying equal control inputs to all segments. Under the influence of the external force F_e, the end-effector moves from the unloaded equilibrium configuration $\left(x_0, y_0\right)^T = \left(4b, 0\right)^T$ to a new equilibrium with the end-effector location $(x, y)^T = (4b - \delta_x, \delta_y)^T$ corresponding to the nonzero angles $\left(q_1, q_2\right)$. Let us evaluate the mechanism resistance to the external force F_e for this "straight" configuration described by the force-deflection relations $F_x(\delta_x, \delta_y)$ and $F_y(\delta_x, \delta_y)$.

It is clear that if the end-effector deflection (δ_x, δ_y) is given, the configuration angles $\left(q_1, q_2\right)$ can be computed from the mechanism geometry, using the triangle equations

$$\begin{aligned} & b + 2bC_1 + bC_{12} = 4b - \delta_x \\ & 2bS_1 + bS_{12} = \delta_y \end{aligned} \tag{3. 1}$$

that can be solved using the technic used in the invers kinematics of the two-link robotic manipulator, which yields

$$\begin{aligned} & q_1 = \operatorname{atan2}(y, x-b) - \operatorname{atan2}\left(bS_2, 2b + bC_2\right) \\ & q_2 = \operatorname{atan2}\left(S_2, C_2\right) \end{aligned} \tag{3. 2}$$

where $C_2 = \left(\left(x-b\right)^2 + y^2 - 5b^2\right) \Big/ 4b^2$, $S_2 = \pm\sqrt{1 - C_2^2}$. It is worth mentioning that two symmetrical solutions are possible here and both of them may be feasible, i.e. belong to the geometric limits described by (1.30). Then, for each segment the torque generated by the elastic virtual spring can be computed using (1.12), which for this mechanism is rewritten as

$$M\left(q_i\right) = 2k\left[\left(b^2 - a^2\right)\sin q_i - bL^o \sin\frac{q_i}{2}\right], \; i = 1, 2 \tag{3. 3}$$

This allows us to obtain the desired equilibrium equation, which relates the virtual spring torques $M\left(q_i\right)$ and the external force $\left(F_x, F_y\right)^T$ in the following form

$$\begin{bmatrix} M\left(q_1\right) \\ M\left(q_2\right) \end{bmatrix} + J_q^T \begin{pmatrix} F_x \\ F_y \end{pmatrix} = 0 \tag{3. 4}$$

where J_q is the Jacobian matrix, which is derived from the geometry model and is written as follows

$$J_q = \begin{bmatrix} -2bS_1 - bS_{1,2} & -bS_{1,2} \\ 2bC_1 + bC_{1,2} & bC_{1,2} \end{bmatrix}; \; \det\left(J_q\right) = 2b^2 S_2 \tag{3. 5}$$

and $C_1 = \cos q_1$, $S_1 = \sin q_1$, $C_{12} = \cos(q_1 + q_2)$, $S_{12} = \sin(q_1 + q_2)$. After substitution of the virtual torques $M(q_i)$ in the above equilibrium equation, we can find the desired external force corresponding to the end-effector displacement (δ_x, δ_y) expressed via the angles (q_1, q_2)

$$\begin{pmatrix} F_x \\ F_y \end{pmatrix} = 2kJ_q^{-T} \begin{bmatrix} -\sin q_1 & \sin(q_1/2) \\ -\sin q_2 & \sin(q_2/2) \end{bmatrix} \begin{bmatrix} b^2 - a^2 \\ bL^0 \end{bmatrix}, \ (q_2 \neq 0) \tag{3. 6}$$

allowing us to obtain the desired force-deflection relation in the neighborhood of the straight configuration where the Jacobian is invertible. Relevant force-deflection curves for different combinations of the mechanism parameters are presented in **Fig. 3. 2**.

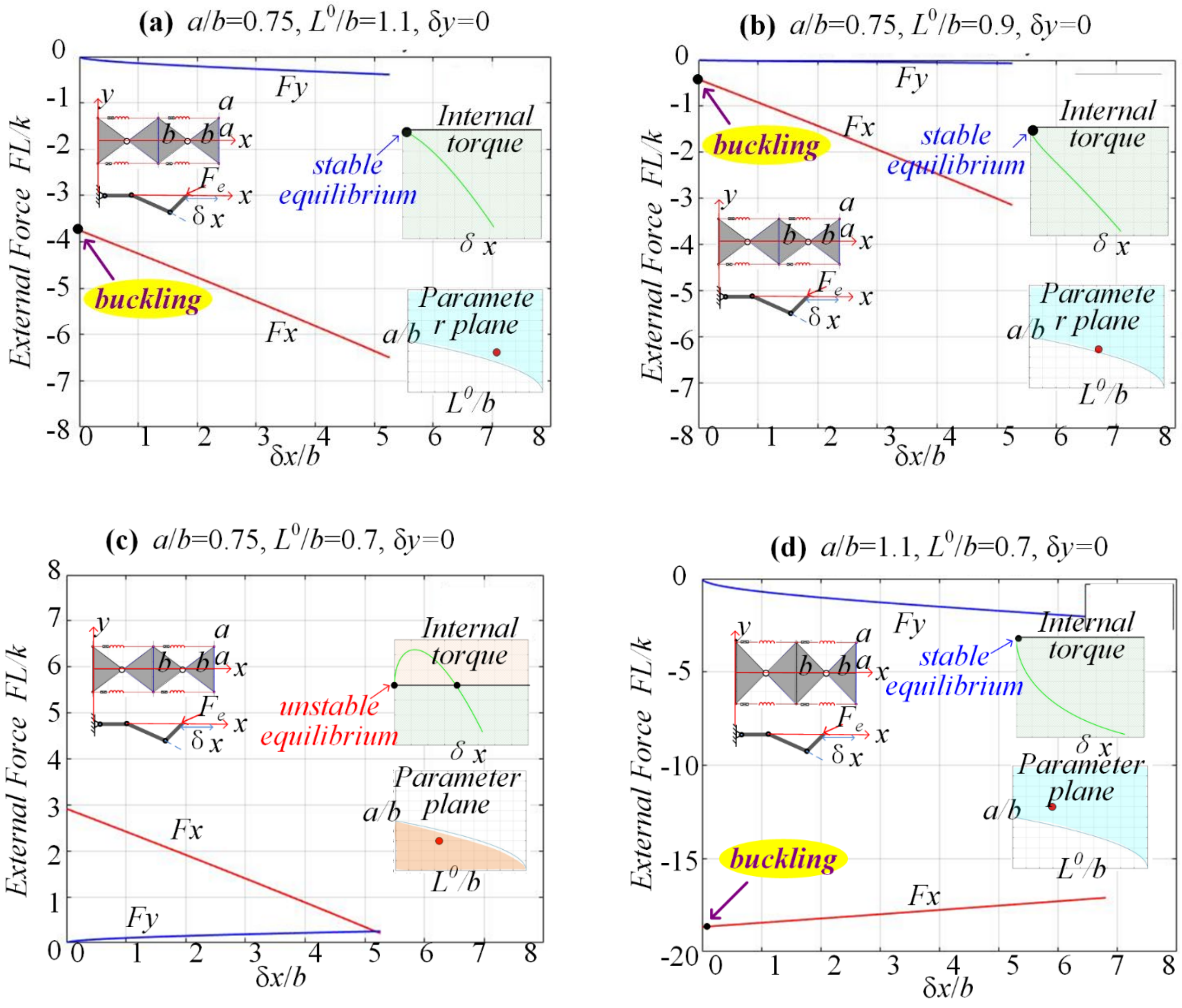

Fig. 3. 2: Force-deflection relations $F_x(\delta x, \delta y)$, $F_y(\delta x, \delta y)$ corresponding to unloaded straight configuration for different combinations of geometric parameters a, b, L^0.

As follows from the force-deflection curves presented in **Fig. 3. 2**, the mechanism stiffness behavior for the considered configuration possesses some particularities. In particular, at the beginning the mechanism resistance in the *x*-direction is infinite (corresponding curves do not go through the zero point). Further, when the loading is increasing, the mechanism resistance behavior is quasi-linear. Hence, the buckling phenomenon is observed when the external force increases gradually and the mechanism configuration angles suddenly change from zero to non-zero values. To find the *critical force* for the buckling, let us compute the limits of $\left(F_x, F_y\right)$ while $\left(\delta x, \delta y\right) \to (0,0)$. As follows from the mechanism geometry, which include a triangle with edges length of *b* and 2*b*, if the first angle $q_1 = \varepsilon$ is small enough, the second angle can be approximately expressed as $q_2 \approx -3\varepsilon$. The later allows us to write the Jacobian in the following form

$$J_q \approx \begin{bmatrix} 0 & 2b\varepsilon \\ 3b & b \end{bmatrix} \tag{3. 7}$$

and rewrite equation (3.6) as

$$\begin{pmatrix} F_x \\ F_y \end{pmatrix} \approx 2k \cdot \begin{bmatrix} 0 & 2b\varepsilon \\ 3b & b \end{bmatrix}^{-T} \begin{bmatrix} -\varepsilon & \varepsilon/2 \\ 3\varepsilon & -3\varepsilon/2 \end{bmatrix} \begin{bmatrix} b^2 - a^2 \\ bL^0 \end{bmatrix} \tag{3. 8}$$

that gives us the desired critical forces in the *x*- and *y*- directions

$$\begin{aligned} F_x^0 &= \lim_{\varepsilon \to 0} F_x(\varepsilon) \; = \; 5k\left[2\left(b^2 - a^2\right) - bL^o\right]\Big/3b \\ F_y^0 &= \lim_{\varepsilon \to 0} F_y(\varepsilon) = 0 \end{aligned} \tag{3. 9}$$

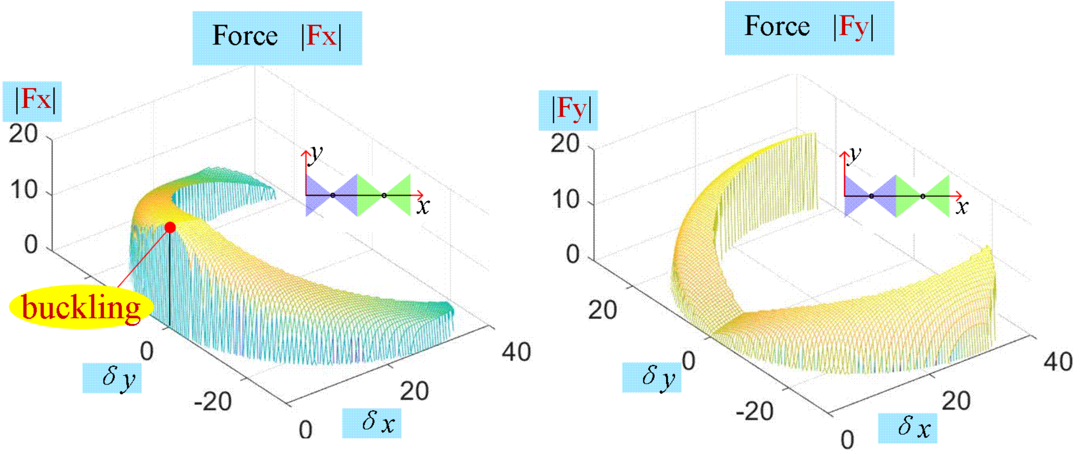

Fig. 3. 3: Force-deflection relations $F_x(\delta x, \delta y)$, $F_y(\delta x, \delta y)$ corresponding to unloaded straight configuration with parameters a/b=1.1, L^o/b=0.7.

It should also be mentioned that the buckling phenomenon can be observed if and only if $L^0/b > 2\left(1 - a^2/b^2\right)$, which in the previous section was considered as the boundary condition separating the monotonic and non-monotonic areas in **Fig. 2.7** (see in (2.15)). In this case, the unloaded straight configuration is stable and it resists to the external loading if $F_x < F_x^0$. In contrast, if the geometry satisfies the opposite condition: $L^0/b < 2\left(1-a^2/b^2\right)$ as shown in **Fig. 3**. **2c**, the unloaded configuration is unstable and the mechanism suddenly jumps from the initial position to slightly different stable equilibriums (even without external loading), which can be treated as the "jumping" phenomenon. The properties of the force-diflection relations $F_x(\delta_x,\delta_y)$ and $F_y(\delta_x,\delta_y)$ can be also estimated from the 3D-plots presented in **Fig. 3**. **3** where the buckling corresponds to the discontinuity at the point $(\delta_x,\delta_y)=(0,0)$.

3.2 Stiffness analysis of non-straight configurations

To evaluate the mechanism stiffness for the general case, let us assume that the initial unloaded configuration is non-straight, i.e. $q_2 \neq 0$, which guaranties that the kinematic Jacobian is non-singular and can be inverted. This allows us to rewrite the equilibrium equation in the following way

$$\begin{pmatrix} F_x \\ F_y \end{pmatrix} = -J_q^{-T} K_q J_q^{-1} \begin{pmatrix} \delta x \\ \delta y \end{pmatrix} \tag{3. 10}$$

where the diagonal matrix $K_q = diag(K_{q1}, K_{q2})$ is composed of the stiffness coefficients of the virtual joints $K_{qi} = dM\left(q_i\right)/dq_i$ described by (2.22). This equation also allows us to express the mechanism 2×2 stiffness matrix explicitly in the following form

$$K_F = J_q^{-T} K_q J_q^{-1} \tag{3. 11}$$

where

$$K_F = \begin{bmatrix} k_{xx} & k_{xy} \\ k_{yx} & k_{yy} \end{bmatrix}_{2\times 2} \tag{3. 12}$$

is the symmetrical positive definite matrix composed of scalar stiffness coefficients k_{xx}, k_{yy} for the directions *x*, *y*, as well as a mixed stiffness coefficient k_{xy}.

Let us investigate now the sensitivity of the above stiffness coefficients with respect to the control inputs L_{i1}^0 and L_{i2}^0, assuming that both segments of the mechanism are controlled by single inputs, i.e. $L_{11}^0 = var_1$, $L_{21}^0 = var_2$ and $L_{12}^0 = L_{22}^0 = const$, which insure the desired unloaded end-point location $(x, y) = (4b - \Delta x, 0)$. Corresponding computation results for several case studies are presented in **Fig. 3**. **4**, they demonstrate that the stiffness of the two-segment mechanism is very sensitive to its initial unloaded configuration. In particular, the mechanism stiffness coefficients for the *x*-direction are essentially reducing while the displacement Δx is increasing. It should be mentioned that, to have the stable equilibrium configuration, both two segments of the mechanism should satisfy the stability condition presented in the previous section. The latter is illustrated by **Fig. 3. 4c**, where the right-hand side segment of the mechanism is stable ($K_{q2} < 0$), while the left-hand side segment is in unstable configuration ($K_{q1} > 0$). So the left-hand side segment moves until being stopped by the rotation angle constrain. This situation is also in accordance with the control inputs location on the parameter plane ($L_1^0/b, L_2^0/b$) shown in **Fig. 2. 9b**, which allows evaluate the segment stability in the unloaded configuration.

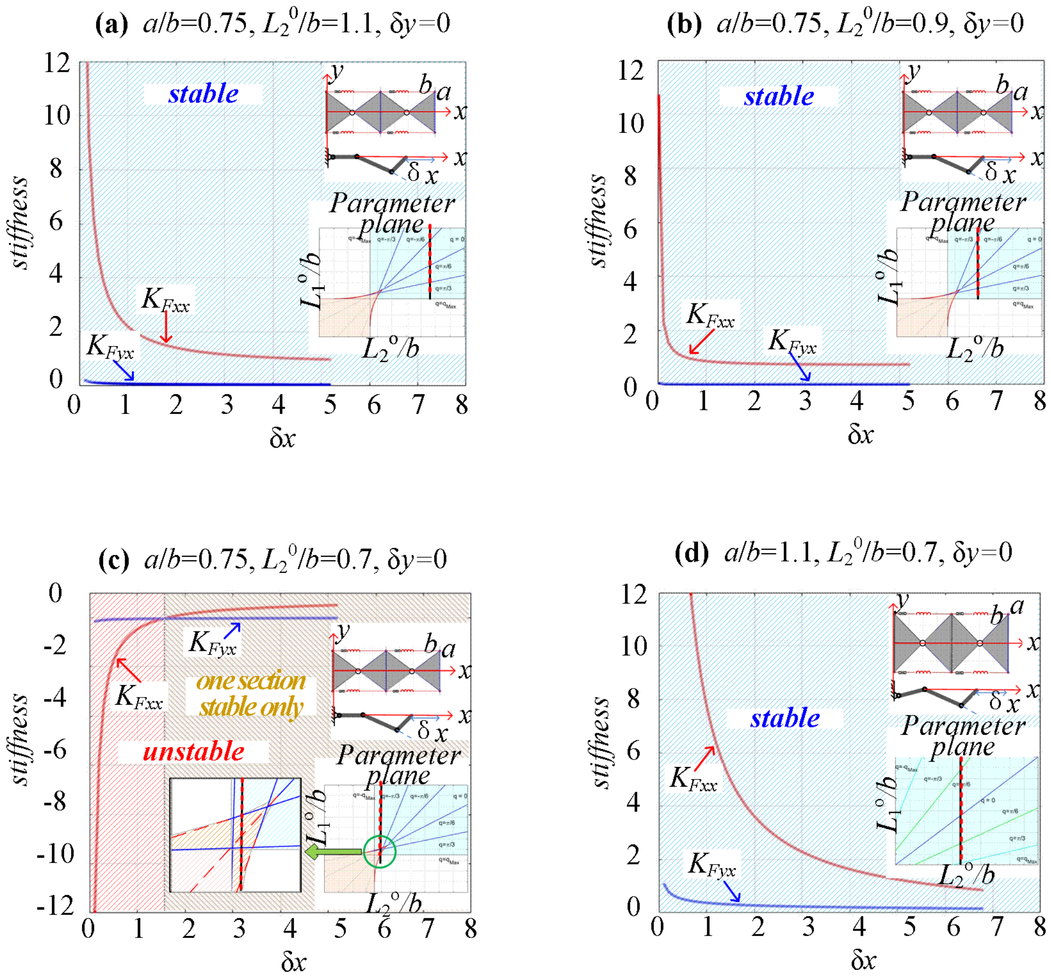
(a) a/b=0.75, L_2^0/b=1.1, δy=0

(b) a/b=0.75, L_2^0/b=0.9, δy=0

(c) a/b=0.75, L_2^0/b=0.7, δy=0

(d) a/b=1.1, L_2^0/b=0.7, δy=0

Fig. 3. 4: Sensitivity of the stiffness coefficients of the two-segment mechanism with respect to initial unloaded configuration for different geometric parameters.

The stiffness properties of the two-segment mechanism for the non-straight initial configuration can be also estimated from 3D-plots of the force-diflection relations $F_x(\delta_x,\delta_y)$ and $F_y(\delta_x,\delta_y)$ presented in **Fig. 3. 5**, which correspond to the non-loaded displacements $(\Delta_x,\Delta_y)=(5,0)$. As follows from this plots, the forces F_x and F_y are changing continuously with respect to the deflections

(δ_x, δ_y) , and there is no the buckling phenomenon, that was detected for the straight initial configuration (see **Fig. 3. 3** in subsection 3.1).

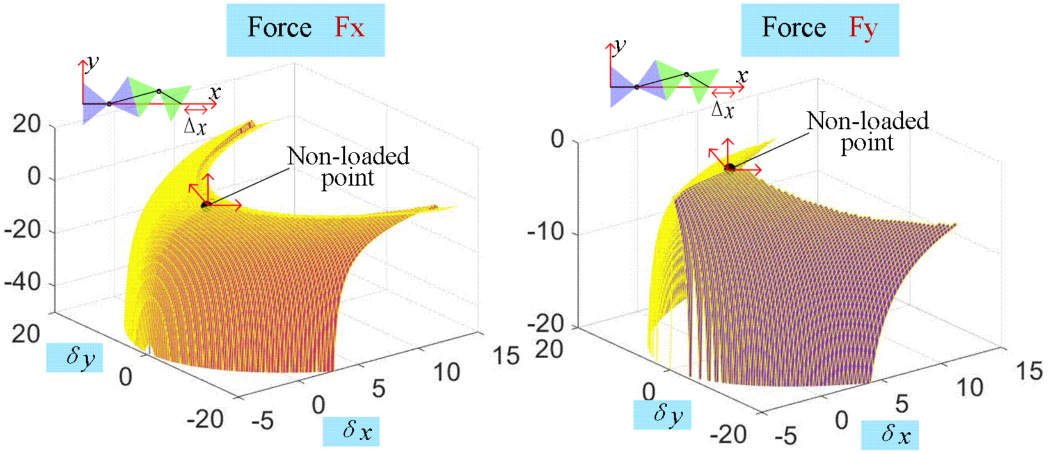

Fig. 3. 5: Force-deflection relations $F_x(\delta x, \delta y)$, $F_y(\delta x, \delta y)$ corresponding to unloaded non-straight configuration $(\Delta x, \Delta y)$=(5, 0) with geometric parameters a/b=1.1, L^o/b=0.7.

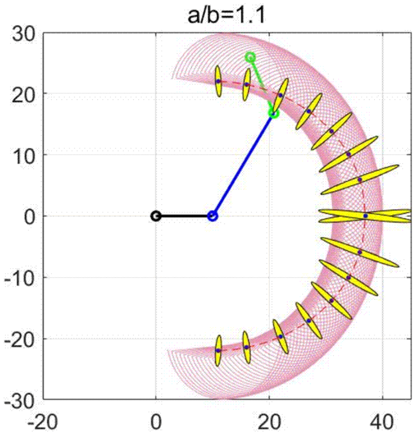

Fig. 3. 6: Unloaded-stiffness ellipses of the two-segment mechanism and the evaluation through the workspace.

Another way of evaluating the mechanism stiffness properties is based on the singular value decomposition (SVD) of the 2x2 stiffness matrix computed at the initial unloaded point. This approach allows us to estimate the max/min compliance of the mechanism via the stiffness matrix singular values. Geometrically, it can be also described by the stiffness ellipse that is produced by the linear mapping (3.10) of the unit circle $\delta_x^2 + \delta_y^2 = 1$ in the deflection space into the force space (F_x , F_y). It can be proved that the lengths of the major and minor semi-axes of this ellipse are equal respectively to the maximum and minimum singular values of the stiffness matrix. Example of the stiffness ellipses for the case a/b=1.1, L^o/b=0.7 and the evaluation though out the workspace is presented in **Fig. 3. 6**. As follows from this figure, the mechanism resistance to the external force in the longitudinal direction is much higher than in the transverse one. Also, the mechanism longitudinal compliance increases while the initial configuration becomes closer to the straight one.

3.3 Controlling mechanism configurations

To achieve the desired end-point position (*x*, *y*), the two-segment mechanism must be controlled by two pairs of the control inputs (L^0_{11}, L^0_{12}) and (L^0_{21}, L^0_{22}). To simplify the mechanism control, let us apply the asymmetrical approach proposed in subsection 1.3 allowing to use only two control variables (Δ_1, Δ_2) producing four physical control inputs: $L^0_{11} = L^0 - \Delta_1$, $L^0_{12} = L^0 + \Delta_1$ for the first segment, and $L^0_{21} = L^0 - \Delta_2$, $L^0_{22} = L^0 + \Delta_2$ for the second one. Since the considered two-segment mechanism is non-redundant, the values of the control variables corresponding to the desired end-point position can be easily computed using the above presented expressions for the two-link manipulator inverse kinematics (2.2) and one-segment mechanism control law (1.26). The latter yields the following algorithm for controlling law of the two-segment mechanism:

① Using expressions (3.2), compute the configuration angles $q_1(x, y)$ and $q_2(x, y)$ corresponding to the desired end-point position (*x*, *y*).

② Using expression (2.29), compute the control inputs $\Delta_1(q_1)$ and $\Delta_2(q_2)$ for the first and second segments corresponding to the configuration angles (q_1, q_2).

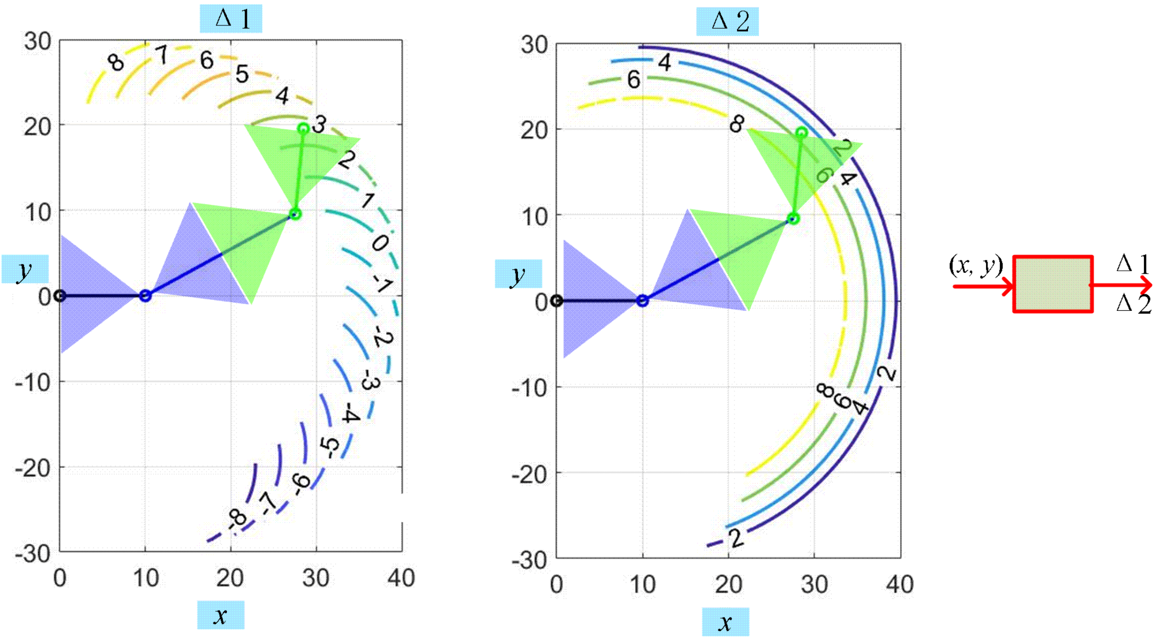

Fig. 3. 7: Relations between the required control inputs Δ_1, Δ_2 and the desired end-point position (*x*, *y*) for the two-segment mechanism with geometric parameters *a*/*b*=1.1, L^o/b=0.7 (unloaded case F_x=F_y=0).

An example of computing based on the above algorithm is presented in **Fig. 3. 7**, where the mechanism parameters a/b=1.1, L^0/b =0.7 were chosen to ensure the mechanism stability in the unloaded mode $M_{ext} = 0$ (see subsection 3.3).

In more general case when the external forces (F_x , F_y) are not equal to zero, the control inputs (Δ_1, Δ_2) should be computed using equation (2.31) that includes the virtual joint torques (M_1, M_2) ensuring the mechanism equilibrium. These torques can be obtained from the static equilibrium (3.4). Corresponding algorithm allowing to find the control inputs (Δ_1, Δ_2) for the desired end-point position (x, y) for the loaded case as presented below.

① Using expressions (3.2), compute the configuration angles $q_1(x, y)$ and $q_2(x, y)$ corresponding to the desired end-point position (x, y).

② Using expression (3.4), compute the joint torques $\left(M_1, M_2\right)$ from the external force (F_x , F_y)

③ Using expression (2.31), compute the control inputs $\Delta_1(q_1, M_1)$ and $\Delta_2(q_2, M_2)$ for the first and second segments corresponding to the configuration angles (q_1, q_2) and the joint torques $\left(M_1, M_2\right)$.

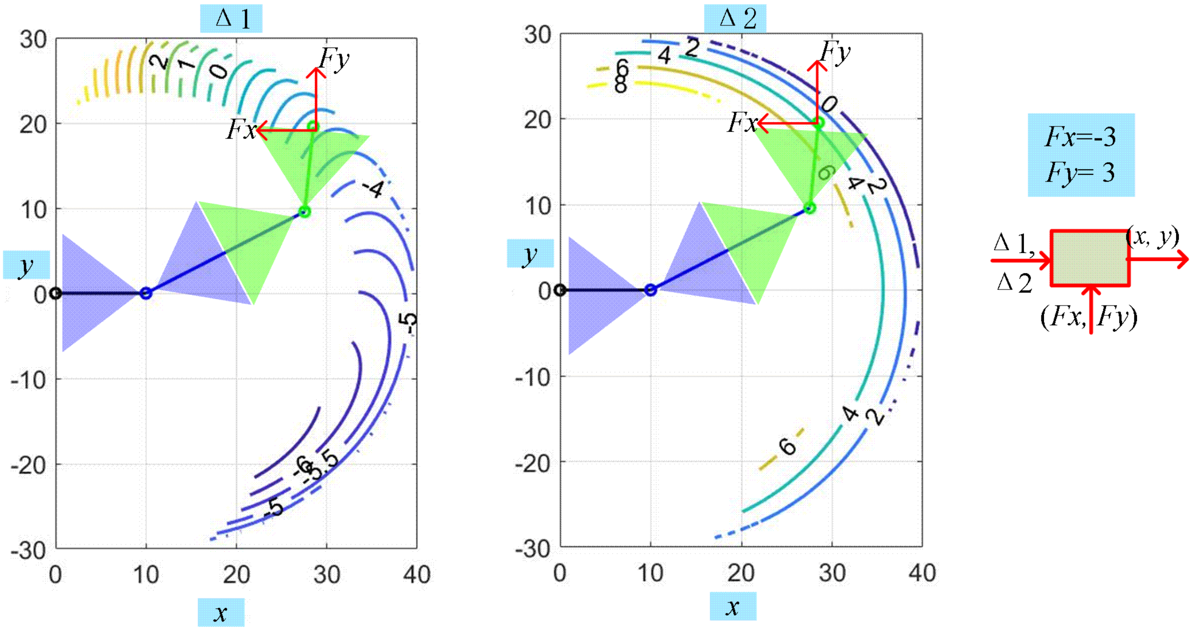

Fig. 3. 8: Relations between the control input Δ and the desired end-point position (x, y) with geometric parameters a/b=1.1, L^o/b=0.7 (unloaded case F_x=-3, F_y=3).

An example of computing based on the above algorithm is presented in **Fig. 3. 8**, where the geometric parameters are similar to the previous figure. To confirm reasonable choice of geometric parameters $a/b \approx 1$ with respect to the mechanism control, **Fig. 3. 9** presents several cases that differ in the workspace shape and size (as well as the workspace area S_W). As follows from this figure, in practice it is preferable to have the (a, b) parameter ratio about $a/b \approx 1$, which ensures the maximum workspace area.

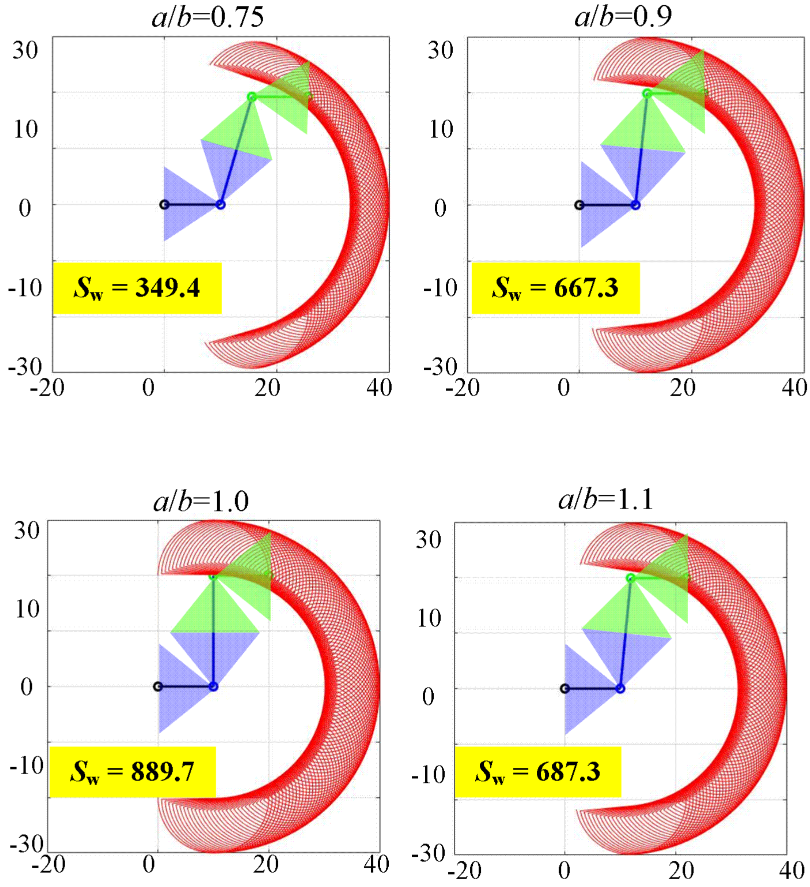
a/b=0.75

a/b=0.9

a/b=1.0

a/b=1.1

Fig. 3. 9: Workspace size/shape of the two-segment mechanism for different geometric parameters (a, b).

3.4 Summary

This chapter deals with the stiffness analysis of the **two-segment serial tensegrity mechanism** based on the dual-triangles architecture, which was selected as the base segment for designing compliant robot- end-effector.

For this mechanism, both straight and non-straight initial configurations were considered; *the **main contributions*** are concentrating on the mechanical stiffness properties. The obtained analytical stiffness matrices derived using the VJM technique allow designers to evaluate the stiffness sensitivity of this structure with respect to an arbitrary initial configuration for different geometric parameters. Besides, the *force-deflection relations* for the desired end-point location were obtained analytically by solving the static equilibrium equation. The latter allowed us to detect the *buckling phenomenon* of this serial mechanism and compute the corresponding critical force.

In more details, new results and contributions of Chapter 3 include the following issues

(i) The ***force-deflection relations*** of this mechanism for both straight and non-straight initial configurations, which were obtained using the VJM technique.

(ii) Specific mechanical property of this mechanism i.e. the ***buckling phenomenon*** was detected if the initial configuration of this serial mechanism is straight and external loading exceeds the certain critical value. This critical value of the loading causing the buckling was obtained analytically by solving the elastostatic equilibrium equations.

(iii) The ***control strategy*** proposed in the previous chapter was extended for the two-segment case. Its efficiency was confirmed by simulation results for both loaded and unloaded modes.

It should mentioning that for this mechanism, the stable states can be easily ensured by choosing suitable geometric parameters and springs pre-stress according to the stability condition obtained in Chapter 2. However, for the large deflection while considering the geometric constraints, the obtained mechanism stability conditions are more complex compared to the single-segment case.

The main results of Chapter 3 are published in the following works: (Zhao et al., 2021a).

CHAPTER 4

ANALYSIS OF THREE-SEGMENT MECHANISM COMPOSED OF DUAL-TRIANGLES

This chapter is devoted to the analysis of the redundant three-segment serial structure composed of the dual-triangles. Both the analytical and numerical methods were used to find the stable and unstable equilibrium configurations, and to predict the corresponding manipulator shapes. Similar to the previous chapter, it was demonstrated that either buckling or quasi-buckling phenomenon may occur under the loading if the manipulator initial configuration is straight or non-straight one, and the critical force was obtained analytically. Further, the stiffness analysis was carried on for both loaded and unloaded modes, the stiffness matrices were computed using the VJM technique. At last, some useful optimization techniques were applied to solve the geometric redundancy problem, and to ensure the stability of the manipulator configurations with respect to the external forces/torques applied to the end-effector. Relevant kinematics control strategies based on these techniques were proposed, the efficiency and accuracy of which were confirmed by the simulation results.

4.1 Stiffness analysis of a straight configuration

Let us consider a manipulator composed of three similar sections connected in series as shown in **Fig. 4. 1**, where the left hand-side is fixed and the initial configuration is a "straight" one ($q_1 = q_2 = q_3 = 0$). This configuration is achieved by applying equal control inputs to all mechanism segments. For this manipulator, it is necessary to investigate the influence of the external force $F_e = (F_x, F_y)$, which causes the end-effector displacements to a new equilibrium location

$(x,y)^T=(6b-\delta_x,\delta_y)^T$ corresponding to the nonzero configuration variables (q_1,q_2,q_3). It is also assumed here the external torque M_{ext} applied to the end-effector is equal to zero.

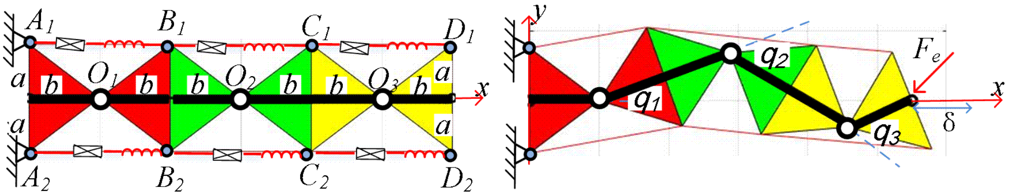

Fig. 4. 1: The three-segment mechanism in the "straight" and "non-straight" configurations.

Let us evaluate first the mechanism resistance with respect to external load for this "straight" configuration, which is described by the force-deflection relations $F_x(\delta_x,\delta_y)$ and $F_y(\delta_x,\delta_y)$. It can be easily proved from the geometry analysis that the configuration angles (q_1,q_2,q_3) satisfy the following direct kinematic equations

$$\begin{aligned} 6b-\delta_x &= b+2bC_1+2bC_{12}+bC_{123} \\ \delta_y &= 2bS_1+2bS_{12}+bS_{123} \end{aligned} \tag{4. 1}$$

where $C_1=\cos q_1$, $S_1=\sin q_1$, $C_{12}=\cos(q_1+q_2)$, $S_{12}=\sin(q_1+q_2)$, $C_{123}=\cos(q_1+q_2+q_3)$ and $S_{123}=\sin(q_1+q_2+q_3)$. These two equations include three unknown variables and allow us to compute two of them assuming that the remaining one is known. For instance, if the angle q_1 is assumed to be known, the rest of the angles q_2, q_3 can be computed from the classical invers kinematics of the two-link manipulator as follows

$$\begin{aligned} &q_3=\operatorname{atan2}(S_3,C_3) \\ &q_2=\operatorname{atan2}(y-2bS_1,x-b-2bC_1)-\operatorname{atan2}(bS_3,2b+bC_3)-q_1 \end{aligned} \tag{4. 2}$$

where $C_3=\left[(x-b-2bC_1)^2+(y-2bS_1)^2-5b^2\right]/4b^2$, $S_3=\pm\sqrt{1-C_3^2}$. It is clear that the latter expressions provides two group of possible solutions corresponding to the positive /negative configuration angles $q_3\ge 0$ and $q_3\le 0$.

To find a stable manipulator configuration under the loading, let us apply the energy method. It is clear that the end-effector displacement caused by the external loading leads to some deflections in the mechanism springs, which allows us to compute the manipulator energy as

$$E=\frac{1}{2}\sum_{i=1}^{3}\sum_{j=1}^{2}k\left(L_{ij}-L_{ij}^{0}\right)^2 \tag{4. 3}$$

where L_{ij} and L_{ij}^{o} are the spring lengths in current and initial (unextended) states respectively.

Because the manipulator end-effector is assumed to be fixed at the point $(x,y)^T = (6b-\delta_x,\delta_y)^T$, the above energy can be expressed via one of the three variables q_1, q_2 or q_3. Assuming that variable q_1 is chosen as an independent one, the desired stable configurations can be found by computing local minima of energy function

$$E(q_1) \to \min_{q_1} \tag{4. 4}$$

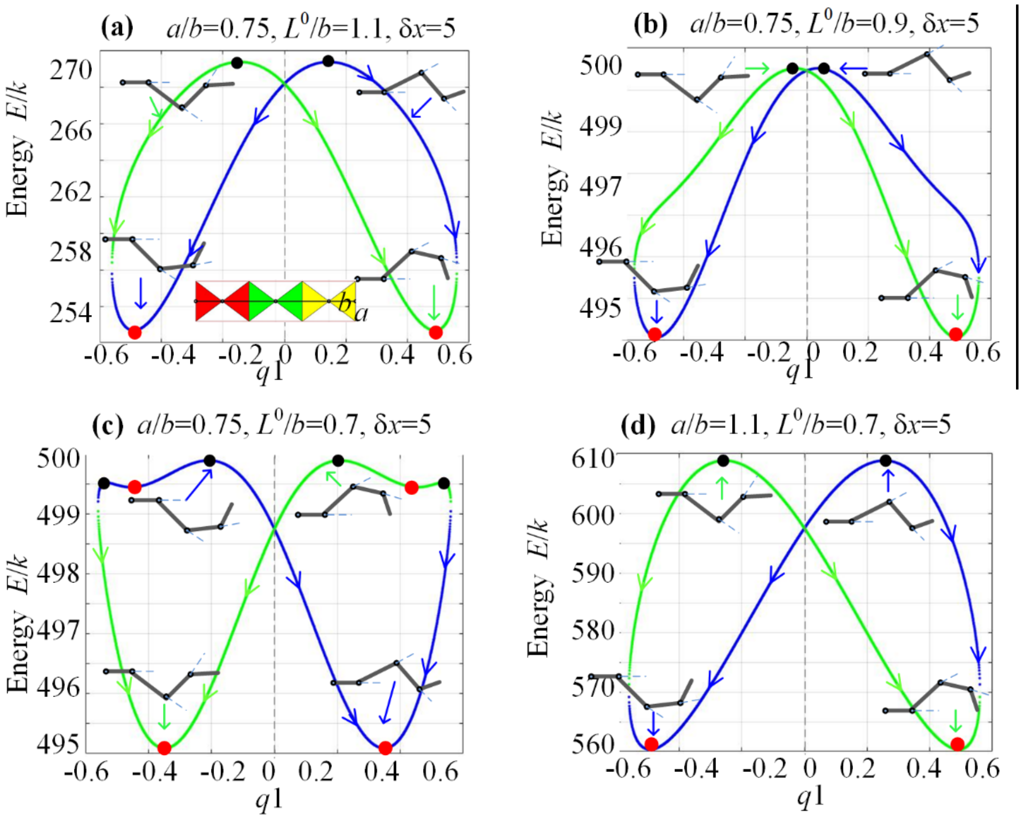

Fig. 4. 2 Energy curves $E(q_1)$ for different combinations of manipulator geometric parameters a/b, L^o/b:
"blue curves"— positive configuration with $q_3>0$; "green curves" — negative configuration with $q_3<0$;
● — stable equilibrium; ● — unstable equilibrium.

Examples of such energy curves $E(q_1)$ for several typical cases are presented in **Fig. 4. 2**. As follows from this figure, the considered curves are symmetrical with respect of the angle q_1 and number of equilibriums can be either four or eight (two stable and two unstable, or four stable and four unstable). However, the number of global minima is always equal to two. It is worth mentioning that while considering the equilibrium configurations defined by minimum/maximum of the energy, it is necessary to be sure that all the configuration angles q_1, q_2, q_3 are feasible, i.e. belong to the geometric limits described by inequalities (2.30). Importance of this issue is illustrated by **Fig. 4. 3**, where the feasible and unfeasible parts of the energy curves are presented by solid and dashed lines respectively.

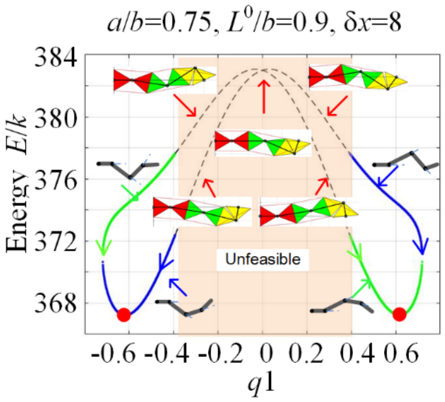

Fig. 4. 3: Feasible (—) and unfeasible (---) configurations caused by geometric constrains on the joint angles.

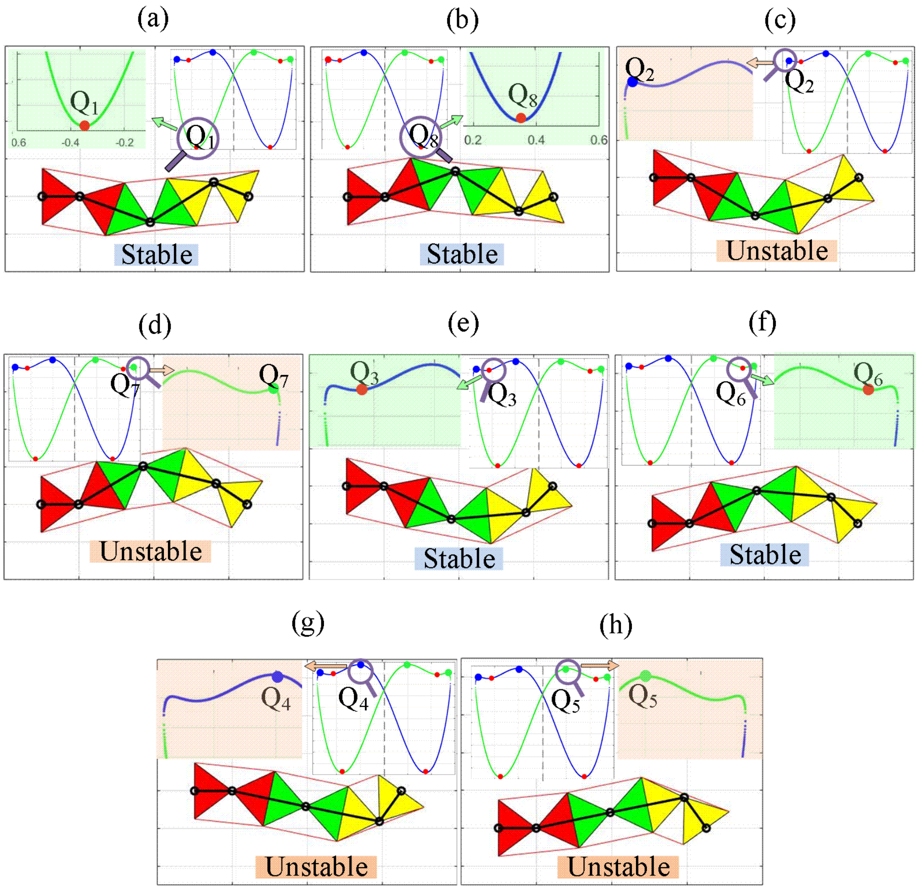

Fig. 4. 4: Eight different stable and unstable equilibriums for manipulator parameters *a*/*b*=0.75, *L*ᵒ/*b*=0.7.

In more detail, the stable and unstable equilibriums are shown in **Fig. 4. 4**, where there are presented both the energy curves and the manipulator shape corresponding to the case study from **Fig. c**. As can be seen from these figures, for such combination of parameters there are two globally stable equilibriums (**Fig. 4. 4a, b**), two locally stable equilibriums (**Fig. 4. 4e, f**) and four unstable equilibriums (**Fig. 4. 4c, d, g, h**). It can be also noticed that the stable equilibriums correspond to the "Z" shape of the manipulator, while the unstable equilibriums correspond to the "U" shape. Besides, for this case study, the “jumping” phenomenon can be observed for which the angle q_1 suddenly jumps from the initial zero value to the non-zero one under the influence of the external loading. The latter is in a good agreement with **Fig. 4. 4c** showing that here the geometric parameters (a/b, L^o/b) belong to the unstable area on the relevant plane.

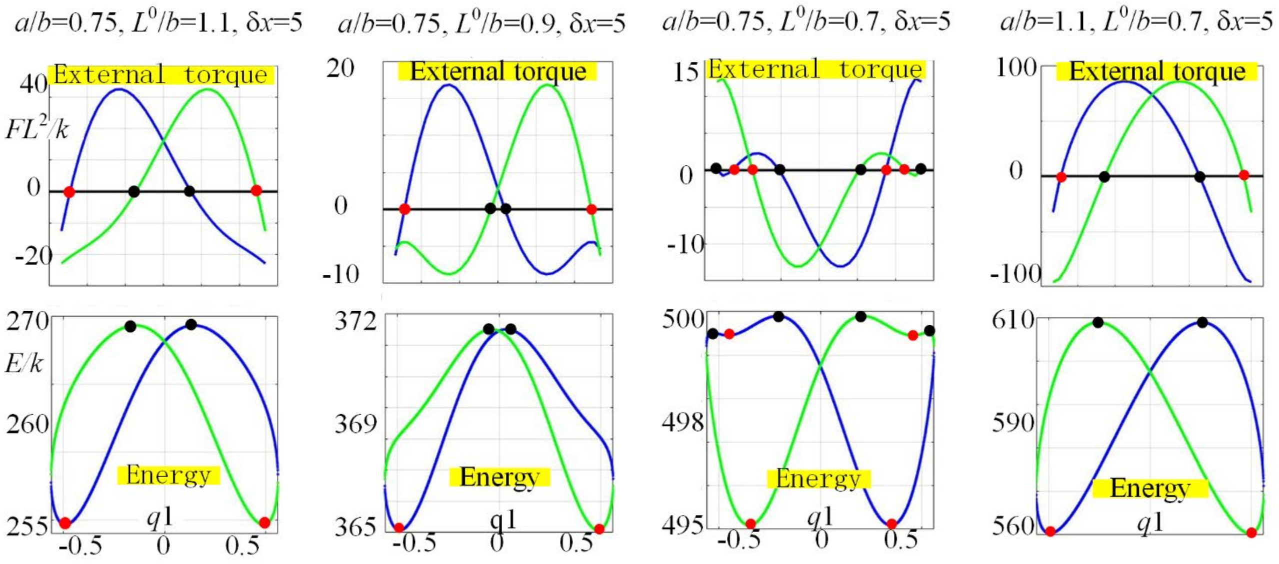

Fig. 4. 5 Correspondence between the maxima/minima of the energy curves $E(q_1)$ and zeros of the external torque $M_e(q_1)$.

An alternative way to compute the configuration angles q_1, q_2, q_3 at the equilibrium state is based on the torque equation $M_e(q_1)=0$, which is implicitly used in the energy method. The latter is illustrated by combined plots of the energy-torque curves computed for the initial “straight” configuration presented in **Fig. 4. 5**, which shows that the max/min of the energy $E(q_1)$ correspond to zeros of the torque $M_e(q_1)=0$. This allows to present the equilibrium equations in the following way.

$$\begin{aligned} f_x(q_1,q_2,q_3) &= x \\ f_y(q_1,q_2,q_3) &= y \\ M_e(q_1,q_2,q_3) &= 0 \end{aligned} \tag{4. 5}$$

where $f_x(.)$ and $f_y(.)$ are the direct kinematic functions from equation (4.3) and $M_e(.)$ is the external torque at the end-point with the Cartesian coordinates (x, y). Further, to find the external forces corresponding to this end-point location, it is necessary to use the force-torque equilibrium equation

$$\begin{bmatrix} M_{q1} \\ M_{q2} \\ M_{q3} \end{bmatrix} + J_q^T \begin{pmatrix} F_x \\ F_y \\ M_e \end{pmatrix} = 0 \tag{4. 6}$$

which relates internal torques M_{q1}, M_{q2}, and M_{q3} in all manipulator segments and the force/torque at the end-point. In this equation, the internal torques can be computed using previously derived expression from **Section 2.1**

$$M_{qi} = 2k\left[\left(b^2 - a^2\right)\cdot \sin q_i - bL^0 \sin\frac{q_i}{2}\right]; \quad i = 1, 2, 3 \tag{4. 7}$$

and the Jacobian matrix J_q can be computed using the standard technique for the three-link manipulator and presented as follows

$$J_q = \begin{bmatrix} -2bS_1 - 2bS_{12} - bS_{123} & -2bS_{12} - bS_{123} & -bS_{123} \\ 2bC_1 + 2bC_{12} + bC_{123} & 2bC_{12} + bC_{123} & bC_{123} \\ 1 & 1 & 1 \end{bmatrix} \tag{4. 8}$$

where S and C with corresponding indices have the same meaning as in (4.1). Assuming that the Jacobian is non-singular (i.e. the loaded manipulator is already out of the straight configuration), the external force/torque can be expressed directly as

$$\begin{pmatrix} F_x \\ F_y \\ M_e \end{pmatrix} = -J_q^{-T} \begin{bmatrix} M_{q1} \\ M_{q2} \\ M_{q3} \end{bmatrix} \tag{4. 9}$$

where the inverse matrix J_q^{-T} can be computed analytically. In particular, a conventional formula

$$J_q^{-T} = \frac{\left[J_q^T\right]^*}{\det\left|J_q^T\right|} \tag{4. 10}$$

with the determinant

$$\det\left|J_q^T\right| = \det(J_q) = L_1 L_2 S_2 \tag{4. 11}$$

and the adjoint matrix

$$\left[J_q^T\right]^* = \begin{bmatrix} L_2 C_{12} & -L_1 C_1 - L_2 C_{12} & L_1 C_1 \\ L_2 S_{12} & -L_1 S_1 - L_2 S_{12} & L_1 S_1 \\ L_2 L_3 S_3 & -L_1 L_3 S_{23} - L_2 L_3 S_3 & L_1 L_2 S_2 + L_1 L_3 S_{23} \end{bmatrix} \tag{4.12}$$

yields the following analytically expression for the external loading

$$\begin{pmatrix} F_x \\ F_y \\ M_e \end{pmatrix} = -\frac{1}{2bS_2} \begin{bmatrix} C_{12} & -C_1 - C_{12} & C_1 \\ S_{12} & -S_1 - S_{12} & S_1 \\ bS_3 & -bS_{23} - bS_3 & 2bS_2 + bS_{23} \end{bmatrix} \begin{bmatrix} M_{q1} \\ M_{q2} \\ M_{q3} \end{bmatrix} \tag{4. 13}$$

where $L_1=2b$,, $L_2=2b$ and $L_3=b$ are the link lengths for the equivalent three-link manipulator. The above expression also gives us an analytical formula for the external torque $M_e(.)$ for the system of equations (4.5)

$$M_e = -\frac{1}{2S_2}\left[S_3 M_{q1} - (S_{23} + S_3) M_{q2} + (2S_2 + S_{23}) M_{q3}\right] \tag{4. 14}$$

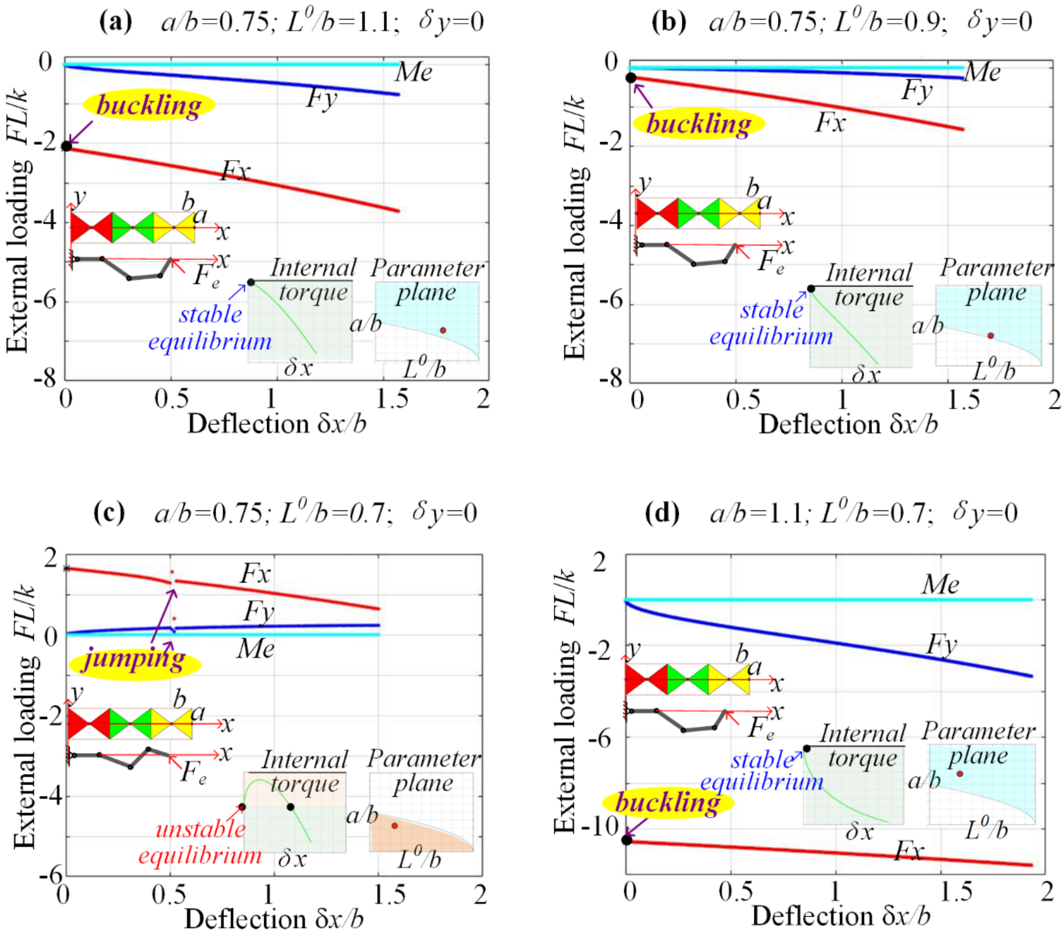

Fig. 4. 6 Force-deflection curves and stiffness coefficients for the "straight" initial configuration.

The above obtained formula for $M_e(q_1, q_2, q_3)$ allows us to rewrite the system of the equilibrium equation (4.5) in the extended form as shown in (4.15) in below, whose solution (q_1, q_2, q_3) may correspond to either to stable or unstable equilibrium of the manipulator configuration. Then, using expressions $F_x(q_1, q_2, q_3)$ and $F_y(q_1, q_2, q_3)$ obtained from (4.13), one can get the external loading (F_x,

F_y) corresponding to the end-effector position (x, y), which finally allows us to generate the desired force-deflection curves.

$$\begin{cases} b+2bC_1+2bC_{12}+bC_{123}-x=0 \\ 2bS_1+2bS_{12}+bS_{123}-y=0 \\ S_3M_{q1}-\left(S_{23}+S_3\right)M_{q2}+\left(2S_2+S_{23}\right)M_{q3}=0 \end{cases} \tag{4. 15}$$

Examples of such curves for several case studies are presented in **Fig. 4**. **6**, where it is assumed that under the loading the manipulator moves along with x-axis, i.e. $\delta x = var$, $\delta y = 0$. As follows from this figure, in the most cases the force-deflection curves are quasi-linear but some of them they include discontinuities (jumps) and do not pass through the zero point. The latter means that the corresponding manipulator possesses very specific particularity known as the "buckling" property, for which the configuration angles may suddenly change their values while the external force increases gradually. Besides, in the case presented in **Fig. 4**. **6c**, the manipulator demonstrates the "jumping" phenomenon, because the initial (unloaded position) is unstable and the manipulator suddenly changes its shape even for extremely low loading.

To compute the critical force F_x^o causing the buckling, let us assume that the configuration angles q_1, q_2 and q_3 are small enough but not equal to zero. This allows us to derive a linearized stiffness model in the neighborhood of q_i=0 (i=1, 2, 3). Under such assumptions, the first and second equations from (4.1 $q_1=\alpha_1\cdot q_2$, $q_3=\alpha_3\cdot q_2$ 5 $q_1+q_{12}+q_{123}/2=0$) can be presented in the following form

$$\begin{aligned} \delta_x &= b(q_1^2+q_{12}^2+\frac{q_{123}^2}{2}) \\ \delta_y &= 2b(q_1+q_{12}+\frac{q_{123}}{2}) \end{aligned} \tag{4. 16}$$

which allows us to present the condition $\delta_y = 0$ as . Applying similar linearization to the third equation from (4.15), one can get the additional relation for the configuration angles $q_1q_3-q_2^2+q_2q_3+q_3^2=0$ ensuring the equality $M_e=0$. Further, combining these two obtained relations and considering q_2 as an independent variable, it is possible to express q_1, q_3 in the following way

(4. 17)

where

$$\alpha_1=-\frac{\pm\sqrt{21}+11}{20}\in\left\{-0.7791,-0.3249\right\};\quad \alpha_3=\frac{\pm\sqrt{21}-1}{4}\in\left\{0.8956,-1.3956\right\}$$

The latter gives us four possible manipulator geometric configurations corresponding to the static equilibrium, two with U-shape and two with Z-shape (see **Table 3**). Corresponding external forces F_x,

F_y ensuring the static equilibrium can be computed from the general expression (4.13), which can be rewritten in scalar form

$$\begin{aligned} F_x &= -\frac{1}{2bS_2}\left[C_{12}M_{q1} - \left(C_1 + C_{12}\right)M_{q2} + C_1 M_{q3}\right] \\ F_y &= -\frac{1}{2bS_2}\left[S_{12}M_{q1} - \left(S_1 + S_{12}\right)M_{q2} + S_1 M_{q3}\right] \end{aligned} \tag{4. 18}$$

and also linearized for small configuration angles, which yields

$$F_x \approx -\frac{k}{2bq_2}\left[2\left(b^2 - a^2\right) - bL^0\right]\left(q_1 + q_3 - 2q_2\right); \quad F_y \approx 0 \tag{4. 19}$$

Further, taking into account (4.17) the desired critical force can be expressed in the following way

$$F_x^o = \lim_{q_i \to 0} F_x = -\lambda \cdot \frac{k}{b}\left[2\left(b^2 - a^2\right) - bL^0\right] \tag{4. 20}$$

where

$$\lambda = \begin{cases} \dfrac{\sqrt{21} - 14}{10} \approx -0.9417 & \text{for U-shape} \\ \dfrac{-\sqrt{21} - 14}{10} \approx -1.8583 & \text{for Z-shape} \end{cases}$$

Table 3 Possible manipulator shapes in static equilibrium

	q1	q2	q3	Geometric configuration	Stability
Case of “+√”	–	+	+	U shape: 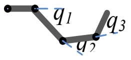	stable
	+	–	–	U shape: 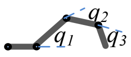	stable
Case of “-√”	–	+	–	Z shape: 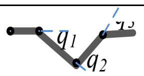	unstable
	+	–	+	Z shape: 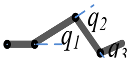	unstable

It is worth mentioning that the obtained expression allows also to derive the static stability condition for the straight configuration. In fact, this configuration is stable if and only if $F_x^o < 0$, which is equivalent to $2\left(b^2 - a^2\right) < bL^o$ and is in agreement with above obtained inequality (1.14) defining the monotonicity of the torque-angle curves for the manipulator segments.

Finally, let us compare the U-shape and S-shape equilibrium configurations from point of view their static stability. It can be easily proved that for the small configuration angles q_i the end-effector deflection δ_x can be expressed in the following way

$$\delta_x = \mu q_2^2 \tag{4. 21}$$

where

$$\mu = \begin{cases} \dfrac{\sqrt{21}+21}{20} \approx 1.2791 & \text{for U-shape} \\ \dfrac{-\sqrt{21}+21}{20} \approx 0.8209 & \text{for Z-shape} \end{cases}$$

The latter means that for the similar deflections δ_x, the U-shape has smaller configuration angles q_i compared to the Z-shape, which ensures smaller energy for the U-shape and in good agreement with the energy curves presented in **Fig. 4. 2**.

4.2 Stiffness analysis of a non-straight configuration

Let us consider now the case when the manipulator initial configuration is a non-straight one, which corresponds to the non-zero angles ($q_i^o \neq 0,\ i = 1,2,3$). Similar to the above section, the equilibrium is defined by three equations (4.5) that are derived from the direct kinematics and from the zero external torque assumption $M_e = 0$. It can be also proved that here the energy curves have the "∞-shape" as for the straight configuration considered before. However, depending on the initial end-effector location (x, y), these energy curves may be non-symmetrical and can be even discontinuous and include cusp points. Typical examples of such curves corresponding to end-point location $(x, y)^T = (5.5b, 0)^T$ are presented in **Fig. 4. 7**, where the discontinuity caused by the geometric constraint (1.27) is clearly visible. In particular, in cases (a) and (b) the energy curves consist of two separate U-shape parts that yield two symmetrical stable equilibriums and four unstable ones. Such separation is caused by the geometric constrains on the angles $|q_i| \leq q_i^{\max}$. In case (d), the energy curve consists of four separate feasible parts that provide four stable and four unstable equilibriums, but only two of them can be observed in practice (corresponding to the global minimum of the energy). However, the energy curves for the case (c) cannot be treated in the same way, because such combination of a, b, L_i^o provides non-monotonic torque-angle curves for the segments (see subsection 1.2), and even separate parts of the manipulator are unstable in this case. It should be stressed that in the cases (a), (b), (d) each segment of the mechanism is statically stable. It should be also noted that there are a number of unfeasible sections (black lines) inside all energy curves, where at least one of the angles q_2 or q_3 is out of the allowable geometric limits.

The above presented case studies corresponding to end-effector initial position $(x, y)^T = (5.5b, 0)^T$ can be also illustrated by the force-deflection curves presented in **Fig. 4. 8**. As follows from them, there is no buckling phenomenon in the cases (a), (b), (d), these curves are quasi-linear and pass through the zero point. Besides, the buckling detected in the case (c) cannot be observed in practice because of non-stability of the separate manipulator segments.

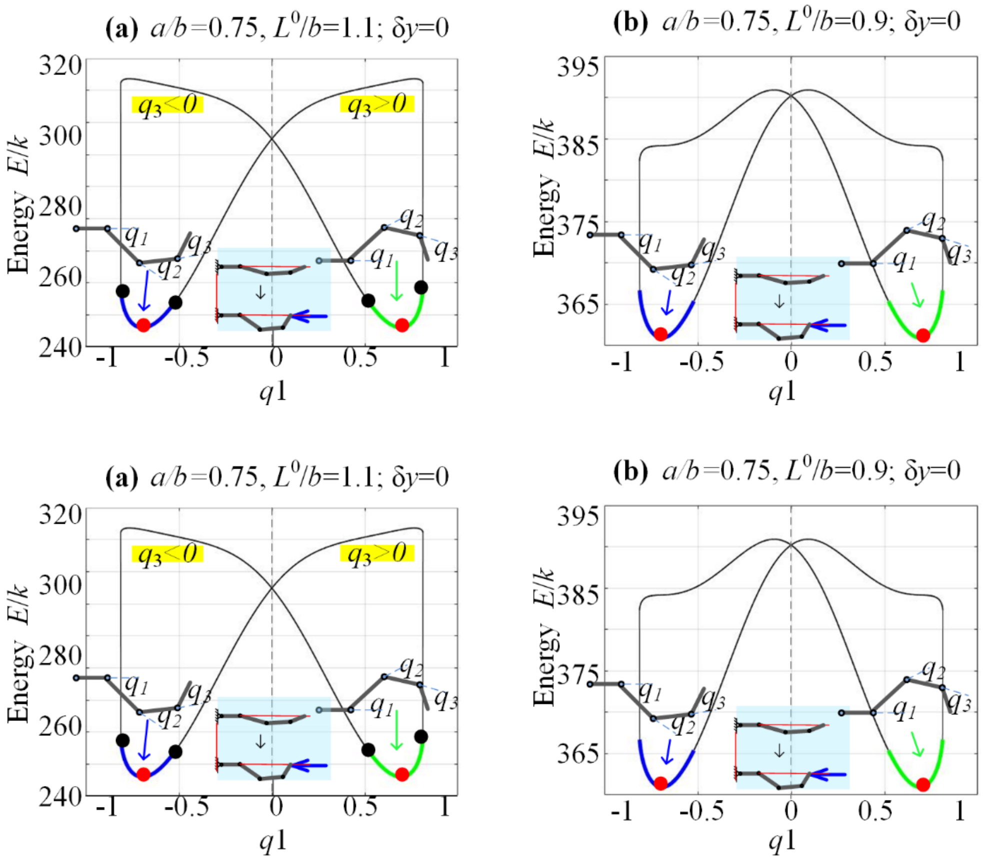

Fig. 4. 7: Energy curves $E(q_1)$ for non-straight initial configuration and displacement $(\Delta x, \Delta y)=(b/2, 0)$, "blue curves" — feasible configuration with $q_3>0$; "green curves" — feasible configuration with $q_3<0$; "black curves"— unfeasible configuration; "red point ●"— stable equilibrium; "black point ●" — unstable equilibrium.

To evaluate the manipulator stiffness matrix for the non-straight configuration, let us first find the joint torques for all manipulator segments using equations (2.8)

$$M_{qi} = k\left[2(b^2 - a^2)\sin q_i - L_{i1}^0\left(a\cdot\cos\frac{q_i}{2} + b\cdot\sin\frac{q_i}{2}\right) + L_{i2}^0\left(a\cdot\cos\frac{q_i}{2} - b\cdot\sin\frac{q_i}{2}\right)\right];\; i = 1,2,3 \qquad (4.\,22)$$

and compute the derivatives providing equivalent stiffness coefficients in the joints $K_{qi} = dM_{qi}/dq_i$

$$K_{qi} = k\left[2(b^2-a^2)\cos q_i - \frac{L_{i1}^0}{2}\left(-a\cdot\sin\frac{q_i}{2}+b\cdot\cos\frac{q_i}{2}\right)+\frac{L_{i2}^0}{2}\left(-a\sin\frac{q_i}{2}-b\cos\frac{q_i}{2}\right)\right];\ i=1,2,3 \tag{4. 23}$$

This allows us to apply the VJM method and to express the unloaded stiffness matrix of the considered manipulator as

$$K_F^0 = \left(J_o K_{qo}^{-1} J_o^T\right)^{-1} \tag{4. 24}$$

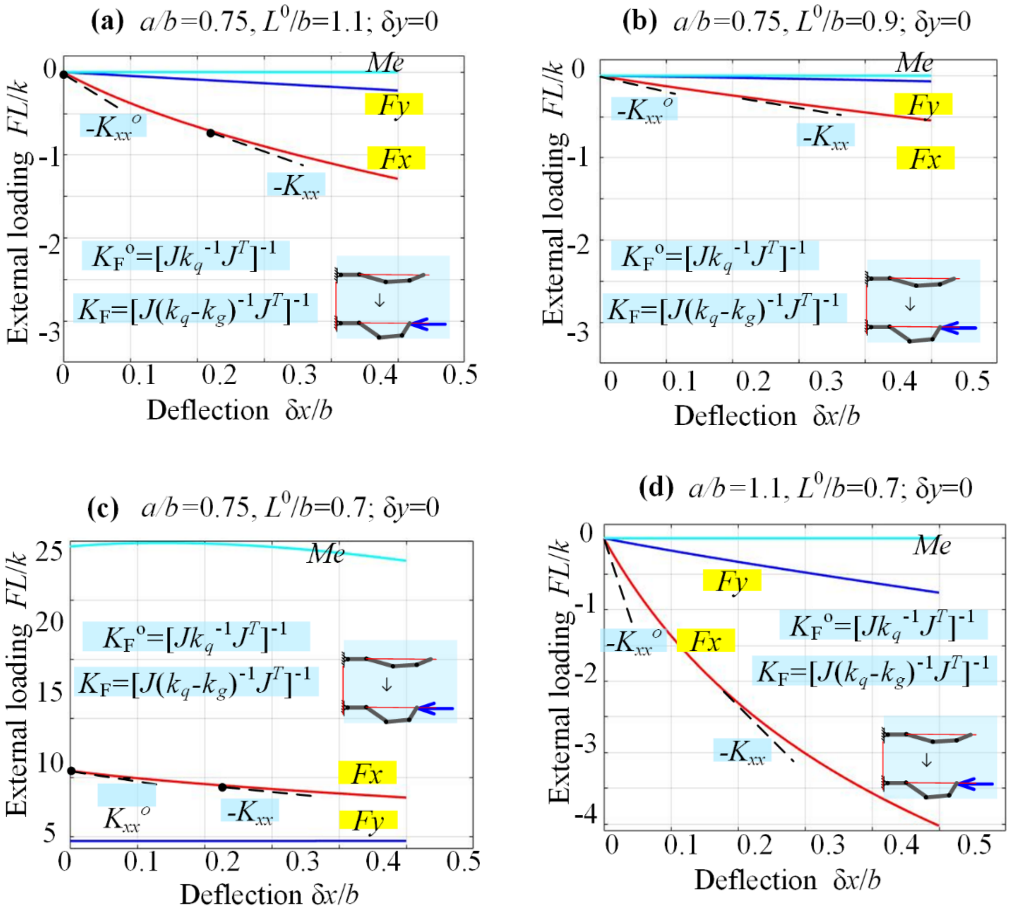

Fig. 4. 8: Force-deflection curves and stiffness coefficients for "non-straight" initial configuration with different parameters (a, b, L^o) and displacement (Δx, Δy)=(b/2, 0).

where the subscript "o" denotes the variables corresponding to the unloaded initial configuration. Further, if we express the 2x3 submatrix of the Jacobian (4.8) for this configuration as

$$J_o = \left[\begin{array}{c|c|c} J_{11} & J_{12} & J_{13} \\ J_{21} & J_{22} & J_{23} \end{array}\right]_{2\times 3}$$

The desired compliance matrix of the unloaded mode can be expressed analytically in the following way

$$C_F^0 = J_o K_{qo}^{-1} J_o^T = \begin{bmatrix} \frac{J_{11}^2}{K_{q1}} + \frac{J_{12}^2}{K_{q2}} + \frac{J_{13}^2}{K_{q3}} & * \\ * & \frac{J_{21}^2}{K_{q1}} + \frac{J_{22}^2}{K_{q2}} + \frac{J_{23}^2}{K_{q3}} \end{bmatrix} \tag{4.25}$$

where $K_{qo} = diag(K_{q1}, K_{q2}, K_{q3})$ is the matrix of size 3×3.

Similar to section 3.2, the stiffness properties of the unloaded manipulator may be also illustrated by the set of ellipses describing mapping of the unit force $\|F\| = 1$ into the deflection $(\delta x, \delta y)$. An example of such analysis for the case of *a*/*b*=1.0, *L*°/*b*=0.9 is presented in **Fig. 4. 9**, which shows that the resistance of the three-segment mechanism to the external force in the longitudinal direction is much higher than in the transverse one. Also, the mechanism longitudinal stiffness essentially increases while the initial configuration becomes closer to the straight one.

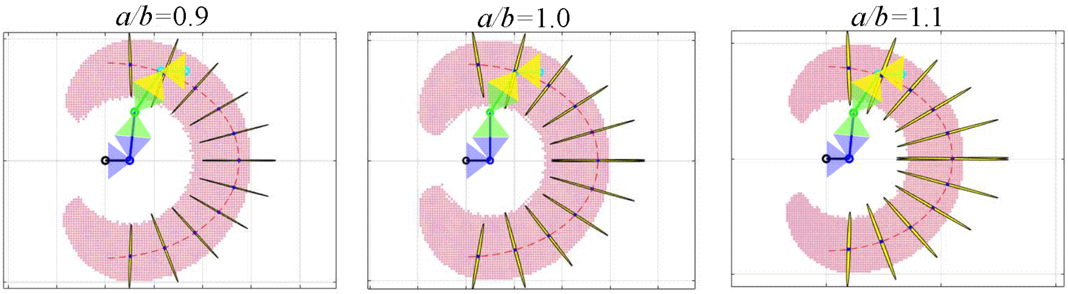

Fig. 4. 9 Stiffness ellipses of the three-segment mechanism for the unloaded mode and their evaluation throughout the workspace.

For the loaded mode, the manipulator stiffness matrix can be computed using the extended VJM technique proposed in (Chen and Kao, 2000). Within this technique, let us assume that there is a non-negligible deflection $\Delta = (\Delta x, \Delta y)^T$ caused by the external force $F = (F_x \;\; F_y)^T$, and there is a small deflection $\delta = (\delta x, \delta y)^T$ caused by this force variation $\delta F = (\delta F_x, \; \delta F_y)^T$ that corresponds to the joint angle variations $\delta q = (\delta q_1, \delta q_2, \delta q_3)^T$.

As follows from the equilibrium equation $M = J^T \cdot F$, corresponding variation of the joint torque can be expressed as

$$\delta M = \left(\frac{dJ^T}{dq} \delta q \right) \cdot F + J^T \cdot \delta F \tag{4.26}$$

where the part including the Jacobian derivative dJ^T / dq can be rewritten as

$$\left(\frac{dJ^T}{dq}\delta q\right)\cdot F=\left[\sum_{i=1}^{3}\frac{\partial J^T}{\partial q_i}\delta q_i\right]\cdot F=\sum_{i=1}^{3}\left(\frac{\partial J^T}{\partial q_i}\cdot F\right)\delta q_i=K_g\cdot\delta q \tag{4. 27}$$

where K_g is the 3×3 matrix describing the influence of loading *F* on the manipulator Jacobian *J*

$$K_g=\left[\begin{array}{c:c:c}\dfrac{\partial J^T}{\partial q_1}\cdot F & \dfrac{\partial J^T}{\partial q_2}\cdot F & \dfrac{\partial J^T}{\partial q_3}\cdot F\end{array}\right]_{3\times3} \tag{4. 28}$$

that can be also written in the extended form as

$$K_g=\left[\begin{array}{c:c:c}-J_{21}F_x+J_{11}F_y & -J_{22}F_x+J_{12}F_y & -J_{23}F_x+J_{13}F_y\\ -J_{22}F_x+J_{12}F_y & -J_{22}F_x+J_{12}F_y & -J_{23}F_x+J_{13}F_y\\ -J_{23}F_x+J_{13}F_y & -J_{23}F_x+J_{13}F_y & -J_{23}F_x+J_{13}F_y\end{array}\right]_{3\times3} \tag{4. 29}$$

Further, after expressing the virtual joint torque variation as $\delta M=K_q\cdot\delta q$ and its substitution to (4.27), the variable δq can be presented as

$$\delta q=\left(K_q-K_g\right)^{-1}\cdot J^T\cdot\delta F \tag{4. 30}$$

which allows us to find the end-effector deflection $\delta=J\cdot\delta q$ and finally to obtain the desired loaded compliance and stiffness matrices

$$\begin{aligned}C_F&=J\left(K_q-K_g\right)^{-1}J^T\\ K_F&=\left[J\left(K_q-K_g\right)^{-1}J^T\right]^{-1}\end{aligned} \tag{4. 31}$$

It is worth mentioning that all the Jacobian and the joint stiffness matrices K_q, K_g must be computed for the loaded equilibrium configuration, which is different from the initial unloaded one. (It requires relevant solution of the non-linear equations considered above.)

To illustrate importance of the loaded stiffness analysis, the obtained expressions were applied to several cases study focusing on the manipulator stiffness changing under the external loading. For all considered cases, it was assumed that the initial manipulator configuration is a non-straight one, with the end point location $\left(x_o,y_o\right)=\left(5.5b,0\right)$. Under the loading the configuration angles corresponding to the external force $F=\left(F_x,F_y\right)^T$ were computed from (4.13) numerically (using *Newton's Method*).

There were compared three combinations of the geometric parameters $a/b\in\{0.75;0.9;1.1\}$, relevant results are presented in Figs. **4.10 - 4.12**. As follows from these figures, in most cases the manipulator stiffness essentially changes if the external loading is applied. In particular, the manipulator resistance in the *x*-direction becomes lower and lower while the force F_x is increasing (see

Fig. 4. 10a). In contrast, the resistance in the *y*-direction with respect to the force F_y becomes higher and higher while this force is increasing (see **Fig. 4. 10b**). These results are also confirmed by the K_{xx} and K_{yy} plots presented in **Fig. 4. 11**, which show enormous lost of *x*-direction resistance under the F_x loading (it can be treated as a "quasi-buckling", see **Fig. 4. 11a** for the stiffness coefficient K_{xx}). On the other side, while increasing the force F_y, the stiffness coefficient K_{yy} is very small at the beginning, then it is increasing until reaches the maximum value, and then it is decreasing (see **Fig. 4. 11b**).

(a) $Fx = \text{var}, \quad Fy = 0$

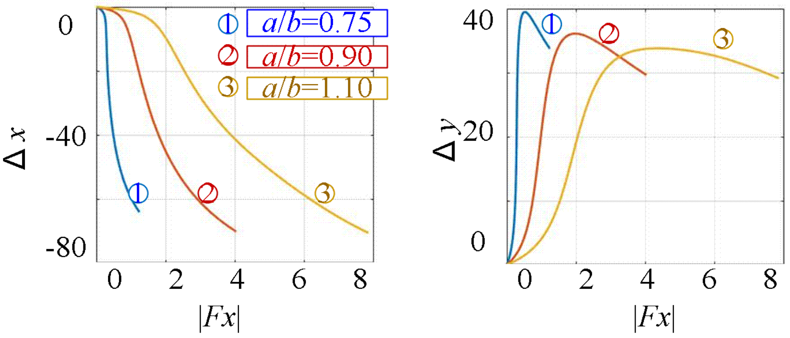

(b) $Fx = 0, \quad Fy = \text{var}$

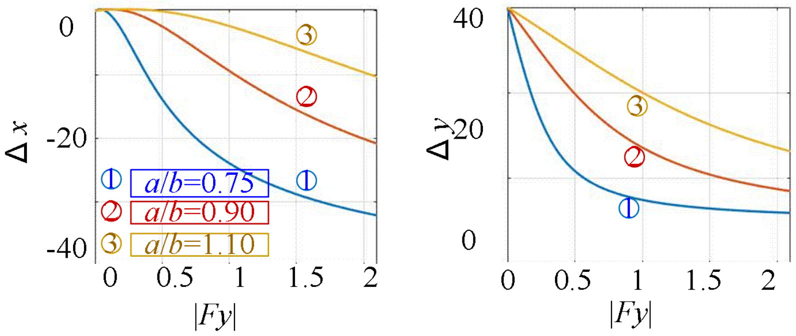

Fig. 4. 10 Force-deflection relations of three-segment mechanism for non-straight initial configuration with $(x, y)_0=(5.5b, 0)$.

To explain the above mention results from geometrical and physical point of view, **Fig. 4. 12** shows an evolution of the manipulator configuration under the loading with relevant stiffness coefficients K_{xx} and K_{yy} plots (corresponding to the case $a/b=0.75$). In this figure, there are presented four representative configurations showing shapes of all segments and their position with respect to the joint limits. As follows from them, the observed sudden change of the stiffness (see **Fig. 4. 12a** and **Fig. b**) occurs when one of the segment is close to its joint limits, when the equivalent rotational stiffness coefficient is very low. Hence, in practice it is necessary to avoid applying too high loading causing approaching to the joint limits and losing the manipulator stiffness.

(a) Fx = var, Fy = 0

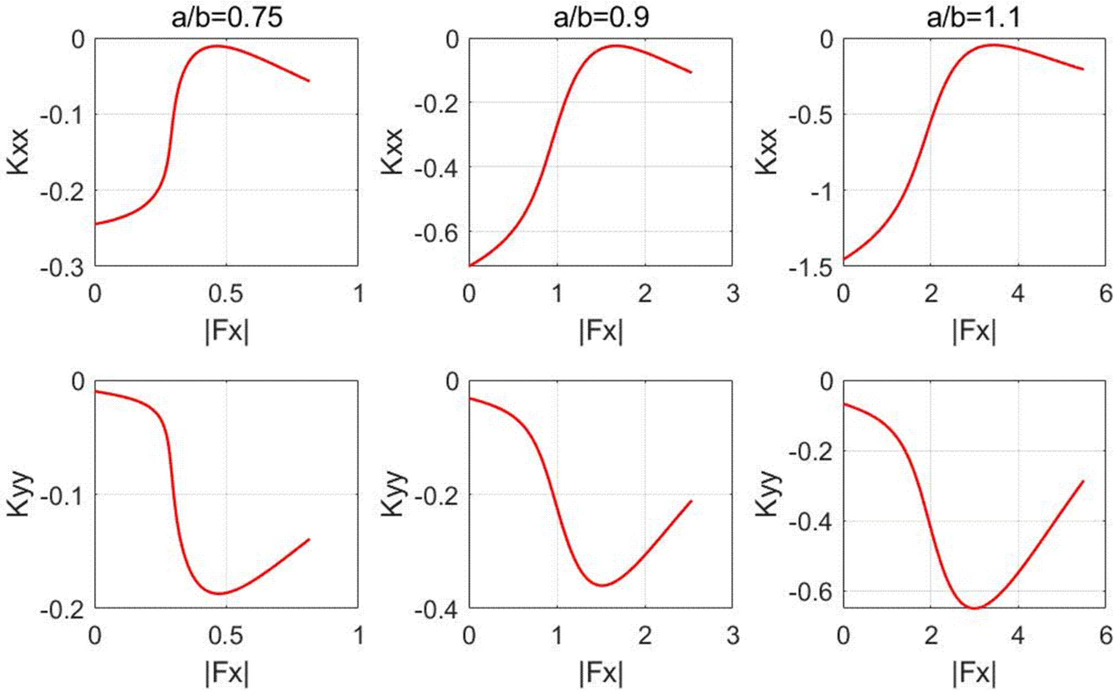

(b) Fx = 0, Fy = var

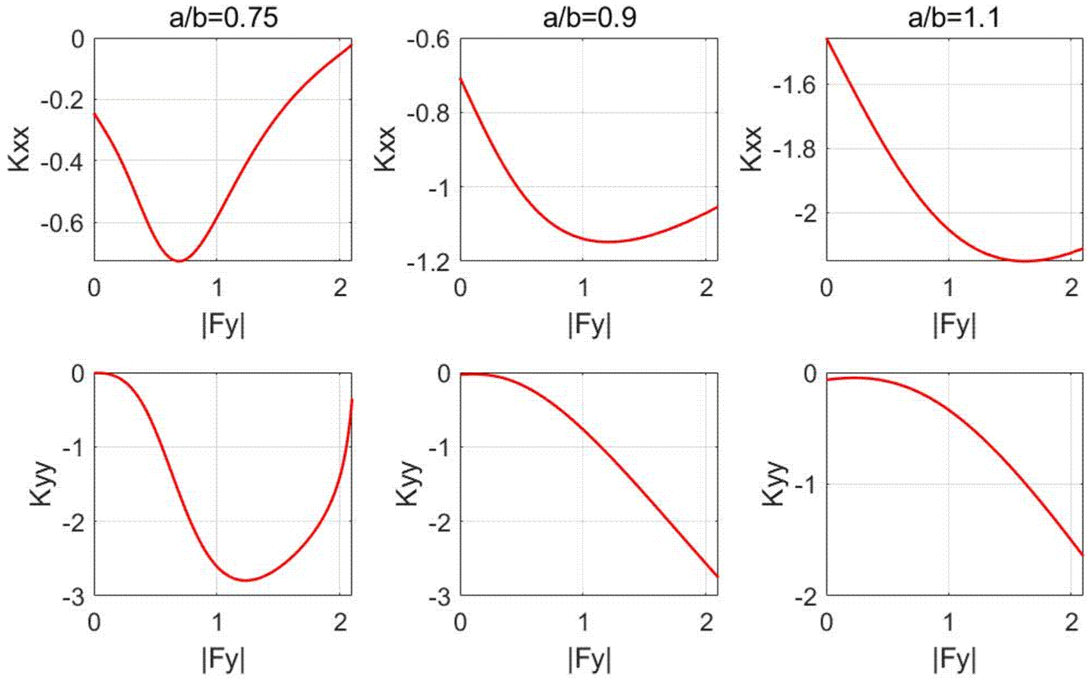

Fig. 4. 11 Stiffness coefficients of three-segment mechanism for non-straight initial configuration with $(x, y)_0=(5.5b, 0)$.

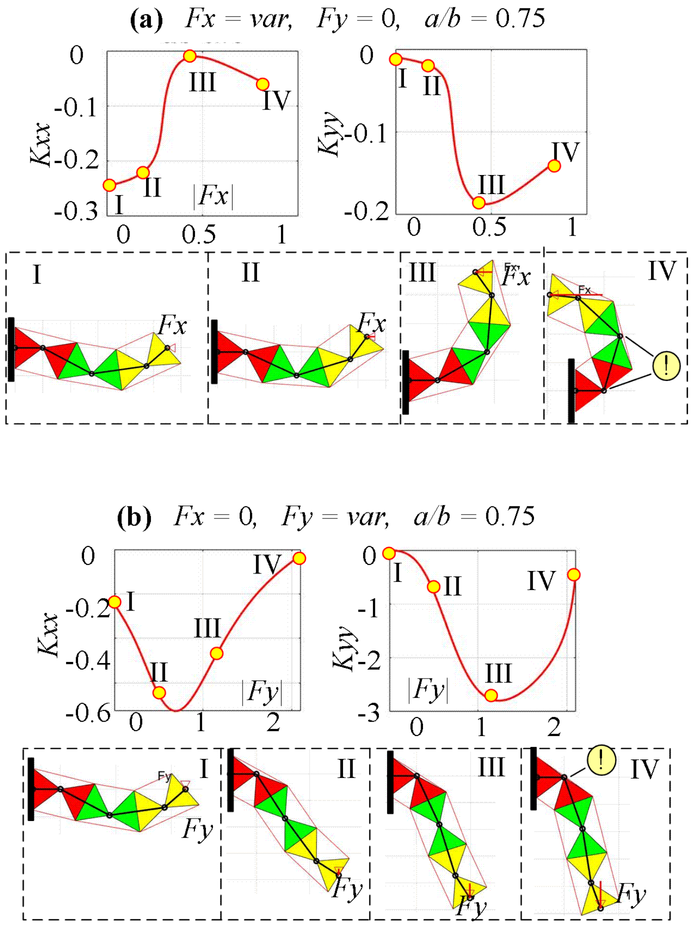

Fig. 4. 12 Evolution of the manipulator configuration under the loading.

4.3 Controlling mechanism configurations

It is clear that to achieve the desired end-point position (x, y), there is an obvious redundancy here related to selection of three configuration angles (q_1, q_2, q_3) allowing to reach the target point described by two Cartesian coordinates (x, y), but this problem is outside of the stiffness analysis and should be solved using other techniques (obstacle avoidance, minimization of joint motions, etc.). The simplest way to overcome the redundancy problem is to *minimize the joint motions* via moving from the initial configuration $(q_1^{\text{o}}, q_2^{\text{o}}, q_3^{\text{o}})$ to a final one (q_1, q_2, q_3) corresponding to the desired end-point (x, y). This objective can be expressed formally in several ways, for example as

#*a* Minimization of the total sum of the joint angle absolute increments

$$\sum_{i=1}^{3} \left| q_i - q_i^o \right| \rightarrow \min \tag{4.32}$$

#*b* Minimization of the largest joint angle absolute increment

$$\max_{i}\left|q_i - q_i^o\right| \rightarrow \min \tag{4.33}$$

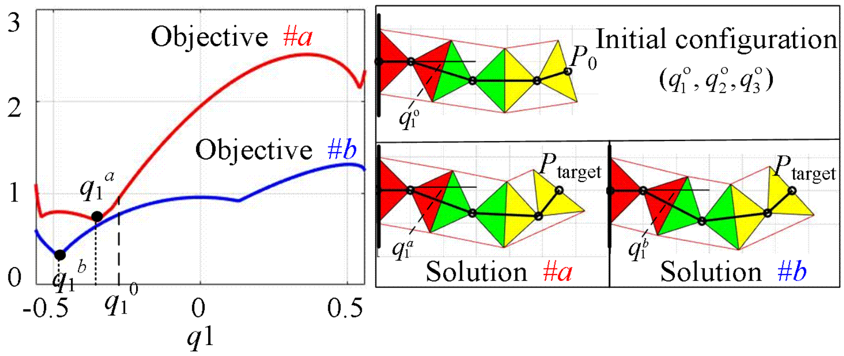

Fig. 4. 13: Kinematic control of a redundant manipulator via minimization of objectives #*a* and #*b*

It is clear that such optimization problem should be solved with respect to the two scalar constraints arising from the direct kinematic equations (4.1). The latter gives us a simple numerical technique where the joint angle q_1 is an independent variable and there are remaining angles q_2, q_3 are computed via the inverse kinematics (4.2) taking into account the duality expressed by the ‘ ± ’ sign. An example of such approach is presented in **Fig. 4. 13** where the objectives #*a* and #*b* give slightly different solutions both of which are acceptable in practice.

An alternative approach to minimize the joint motion quantity is to use the sum of increment squares as an optimization objective

$$\sum_{i=1}^{3}\left(q_i - q_i^o\right)^2 \rightarrow \min \tag{4.34}$$

which will be further referred to as the strategy #c. For this objective, if the initial and target points are close enough, we can apply linearization and express the direct kinematic constraints in the form of two linear equations

$$\begin{bmatrix} x - x_o \\ y - y_o \end{bmatrix} = \left[\mathbf{J}_{ij}\right]_{2\times 3} \cdot \begin{bmatrix} q_1 - q_1^o \\ q_2 - q_2^o \\ q_3 - q_3^o \end{bmatrix} \tag{4. 35}$$

where

$$\mathbf{J}_{ij} = \left[\begin{array}{c:c:c} -2bS_1 - 2bS_{12} - bS_{123} & -2bS_{12} - bS_{123} & -bS_{123} \\ 2bC_1 + 2bC_{12} + bC_{123} & 2bC_{12} + bC_{123} & bC_{123} \end{array}\right] = \left[\begin{array}{c:c:c} J_{11} & J_{12} & J_{13} \\ J_{21} & J_{22} & J_{23} \end{array}\right]_{2\times 3} \tag{4. 36}$$

Such approach leads the following constraint optimization problem: minimize the function of the joint angle increments $\Delta q_1, \Delta q_2, \Delta q_3$

$$f(\Delta q_1, \Delta q_2, \Delta q_3) \triangleq \frac{1}{2}\left(\Delta q_1^2 + \Delta q_2^2 + \Delta q_3^2\right) \to \min \tag{4. 37}$$

subject to the equality constraints

$$\begin{aligned} g_1(\Delta q_1, \Delta q_2, \Delta q_3) &\triangleq \Delta x - \left(J_{11}\Delta q_1 + J_{12}\Delta q_2 + J_{13}\Delta q_3\right) = 0 \\ g_2(\Delta q_1, \Delta q_2, \Delta q_3) &\triangleq \Delta y - \left(J_{21}\Delta q_1 + J_{22}\Delta q_2 + J_{23}\Delta q_3\right) = 0 \end{aligned} \tag{4. 38}$$

These problem can be solved using the *Lagrange technique* by minimizing the function of five variables

$$L(\Delta q_1, \Delta q_2, \Delta q_3, \lambda_1, \lambda_2) \triangleq f(.) + \lambda_1 g_1(.) + \lambda_2 g_2(.) \to \min \tag{4. 39}$$

where λ_1 and λ_2 are Lagrange multipliers. Further, after setting to zero the gradient $\nabla L = 0$, which is composed of the partial derivatives $\partial L/\partial \Delta q_i$, $\partial L/\partial \Delta \lambda_j$, one can obtain the following scalar equations with respect to the variables q_i and λ_j .

$$\begin{gathered} \Delta q_i - \sum_{j=1}^{2} \lambda_j J_{ji} = 0\,; \quad i = 1, 2, 3 \\ \sum_{i=1}^{3} J_{1i} q_i = \Delta x \;\; ; \;\; \sum_{i=1}^{3} J_{2i} q_i = \Delta y \end{gathered} \tag{4. 40}$$

that can be presented in the matrix form as follows

$$\begin{bmatrix} \mathbf{I}_{3\times3} & -\mathbf{J}^{\mathrm{T}}_{3\times2} \\ \mathbf{J}_{2\times3} & \mathbf{0}_{2\times2} \end{bmatrix} \cdot \begin{bmatrix} \Delta\mathbf{q} \\ \boldsymbol{\lambda} \end{bmatrix} = \begin{bmatrix} \mathbf{0}_{3\times1} \\ \Delta\mathbf{p} \end{bmatrix} \tag{4. 41}$$

where $\Delta\mathbf{q} = \left(\Delta q_1, \Delta q_2, \Delta q_3\right)^{\mathrm{T}}$, $\boldsymbol{\lambda} = \left(\lambda_1, \lambda_2\right)^{\mathrm{T}}$, $\Delta\mathbf{p} = \left(\Delta x, \Delta y\right)^{\mathrm{T}}$. Using the block matrix inverse, the desired solution can be expressed as

$$\begin{bmatrix} \Delta\mathbf{q} \\ \boldsymbol{\lambda} \end{bmatrix} = \begin{bmatrix} \mathbf{I} - \mathbf{J}^{\mathrm{T}}(\mathbf{J}\mathbf{J}^{\mathrm{T}})^{-1}\mathbf{J} & \mathbf{J}^{\mathrm{T}}(\mathbf{J}\mathbf{J}^{\mathrm{T}})^{-1} \\ -(\mathbf{J}\mathbf{J}^{\mathrm{T}})^{-1}\mathbf{J} & (\mathbf{J}\mathbf{J}^{\mathrm{T}})^{-1} \end{bmatrix} \cdot \begin{bmatrix} \mathbf{0}_{3\times1} \\ \Delta\mathbf{p} \end{bmatrix} \tag{4. 42}$$

which yields the following vector of the joint angle increments

$$\Delta\mathbf{q} = \mathbf{J}^{\mathrm{T}}\left(\mathbf{J}\mathbf{J}^{\mathrm{T}}\right)^{-1}\Delta\mathbf{p} \tag{4. 43}$$

where the term $\mathbf{J}^{\mathrm{T}}\left(\mathbf{J}\mathbf{J}^{\mathrm{T}}\right)^{-1}$ is the matrix pseudo-inverse of Moore-Penrose. It should mentioned that here the endpoint deflection dp should be small enough to ensure the implementability of the linearization (4.35).

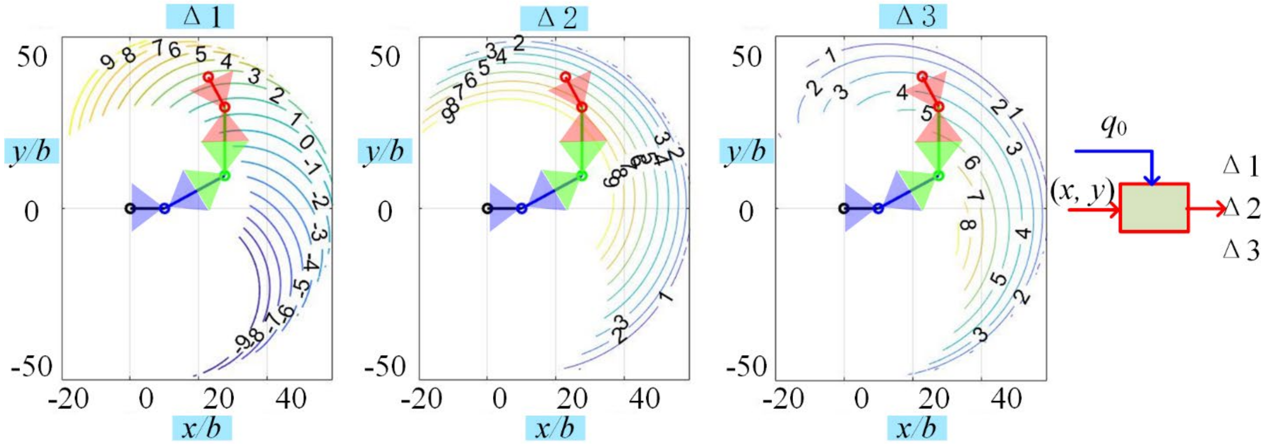

Fig. 4. 14: Relations between the control inputs (Δ_1, Δ_2, Δ_3) and the desired end-point position (x, y) with an initial configuration q_0=(-0.1. 0.1, 0.1) and parameters a/b=1.0, L^o/b=1.0 (unloaded case F_x=F_y=0).

To achieve the equilibriums of the three-segment manipulator with respect to the desired configurations obtained through the above methods, the three-segment mechanism must be controlled by three pairs of the control inputs (L^0_{11}, L^0_{12}), (L^0_{21}, L^0_{22}) and (L^0_{31}, L^0_{32}). To simplify the mechanism control, let us apply the asymmetrical approach used in subsections 1.3 and 2.3, which allows to use only three control variables ($\Delta_1, \Delta_2, \Delta_3$) producing six physical control inputs $L^0_{i1} = L^0 - \Delta_i$, $L^0_{i2} = L^0 + \Delta_i$ with $i = 1, 2, 3$, where the values of Δ_i are computed using formulas from the one-segment mechanism control law (2.29). These give us the following algorithm for the control of the three-segment mechanism:

① Using the direct kinematics equations (4.1) and additional objectives allowing to resolve the kinematic redundancy, compute the configuration angles $q_1(x,y)$, $q_2(x,y)$ and $q_3(x,y)$ corresponding to the desired end-point position (x, y) and ensuring the manipulator "minimum motions" of the joints.

② Using expression (2.29), compute the control inputs $\Delta_1(q_1)$, $\Delta_2(q_2)$ and $\Delta_3(q_3)$ for the three segments corresponding to the configuration angles (q_1, q_2, q_3).

An example of computing based on the above algorithm is presented in Fig. **Fig. 4. 14**~~,~~ where the mechanism parameters a/b=1.1, L^0/b =0.7 were chosen to ensure the mechanism stability in the unloaded mode $M_{ext} = 0$ (see **Section 2.3**), and the initial configuration is $q_0 = (-0.1, 0.1, 0.1)$.

In more general case when the external forces (F_x, F_y) are not equal to zero, it is also suggested to solve the redundant invers kinematic problem using the above presented objectives #*a*, #*b*, #*c* (i.e. to use the configuration angles q_1, q_2, q_3 from the unloaded case), but to compute the modified control inputs allowing to compensate the external load. Corresponding algorithm implementing such technique is presented below.

① Using the direct kinematics equations (4.1) and additional objectives allowing to resolve the kinematic redundancy, compute the configuration angles $q_1(x, y)$, $q_2(x, y)$, and $q_3(x, y)$, corresponding to the desired end-point position (x, y) and ensuring the manipulator "minimum motions" of the joints.

② Using expression (4.6), compute the joint torques (M_1, M_2, M_3) allowing to compensate the external force (F_x, F_y) applied at the manipulator end-point.

③ Using expression (2.31), compute the control inputs $\Delta_1(q_1)$, $\Delta_2(q_2)$ and $\Delta_3(q_3)$ for the three segments corresponding to the configuration angles (q_1, q_2, q_3) and the joint torques (M_1, M_2, M_3).

An example of computing based on the above algorithm is presented in **Fig. 4. 15**, where the geometric parameters are similar to the previous figure. It can be demonstrated that such algorism can ensure the stable configurations of the manipulator.

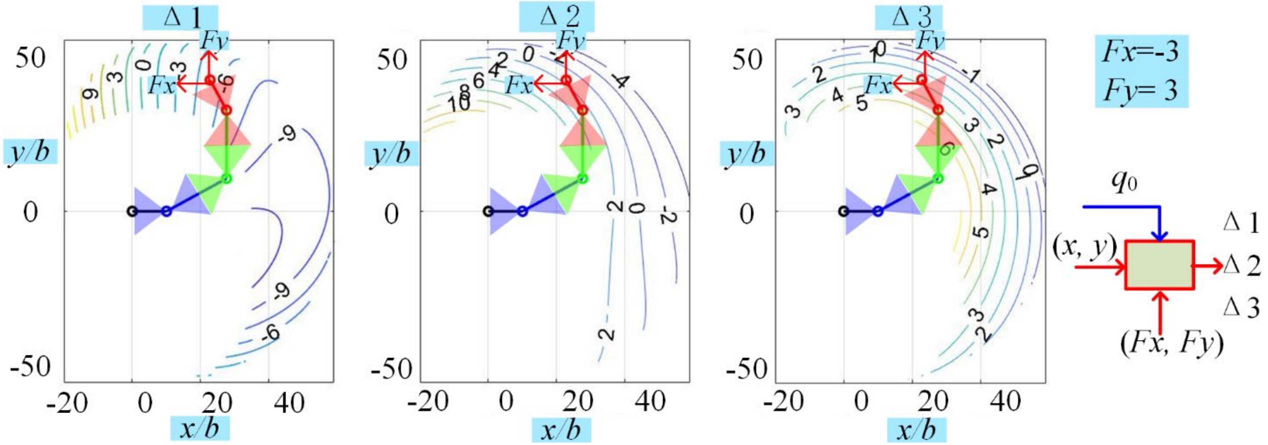

Fig. 4. 15: Relations between the control inputs (Δ_1, Δ_2, Δ_3) and the desired end-point position (x, y) with an initial configuration q_0=(-0.1. 0.1, 0.1) and parameters a/b=1.0, L^o/b=1.0 (loaded case F_x= -3, F_y=3).

It should be noted that the above presented methods allow to find the manipulator configuration angles at the target point only, without answering the question how to move the joints from the initial q_i^0 to the goal q_i^g values. However in practice, the manipulator controller must implement continuous motion allowing to achieve the target point while moving the end-effector along some desired curves (linear, circular, etc.). The latter requires computing the time-profiles of the joint coordinates $q_i(t)$, $t \in [0, t_g]$, which are usually based on the linear interpolation either in joint space (q_1, q_2, q_3) or task space (x, y). These techniques are also known in industry as *PTP* and *LIN* motion planning methods respectively, they are considered below in detail.

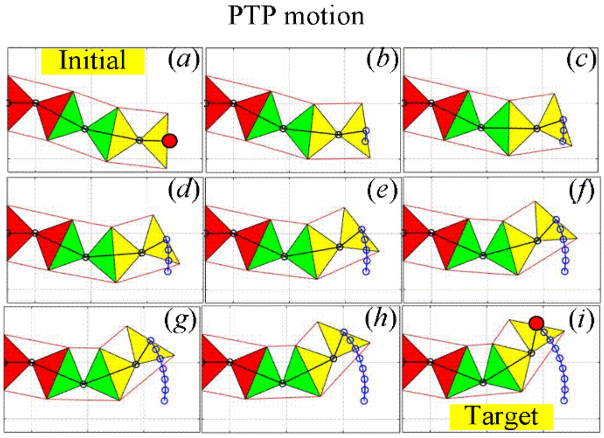

Fig. 4. 16: Kinematic control of the 3-segment manipulator using linear interpolation in (q_1, q_2, q_3)-space and global minimization of the joint increments (PTP motion, objective #***b***).

PTP motion: In this case, it is assumed that the target configuration angles q_i^g (i=1, 2, 3) corresponding to the given target point (x^g, y^g) are obtained before the motion planning, using numerical minimization of any of the objectives #***a***, #***b***, #***c*** , which evaluate the difference $\|\mathbf{q}^g - \mathbf{q}^0\|$ in joint angles between the initial $\mathbf{q}^0$ and final $\mathbf{q}^g$ configurations. Further, the intermediate configurations $q_i(t)$ $(t \in [0, t_g])$ are computed via straightforward linear interpolation in the following way

$$q_i(t) = \left[1-\alpha(t)\right]\cdot q_i^0 + \alpha(t)\cdot q_i^g;\ t\in[0,t_g],\ \left(i=1,\ 2,\ 3\right) \tag{4. 44}$$

where the interpolation parameter $\alpha(t) \in [0,1]$, $\left(0 \le t \le t_g\right)$ satisfies the boundary constraints $\alpha(0) = 0$, $\alpha(g) = 1$. Simulation example of the *PTP* (point-to-point) *motion* is presented in **Fig. 4. 16**, which clearly shows that this type of kinematic control allows to achieve the desired target point (x^g, y^g) but the task space trajectory is essentially nonlinear.

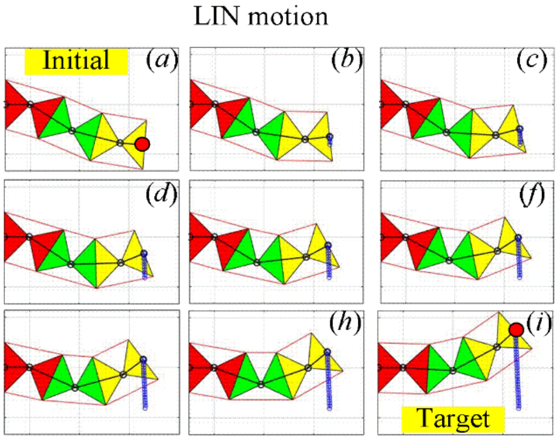

Fig. 4. 17: Kinematic control of 3-segment manipulator using linear interpolation in (x, y)-space and local

minimization of the joint squared increments (LIN motion, objective #*c*).

LIN motion: For this type of motion, the intermediate configurations $q_i(t)$ ($0 < t < t_g$) are computed using the linear interpolation in the (*x*, *y*) space

$$\begin{aligned} x(t) &= \left[1-\alpha(t)\right]\cdot x^0 + \alpha(t)\cdot x^g \\ y(t) &= \left[1-\alpha(t)\right]\cdot y^0 + \alpha(t)\cdot y^g \end{aligned}; \quad t \in [0, t_g], \tag{4.45}$$

and local minimization of the local joint increments Δq_i, (*i* =1,2,3) corresponding to the Cartesian increments,

$$\begin{aligned} \Delta x_j &= x(t_j) - x(t_j - t_{j-1}) \\ \Delta y_j &= y(t_j) - y(t_j - t_{j-1}) \end{aligned}; \quad j = 1, 2, \ldots n \tag{4. 46}$$

where the interpolation parameter is computed as $\alpha_i = i/n$ that ensures uniform discretization of the time interval $t \in [0, t_g]$. It is clear that the minimization of the local joint increments

$$\left\| \left[\Delta q_1, \Delta q_2, \Delta q_3\right] \right\| \to \min$$

can be executed using any of the above objectives #***a***, #***b***, #**c**, but the last one #**c** is the most attractive computationally because it allows to apply the analytical expression (4.43) for computing Δq_i. It should be stressed here, ($\Delta x_j, \Delta y_j$) are small and the linearization via Jacobian is justified. Simulation example of the *LIN* (linear) *motion* is presented in **Fig. 4**. **17**, which clearly shows that this type of kinematic control allows to achieve the desired target point (x^g, y^g) and the task space trajectory is strictly linear.

And it should be also noted that for the given initial endpoint position $\mathbf{p}^0 = [x^0, y^0]^T$ of manipulators, the corresponding initial configuration angles $\mathbf{q}^0$ are usually known in practice. But theoretically if designers can ensure that the given initial configuration angles correspond to the stable equilibrium of the manipulators, then there are many possible configurations for redundant serial manipulators

In this case, for our redundant serial manipulator composed of dual-triangle tensegrity mechanisms, one simple way to define the initial configuration angles $\mathbf{q}^0$ correspond to the initial endpoint position $\mathbf{p}^0 = [x^0, y^0]^T$ is using the minimum elastic energy approach min*E*(*q*). Let us first assume that the symmetrically distributed linear springs have the same initial lengths $L_1^0 = L_2^0$ (see the mechanism structural in **Fig.** 2.5 and 4.1), then users can find the configuration angles corresponding to the stable equilibrium (minimum energy point) from the energy method presented in the previous (see section 4.1). Further, users can also redefine the control inputs (spring initial lengths) corresponding to the obtained configuration angles by using our control law presented in **Chapter 2,** i.e. the expression (2.31), which allows the manipulator to achieve the absolute minimum elastic energy (zero energy value) corresponding to the initial configuration. The the algorithm of the continuous motion control of this manipulator is presented in **Table 4**.

Table 4 Linear kinematic control of serial manipulator based on the least square joint increments (LIN motion, objective #c)

Inputs	**p0**	$\mathbf{p0} = [x0, y0]^T$, manipulator end-defector initial location
	pg	$\mathbf{pg} = [xg, yg]^T$, manipulator end-defector target location
	q0	$n\times1$ vector, the initial configuration angles of the manipulator
	F	$\mathbf{F} = [Fx, Fy]^T$, external loading on the end-effector of the manipulator
	k	$n\times1$ vector, stiffness coefficient of each joints of the manipulator
	L0	$2\times n$ matrix, the symmetrically distributed linear springs initial lengths of the manipulator (see structure figure 5.1)
	a, *b*	geometric parameters of the manipulators
	m	Number of motion steps between the initial and target end-effector position
Local variables	**pt**	$\mathbf{pt} = [xt, yt]^T$, points locating on the path between the initial and target end-effector location
	pc	Current endpoint location of the manipulator
	dp	**dp** = **pt** - **pc** , current end-effector deflection
	dq	$n\times1$ vector, current joint increment corresponding to **dp**
	qc	$n\times1$ vector, current joint configuration angles
	Me	External torque of each joint of the manipulator
	Delt_L0	$n\times1$ vector, configuration control inputs of each segment of the manipulator
	J	$2\times n$ Jacobian matrix that corresponding to **qc**
	alpha	Interpolation parameter
Outputs	**Set_Qout**	$n\times m$ matrix, joint configuration angles corresponding to all the manipulator current motion
	Set_Delt	$n\times m$ matrix, configuration control inputs of each segment corresponding to all the manipulator current motion

(1) Joint limit of manipulator segments

```
If  $a/b<=1$
        $Joint\_limit = 2*\text{atan}(a/b)$;
Else
```

```
        Joint_limit = pi - 2*atan (a/b);
End
```

(2) Main algorithm loop of continuous motion configurations control

```
Set_Qout:=zeros(m, n);    Set_Delt:=zeros(m, n);    qc: = q0;    pc = p0
For   i = 1 to m
        alpha: = i/m;
        pt: = (1 - alpha) · p0 + alpha · pg;
        dp: = pt – pc;
        J: = fun_of_Jacobian(qc, b);
        dq: = J’ · inv(J · J’) · dp;
        qc: = qc + dq;
        For   j = 1 to n
        If   Abs( qc(j) ) > Joint_limit;
                qc(j): = sign( qc(j) ) · Joint_limit;
        End
        End
        pc = fun_direct_kinematic(qc, b);
        Set_Qout (:, i): = qc;
        Me: = J’ · F;
        Delt_L0: = fun_of_Delt_L0(a, b, k, L0, qc, Me);
        Set_Delt (:, i): = Delt_L0;
End
```

Summarizing results presented in this section, it should be noted that here the kinematic redundancy of the 3-segment manipulator was created by the special definition of the 2-dimentional task space (*x*, *y*), which does not take into account the end-effector orientation φ. It is clear that an alternative definition of the task space (3-dimentional) with the orientation component (x, y, φ) eliminates the redundancy, so the relevant control strategies do not require any minimization of the joint angle increments (similar to section 2.3). However, in the case of the multi-segments serial manipulators with higher redundancy, the *minimum joint motion* principle is useful while is more difficult computationally. It will be considered in detail in the next chapter.

4.4 Summary

This chapter deals with the analysis of the redundant ***three-segment serial tensegrity mechanism*** composed of the dual-triangles, which was selected as the base structure for designing compliant robot-end-effector.

The ***main contributions*** are in the area of specific mechanical properties of this redundant mechanism under the loading, and also in the domain of the kinematic control strategies allowing to reach the target end-point location. Similar to the previous chapters, some complicated behavior under the loading (such as *buckling*) was detected, which allows designers to choose proper geometric parameters and control inputs to avoid the dangerous states of this mechanism. An analytical way for obtaining the force-deflection relations and the equilibriums is presented and confirmed by the energy method. That allows find the possible manipulator shapes under the loading and to estimate the stability of the corresponding configuration. Relevant *kinematics control strategies* based on the nonlinear optimization techniques were proposed, which allow to achieve minimum increments of the joint motions. These strategies were carefully investigated via simulation, and the approach based on quadratic optimization techniques with linear equality constraints (minimizing the sum of the joint increments square) is selected, which was confirmed more efficient from the results. This idea will be extended in the following chapter and used for controlling more complicated manipulator motions in a constrained environment.

In more details, new results and contributions of Chapter 4 include the following issues:

(i) *The* ***stiffness matrices*** of this mechanism for both unloaded and loaded mode were obtained using VJM technique, and the relations between the end-effector deflection and the external load were derived analytically by eliminating the mechanism redundancy using the extended Jacobian matrix.

(ii) *The* ***equilibrium configurations*** were obtained using the energy method for different combinations of geometrical and mechanical parameters; corresponding results show that both symmetrical stable and unstable equilibriums may exist.

(iii) *The* ***quasi-buckling phenomenon*** was detected, when the mechanism resistance in one direction (in Cartesian coordinates) may suddenly disappear during the deformation under the loading, while the resistance in another direction still exists.

(iv) *The* ***critical force*** causing the buckling was obtained analytically by solving the system of static equilibrium and kinematic equations; and the classification of possible equilibrium configurations of this mechanism was given (including stable and unstable ones).

(v) ***Kinematic control strategies*** for the considered tensegrity mechanism were proposed, which are based on the quadratic optimization techniques with linear equality constraints, ensuring the end-effector displacement to the desired location using minimal increments of joint motions, and ensuring elastostatic stability of the manipulator shape with respect to the external forces/torques applied on the end-point.

It should mentioning that the observed quasi-buckling or jumping phenomenon was detected when one of the segments is close to its joint constraints. Hence, in practice it is necessary to avoid applying too high loading causing this dangerous state. It is also worth mentioning that in this chapter, the kinematic redundancy of this mechanism is considered only for the desired end-point location in the 2-dimentional task space (x, y). However, similar control strategies can be applied in three-dimensional space for the multi-segments serial manipulators with higher redundancy while taking into account the orientation angle. This idea is used in the following chapter.

The main results of Chapter 4 are published in the following works: [Zhao, W.; Pashkevich, 2021a], [Zhao, W.; Pashkevich, 2021b].

CHAPTER 5

ANALYSIS OF MULTI-SEGMENT MECHANISM COMPOSED OF DUAL-TRIANGLES

This chapter is devoted to the general case, dealing with the analysis of the redundant multi-segment serial structure composed of the dual-triangles. For practical convenience, the four-segment manipulator is considered as the basic illustrated example. It was discovered that under the external loading such manipulator may have six equilibrium configurations but only two of them are stable. In the neighborhood of these configurations, the manipulator behavior was analyzed using the VJM technique. This approach allowed us to propose an analytical technique for computing the critical force causing the buckling and evaluate the manipulator shape under the loading. Further, the redundancy resolution in kinematic control of such mechanism while moving in a multi-obstacle environment was considered. The general problem was decomposed into two sub-problems, which deal consequently with the collision-free path planning for the mechanism end-point and the collision-free motion planning for the mechanism body. The first of them was solved via discrete dynamic programming, the second one was solved using quadratic programming with mixed linear equality/inequality constraints. Relevant simulation studies confirmed the efficiency of the proposed technique.

5.1 Stiffness analysis of a straight configuration

Let us consider now a general case dealing with a manipulator composed of n similar sections connected in series as shown in **Fig. 5. 1**, where the left hand-side is assumed to be fixed. First, let us concentrate on the stiffness analysis of the "straight" initial configuration for which $q_i = 0, \forall i$

$(x,y)=(2nb,0)$ and the external loading $F_e=(0,0)$. This configuration is achieved by applying equal control inputs ($L_{ij}^0, i=1,2,...,n,\ j=1,2$) to all mechanism segments. Under such assumptions, it is necessary to investigate the influence of the external force $F_e=(F_x,F_y)$, which causes the end-effector displacements in the neighborhood of $(x,y)=(2nb,0)$, moving it to a new equilibrium location $(x,y)=(2n\cdot b-\delta_x,\delta_y)$ corresponding to some nonzero configuration variables ($q_1,q_2,...,q_n$). It is also assumed here the external torque M_{ext} applied to the end-effector is equal to zero.

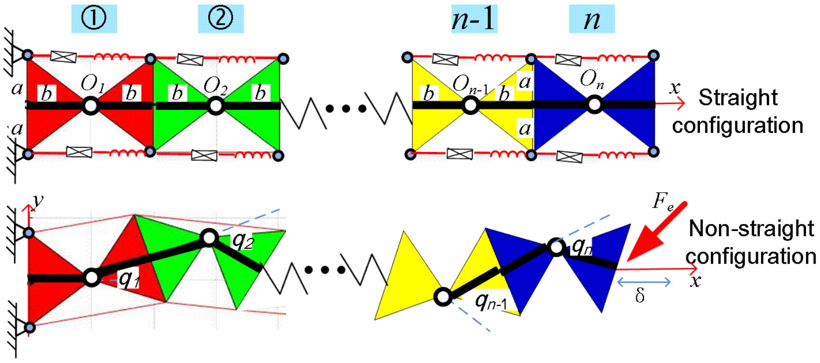

Fig. 5. 1: The multi-segment manipulator in the “straight” and “non-straight” configurations.

In engineering practice, the mechanism resistance to the external load is usually described by the force-deflection relations $F_x(\delta_x,\delta_y)$ and $F_y(\delta_x,\delta_y)$, which can be derived from the manipulator kinematic and elastostatic analysis. As follows from the manipulator geometry, to achieve the desired end-effector displacement (δ_x,δ_y), the manipulator configuration angles ($q_1,q_2,...,q_n$) must satisfy the following direct kinematic equations

$$\begin{aligned} 2n\cdot b-\delta_x &= b+2b\sum_{j=1}^{n\text{-}1}\left(\cos(\sum_{i=1}^{j}q_i)\right)+b\cos(\sum_{i=1}^{n}q_i) \\ \delta_y &= 2b\sum_{j=1}^{n\text{-}1}\left(\sin(\sum_{i=1}^{j}q_i)\right)+b\sin(\sum_{i=1}^{n}q_i) \end{aligned} \tag{5.1}$$

where the parameter b defines the length of separate segments (see **Fig. 2.5**). It is clear that these two equations include n unknown variables ($q_1,q_2,...,q_n$), which create redundancy of the order n-2. This redundancy will be resolved below by applying the minimum elastic energy principle allowing to find the desired equilibrium configuration angles. And as known from the static analysis, the manipulator equilibriums must satisfy the following matrix equation

$$\begin{bmatrix} M_{q1} \\ \cdots \\ M_{qn} \end{bmatrix} + \left[\mathbf{J}_{\mathbf{q}}^{\mathrm{T}}\right]_{n\times 2}\cdot\begin{bmatrix} F_x \\ F_y \end{bmatrix} = \begin{bmatrix} 0 \\ \cdots \\ 0 \end{bmatrix} \tag{5.2}$$

which includes the manipulator Jacobian

$$\mathbf{J}_{\mathbf{q}} = b \cdot \begin{bmatrix} -\sum_{j=1}^{\mathrm{N}}\left(\eta_j \sin\sum_{i=1}^{j} q_i\right) & -\sum_{j=2}^{\mathrm{N}}\left(\eta_j \sin\sum_{i=1}^{j} q_i\right) & \cdots & -\sum_{j=\mathrm{N}}^{\mathrm{N}}\left(\eta_j \sin\sum_{i=1}^{j} q_i\right) \\ \sum_{j=1}^{\mathrm{N}}\left(\eta_j \cos\sum_{i=1}^{j} q_i\right) & \sum_{j=2}^{\mathrm{N}}\left(\eta_j \cos\sum_{i=1}^{j} q_i\right) & \cdots & \sum_{j=\mathrm{N}}^{\mathrm{N}}\left(\eta_j \cos\sum_{i=1}^{j} q_i\right) \end{bmatrix}_{2\times n} \tag{5.3}$$

where

$$\eta_j = \begin{cases} 2 & for \quad j = 1,2,...,n-1 \\ 1 & for \quad j = n \end{cases}$$

It should be noted that the static equilibrium equation provides *n* additional scalar relations applied to the *n*+2 variables (q_1, q_2,…, q_n) and (F_x, F_y). So totally, combining both geometric and elastostatic equations (5.1) and (5.2) one can obtain *n*+2 nonlinear equations for *n*+2 unknowns, assuming that (δ_x, δ_y) are known.

Obviously, in general case such nonlinear system can only be solved numerically, using Newton' method for example. However, for relatively small *n* it is possible to apply the technique from the previous section 3.1. For instance, if *n*= 4 the geometric model (5.1) allows us to reduce analytically the number of unknown variables down to two. In particular, if the angles q_1 and q_2 are assumed to be known, the remaining ones q_3 and q_4 can be computed from the classical invers kinematics of the two-link manipulator as follows

$$\begin{aligned} q_4 &= \operatorname{atan2}\left(S_4, C_4\right) \\ q_3 &= \varphi_1 - \varphi_2 - (q_1 + q_2) \end{aligned} \tag{5.4}$$

where $C_4 = \left[\left(x - x_2\right)^2 + \left(y - y_2\right)^2 - 5b^2\right] \big/ 4b^2$, $S_4 = \pm\sqrt{1 - C_4^2}$, the coordinates (x_2, y_2) are computed as $x_2 = b + 2b\cos(q_1) + 2b\cos(q_1 + q_2)$, $y_2 = 2b\sin(q_1) + 2b\sin(q_1 + q_2)$, and $\varphi_1 = \operatorname{atan2}\left((y - y_2), (x - x_2)\right)$, $\varphi_2 = \operatorname{atan2}\left(bS_4, 2b + bC_4\right)$. It is clear that the above latter expressions provides two group of possible solutions corresponding to the positive /negative configuration angles $q_4 \geq 0$ and $q_4 \leq 0$ corresponding to $\pm\sqrt{\ldots}$.

Further, similar to the **Section 4.1**, instead of directly using static equilibrium condition (5.2), it is possible to compute the two-variable energy function $E(q_i, q_j)$ and find its minimums and maximums numerically,

$$E(q_i, q_j) \to \min_{q_i, q_j}, \qquad E(q_i, q_j) \to \max_{q_i, q_j}$$

which obviously define the stable and unstable equilibriums respectively. Examples of such computations are presented in **Fig. 5. 2** and **Fig. 5. 3**, where two cases are considered with the independent variables (q_1, q_4) and (q_1, q_2).

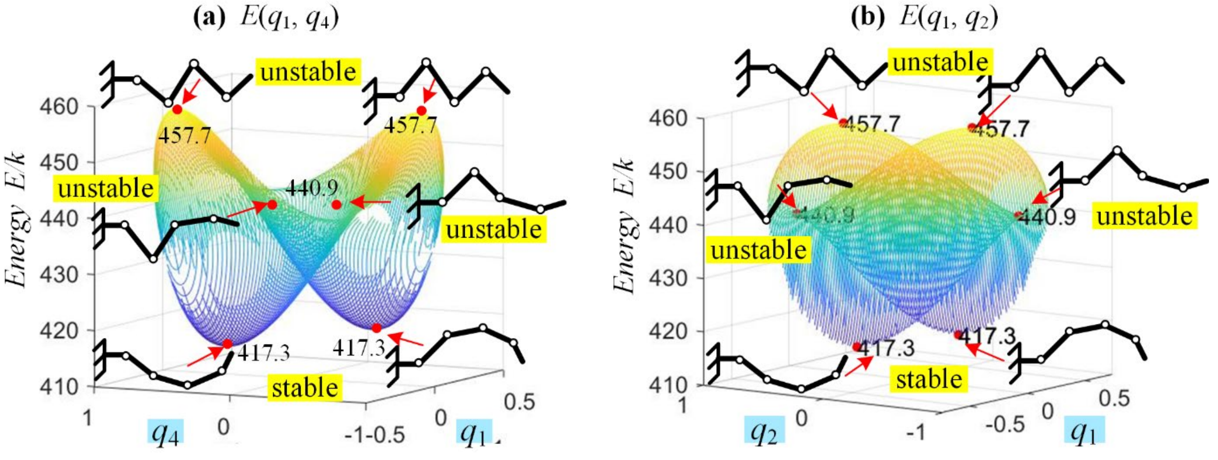

Fig. 5. 2: The energy functions $E(q_1, q_4)$, $E(q_1, q_2)$ and their critical points corresponding to the static equilibriums for the end-effector location $\delta x/b$=0.3, δy=0 and manipulator parameters a/b=1.0, L^0/b=1.0

As follows from these figures, in each case there are two global maximums and two global minimums corresponding to the stable and unstable equilibriums respectively. Besides, there are also two saddle points here that were discovered after numerical analysis of the energy function gradient. Obviously, the saddle points correspond to the unstable equilibriums. So totally, for the considered combination of the geometric parameters (a/b, L^o/b) and end-effector deflections (δx, δy), the energy functions $E(q_i, q_j)$ allows to detect six equilibriums: two stable ones with "U-shape" of the manipulator and for unstable ones where the manipulator has "Z-shape". It should be noted that these results is in good agreement with section 3.1, where for the three-link manipulator the "U-shape" equilibriums were stable and the "Z-shape" equilibriums were unstable. Besides, it is also worth mentioning that for other combination of the geometric parameters (a/b, L^o/b) and end-effector deflections (δx, δy), the energy function may have higher number of critical points (with local min/max) and corresponding equilibriums, similar to **Fig. 4.2** from section 4.1.

The energy method allows us also to obtain the force-deflection relations describing the manipulator resistance to the external force. In fact, the energy minimums defining stable equilibriums provides us with the configuration angles $(q_1, q_2, ..., q_n)$ allowing to find the force (F_x, F_y) corresponding to the given displacement (δ_x, δ_y). This force can be directly computed from the over determined system of n linear equations (5.2), which includes only two unknown variables (F_x, F_y). It can be easily proved that, for the equilibrium configurations, this linear system is consistent because it is derived from the zero-gradient condition $\nabla E(q_1, ..., q_n) = 0$. The latter allows us to apply the Moore-Penrose pseudo-inverse yielding the following expression for the forces

(a) $E(q_1, q_4)$ for $q_3>0$ **(b)** $E(q_1, q_4)$ for $q_3<0$

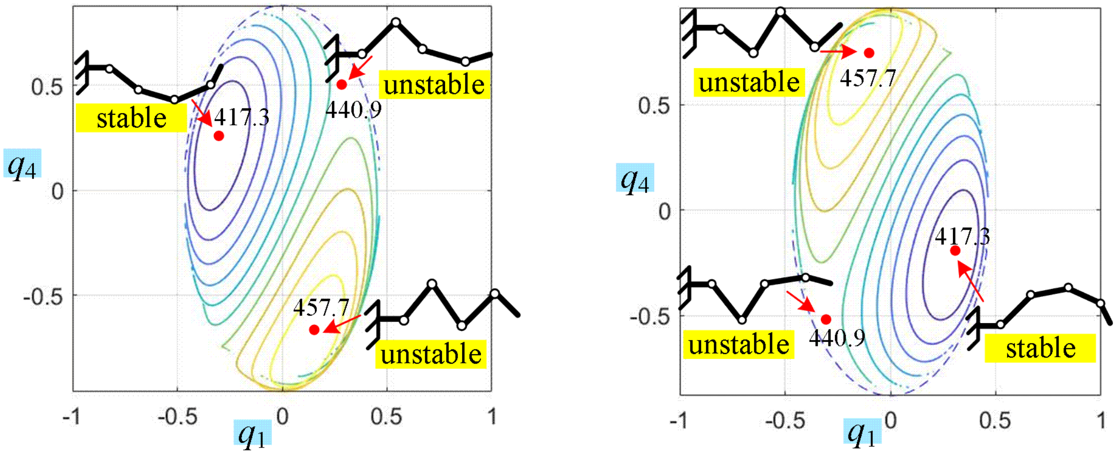

(c) $E(q_1, q_2)$ for $q_4<0$ **(d)** $E(q_1, q_2)$ for $q_4>0$

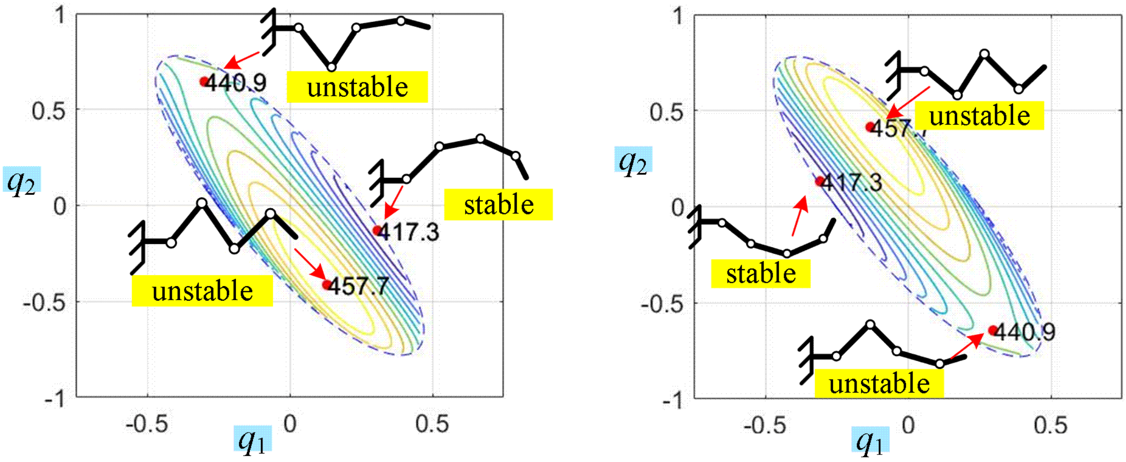

Fig. 5. 3: The contour plots of the energy functions $E(q_1, q_4)$, $E(q_1, q_2)$ for different manipulator configurations at the end-effector location $\delta x/b=0.3$, $\delta y=0$ and geometric parameters $a/b=1.0$, $L^0/b=1.0$

$$\begin{bmatrix} F_x \\ F_y \end{bmatrix} = -\left[\mathbf{J_q}\right]\cdot\left[\mathbf{J_q^T J_q}\right]^{-1}\cdot\begin{bmatrix} M_{q1} \\ \dots \\ M_{qn} \end{bmatrix} \tag{5.5}$$

where both the Jacobian $\mathbf{J_q}$ and the joint torques Mq_i are computed using the configuration angles of the stable equilibriums. Applying such technique for different (δ_x, δ_y) one can get the desired force-deflection relations $F_x(\delta_x, \delta_y)$ and $F_y(\delta_x, \delta_y)$. Examples of such curves for the case $n=4$ and ($\delta x=var$, $\delta y=0$) are presented in **Fig. 5. 4**, which clearly demonstrate the buckling phenomenon occurring at the beginning of deflection. Besides, after the buckling the force F_x increases very slowly, i.e. the stiffness coefficient in the x-direction is very small. It should be mentioned that, these curves are similar to the ones obtained above for the cases $n=2$ and $n=3$ (see sections 3.1 and 4.1). This allows us to assume that in the general case with $n \geq 2$, in the “straight configuration”, the stiffness properties of the considered multi-segment manipulator are essentially nonlinear and force-deflection relations are discontinuous, which is observed physically as the “buckling” phenomenon. This conclusion will be strictly proved below using the linearization technique allowing us also to compute the buckling critical force, as well as the stiffness coefficients after the buckling.

Similar to the previous study for solving the configuration angles corresponding to the given endpoint position of the redundant manipulator from the underdetermined system (see equation 4.37 and 4.43). Here this formula also allows us to find a least-squares solution that minimizes the error $\left|\mathbf{M}_q - \mathbf{J}_q \cdot \mathbf{F}\right|$ of the overdetermined system (5.5). For redundant serial manipulators, theoretically, there may be more than one possible configurations corresponding to the desired endpoint deflection. But it should be mentioned that the above formula is derived from the static equilibrium equation (5.2), which means that it should be applied only for computing the external loading corresponding to the equilibrium configurations of the manipulator.

From the previous analysis it is clear that the redundant serial manipulators may have either stable or unstable static equilibrium configurations, which can be achieved by applying different external loading. However, in practice, only the stable static equilibrium is feasible, since any influence can cause a sudden big change in the configuration corresponding to the unstable equilibrium, which can be treated as a “jump motion”. Thus, the considered configuration angles $\mathbf{q}$ in formula (5.5) are corresponded to the stable static equilibrium, which can be obtained from the minimum elastic energy approach min$E(q)$ that mentioned in the previous. And for any other different endpoint deflection of the manipulator, users should first find the corresponding configuration angles by using the energy approach, then get the corresponding external loading through the formula (5.5)

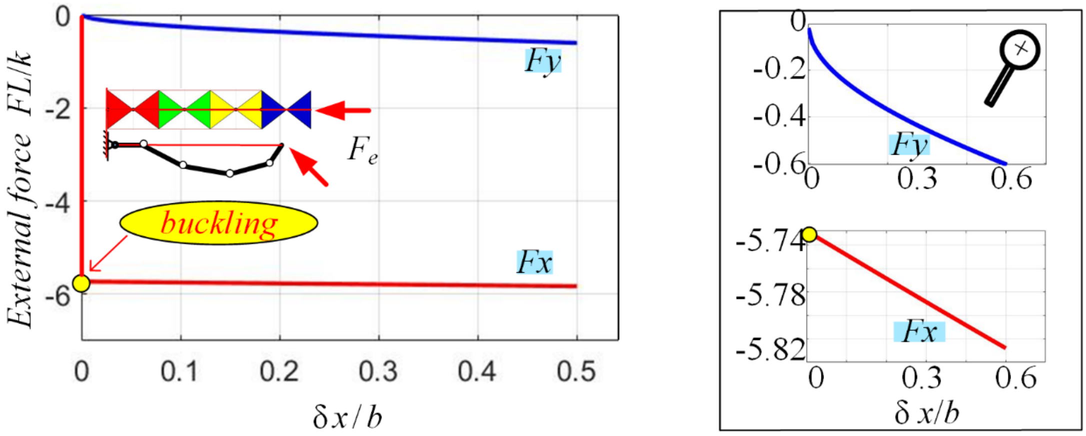

Fig. 5. 4: The force-deflection curves for the 4-link manipulator with the geometric parameters a/b=1.0, L^0/b=1.0, k=1, (δx=*var,* δy=0).

The algorithm of get the force-deflection relation of the n-segment serial manipulators is shown **Table**

Table 5 Algorithm of the force-deflection relation of redundant serial manipulators

inputs	**dp**	**dp** = **pt** – **pc,** manipulator end-defector deflection
	k	$n\times 1$ vector, stiffness coefficient of each joints of the manipulator
	L0	$2\times n$ matrix, the symmetrically distributed linear springs initial lengths of the manipulator (see structure figure 5.1)
	a, b	geometric parameters of the manipulators
Local variables	E(**k**, **L0**, a, b, q(**dp**)) Elastic potential energy function for the given end-defector deflection dt corresponding to all the possible configuration angles q(dt) of the serial manipulator. notation: theoretically there are infinite possible configurations when n >2	
	min$E$	scalar, global minimum value of the elastic potential energy function E(**k**, **L0**, a, b, q(**dp**))
	qE	$n\times 1$ vector, the configuration angles corresponding to min$E$, which is the stable static equilibrium configuration of the manipulator
	$\mathbf{M}_q(qE)$	nx1 vector, joint torques corresponding to the stable static equilibrium configuration of the manipulator, which can be obtained by the general equation (2.21)
	$\mathbf{J}_q(qE)$	2xn matrix, jacobian matrix corresponding to the stable static equilibrium configuration of the manipulator
outputs	**F**	$\mathbf{F}=[Fx,Fy]^T$, external loading corresponding to the stable static equilibrium configuration of the manipulator, which are obtained by (5.5)

The above presented numerical results can be confirmed analytically, assuming that both the end-effector displacement (δ_x,δ_y) and the angles $(q_1,q_2,...,q_n)$ are small enough to apply the geometric model linearization. This technique allows us to rewrite the geometric equation (5.1) as

$$\begin{aligned} \delta_x/b &= \sum_{j=1}^{n\text{-}1}\left(\sum_{i=1}^{j}q_i\right)^2+\frac{1}{2}\left(\sum_{i=1}^{n}q_i\right)^2 \\ \delta_y/b &= 2\sum_{j=1}^{n\text{-}1}\left(\sum_{i=1}^{j}q_i\right)+\sum_{i=1}^{n}q_i \end{aligned} \tag{5.6}$$

and to present the Jacobian in the following form

$$\mathbf{J_q}=b\cdot\begin{bmatrix} -\sum_{j=1}^{n}\left(\eta_j\sum_{i=1}^{j}q_i\right) & -\sum_{j=2}^{n}\left(\eta_j\sum_{i=1}^{j}q_i\right) & \cdots & -\sum_{j=n}^{n}\left(\eta_j\sum_{i=1}^{j}q_i\right) \\ 2n-1 & 2n-3 & \cdots & 1 \end{bmatrix}_{2\times n} \triangleq b\cdot\left[\mathbf{S}_1\cdot\mathbf{q}\,\vdots\,\mathbf{S}_0\right]^{\mathrm{T}} \tag{5.7}$$

For example, for n=4 the simplified Jacobian and corresponding matrices $\mathbf{S}_1$, $\mathbf{S}_0$ are expressed as

$$\mathbf{J}_{\mathbf{q}}^{\mathrm{T}} = b \cdot \left[\begin{array}{c:c} -7q_1 - 5q_2 - 3q_3 - q_4 & 7 \\ -5q_1 - 5q_2 - 3q_3 - q_4 & 5 \\ -3q_1 - 3q_2 - 3q_3 - q_4 & 3 \\ -q_1 - q_2 - q_3 - q_4 & 1 \end{array}\right]; \quad \mathbf{S}_1 = -\begin{bmatrix} 7 & 5 & 3 & 1 \\ 5 & 5 & 3 & 1 \\ 3 & 3 & 3 & 1 \\ 1 & 1 & 1 & 1 \end{bmatrix}; \quad \mathbf{S}_0 = \begin{bmatrix} 7 \\ 5 \\ 3 \\ 1 \end{bmatrix} \tag{5.8}$$

The latter allows us to rewrite the static equilibrium equation (5.2) as

$$K_{eq} b^{-1} \cdot \mathbf{q} + \mathbf{S}_1 \mathbf{q} \cdot F_x + \mathbf{S}_0 \cdot F_y = \mathbf{0} \tag{5.9}$$

where $K_{eq} = dMq_i / dq_i$ is the equivalent stiffness of the manipulator rotation joints computed by linearization $Mq_i \approx K_{eqi} \cdot q_i$ of the torque expression (2.3) for $q_i \to 0$ which yields

$$K_{eqi} = \frac{k}{b}\left[2\left(b^2 - a^2\right) - bL^0\right] \tag{5.10}$$

Further, let us assume that δy=0 and combine corresponding constraints obtained from the geometric model (5.6)

$$\begin{bmatrix} 2n-1 & 2n-3 & \dots & 1 \end{bmatrix} \cdot \mathbf{q} \equiv \mathbf{S}_0^{\mathrm{T}} \mathbf{q} = 0 \tag{5.11}$$

with the static equilibrium condition (5.9), which yields the following matrix equation with n+2 unknowns $\mathbf{q} \in \mathbf{R}^n$ and F_x, F_y

$$\begin{bmatrix} \mathbf{S}_1 & \mathbf{0}_{n\times 1} \\ \mathbf{0}_{1\times n} & 0 \end{bmatrix} \cdot \begin{bmatrix} \mathbf{q} \\ F_y \end{bmatrix} \cdot F_x + \begin{bmatrix} K_{eq} b^{-1} \mathbf{I}_{n\times n} & \mathbf{S}_0 \\ \mathbf{S}_0^{\mathrm{T}} & 0 \end{bmatrix} \cdot \begin{bmatrix} \mathbf{q} \\ F_y \end{bmatrix} = \mathbf{0} \tag{5.12}$$

that can be further rewritten in the form

$$\left(\mathbf{A} \cdot F_x + \mathbf{B}\right) \boldsymbol{\nu} = \mathbf{0} \tag{5.13}$$

where

$$\mathbf{A} = \begin{bmatrix} \mathbf{S}_1 & \mathbf{0}_{n\times 1} \\ \mathbf{0}_{1\times n} & 0 \end{bmatrix}; \qquad \mathbf{B} = \begin{bmatrix} K_{eq} b^{-1} \mathbf{I}_{n\times n} & \mathbf{S}_0 \\ \mathbf{S}_0^{\mathrm{T}} & 0 \end{bmatrix}; \qquad \boldsymbol{\nu} = \begin{bmatrix} \mathbf{q} \\ F_y \end{bmatrix} \tag{5.14}$$

It can be easily seen that, the obtained matrix equation (5.13) with unknowns $\boldsymbol{\nu} \in \mathbf{R}^{n+1}$ and F_x is similar to the equation considered in the classical matrix analysis for computing of the matrix eigenvectors and eigenvalues. In fact, it can be proved that the matrix **B** is invertible, i.e. $\det(\mathbf{B}) \neq 0$, so (5.13) can be presented in the standard form as

$$\left(\mathbf{B}^{-1}\mathbf{A} - \lambda \cdot \mathbf{I}\right)\mathbf{v} = \mathbf{0}; \qquad \lambda = -1/F_x \tag{5.15}$$

Hence, the desired critical force F_x^0 for the buckling can be computed using the largest (in absolute value) eigenvalue of the matrix $\mathbf{B}^{-1}\mathbf{A}$

$$F_x^0 = -\left(\max_i |\lambda_i|\right)^{-1} \tag{5.16}$$

which corresponds to the smallest amplitude of the external force F_x ensuring the equilibrium with $\mathbf{q} \neq 0$. For example, for n=4 and $K_{eq}b^{-1} = 1$, relevant computing yields the following eigenvalues

$$\lambda_i \in \{-1.746, -0.734, -0.520, 0, 0\}$$

whose eigenvectors are presented in **Table 1**. It can be also proved that in general case $n \geq 3$, there are exactly n-1 nonzero eigenvalues here, it can be proved by analyzing the roots of polynomial $\det(\mathbf{A} - \lambda\mathbf{B}) = 0$.

Table 6 Nonzero eigenvalues and corresponding eigenvectors of matrix $\mathbf{B}^{-1}\mathbf{A}$ for 4-segment manipulator with the geometric parameters *a/b*=1.0, *L*⁰*/b*=1.0, *k*=1.

	λ	α_1	α_2	α_3	α_4	α_5
#1	-1.746	0.525	-0.227	-0.719	-0.388	-0.075
#2	-0.734	0.352	-0.707	0.162	0.590	-0.050
#3	-0.520	0.124	-0.387	0.589	-0.699	-0.018

Using the obtained eigenvectors $\mathbf{v}_1, ..., \mathbf{v}_{n-1}$ corresponding to the nonzero eigenvalues, it is possible to express the joint variables q_i and the force F_y as

$$q_i = \alpha_i \cdot t, \quad i = 1, ..., n; \quad F_y = \alpha_{n+1} \cdot t \tag{5.17}$$

where α_i are the components of the eigenvector $\mathbf{v} = \left[\alpha_1, ..., \alpha_{n+1}\right]^{\mathrm{T}}$ and t is an arbitrary small number. This presentation allows us to express the manipulator elastostatic energy

$$E_{eq} = K_{eq} \sum q_i^2 / 2$$

in equilibrium configuration as

$$E_{eq} = \frac{1}{2} K_{eq} \sum_{i=1}^{n} \alpha_i^2 \cdot t^2 \tag{5.18}$$

and also to compute from (5.6) the corresponding deflection δx, which yields

$$\delta_x / b = \sum_{j=1}^{n\text{-}1} \left(\sum_{i=1}^{j} \alpha_i \right)^2 t^2 + \frac{1}{2} \left(\sum_{i=1}^{n} \alpha_i \right)^2 t^2 \triangleq \mu_x \cdot t^2 \tag{5.19}$$

The latter allows us to compare the elastostatic energy corresponding to different equilibriums with the same δ_x, which defines the parameters $t = \sqrt{\delta_x b^{-1} \mu_x^{-1}}$ and leads to the following expression for the energy

$$E_{eq} = \frac{\mu_{eq}}{2b} K_{eq} \cdot \delta_x \tag{5.20}$$

where

$$\mu_{eq} = \frac{\sum_{i=1}^{n} \alpha_i^2}{\left(\sum_{j=1}^{n\text{-}1} \left(\sum_{i=1}^{j} \alpha_i \right)^2 + \frac{1}{2} \left(\sum_{i=1}^{n} \alpha_i \right)^2 \right)} \tag{5.21}$$

Table 7 Possible manipulator shapes in static equilibrium after the buckling for n=4.

	$q1$	$q2$	$q3$	$q4$	Geometric shape	Stability	Energy factor μ_{eq}
Case **#1** q1<0	–	+	+	+	U shape: 	stable	1.1447
	–	+	–	+	Z shape: 	unstable	3.8429
	–	+	–	–	ZU shape: 	unstable	2.7272
Case **#2** q1>0	+	–	–	–	U shape: 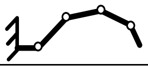	stable	1.1447
	+	–	+	–	Z shape: 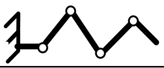	unstable	3.8429
	+	–	+	+	ZU shape: 	unstable	2.7272

Besides, such presentation allows us to express the forces F_x, F_y in the equilibrium neighborhood after buckling as

$$F_x \approx F_x^0, \qquad F_y \approx \frac{\alpha_{n+1}}{\sqrt{b\mu_x}}\sqrt{\delta_x} \tag{5.22}$$

which is in good agreement with Fig. 4.4, where the curve $F_x(\delta_x)$ is quasi-linear and the shape of the curve $F_y(\delta_x)$ follows to the shape of $\sqrt{\bullet}$.

The obtained presentation of the joint angles $q_i = \alpha_i \cdot t$ allows also to evaluate the manipulator shape in the possible equilibrium configurations. As follows from the above, the eigenvector computing for the matrix $\mathbf{B}^{-1}\mathbf{A}$ provides us with *n*-1 different sets of $\{\alpha_1, ..., \alpha_n\}$ corresponding to nonzero eigenvalues. Each of such set yields to two symmetrical equilibriums (one for *t*>0 and another for *t*<0), whose shape can be evaluated by analyzing the signs of α_i. Hence, the total number of the different equilibriums is equal to 2(*n*-1), and two of them providing the minimum of the elastostatic energy (5.20) are globally stable. Example of possible manipulator shapes in static equilibrium after the buckling for *n*=4 are presented in **Table 7**, where similar to the previous chapter (dealing with *n*=3) the "U-shape" is stable and "Z-shape" is unstable. Besides, there is here an additional "ZU-shape" that is also unstable.

5.2 Stiffness analysis of a non-straight configuration

Let us consider now the case when the initial configuration of the *n*-link manipulator is a non-straight one, which corresponds to the non-zero angles ($q_i^0 \neq 0,\ i = 1, 2, ..., n$) and the initial end-point location $(x_0, y_0) = (2n \cdot b - \Delta x, 0)$ with $\Delta x > 0$. Similar to the previous chapters, it is assumed that the corresponding control inputs $(L_{i1}^0, L_{i2}^0)\ i = 1, 2, .., n$ are computed from expression (2.31), where $L_{i1}^0 = L^0 - \Delta_i$, $L_{i2}^0 = L^0 + \Delta_i$ and $L^0 = b$. It is clear that if $n \geq 3$ this manipulator is redundant with respect to the end-effector location control in the (*x*, *y*)-plane. So, for given (x_0, y_0) the configuration angles q_i^0 cannot be computed in a unique way. For this reason, we will consider two typical initial shapes of the manipulator, which were previously referred to as the U-shape and Z-shape (**Section 4.2**).

Table 8 Different initial configurations of the manipulator for the end-point location (x_0, y_0) = (7.7*b*, 0).

	Initial shape	Initial configuration angles			
		*q*1	*q*2	*q*3	*q*4
Case #**1**	U-shape: 	–0.3093	+0.1348	+0.4246	+0.2288
Case #**2**	Z-shape: 	–0.1136	+0.3768	–0.6242	+0.7869

Examples of such initial shapes for n=4 are presented in **Table 8**, their elastostatic properties will be carefully studied below.

First, let us investigate the force-deflection relations $F_x(\delta x)$ and $F_y(\delta x)$ corresponding to the end-effector displacement with $\delta y = 0$, i.e. from the initial location $(x_0, y_0) = (2n \cdot b - \Delta x, 0)$ to the current one $(x, y) = (2n \cdot b - \Delta x - \delta x, 0)$ where δx is the end-effector deflection caused by the external forces (F_x, F_y) and Δx denotes the initial displacement of the end-effector. Similar to the **Section 4.1**, let us apply the energy method allowing us to find possible equilibrium configurations corresponding to the given δx. In this case, the geometric constraint coming from the given end-effector location can be presented in the form

$$\begin{aligned} b + 2b\sum_{j=1}^{n\text{-}1}\left(\cos(\sum_{i=1}^{j} q_i)\right) + b\cos(\sum_{i=1}^{n} q_i) &= 2n \cdot b - \Delta x - \delta_x \\ 2b\sum_{j=1}^{n\text{-}1}\left(\sin(\sum_{i=1}^{j} q_i)\right) + b\sin(\sum_{i=1}^{n} q_i) &= 0 \end{aligned} \qquad (5.23)$$

allowing us to reduce the number of variables in the energy function $E(q_1, q_2, \ldots q_{n-2})$ by applying the 2-link manipulator inverse kinematics to compute the remaining angles (q_{n-1}, q_n). Further, by detecting the max/min and saddle points of the function $E(q_1, q_2, \ldots q_{n-2})$ it is possible to find the configuration angles for all possible equilibriums, to evaluate their stability and compute the external forces (F_x, F_y) corresponding to the end-effector deflection δx from (5.5).

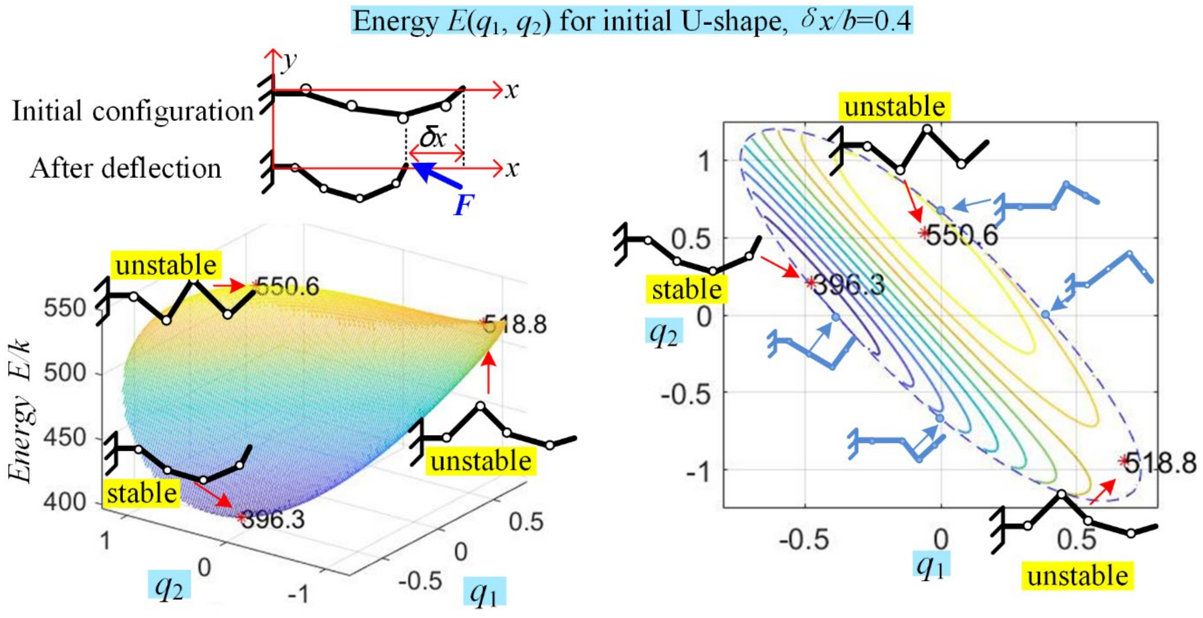

Fig. 5. 5: The energy function $E(q_1, q_2)$ and manipulator equilibriums of initial U-shape configuration (end-effector deflection $\delta x/b$=0.4, δy=0; geometric parameters a/b=1.0; $q4$>0).

Examples of such computations for n=4 are presented in **Figs 5.5, 5.6** and **5.7,** where the end-

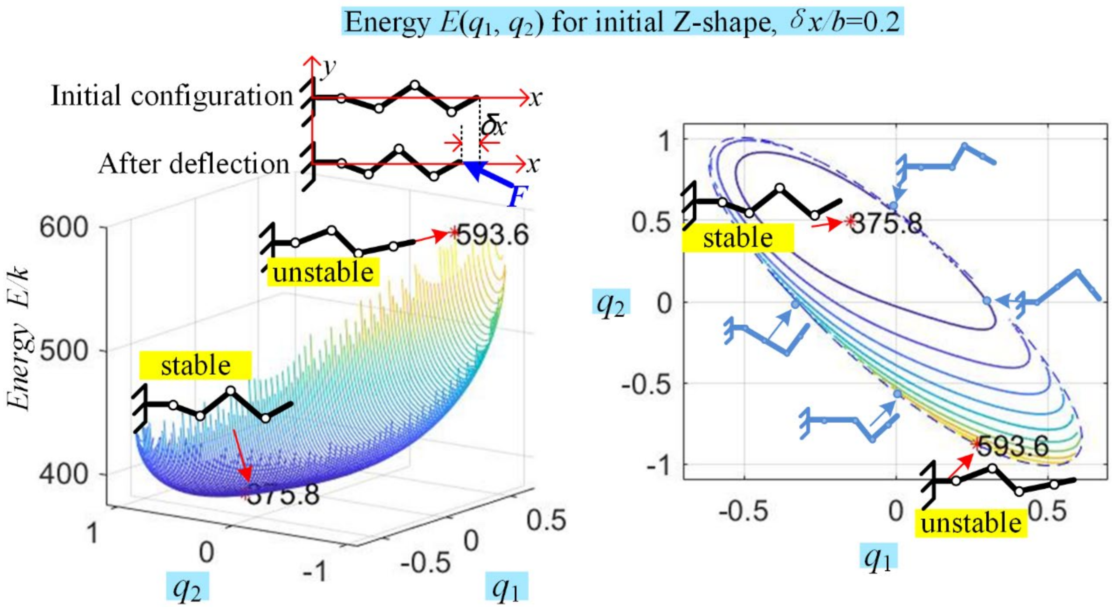

Fig. 5. 6: The energy function $E(q_1, q_2)$ and manipulator equilibriums of initial Z-shape configuration (end-effector deflection $\delta x/b$=0.2, δy=0; geometric parameters a/b=1.0; $q4$>0).

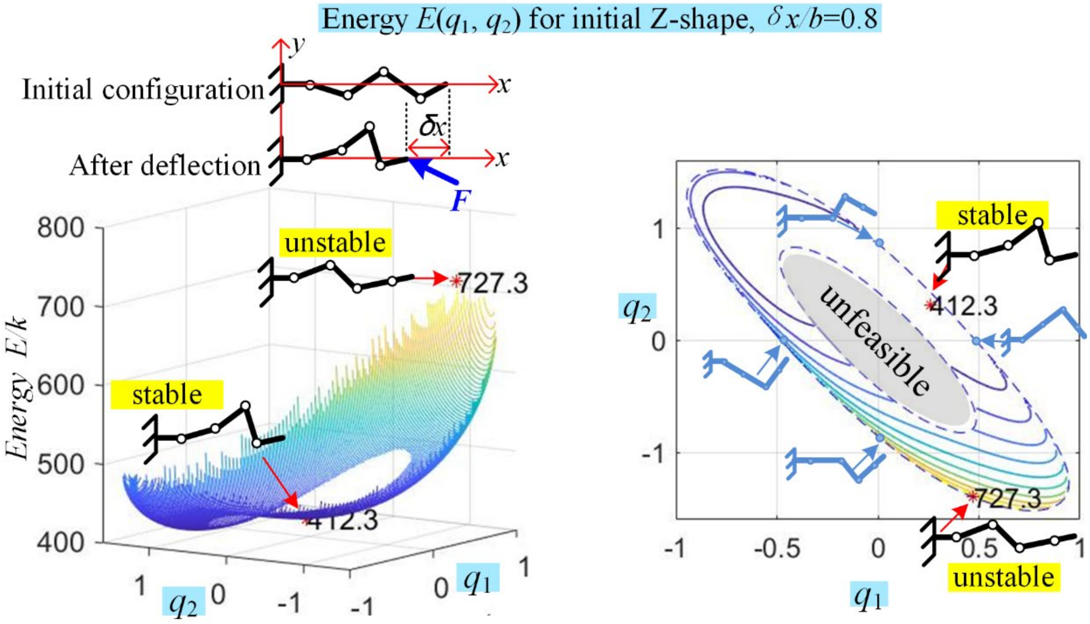

Fig. 5. 7: The energy function $E(q_1, q_2)$ and manipulator equilibriums of initial U-shape configuration (end-effector deflection $\delta x/b$=0.8, δy=0; geometric parameters a/b=1.0; $q4$>0).

effector elastic deflection is $\delta x \in \{0.2b, 0.4b, 0.8b\}$ and the initial shapes correspond to $\Delta x = 0.3b$ (see **Table 8**). As follows from these figures, for the initial U-shape the energy surfaces $E(q_1, q_2)$ are similar to ones presented in **Fig. 5. 5b**. In particular, all these surfaces contain a single maximum, a single minimum and a single saddle point. Also, their evolution with respect to δx is continuous, their topology remains the same while increasing the deflection δx. In contrast, for the initial Z-shape, the energy surfaces $E(q_1, q_2)$ are quite different, their evolution with respect to δx is discontinuous. The latter leads to sign-changing of some configuration angles q_i under the external loading F as shown **Fig. 5. 6** (see angle q_1 for instance). Besides, if the deflection δx is big enough as in **Fig. 5. 7**, the energy surfaces may contain a "hole", i.e. an unfeasible area, caused by violation of the geometric constraints $|q_i| \le q_i^{\max}$ (2.27) inside of the manipulator segments (see **Section 2.3**).

By applying the above presented energy method and computing minimums of the energy function $E(q_1, q_2, ... q_{n-2}) \rightarrow \min$ for different δx, it is possible to obtain the desired force-deflection relations $F_x(\delta x)$ and $F_y(\delta x)$. It is clear that these minimums correspond to the stable equilibriums that are observed in practice. Examples of such computations for n=4 are presented in **Fig. 5. 8** and **Fig. 5. 9**.

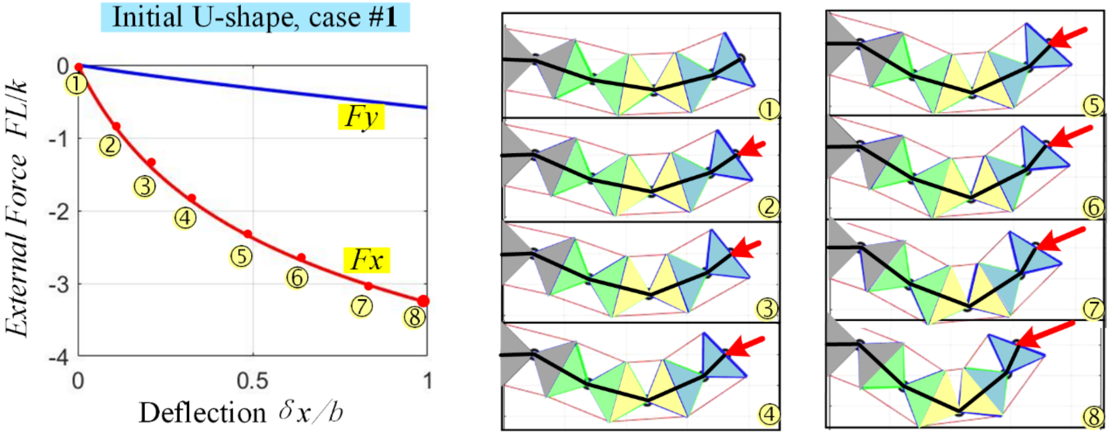

Fig. 5. 8: Force-deflection curves $F_x(\delta x)$, $F_y(\delta x)$ and manipulator shape changing under the loading for initial U-shape with $(x_0, y_0) = (7.7b, 0)$, geometric parameters a/b=1.0 and δy=0.

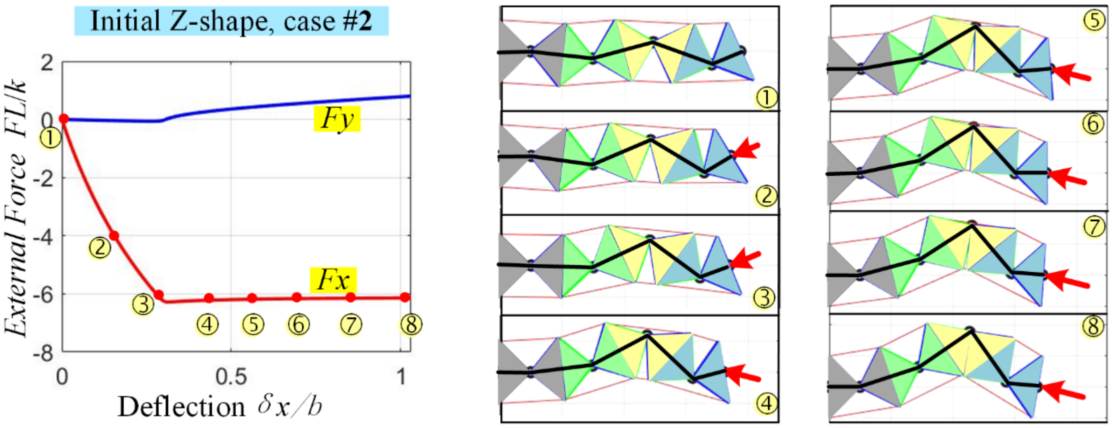

Fig. 5. 9: Force-deflection curves $F_x(\delta x)$, F_y (δx) and manipulator shape changing under the loading for initial Z-shape configuration with $(x_0, y_0) = (7.7b, 0)$, geometric parameters a/b=1.0 and δy=0.

For the initial U-configuration, the change of the manipulator shape is smooth, the resistance of the manipulator is gradually increasing while the deflection δx becomes bigger. However, the stiffness coefficient in the *x*-direction is continuously decreasing. This tendency is observed until the manipulator reaches its geometric constraints. In contrast, for the initial Z-configuration, there are two intervals of the manipulator deformation. At the beginning when δx is relatively small the manipulator maintains its Z-shape and the resistance against the external force is monotonically increasing, similar to the previous case. Further, when the deflection δx is bigger than some critical value, the buckling phenomenon is occurring, and the manipulator resistance against the external force is not increasing any more. Correspondingly, the stiffness coefficient dF_x/dx becomes very small, the stiffness coefficient dF_y/dx changes its sign and the manipulator does not keep its initial Z-shape (some of the angles q_i change the signs). Finally, after the buckling, the manipulator moves in the direction of its internal geometric constraints. Some more details concerning evolution of the manipulator shape and its stiffness coefficients under the loading for both *x*- and *y*-directions are presented in **Table 9**.

Table 9: Evolution of the manipulator shape under the loading for δx=*var*, δy=0.

	Initial shape	Stiffness coefficients and shape under the loading	
Case #1	U-shape:  $\begin{pmatrix}x_0\\y_0\end{pmatrix}=\begin{pmatrix}7.7b\\0\end{pmatrix}$	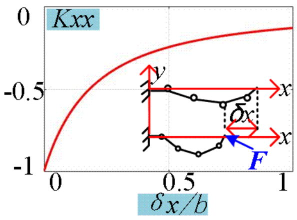	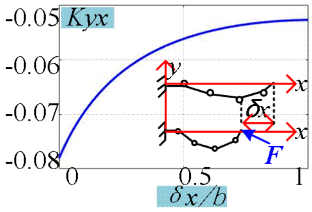
Case #2	Z-shape:  $\begin{pmatrix}x_0\\y_0\end{pmatrix}=\begin{pmatrix}7.7b\\0\end{pmatrix}$	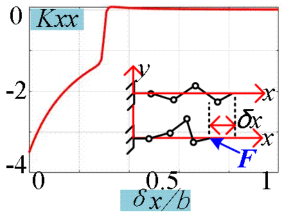	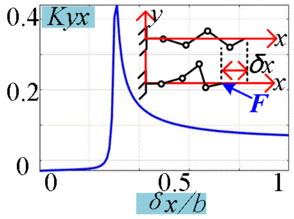

Hence, in practice, it is preferable to use the U-shape if the workspace obstacles (external constraints) allows. It should be also noted that for the Z-shape it is necessary to avoid high loadings exceeding the critical force causing buckling.

Now, in addition to the above presented force-deflection relations $F_x(\delta x)$ and $F_y(\delta x)$ derived from the assumption of $\delta x = \text{var}\,, \delta y = 0$, let us analyze the changing of the manipulator stiffness coefficients under the loading (F_x, F_y) without imposing any kinematic constraints of the end-effector location. To obtain the desired relations it is necessary to compute the configuration angles $(q_1,...,q_n)$ corresponding to the manipulator equilibriums for different given external loading $\left(F_x, F_y\right)$. It is clear that these angles can be found numerically by solving system of *n* independent equations (5.2) describing the static equilibrium condition (by applying Newton's method for instance). However, the initial guess of the angles $(q_1^0,...,q_n^0)$ should be evaluated correctly, to ensure that they are in the neighborhood of the minimum energy configuration, because only such cases can be observed in practice. Such initial guess can be obtained using the above presented energy method applied in the space $(q_1,...,q_n)$ with rather rough grid with large step. Also the desired angles corresponding to the external loading $\left(F_x, F_y\right)$ can be found using the Matlab function *fminsearch* which minimizes the sum of the squared residuals i.e.

$$\left(q_1,...,q_n\right) = fminsearch\left(\left\| \left[\mathbf{M_q}\right]_{n\times 1} + \left[\mathbf{J}_\mathbf{q}^{\mathrm{T}}\right]_{n\times 2} \cdot \begin{bmatrix} F_x \\ F_y \end{bmatrix} \right\|^2\right) \tag{5.24}$$

where both the internal torques $\mathbf{M_q}$ and the Jacobian $\mathbf{J_q}$ depend on the angles $(q_1,...,q_n)$. It should be also mentioned that it is possible to simplify the problem of the initial guess $(q_1^0,...,q_n^0)$ selection by gradually increasing the forces $\left(F_x, F_y\right)$ and using solutions from the previous loaded equilibrium as the initial guess for the next one corresponding to $\left(F_x + \Delta F_x, F_y + \Delta F_y\right)$. However, when the forces $\left(F_x, F_y\right)$ approach the buckling point, the initial guess from the previous step is not suitable because the configuration angles are changing essentially and only the straightforward energy method allows to obtain the correct initial guess.

Further, when the equilibrium configuration angles $(q_1,...,q_n)$ corresponding to the given forces $\left(F_x, F_y\right)$ are computed, it is possible to find the desired stiffness coefficients using the formula (4.31) from the previous chapter

$$\mathbf{C_F} = \mathbf{J_q}\left(\mathbf{K_q} - \mathbf{K_g}\right)^{-1}\mathbf{J}_\mathbf{q}^{\mathrm{T}}; \qquad \mathbf{K_F} = \left[\mathbf{J_q}\left(\mathbf{K_q} - \mathbf{K_g}\right)^{-1}\mathbf{J}_\mathbf{q}^{\mathrm{T}}\right]^{-1} \tag{5. 25}$$

where the $n\times n$ matrix of the joint elastic stiffness coefficients $\mathbf{K_q} = diag(K_{eq1},...,K_{eqi})$ can be computed similarly as in the **Section** 2.2.

$$K_{eqi} = 2k\left(b^2 - a^2\right)\cos q_i - k\left(\frac{L_{i1}^0 + L_{i2}^0}{2} b\cdot\cos\frac{q_i}{2} - \frac{L_{i1}^0 - L_{i2}^0}{2} a\cdot\sin\frac{q_i}{2}\right), \; i = 1,2,...,n \tag{5. 26}$$

It should be stressed that here, the control inputs L_{i1}^0 and L_{i2}^0 are constant values, which correspond to the initial unloaded joint angles q_i. The second matrix $\mathbf{K_g}$ containing the stiffness coefficients caused by the loading is symmetrical and can be computed as follows

$$\mathbf{K_g} \triangleq \frac{\partial \mathbf{J}^{\mathrm{T}}}{\partial q_i}\mathbf{F} = \begin{bmatrix} -J_{21}F_x + J_{11}F_y & -J_{22}F_x + J_{12}F_y & \cdots & -J_{2n}F_x + J_{1n}F_y \\ \cdots & -J_{22}F_x + J_{12}F_y & \cdots & -J_{2n}F_x + J_{1n}F_y \\ \cdots & \cdots & \cdots & \cdots \\ \cdots & \cdots & \cdots & -J_{2n}F_x + J_{1n}F_y \end{bmatrix}_{n\times n} \tag{5. 27}$$

It is obviously that when the external forces are equal to zero $F=(0,0)$, the stiffness matrix expression is reduced to the form, which is known from the unloaded mode analysis

$$\mathbf{K} = \left[\mathbf{J_q}\mathbf{K_q^{-1}}\mathbf{J_q^{\mathrm{T}}}\right]^{-1} \tag{5. 28}$$

It should be also mentioned that, in contrast to the classical n-link serial manipulators, here the diagonal matrix $\mathbf{K_q}$ is configuration dependent (not constant) because each initial configuration with the angles $(q_1,\ldots,q_n)$ produces its own control inputs L_{i1}^0 and L_{i2}^0 included in the expression (5.29). Besides, similarly to the **Section 4.2**, here the unloaded compliance matrix $\mathbf{C}_0$ can be expressed analytically in the following way

$$\mathbf{C}_0 = \mathbf{J_q}\mathbf{K_q^{-1}}\mathbf{J_q^{\mathrm{T}}} = \begin{bmatrix} \dfrac{J_{11}^2}{K_{q1}} + \dfrac{J_{12}^2}{K_{q2}} + \ldots + \dfrac{J_{1n}^2}{K_{qn}} & * \\ * & \dfrac{J_{21}^2}{K_{q1}} + \dfrac{J_{22}^2}{K_{q2}} + \ldots + \dfrac{J_{2n}^2}{K_{qn}} \end{bmatrix} \tag{5. 29}$$

Further, to illustrate practical importance of the above presented results, they were applied to the case n=4 assuming that the initial (unloaded) end point location is $(x_0, y_0) = (7.7b, 0)$, and the initial shape is either U- or Z- one. The configuration angles under the loading, corresponding to the external force $F = (F_x, F_y)$, were computed numerically using the technique proposed above. Relevant results of the initial U-shape and Z-shape are presented in **Fig. 5. 10** and **Fig. 5. 11** respectively.

As follows from these figures, the manipulator stiffness essentially changes if the external loading is applied. For the initial U-shape case, the absolute value of the manipulator stiffness coefficient $|K_{\mathrm{xx}}|$ decreases first, while the force F_{x} is increasing (see **Fig. 5. 10a**), until F_{x} is reaching some critical value when $|K_{\mathrm{xx}}|$ is the minimum, then it begins to increase slowly. In contrast, the stiffness coefficient K_{xy} (describing the manipulator reaction in the y-direction) changes its sign under the loading. These stiffness properties can be also interpreted from the geometrical and physical point of view, using the right-hand side of the **Fig. 5. 10a**, which shows the evolution of the manipulator configuration under the loading. In general, such manipulator behavior can be treated as "*quasi-buckling*", because for certain loading F_{x} the stiffness in both x- and y-direction is very small. And the manipulator rotates quickly until one of the segment goes close to its joint limits, where the equivalent rotational stiffness coefficient is very low. Hence, in practice it is necessary to avoid applying too high loading in x-direction causing approaching either to the "*quasi-buckling*" or the joint limits and losing the manipulator stiffness.

(*a*) $Fx = var, \quad Fy = 0$

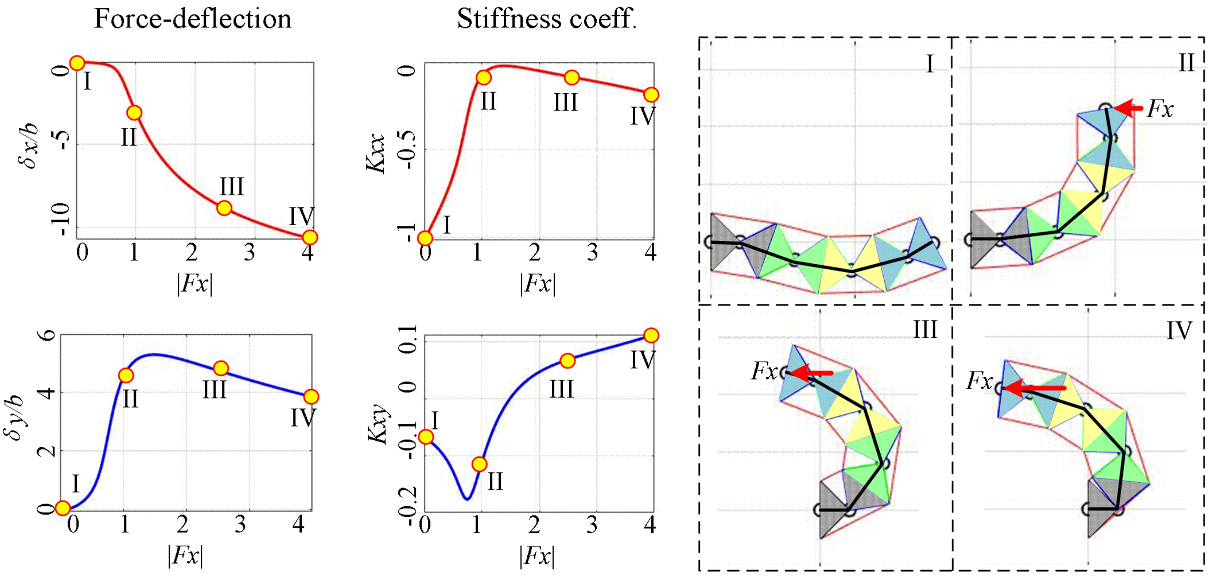
Force-deflection

Stiffness coeff.

(*b*) $Fx = 0, \quad Fy = var$

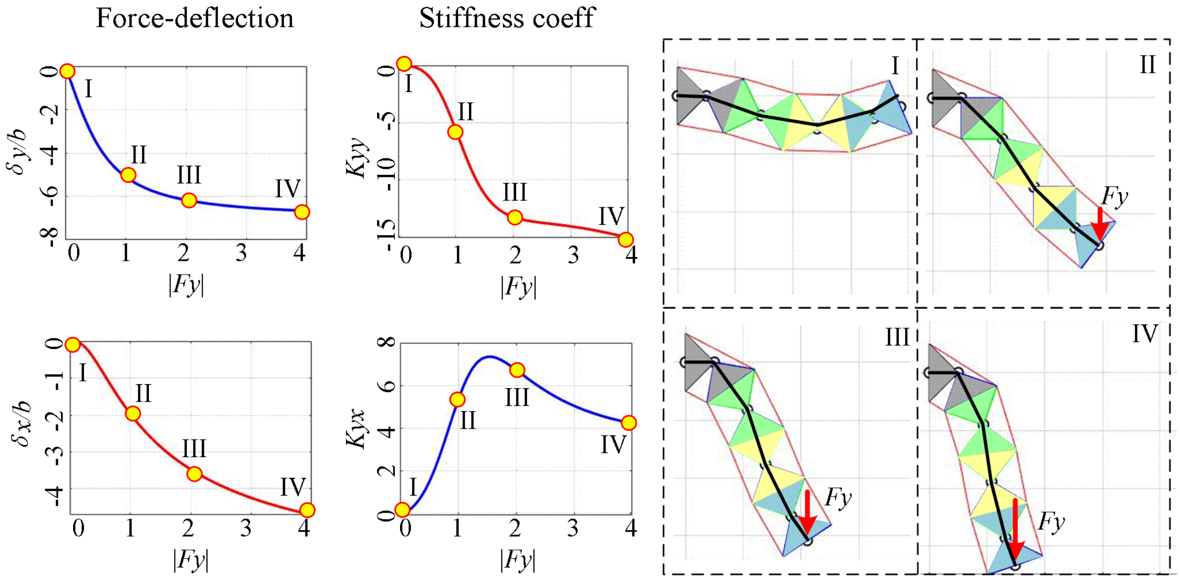
Force-deflection

Stiffness coeff

Fig. 5. 10: Stiffness coefficients under the F_x- and F_y-loading for initial U-shape configuration with $(x_0, y_0) = (7.7b, 0)$ and geometric parameters a/b=1.0

On the other side, while increasing the force F_y (i.e. in the orthogonal direction), the absolute value of the stiffness coefficient $|K_{yy}|$ is monotonically increasing first, then it keeps the same tendency slowly (see **Fig. 5. 10b**) because of the restriction of the geometric length of the manipulator. At the same time, the stiffness coefficient K_{yx} demonstrates non-monotonic behavior. Such performance can be seen from the evolution of the manipulator configuration at the right-hand side of **Fig. 5. 10b**, where the manipulator end-point moves towards the extreme location, as far as possible from the initial one.

Therefore, the high loading in *y*-direction should be also avoided, to prevent from the manipulator changing its shape change to a pure straight line (see case IV).

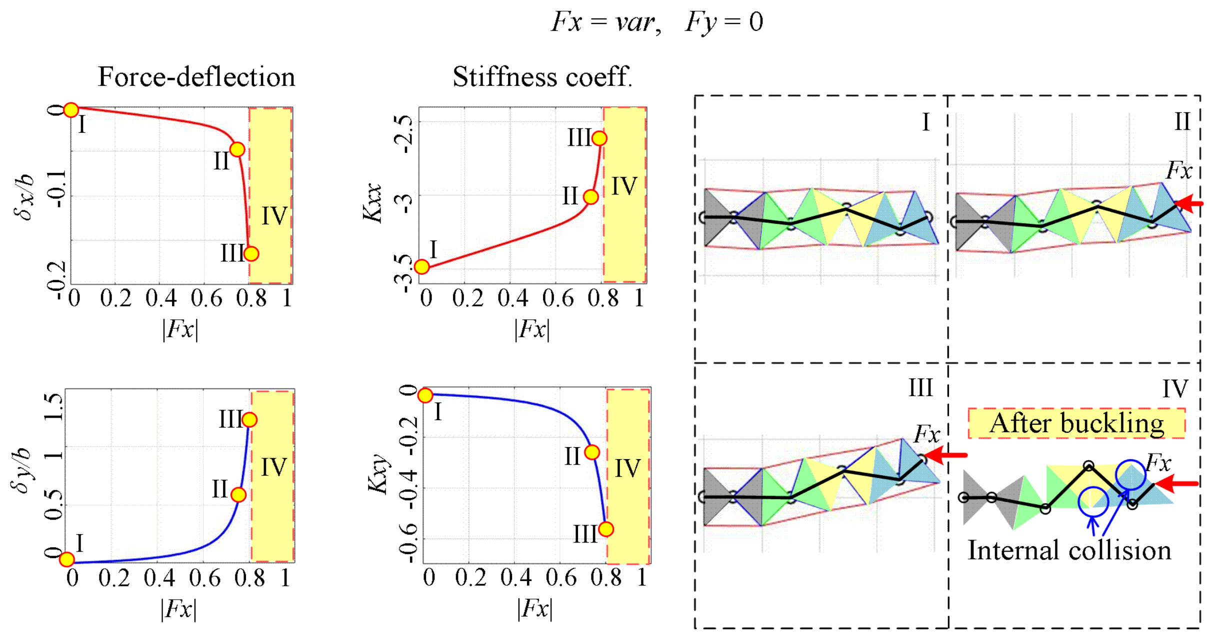

Fig. 5. 11: Stiffness coefficients under the F_x-loading for initial Z-shape configuration with $(x_0, y_0) = (7.7b, 0)$ and geometric parameters a/b=1.0

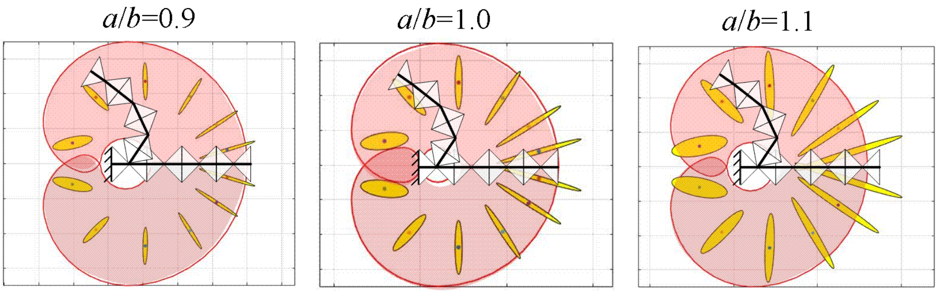

Fig. 5. 12: Unloaded stiffness ellipses of the four-segment manipulator inside the workspace.

However, for the second case study dealing with the initial Z-shape, the stiffness properties under the loading are quite different compared to the U-shape case. In particular, as follows from **Fig. 5. 11**, under the F_x-loading, the absolute value of the stiffness coefficient $|K_{xx}|$ decreases gradually at the beginning, then it decrease quickly to zero. In contrast, the absolute value of the stiffness coefficient $|K_{xy}|$ increases monotonically. This phenomenon can be also treated as *"quasi-buckling"* because for certain loading the manipulator stiffness in *x*-direction is equal to zero, and the stiffness in *y*-direction is very high. These results are illustrated geometrically by the right-hand side of **Fig. 5. 11** showing the evolution of the manipulator configuration under the F_x –loading. It is clear that here each segment of the manipulator tends to move close to its geometric limits before the *"quasi-buckling"* is occurring. In such configuration, even quite small change of the external force may lead to large manipulator deflection, so in practice, it is reasonable to avoid such situations. It is worth mentioning that the case of F_Y –loading is not presented in **Fig. 5. 11**, because it is quite similar to the U-shape case.

Similar to the previous chapters, the stiffness properties of the unloaded manipulator may be also illustrated by the set of ellipses describing mapping of the unit force $\|F\|=1$ into the deflection $(\delta x,\delta y)$. An example of such analysis for the case of *n*=4 is presented in **Fig. 5. 12**, which shows that the resistance of the four-segment manipulator to the external force in the longitudinal direction is much higher than in the transverse one. Also, the mechanism longitudinal stiffness essentially increases while the initial configuration becomes closer to the straight one.

5.3 Controlling mechanism configurations

To control motions of the considered multi-segment mechanism it is necessary to develop special technique that allows user to achieve two goals: (**i**) *minimize the redundant joint motions while ensuring the desired end-effector location*; (**ii**) *ensure safe distances between the manipulator segments and the obstacles located inside of the workspace*. The first of these problems, the *redundancy resolution*, was considered in detail in previous section 3.3, which demonstrate that the most attractive computation technique is based on local *minimization of square sum of the joint angle increments* $\Delta\mathbf{q}$.

$$\sum_{i=1}^{n}\Delta\mathbf{q}_i^{\mathrm{T}}\cdot\Delta\mathbf{q}\rightarrow\min_{\Delta\mathbf{q}} \tag{5. 30}$$

subject to the geometric constraint

$$\Delta\mathbf{p}=\mathbf{J}\cdot\Delta\mathbf{q} \tag{5. 31}$$

where $\Delta\mathbf{p}$ is the desired end-effector displacement (small enough to apply the linearization) , $\mathbf{J}$ is the kinematic Jacobian corresponding to the current manipulator configuration $\mathbf{q}$. As it was proved before, the solution of this constraint optimization problem can be easily found analytically, by means of the Jacobian pseudo-inverse

$$\Delta\mathbf{q}=\mathbf{J}^{\mathrm{T}}\left(\mathbf{J}\mathbf{J}^{\mathrm{T}}\right)^{-1}\Delta\mathbf{p} \tag{5. 32}$$

which gives obviously advantages compared to alternative approaches based on minimization of the sum or absolute value of the increments Δq_i (see expressions (3.32) and (3.33) from the previous chapter). It should be mentioned that this technique is suitable for redundancy resolution for both two- and three-dimensional task spaces (x,y) and (x,y,φ) considered above, which create redundancies of order *n*-2 and *n*-3 respectively.

The second problem dealing with the workspace *obstacle avoidance* can be also divided in two steps: (a) collision-free path planning for the manipulator end-effector; (b) collision-free path planning for the manipulator body, i.e. intermediate segments. Let us consider them consecutively.

To find the best ***collision-free path for the end-effector*** let us apply the discrete dynamic programming technique allowing to generate the shortest trajectory in the task space, which connects the initial and target points $\mathbf{p}^0$, $\mathbf{p}^g$ while avoiding the given obstacles. To apply this technique, let us discretize first the task space (x, y) and present it as a two-dimensional set of nodes defined in the following way

$$\mathbf{L}(i,j) = \left(x^0 + \Delta x \cdot j,\ y^0 + \Delta y \cdot i\right), \quad i = 0,1,...m, j = 0,1,...n \tag{5. 33}$$

Δx, Δy are the discretization steps such that the index j=0 corresponds to the initial point $\mathbf{p}^0$ and the index j=n corresponds to the target point $\mathbf{p}^g$, i.e. $x^g = x^0 + \Delta x \cdot n$. Using such presentation the desired trajectory can be presented as the sequence of the nodes

$$\mathbf{L}(i_0,0) \to \mathbf{L}(i_1,1) \to ... \to \mathbf{L}(i_{n-1},n-1) \to \mathbf{L}(i_n,n) \tag{5. 34}$$

with the purely geometric definition of the distances between the successive nodes as

$$dist\left\{\mathbf{L}(i,j),\ \mathbf{L}(i',j+1)\right\} = \sqrt{\Delta y^2 \cdot (i'-i)^2 + \Delta x^2} \tag{5. 35}$$

To take into account possible collisions between the robot end-effector and the workspace obstacles, let us also define the binary matrix **B** of size $m \times n$ whose elements $\mathbf{B}(i,j) \in \{0,\ 1\}$ are equal to zero if there is no collision between the manipulator end-effector and the workspace obstacles at the node $\mathbf{L}(i,j)$, (otherwise, it is equal to one). It is worth mentioning that the above presentation neglects the robot end-effector dimensions and presents it as a point. For this reason, while computing the matrix **B** it is reasonable to modify slightly the obstacle models and increase their dimensions by the value of $\sqrt{a^2+b^2}$, where a, b are the geometric parameters of the manipulator segments (see **Fig 2.5**).

Such formalization operating with the discretized task space $\{\mathbf{L}(i,j)\}$, which includes the obstacles defined by the binary matrix **B**, allows us to present the original problem of the collision-free path planning for the manipulator end-effector as the classical shortest-path searching on the graph:

find the optimal path (5.34) on the graph connecting adjacent columns of $\{\mathbf{L}(i,j)\}$, which (i) connects the given nodes $\mathbf{L}(i_0,0)$ and $\mathbf{L}(i_n,n)$, (ii) passes through allowable nodes only $\mathbf{B}(i,j)=0$ and (iii) satisfies the optimization criterion

$$\sum_{j=0}^{n-1} dist\left\{\mathbf{L}(i_j,j),\ \mathbf{L}(i_{j+1},j+1)\right\} \to \min_{\{i\}} \tag{5. 36}$$

It should be noted that the desired trajectory is defined by the sequence of the row indices $\{i_0, i_1, ..., i_n\}$, where both i_0 and i_n are given (they are defined by the initial and target points). It is clear that the above shortest-path problem can be solved via the discrete dynamic programming that is based on the following expression

$$d^*_{j+1}(i') = \min_i \left\{ d^*_j(i) + dist\left\{ \mathbf{L}(i,j),\ \mathbf{L}(i', j+1) \right\} \right\},\ \forall i' = 0,1,...,m \tag{5. 37}$$

where $d^*_j(i)$ denotes the shortest distance between the initial node $\mathbf{L}(i_0,0)$ and the node $\mathbf{L}(i,j)$ corresponding to the optimization of the lower dimension ($j \le n$). This expression is applied sequentially starting from j=1 and ending with j=n-1, and memorizing the row indices $\{i^*_1, ..., i^*_{n-1}\}$ obtained form (5.40), and corresponding to all intermediate optimal paths. At the final step, a single node $\mathbf{L}(i^*_n, n)$ corresponding to the desired endpoint is selected, and the desired solution is obtained through the backtracking allowing to find the remaining row indices $\{i^*_1, ..., i^*_{n-1}\}$ describing the optimal path.

Table 10 Optimal path searching algorithm for the robot end-effector based on the discrete dynamic programing

Inputs	$\mathbf{L}(i,j)$	$m \times n$ matrix of point locations in task space
	i_0	row index defining the initial point location $\mathbf{L}(i_0,0)$
	i_n	row index defining the target point location $\mathbf{L}(i_n,n)$
	$\mathbf{B}(i,j)$	$m \times n$ binary matrix describing the obstacle locations: B(i,j)=1 denotes the point $\mathbf{L}(i,j)$ inside of the obstacle
Outputs	**indP**(j)	Vector of optimal row indices $\{i_0, i_1, ..., i_n\}$ describing the collision-free shortest path between the initial point $\mathbf{L}(i_0,0)$ and the target point $\mathbf{L}(i_n,n)$
	optP	Length of the shortest collision-free path connecting the initial point $\mathbf{L}(i_0,0)$ and the target point $\mathbf{L}(i_n,n)$
Local variables	**Path**(i,j)	$m \times n$ matrix of the minimum optimal sub-paths lengths connecting the initial point $\mathbf{L}(i_0,0)$ and an arbitrary intermediate target point $\mathbf{L}(i,j)$
	ind(i,j)	$m \times n$ matrix of the previous row indices for the optimal sub-paths connecting the initial point $\mathbf{L}(i_0,0)$ and an arbitrary point $\mathbf{L}(i,j)$
	dst(i)	Vector, containing the shortest sub-paths lengths of connecting the initial point $\mathbf{L}(i_0,0)$ and an arbitrary intermediate target point $\mathbf{L}(i,j)$

	Dst(i)	Internal vector containing the lengths for all possible sub-paths between the initial point $\mathbf{L}(i_0,0)$ and an arbitrary intermediate point $\mathbf{L}(i,j)$
	$optPij$	Element of $\mathbf{Path}(i,j)$
	ind_optPij	Element of $\mathbf{ind}(i,j)$
	$delta$	Distance increment between the points $\mathbf{L}(i,j)$ and $\mathbf{L}(i',j+1)$ computed using the function $dist(\_,\_)$

(1)Path searching

```
$\mathbf{ind} := \text{zeros}(m,n)$;   $\mathbf{Path} := \text{zeros}(m,n)$;   $\mathbf{dst} := \lceil dist\{\mathbf{L}(i_0,0),\ \mathbf{L}(i,1)\}\rceil_{m\times1}$,  $\forall i$;
For  $j$ = 1 to $n$-1;
    For  $i$ = 1 to $m$;
        If  B($i$,$j$+1) = 1
        $delta := NaN$;
        Else
            $\mathbf{Dst} := \text{zeros}(m,1)$
            For  $k$ = 1, $m$;
                    If  B($k$,$j$) = 0
                    $delta := dist\{\mathbf{L}(k,j),\ \mathbf{L}(i,j+1)\}$;
                    Else
                    $delta := NaN$;
                    End
            $\mathbf{Dst}(k) := \mathbf{dst}(k) + delta$;
            End
        $[optPij, ind\_optPij] := \min(\mathbf{Dst})$;   $\mathbf{ind}(i,j) := ind\_optPij$;   $\mathbf{Path}(i,j) := optPij$;
        End
    End
    $\mathbf{dst} =: \mathbf{Path}(:,j)$;

End
$optP := \mathbf{ind}(i_n,n)$
```

(2)Backtracking

```
$\mathbf{indP} := \text{zeros}(n-1,1)$;   $i\_\text{target} := i_n$;
For  $j$ = 1 to $n$-1

    $i\_\text{target} := \mathbf{ind}(i_{\text{target}}, n-j)$;
    $\mathbf{indP}(n-j) := i\_\text{target}$;

End
```

More detailed description of the develop algorithm is presented in **Table 10**, it consists of two main sections. The first section implements the dynamic programming technique described by (5.40), by applying it sequentially to the problems of order 2, 3, … , *n*. This allows us to find a number of optimal sub-paths connecting the given initial point $\mathbf{L}(i_0,0)$ and an arbitrary intermediate target point $\mathbf{L}(i,j)$. Corresponding shortest sub-path lengths are stored in the matrix $\mathbf{Path}(i,j)$, while the matrix $\mathbf{ind}(i,j)$ contains the pointers to the previous optimal nodes. By repeating this procedure and increasing the second index up to $j = n$, the desired optimal solution is obtained that corresponds to the collision-free shortest path connecting the points $\mathbf{L}(i_0,0)$ and $\mathbf{L}(i_n,n)$. This solution is extracted from the matrices $\mathbf{Path}(i,j)$ and $\mathbf{ind}(i,j)$ as the second stage by applying the backtracking: $i_{n-1} = \mathbf{ind}(i_n,n)$, $i_{n-2} = \mathbf{ind}(i_{n-1},n-1)$, … .

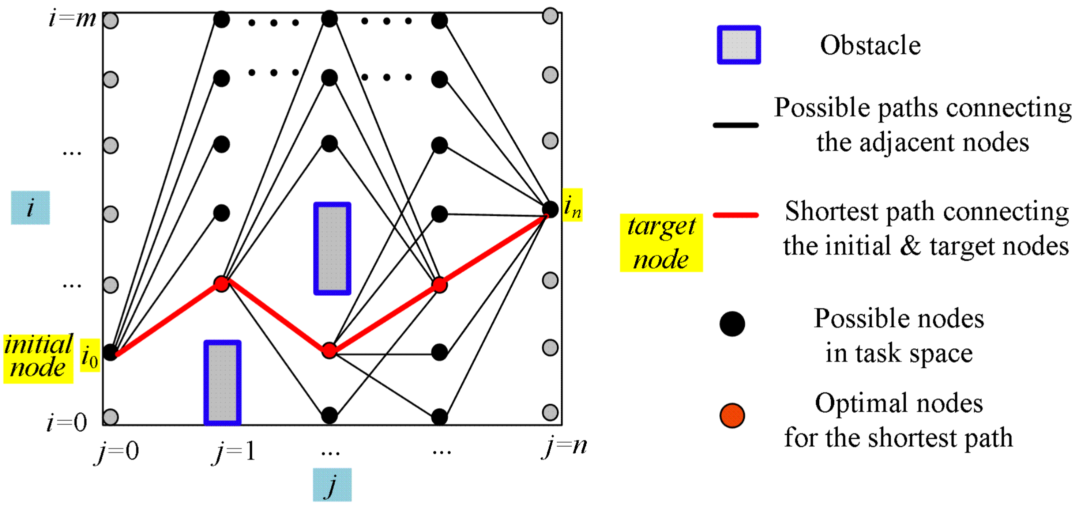

Fig. 5. 13: Generation of obstacle-free path using graph-base presentation of the task space and discrete dynamic programming

Geometric explanation of this technique is given as in **Fig. 5. 13**, where it is assumed that the spatial location of the initial and target points corresponds to the motion "from left to right". It is clear that all other type of motions can be easily found by applying slightly different task space discretization as shown in **Fig. 5. 14**.

Efficiency of this technique has been confirmed by the simulation study. An example of obstacle-free path generation with discretization of 20×20 is presented in **Fig. 5. 15**. It should be mentioned that here, to take into account the end-effector size, the obstacles were slightly increased. As follows from this study, for such relatively rough discretization the algorithm is very fast (it took only 46ms to find the optimal solution for this case). However, for finer discretization the computing time may increase essentially. To over this difficulty, a two-step modification of the path-generation algorithm was also proposed.

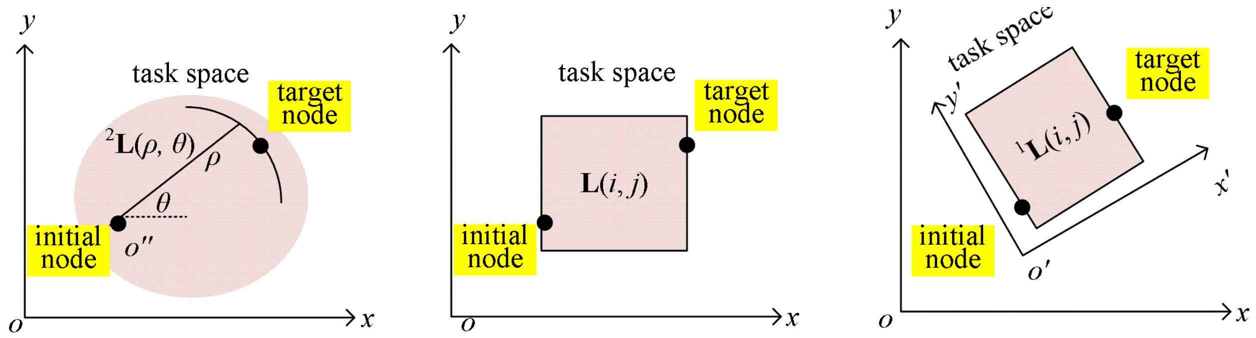

Fig. 5. 14: Task space coordinate transformation for the discretization.

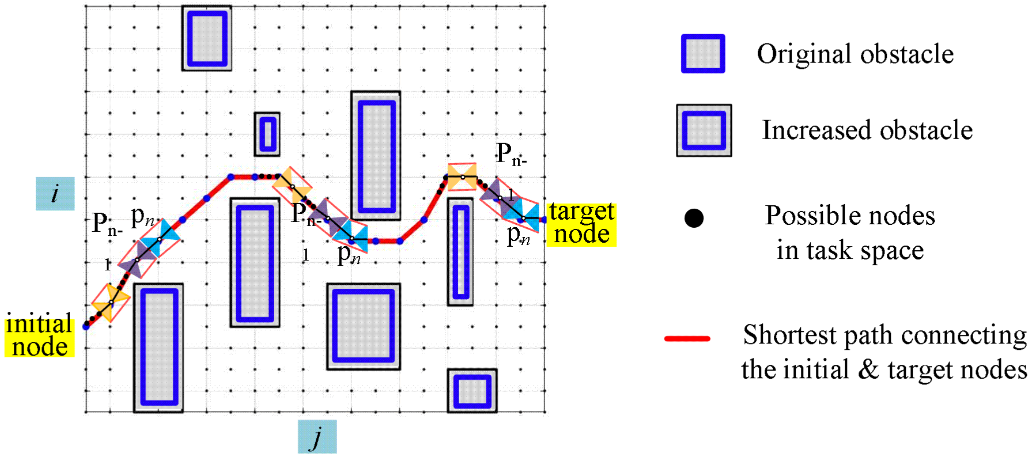

Fig. 5. 15: Example of obstacle-free path generation for the robot end-effector (obstacle dimensions are increased to take into account the end-effector size)

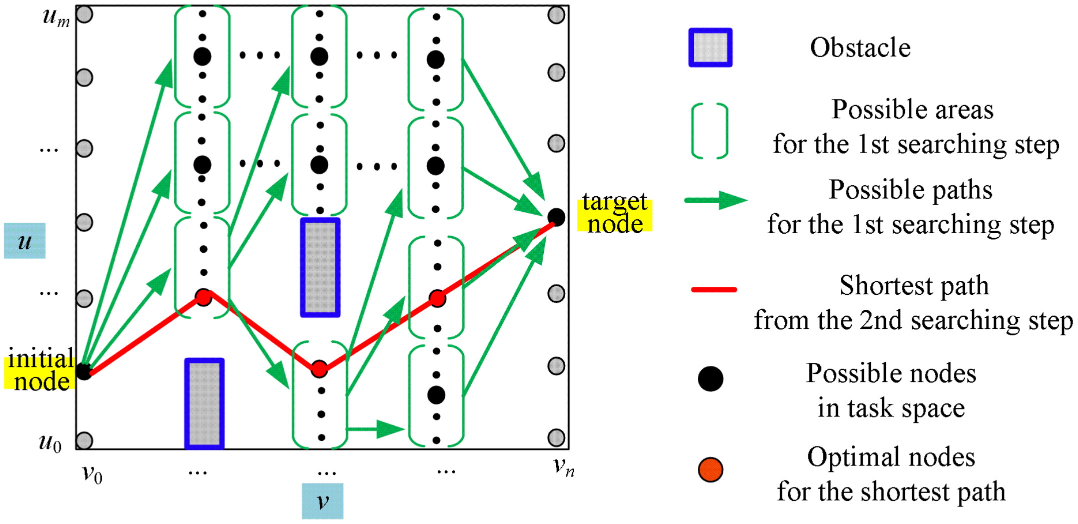

Fig. 5. 16: Speed-up of searching algorithm for generating obstacle-free path by applying dynamic programming with decreasing discretization step

The basic idea of the proposed modification is to find first an initial solution with the rough discretization and to improve it further using relatively small discretization step (and applying at the both steps the same numerical technique based on the discrete dynamic programming). Geometric explanation of this approach is presented in Fig. 4.14, where at the first step the task space is divided into several big areas $\mathbf{S}(u,v)$, $u \subset \{0,1,...m\}$, $v = \{0,1,...n\}$. Then after applying the above presented technique, the confident areas in every column in the task space could be found, which contain the possible points for connecting the shortest path, and the corresponding trajectory could be obtained with the indices expressed as follows $\mathbf{S}(u_0,0) \to \mathbf{S}(u_1,1) \to ... \to \mathbf{S}(u_{n-1},n-1) \to \mathbf{S}(u_n,n)$. As the second step, it is only necessary to search for the points $\mathbf{L}(i_v,v) \in \mathbf{S}(u_v,v)$ inside of the confident areas obtained from the first step. It is clear that this approach allows us to essentially increase the computing speed.

The basic idea of the proposed modification is to find first an initial solution with the rough discretization and to improve it further using relatively small discretization step (and applying at the both steps the same numerical technique based on the discrete dynamic programming). Geometric explanation of this approach is presented in **Fig. 5. 16**, where at the first step the task space is divided into several big areas $\mathbf{S}(u,v)$, $u \subset \{0,1,...m\}$, $v = \{0,1,...n\}$. Then after applying the above presented technique, the confident areas in every column in the task space could be found, which contain the possible points for connecting the shortest path, and the corresponding trajectory could be obtained with the indices expressed as follows $\mathbf{S}(u_0,0) \to \mathbf{S}(u_1,1) \to ... \to \mathbf{S}(u_{n-1},n-1) \to \mathbf{S}(u_n,n)$. As the second step, it is only necessary to search for the points $\mathbf{L}(i_v,v) \in \mathbf{S}(u_v,v)$ inside of the confident areas obtained from the first step. It is clear that this approach allows us to essentially increase the computing speed. (reduce .. ms in our simulation example).

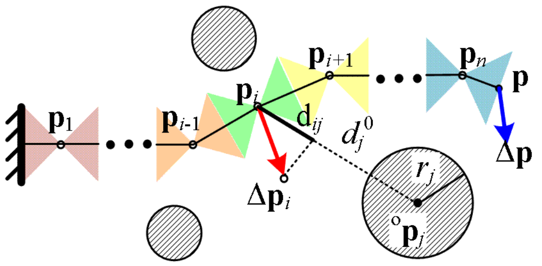

Fig. 5. 17: Computing the distances dij between the robot joints and obstacles

To solve the second sub-problem from the above defined ones, which deals with ***collision-free path planning for the manipulator body***, let us assume that the optimal path for the end-effector is already known and the kinematic redundancy resolution technique must ensure not only the minimum of the joint increments (5.32), but also guarantee the safety distances between the obstacles and the manipulator intermediate segments. The latter condition can be expressed in the following way

$$d_{ij} \triangleq dist(\mathbf{p}_i, {}^{o}\mathbf{p}_j) \ge d_j^0, \qquad \forall i = 1,2,...n; \quad \forall j = 1,2,...,m \tag{5. 38}$$

where d_{ij} denotes the distance between the *i*th joint and the *j*th obstacle, and d_j^0 is the allowable minimum value for the *j*th obstacle that takes into account its size (equivalent radius). In more details, these definitions are explained in **Fig. 5. 17**, where the joint axis locations are described by the points $\{\mathbf{p}_i,\ \forall i\}$ and the obstacles are approximated by the circles with the centers $\{{}^{o}\mathbf{p}_j\}$ and radiuses $\{r_j\}$. To present the above collision-free constraints in more convenient way, let us take into account that for small $\Delta\mathbf{q}$ the joint axis displacement $\Delta\mathbf{p}_i$ can be computed using the linearized expression $\Delta\mathbf{p}_i = \mathbf{J}_i \cdot \Delta\mathbf{q}$, where $\mathbf{J}_i$ is the manipulator partial Jacobian matrix with respect to the *i*th joint that can be expressed as

$$\mathbf{J}_i = b \cdot \begin{bmatrix} -\sum\limits_{k=1}^{i}\left(\eta_k \sin\sum\limits_{s=1}^{k} q_s\right) & -\sum\limits_{k=2}^{i}\left(\eta_k \sin\sum\limits_{s=1}^{k} q_s\right) & \cdots & -\sum\limits_{k=n}^{i}\left(\eta_k \sin\sum\limits_{s=1}^{k} q_s\right) \\ \sum\limits_{k=1}^{i}\left(\eta_k \cos\sum\limits_{s=1}^{k} q_s\right) & \sum\limits_{k=2}^{i}\left(\eta_k \cos\sum\limits_{s=1}^{k} q_s\right) & \cdots & \sum\limits_{k=n}^{i}\left(\eta_k \cos\sum\limits_{s=1}^{k} q_s\right) \end{bmatrix}_{2\times n} \tag{5. 39}$$

Here similar to (5.3), *b* is the manipulator geometric parameter, $\eta_k = 2$ for $k < n$ and $\eta_k = 1$ for $k = n$. It worth mentioning that in contrast to (5.3), here the last $(n-i)$ columns of Jacobian $\mathbf{J}_i$ are composed of zeros. Such linearization allows us to present the desired $dist(\mathbf{p}_i, {}^{o}\mathbf{p}_j)$ as the projection of the displacement vector $\Delta\mathbf{p}_i$ onto the line segment connecting the points $\mathbf{p}_i$ and ${}^{o}\mathbf{p}_j$ (see **Fig. 5. 17**), i.e. in the following form

$$d_{ij} = \mathbf{e}_{ij}^T \cdot \mathbf{J}_i \cdot \Delta\mathbf{q} \tag{5. 40}$$

where the unit vector $\mathbf{e}_{ij}$ is computed as $\mathbf{e}_{ij} = \left(\mathbf{p}_i - {}^{o}\mathbf{p}_j\right) / \left\|\mathbf{p}_i - {}^{o}\mathbf{p}_j\right\|$. So finally, for the *n* segment manipulator with *m* different task space obstacles, the $m \times n$ collision-free constraints (5.40) can be rewritten as the following way

$$\mathbf{e}_{ij}^T \cdot \mathbf{J}_i \cdot \Delta\mathbf{q} - d_j^0 \geq 0, \quad i = 1,2,...n; \quad j = 1,2,...,m \tag{5. 41}$$

where the safety parameter $d_j^0 = r_j + \sqrt{a^2 + b^2}$ is computed taking into account both the obstacle equivalent radius r_j and the manipulator geometric parameters *a*, *b*. Such presentation of the collision-free constraints allow us to replace the optimization problem (5.29), (5.30) involved the manipulator redundancy resolution by the following one.

minimize the square sum of the joint angle increments $\Delta\mathbf{q}$

$$\sum_{i=1}^{n} \Delta\mathbf{q}_i^{\mathrm{T}} \cdot \Delta\mathbf{q} \rightarrow \min_{\Delta\mathbf{q}} \tag{5. 42}$$

subject to the geometric constraint on the end-effector displacement

$$\Delta\mathbf{p} = \mathbf{J}\cdot\Delta\mathbf{q} \tag{5. 43}$$

and the collision-free constraints

$$\mathbf{e}_{ij}^{T}\cdot\mathbf{J}_{i}\cdot\Delta\mathbf{q} \geq d_{j}^{0}, \qquad \forall i=1,2,...n;\ \ \forall j=1,2,...,m \tag{5. 44}$$

applied to the intermediate joint locations

It is clear that from the mathematical point of view it is the quadratic optimization with the *mixed linear equality and inequality constraints*,

The main particularity of the above optimization problem is related to influence of the inequality constraints (5.44) on the final solution. In particular, some of them can be stronger than the other ones, leading to the situation when only limited number of non-equalities (5.44) are active. However, the constraint classification on the active/non-active ones is not a trivial problem. In this work, it is proposed the following technique to solve this optimization problem:

(1) First, try to release all inequality constraints and find the optimal solution $\Delta\mathbf{q}^{*}$ of this reduced problem using the formula (5.44).

(2) For the obtained solution $\Delta\mathbf{q}^{*}$, verify all inequality constraints (5.44) and find those that are violated. If no one of constraints is violated, $\Delta\mathbf{q}^{*}$ is treated as the final solution.

(3) If some of the inequality constraints are violated, the strongest of them is selected for each joint and transformed into the equality constraint. This selection is executed on the base of "the distance to the obstacle" computed straightforwardly from the left-hand side of (5.43).

(4) Then the problem is solved for the extended set of equality constraints and the obtained new optimal solution $\Delta\mathbf{q}^{*}$ is evaluated by starting from the step (2).

To find the optimal solution for the extended optimization problem at step (4), the Lagrange technique can be applied dealing with the minimization of the function

$$L(\Delta\mathbf{q},\boldsymbol{\lambda},\boldsymbol{\mu}) = \frac{1}{2}\Delta\mathbf{q}^{\mathrm{T}}\Delta\mathbf{q} + \boldsymbol{\lambda}^{T}\cdot\left(\mathbf{J}\cdot\Delta\mathbf{q}-\Delta\mathbf{p}\right) + \sum_{active}\mu_{ij}\left(\mathbf{e}_{ij}^{T}\cdot\mathbf{J}_{i}\cdot\Delta\mathbf{q}-d_{j}^{0}\right) \rightarrow \min \tag{5. 45}$$

which requires the zero-gradient $\nabla L(\Delta\mathbf{q},\boldsymbol{\lambda},\boldsymbol{\mu})=0$ and leads to the following linear system

$$\Delta\mathbf{q}-\boldsymbol{\lambda}^{T}\cdot\mathbf{J}-\boldsymbol{\mu}^{T}\cdot\mathbf{J}_{a}=\mathbf{0}; \qquad \mathbf{J}\cdot\Delta\mathbf{q}-\Delta\mathbf{p}=\mathbf{0}; \qquad \mathbf{J}_{a}\cdot\Delta\mathbf{q}-\mathbf{d}_{a}=\mathbf{0} \tag{5. 46}$$

where the matrix $\mathbf{J}_a$ and the vector $\mathbf{d}_a$ are composed of element $\mathbf{e}_{ij}^{T}\cdot\mathbf{J}_{i}$ and d_{j}^{0} corresponding to the active constraints, and $\boldsymbol{\lambda}$ and $\boldsymbol{\mu}$ are the Lagrange multipliers. It is clear that this system can be solved in a usual way that produces the following expression

$$\Delta\mathbf{q} = \begin{bmatrix} \mathbf{J} \\ \mathbf{J}_a \end{bmatrix}^{\dagger} \cdot \begin{bmatrix} \Delta\mathbf{p} \\ \mathbf{d}_a \end{bmatrix} \qquad (5.\ 47)$$

where the symbol denotes the matrix pseudo-inverse of Moore-Penrose, i.e. $\mathbf{A}^{\dagger} = \mathbf{A}^T(\mathbf{A}\mathbf{A}^T)^{-1}$.

The above presentation technique is simple and easy to implement. However sometimes it can produce sub-optimal solutions that can be essentially improved. In this cases, it is reasonable to apply the Karush-Kuhn-Tucker (KKT) approach, which generalizes the method of Lagrange multipliers allowing only equality constraints. Corresponding system of equations derived from the necessary condition of optimality

$$\Delta\mathbf{q} - \boldsymbol{\lambda}^T \cdot \mathbf{J} - \boldsymbol{\mu}^T \cdot \mathbf{J}_\mathbf{e} = \mathbf{0}; \qquad \mathbf{J} \cdot \Delta\mathbf{q} - \Delta\mathbf{p} = \mathbf{0}; \qquad \mathbf{J}_\mathbf{e} \cdot \Delta\mathbf{q} - \mathbf{d} - \mathbf{s} = \mathbf{0} \qquad (5.\ 48)$$

which includes an additional slack variable vector $\mathbf{s} \geq 0$ allowing to transform the inequality constraints to equality ones, and where the matrix $\mathbf{J}_\mathbf{e}$ and the vector $\mathbf{d}$ are composed of all elements $\mathbf{e}_{ij}^T \cdot \mathbf{J}_i$ and d_j^0 from the inequality constraints (5.44). As follows from the KKT technique, the vectors $\boldsymbol{\mu}$ and $\mathbf{s}$ corresponding to the desired minimum must satisfy the following condition

$$\boldsymbol{\mu}^T\mathbf{s} = 0; \qquad \mathbf{s} \geq 0; \ \boldsymbol{\mu} \geq 0$$

So, if $s_k = 0$ the corresponding inequality constraint is active. Otherwise, if $s_k > 0$ this constraint is ignored by setting $\mu_k = 0$. As follows from literature (Allende and Still, 2013; Gordon and Tibshirani, n.d.; Izmailov and Solodov, 2003), KKT algorithm can be easily implemented using the Newton's method.

To demonstrate the efficiency of the developed approach, it was applied to a case studies dealing with 20-segment manipulator control in environment with multiple obstacles. Relevant simulation results are presented in **Fig. 5. 18** where the manipulator end-effector is assumed to move along the straight line (LIN motion), and the manipulator body motion is limited by two obstacles located in opposite sides. As follows from this figure, the proposed approach is able to adjust the manipulator shape at each step to avoid collision while ensuring the desired location of the end-effector. It should be stressed that here the desired end-effector orientation is not defined, the task is only to ensure the desired end-effector position (x, y).

Finally, it should be mentioned that the above presented results can be also generalized for the 3-dimention φ al task space (x, y, φ), which in addition to the end-effector location (x, y) takes into account the end-effector orientation angle. This generalization leads to an additional equality constraint that can be easily expressed via the configuration angles $\mathbf{q}$ and included in (5.47) by using the extended Jacobian of size 3×n obtained by adding the third line composed of ones [1, 1, …, 1] to the matrix

(5.42) of size 2×n. Relevant simulation results are presented in **Fig. 5. 19**, where the manipulator end-effector must follow the curved path located inside of the narrow gap between the obstacles. In addition, it is required that the end-effector orientation φ should be tangent to the prescribed path. This case study also confirms the efficiency of the developed control algorithms which ensure both the manipulator body and the end-effector passing through the narrow gap. The algorithm of this motion control is shown in **Table 11**, where the shortest path from the initial to the target point in the workspace is assumed already obtained based on the above dynamic programming technique (see **Table 10**).

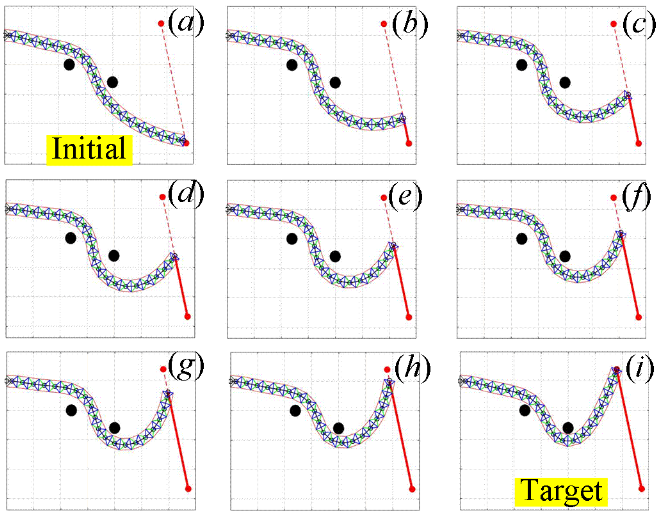

Straight line motion with (x, y) control

Fig. 5. 18:: Example of collision-free motion control for multi-segment manipulator (for the case when the end-effector is moved along the given straight line without the orientation constraint).

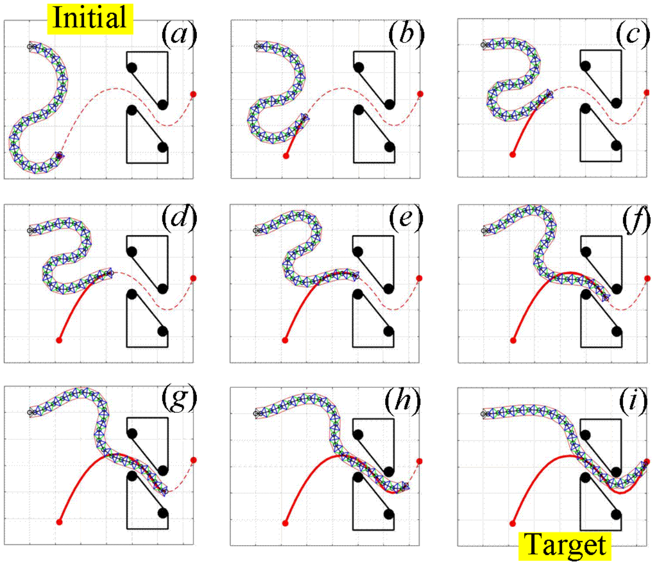

Curved line motion with (x, y, φ) control

Fig. 5. 19: Example of collision-free motion control for multi-segment manipulator (for the case when the end-effector is moved along the given curve with the orientation constraint).

Table 11 Algorithm of collision-free motion control for multi-segment manipulator when the end-effector is moved along the given path with the orientation constraint.

Inputs	**p0**	$\mathbf{p0}=[x0,y0]^T$, manipulator end-defector initial location
	pg	$\mathbf{pg}=[xg,yg]^T$, manipulator end-defector target location
	q0	n×1 vector, the initial configuration angles of the manipulator
	F	$\mathbf{F}=[Fx,Fy]^T$, external loading on the end-effector of the manipulator
	k	n×1 vector, stiffness coefficient of each joints of the manipulator
	L0	2×n matrix, the symmetrically distributed linear springs initial lengths of the manipulator (see structure figure 5.1)
	path	2× w matrix, point locations on the path from the initial **p0** to target point **pg.**
	pob	2×m matrix, location of the obstacles
	rob	m×1 vector, radius of the obstacles
	a, *b*	geometric parameters of the manipulators
	m	Number of motion steps between the initial and target end-effector position
Local variables	**pt**	$\mathbf{pt}=[xt,yt]^T$, points locating on the path between the initial and target end-effector location
	pc	Current endpoint location of the manipulator
	dp	**dp** = **pt** - **pc** , current end-effector deflection
	dq	n×1 vector, current joint increment corresponding to **dp**
	qc	n×1 vector, current joint configuration angles
	P*ij*	Vector, from the *i*th joint to the *j*th obstacle
	e*ij*	Unit vector of **P***ij*
	bj	n×1 vector, composed of *dmin_ij*
	b_eq	3×1 vector related to **dp** and manipulator orientation angles, equality constraints
	b_Neq	Vector, inequality constraints
	Me	External torque of each joint of the manipulator
	Delt_L0	n×1 vector, configuration control inputs of each segment of the manipulator
	J	2×n Jacobian matrix that corresponding to **qc**
	Aj	n×n matrix, composed of inequality constraints
	A_eq	3×n Jacobian matrix related to **J**, equality constraints parameters,

	A_Neq	Matrix, inequality constraints parameters
	phi	Manipulator orientation angles
	dmin_ij	The minimum safe distance between the *i*th joint and the *j*th obstacle
Outputs	**Set_Qout**	*n*×*w* matrix, joint configuration angles corresponding to all the manipulator current motion
	Set_Delt	*n*×*w* matrix, configuration control inputs of each segment corresponding to all the manipulator current motion

(1) Joint limit of manipulator segments

```
If  a/b<=1
    Joint_limit = 2*atan (a/b);
Else
    Joint_limit = pi - 2*atan (a/b);
End
```

(2) Main algorithm loop of continuous motion configurations control

```
Set_Qout:=zeros(m, n);      Set_Delt:=zeros(m, n);      qc: = q0;       pc = p0
For  s = 1 to w
    pt: = path(:,w);
    dp: = pt – pc;
    J: = fun_of_Jacobian(qc, b);
    pc: = fun_direct_kinematic(qc, b);
    phi: = atan2( pt(2), pt(1) );
    H:= eye(n);   f: = zeros(n, 1);   A_eq: = [J; ones(1, n)];   b_eq:= [dp; phi – sum(qc)];
    A_Neq: = [];   b_Neq:= [];
    For  j = 1 to m
        Aj: = zeros(n, n);   bj:=  zeros(n, 1);
        For  i = 1 to n
            Pij:= pob(:, j) - pc(:, i);
            eij:= Pij · inv( norm(Pij) );   dmin_ij:= norm(Pij) - rob(j) - sqrt($a^2 + b^2$);
            Aj(i, 1:i): = eij' · J(:, 1:i);   bj(i, 1):=  dmin_ij
        End
        A_Neq: = [ A_Neq; Aj];   b_Neq:= [ b_Neq; bj];
    End
    dq: = quadprog(H, f, A_Neq , b_Neq , A_eq, b_eq);
    qc: = qc + dq;
    For  t = 1 to n
        If  Abs( qc(t) ) > Joint_limit;
            qc(t): = sign( qc(t) ) · Joint_limit;
        End
```

```
        End
        Set_Qout (:, s): = qc;
        Me: = J' · F;
        Delt_L0: = fun_of_Delt_L0(a, b, k, L0, qc, Me);
        Set_Delt (:, s): = Delt_L0;
End
```

5.4 Summary

This part is focusing on the general case dealing with the analysis of mechanical properties and kinematic control of the redundant ***multi-segment serial tensegrity mechanism*** composed of the dual-triangles. ***The main contributions*** are related to the *stiffness analysis* as well as investigating of the stability and buckling phenomenon for this serial structure. Another contribution of this part is the *optimization-based kinematic control strategy* for this redundant mechanism allowing to minimize the joint motions and avoiding the workspace obstacles.

The structure of this chapter as well as the applied methods are similar to the previous ones, however it deals with the general case where the number of segments is arbitrary. Compared to the previous chapters, here the number of equilibriums may be quite large. For example, for the four-segment mechanism, there are six equilibrium configurations (two symmetrical stable ones). For the general case, the stiffness/compliance matrices for both unloaded and loaded mode were obtained using the VJM technique, as well as analytical force-deflection relations. Besides, the buckling and quasi-buckling phenomenon for this serial mechanism were also detected; and an analytical method was proposed allowing computing the critical force causing the buckling. Also, the optimization-based kinematic control strategies from the precious chapters were generalized allowing to generate collision-free motions with the shortest end-point path and minimum increments in the actuated joints. The efficiency of the proposed technique was confirmed by simulation results, which shows that such control allows manipulator achieving excellent flexibility and ability of shape changing.

In more details, new results and contributions of Chapter 5 include the following issues

(i) *The **equilibrium configurations*** for multi-segment mechanism were obtained using the energy method, and the classification of stable/unstable shapes were presented.

(ii) *The **stiffness matrices*** of this mechanism for both unloaded and loaded mode were obtained using VJM technique, and the relations between the end-effector deflection and the external load were derived analytically.

(iii) *The **buckling and quasi-buckling*** phenomenon were detected via the stiffness and stability analysis for both unloaded and loaded modes. The critical values of the loading causing the buckling were obtained analytically using eigenvalues technique, which can be generally used for the similar structure of serial manipulators.

(iv) *The **collision-free path planning*** technique based on discrete dynamic programming was proposed, which provides the shortest path for the mechanism ***end-point*** reaching the desired target point without collisions with workspace obstacles.

(v) *The **obstacle-avoidance kinematic control strategies*** for the ***mechanism body*** was proposed, which is based on quadratic programming with mixed linear equality and inequality constraints. Efficiency of this technique was evaluated via simulation, which confirmed the mechanism ability of achieving excellent variable-stiffness properties and collision-free passing through the multi-obstacle environment.

It should mentioning that the universality of the main results of this chapter allow easily generalizing them for the serial multi-segment manipulators that are based on other mechanisms (different from dual-triangles). Also, slight modification of the proposed kinematic control algorithms allows to generate collision-free trajectories controlling both position and orientation of the end-effector.

The main results of Chapter 5 are published in the following works: [Zhao, W.; Pashkevich, 2021a], [Zhao, W.; Pashkevich, 2021b], [Zhao, W.; Pashkevich, 2021c].

CONCLUSIONS AND PERSPECTIVES

Contributions of the thesis

This thesis focuses on the design of new versatile and compliant end-effectors for collaborative work of robots and human operators, which are based on multi-segment planar tensegrity mechanisms that can be actuated independently to achieve the desired configuration with the required stiffness properties. To achieve this goal, three main problems were considered, which were solved gradually by increasing number of segments in the considered compliant mechanism. The main results and contributions of this thesis can be summarized as follows.

For the ***Problem 1***, dealing with the **comparison study** of different mechanisms that can be used for designing compliant end-effectors, two potential tensegrity architectures (*X-shape* and *dual-triangles*) were considered. For both of them, configuration can be adjusted by means of the controllable elastic springs locating on the two edges. It was shown that both of these two options ensure high flexibility and may be potentially used for designing soft robot end-effectors. For practical reasons, the main attention was paid to the symmetrical structure and to the case of equal spring pre-stress, for which the *analytical condition of equilibrium stability* was derived. Also, the relation between the external torque and the deflection was obtained which showed that the X-shape mechanism has always ***non-monotonic*** force-deflection relation, while for the dual-triangle one it is possible to achieve the ***monotonic force-deflection*** curve. The latter allowed us to conclude that the dual-triangle tensegrity mechanism has essential advantages for the considered application, and it was chosen as the basic structure for the compliant serial manipulator considered in this thesis.

The main results and contributions related to the *problem* 1 include the following issues

(i) There were obtained analytical ***stability conditions*** and **equilibrium configurations** (stable and unstable) for both X-shape and dual-triangle tensegrity mechanisms for unloaded and loaded modes, which allow user to select the mechanical architecture ensuring the controllability of the manipulator based on such segments.

(ii) It was shown that for different combinations of the geometric parameters for the ***dual-triangle mechanisms,*** the force-deflection relation curves may be *either monotonic* (a single stable equilibrium) *or non-monotonic* (one stable and two unstable equilibriums). While for the ***X-shape mechanisms,*** the force-deflection relation curve is *always non-monotonic* with one stable and two unstable equilibriums.

For the ***Problem 2,*** dealing with the ***stiffness analysis*** of the multi-segment dual-triangle mechanism, both unloaded and loaded modes were considered, and specific mechanical properties were analysed in detail. Particular attention was paid to the mechanism stiffness behaviour for the straight and non-straight initial configurations. In this study, the *analytical stiffness/compliance matrices* were derived using the VJM technique that allow designers to evaluate the stiffness sensitivity of this structure with respect to an arbitrary initial configuration for different geometric parameters, external loading and the springs pre-stresses. Besides, the force-deflection relations were obtained, which allowed us to detect the *buckling and quasi-buckling phenomenon* in this serial mechanism under the loading. The main *theoretical contribution* is an analytical method allowing to compute the critical force causing the buckling for the serial structure with an arbitrary number of segments, which is based on the eigenvalue analysis of the some special matrix depending on both geometric and elastostatic parameters. This allows designers to predict or avoid the dangerous states of this mechanism by properly changing the geometric parameters and control inputs.

The main results and contributions related to the *problem* 2 include the following issues

(i) The ***stiffness/compliance matrices*** of this mechanism for both unloaded and loaded mode, which were obtained using the VJM technique, as well as the mechanism **force-deflection curves**.

(ii) ***Mechanism equilibrium configurations*** (both stable and unstable ones) and their classification, which were obtained using the energy method.

(iii) Detection of specific mechanical property of this mechanism i.e. the ***buckling phenomenon*****,** which can be observed for the straight initial configuration if the external loading exceeds certain critical value.

(iv) Detection of the ***quasi-buckling phenomenon*** for the non-straight configuration, when the mechanism resistance in certain direction may be suddenly lost under the loading, while the resistance in other directions still exists.

(v) Analytical technique for ***computing the critical force*** causing the buckling, which is based on the eigenvalues analysis applied to some special matrix. This technique is rather general and can be applied to other serial manipulators of similar structure.

For the ***Problem 3***, dealing with the ***kinematic control*** of considered redundant multi-segment mechanism, the optimization-based control strategies were proposed allowing to achieve the target endpoint location and avoid collisions to the workspace obstacles. To generate the desired motions, it is proposed to decompose the general control problem in three separate ones. *The* ***first*** of them focuses on the separate segments and is targeting on achieving the desired joint angles of the dual-triangle mechanisms via adjusting the spring pre-stresses. *The* ***second*** sub-problem concentrates on the redundancy resolution for the multi-segment manipulator ensuring the end-point displacement to the desired location using minimal joint motion increments. *The* ***third*** sub-problem deals with the obstacle-avoidance kinematic control ensuring safe distances between the manipulator segments and some objects located inside of the manipulator workspace. Because of computation of complexity, the last sub-problem was further divided in two sequential steps: (a) *collision-free path planning for the manipulator end-effector*; (b) *collision-free path planning for the manipulator body*, i.e. including intermediate segments. The proposed kinematic control strategy was carefully verified via the computing simulation, which confirmed its advantages and abilities in achieving of the desired manipulator flexibility and shape changing capacity.

The main results and contributions related to the *problem* 3 include the following issues

(i) The kinematic ***control technique for a single segment,*** which allows to achieve the desired joint angles of the dual-triangle tensegrity mechanism via anti-symmetrical adjusting the spring pre-stresses (for both loaded and unloaded modes).

(ii) The ***collision-free path planning*** technique for the mechanism ***end-point***, which is based on discrete dynamic programming that provides the shortest path for reaching the desired target point avoiding the workspace obstacles.

(iii) ***The minimum joint motion control technique***, which is based on the quadratic optimization with linear equality constraints that ensures the redundancy resolution and the manipulator **end-point** displacement to the desired location with minimal joint increments.

(iv) *The* ***obstacle-avoidance kinematic control technique*** for the ***manipulator body***, which is based on quadratic programming with mixed linear equality and inequality constraints, allowing to pass through the multi-obstacle environment without collisions while implementing the desired end-point path.

In general, combination of all results related to the problems 1, 2, 3 allow to achieve the desired goal, i.e. to develop a new robot end-effectors based on compliant serial structures composed of a number of similar modules or segments, each of which contains a tensegrity mechanism.

Limitations of obtained results

In spite of numerous essential advantages, there are still several limitations in the obtained results that are presented below

(i) ***Only serial structure*** is considered in this thesis, while for the parallel or serial-parallel manipulators composed of the dual-triangle tensegrity mechanisms, the corresponding stiffness properties and stability conditions may be essentially different, as well as some specific mechanical phenomenon (i.e. the buckling or quasi buckling) may be observed in other configurations.

(ii) It is assumed here that the ***external loading is applied to the manipulator end-point*** only, but in practice there are some cases when several external loadings are acting on the manipulator; also, there may exist some other specific phenomenon, such as the ***local buckling*** (when partial shape of some segments is straight).

(iii) The ***quasi-buckling*** phenomenon (i.e. when the mechanism resistance to the external loading is suddenly lost for one direction only) was analysed for several case studies only, the general technique for computing the corresponding critical force causing this phenomenon and the condition when it occurs was not developed.

(iv) ***Accuracy*** of the proposed obstacle-avoidance ***kinematic control strategy*** is limited. Because of the imperfection of the selected optimization method and large number of the related constraints, the manipulator body cannot move exactly along the required end-point trajectory while passing through the multi-obstacle environment.

It should be stressed that the first two limitations are related to some more general cases of manipulator architectures, the third one is not typical for the considered applications, and the last one can be overcome by selection proper optimization software. So, all these limitations are not critical with respect to the main results obtained in this thesis. Some of these issues will be in the focus of the future work.

Further investigations and perspectives

To generalize the obtained results, it is reasonable to continue research in several directions and to concentrate on the following issues

(i) To improve the considered dual-triangle tensegrity mechanism by using some ***non-linear elastic components*** instead of the linear springs. This allows us to achieve more flexible motions and better compliance properties, but related elastostatic analysis will produce the stiffness/compliance matrices of more complicated nonlinear form. From the practical point of view, this approach allows the manipulator to generate larger loading with less deflection, and vice versa.

(ii) To extend the investigation of the dual-triangle tensegrity mechanism considered in this thesis for the ***three-dimensional case***. It is expected that for the single segment, there may be many similarities with the two-dimensional case, so the stiffness and stability conditions can be obtained using the developed technique. However, for the serial manipulator composed of several three-dimensional dual-triangles, there may be some particularities during the analysis, new stable configurations and buckling phenomenon, which may produce some new results of practical significance.

(iii) To extend the presented elastostatic analysis of the considered manipulator for the cases of more ***complicated or large external loadings***. First, it is reasonable to consider the case when there are many external/internal loadings acting on the manipulator body, which is quite similar to that when the human arms or elephant trunks holding some objects. Second, it is important to study the cases when the external loading is large enough (larger than some critical values) that causing the rigid components bending or even failure; the condition of such phenomenon should be obtained, as well as the loading critical values.

(iv) To investigate the ***parallel or serial-parallel*** multi-segment manipulators composed of the dual-triangle tensegrity mechanisms. Similar investigation techniques and methods may be used in this case, but the corresponding stiffness and stability conditions may be essentially different, as well as some specific mechanical properties (buckling). This allows us to select the best structure after comparison analysis and design a more stable and flexible manipulator in practice.

(v) To analyse the ***quasi-buckling*** phenomenon in the compliant serial manipulators (i.e. when the mechanism resistance to the external loading is suddenly lost in one direction only); the corresponding critical force causing this phenomenon and the condition when it occurs should be obtained for general cases.

(vi) To investigate some ***other specific mechanical properties*** that can be observed for the considered compliant serial manipulator, such as the ***local buckling phenomenon*** (when partial shape of some segments is straight). This phenomenon may occur in some special case, such as when there are more than one external loadings acting at different joints.

(vii) To improve the proposed obstacle-avoidance ***kinematic control strategy*** by taking into account more constraints (arising from manipulator geometry or desired shape of manipulator body). The main goal of this problem is to increase the flexibility and controllability of this manipulator, let the manipulator move along the required end-point trajectory while passing through the multi-obstacle environment with the desired manipulator shape.

The research results presented in this thesis were obtained in the frame of financial support

provided by the China State Scholarship Fund (No. 201801810036) of the project "CSC-Centrale Schools Program" founded by the China Scholarship Council. Their practical implementation and further development will be performed in frame of the subsequent projects that have recently been started by REV team of LS2N.

Publications

Journal papers

Zhao, W., Pashkevich, A., Chablat, D., Klimchik, A., 2021a. Mechanics of compliant serial manipulator composed of dual-triangle segments. Int. J. Mech. Eng. Robot. Res. 10, 169–176. https://doi.org/10.18178/ijmerr.10.4.169-176.

Zhao, W., Pashkevich, A., Klimchik, A., Chablat, D., 2021b. Elastostatic modeling of multi-link flexible manipulator based on 2D dual-triangle tensegrity mechanism. J. Mech. Robot. 1–31. https://doi.org/10.1115/1.4051789.

Zhao, W., Pashkevich, A., Klimchik, A., Chablat, D., 2021c. Non-linear stiffness behavior of robotic manipulators. *J. Mechanism & Machine Theory*. (submitted in Nov 27).

Book chapters

Zhao, W.; Pashkevich, A.; Klimchik, A. and Chablat, D. 2020a. Equilibrium configurations of compliant tensegrity mechanism based on planar dual-triangles. Lecture Notes in Electrical Engineering LNEE, Springer, 2020 (in press).

International conference proceedings

Zhao, W., Pashkevich, A., Klimchik, A., Chablat, D., 2020b. The Stability and Stiffness Analysis of a Dual-Triangle Planar Rotation Mechanism, in: IDETC-CIE2020. Volume 10: 44th Mechanisms and Robotics Conference (MR). https://doi.org/10.1115/DETC2020-22076

Zhao, W., Pashkevich, A., Klimchik, A., Chablat, D., 2021d. Stiffness Analysis of a New Tensegrity Mechanism based on Planar Dual-triangles. Presented at the 17th International Conference on Informatics in Control, Automation and Robotics (ICINCO2020), pp. 402–411.

Zhao, W., Pashkevich, A., Klimchik, A., Chablat, D., 2021e. Kinematic Control of Compliant Serial Manipulators Composed of Dual-Triangles, in: 2021 International Conference on Computer, Control and Robotics (ICCCR). Presented at the 2021 International Conference on Computer, Control and Robotics (ICCCR), pp. 93–97. https://doi.org/10.1109/ICCCR49711.2021.9349285

Zhao, W., Pashkevich, A., Pashkevich, A., Chablat, D., Chablat, D., 2021f. Stiffness Modeling of Compliant Serial Manipulators based on Tensegrity Mechanism under External Loading. Presented at the 18th International Conference on Informatics in Control, Automation and Robotics (ICINCO 2021), pp.

254–262.

Zhao, W.; Pashkevich, A.; and Chablat, D., 2021g. Redundancy resolution in kinematics control of multi-link serial manipulators in multi-obstacle environment. 60th Advances in production management systems, APMS 2021 (IFIPAICT, volume 633).

Zhao, W.; Pashkevich, A.; and Chablat, D., 2021h. Non-linear stiffness modeling of multi-link compliant serial manipulator composed of multiple tensegrity segments. IEEE 2021 International Conference on Automation Science and Engineering (CASE 2021).

REFERENCES

Abele, E., Weigold, M., Rothenbücher, S., 2007. Modeling and Identification of an Industrial Robot for Machining Applications. CIRP Ann. 56, 387–390. https://doi.org/10.1016/j.cirp.2007.05.090

Albu-Schaffer, A., Eiberger, O., Grebenstein, M., Haddadin, S., Ott, C., Wimbock, T., Wolf, S., Hirzinger, G., 2008. Soft robotics. IEEE Robot. Autom. Mag. 15, 20–30. https://doi.org/10.1109/MRA.2008.927979

Aldrich, J.B., Skelton, R.E., Kreutz-Delgado, K., 2003. Control synthesis for a class of light and agile robotic tensegrity structures, in: Proceedings of the 2003 American Control Conference, 2003. Presented at the Proceedings of the 2003 American Control Conference, 2003., pp. 5245–5251 vol.6. https://doi.org/10.1109/ACC.2003.1242560

Alici, G., Shirinzadeh, B., 2005. Enhanced stiffness modeling, identification and characterization for robot manipulators. IEEE Trans. Robot. 21, 554–564. https://doi.org/10.1109/TRO.2004.842347

Allende, G.B., Still, G., 2013. Solving bilevel programs with the KKT-approach. Math. Program. 138, 309–332. https://doi.org/10.1007/s10107-012-0535-x

Amendola, A., Krushynska, A., Daraio, C., Pugno, N.M., Fraternali, F., 2018. Tuning frequency band gaps of tensegrity mass-spring chains with local and global prestress. Int. J. Solids Struct. 155, 47–56. https://doi.org/10.1016/j.ijsolstr.2018.07.002

Arsenault, M., Gosselin, C.M., 2008. Kinematic and Static Analysis of a Three-degree-of-freedom Spatial Modular Tensegrity Mechanism. Int. J. Robot. Res. 27, 951–966. https://doi.org/10.1177/0278364908091152

Arsenault, M., Gosselin, C.M., 2006. Kinematic, static and dynamic analysis of a planar 2-DOF tensegrity mechanism. Mech. Mach. Theory 41, 1072–1089. https://doi.org/10.1016/j.mechmachtheory.2005.10.014

Bathe, K.-J., Dvorkin, E.N., 1986. A formulation of general shell elements—the use of mixed interpolation of tensorial components. Int. J. Numer. Methods Eng. 22, 697–722. https://doi.org/10.1002/nme.1620220312

Becedas, J., Payo, I., Feliu, V., 2011. Two-Flexible-Fingers Gripper Force Feedback Control System for Its Application as End Effector on a 6-DOF Manipulator. IEEE Trans. Robot. 27, 599–615. https://doi.org/10.1109/TRO.2011.2132850

Bel Hadj Ali, N., Smith, I.F.C., 2010. Dynamic behavior and vibration control of a tensegrity structure. Int. J. Solids Struct. 47, 1285–1296. https://doi.org/10.1016/j.ijsolstr.2010.01.012

Bicchi, A., 2000. Hands for dexterous manipulation and robust grasping: a difficult road toward simplicity. IEEE Trans. Robot. Autom. 16, 652–662. https://doi.org/10.1109/70.897777

Bing, W.B., 2019. Free-standing Tension Structures: From tensegrity systems to cable-strut systems. CRC Press, London. https://doi.org/10.1201/9781482288308

Boehler, Q., Charpentier, I., Vedrines, M.S., Renaud, P., 2015. Definition and Computation of Tensegrity Mechanism Workspace. J. Mech. Robot. 7, 044502. https://doi.org/10.1115/1.4029809

Booth, J.W., Cyr-Choinière, O., Case, J.C., Shah, D., Yuen, M.C., Kramer-Bottiglio, R., 2020. Surface Actuation and Sensing of a Tensegrity Structure Using Robotic Skins. Soft Robot. https://doi.org/10.1089/soro.2019.0142

Borst, R. de, Crisfield, M.A., Remmers, J.J.C., Verhoosel, C.V., 2012. Nonlinear Finite Element Analysis of Solids and Structures. John Wiley & Sons.

Bugday, M., Karali, M., 2019. Design optimization of industrial robot arm to minimize redundant weight. Eng. Sci. Technol. Int. J. 22, 346–352. https://doi.org/10.1016/j.jestch.2018.11.009

Caluwaerts, K., Despraz, J., Işçen, A., Sabelhaus, A.P., Bruce, J., Schrauwen, B., SunSpiral, V., 2014. Design and control of compliant tensegrity robots through simulation and hardware validation. J. R. Soc. Interface 11, 20140520. https://doi.org/10.1098/rsif.2014.0520

Camarillo, D.B., Carlson, C.R., Salisbury, J.K., 2009. Configuration Tracking for Continuum Manipulators With Coupled Tendon Drive. IEEE Trans. Robot. 25, 798–808. https://doi.org/10.1109/TRO.2009.2022426

Carpentieri, G., Modano, M., Fabbrocino, F., Feo, L., Fraternali, F., 2017. On the minimal mass reinforcement of masonry structures with arbitrary shapes. Meccanica 52, 1561–1576. https://doi.org/10.1007/s11012-016-0493-0

Chen, B., Jiang, H., 2019. Swimming Performance of a Tensegrity Robotic Fish. Soft Robot. 6, 520–531. https://doi.org/10.1089/soro.2018.0079

Chen, L.-H., Kim, K., Tang, E., Li, K., House, R., Zhu, E.L., Fountain, K., Agogino, A.M., Agogino, A., Sunspiral, V., Jung, E., 2017. Soft Spherical Tensegrity Robot Design Using Rod-Centered Actuation and Control. J. Mech. Robot. 9. https://doi.org/10.1115/1.4036014

Chen, M., Skelton, R.E., 2020. A general approach to minimal mass tensegrity. Compos. Struct.

248, 112454. https://doi.org/10.1016/j.compstruct.2020.112454

Chen, S.-F., Kao, I., 2000. Conservative Congruence Transformation for Joint and Cartesian Stiffness Matrices of Robotic Hands and Fingers. Int. J. Robot. Res. 19, 835–847. https://doi.org/10.1177/02783640022067201

Chirikjian, G.S., 1993. A general numerical method for hyper-redundant manipulator inverse kinematics, in: [1993] Proceedings IEEE International Conference on Robotics and Automation. Presented at the [1993] Proceedings IEEE International Conference on Robotics and Automation, pp. 107–112 vol.3. https://doi.org/10.1109/ROBOT.1993.291863

Chirikjian, G.S., Burdick, J.W., 1995. Kinematically optimal hyper-redundant manipulator configurations. IEEE Trans. Robot. Autom. 11, 794–806. https://doi.org/10.1109/70.478427

Chirikjian, G.S., Burdick, J.W., 1994. A modal approach to hyper-redundant manipulator kinematics. IEEE Trans. Robot. Autom. 10, 343–354. https://doi.org/10.1109/70.294209

Chung, Y.S., Lee, J.-H., Jang, J.H., Choi, H.R., Rodrigue, H., 2019. Jumping Tensegrity Robot Based on Torsionally Prestrained SMA Springs. ACS Appl. Mater. Interfaces 11, 40793–40799. https://doi.org/10.1021/acsami.9b13062

Ciblak, N., Lipkin, H., 2021. Synthesis of Stiffnesses by Springs. Presented at the ASME 1998 Design Engineering Technical Conferences, American Society of Mechanical Engineers Digital Collection. https://doi.org/10.1115/DETC98/MECH-5879

Ciblak, N., Lipkin, H., 1999. Synthesis of Cartesian stiffness for robotic applications, in: Proceedings 1999 IEEE International Conference on Robotics and Automation (Cat. No.99CH36288C). Presented at the Proceedings 1999 IEEE International Conference on Robotics and Automation (Cat. No.99CH36288C), pp. 2147–2152 vol.3. https://doi.org/10.1109/ROBOT.1999.770424

Cieślak, R., Morecki, A., 1999. Elephant trunk type elastic manipulator - a tool for bulk and liquid materials transportation. Robotica 17, 11–16. https://doi.org/10.1017/S0263574799001009

Clinton, C.M., Zhang, G., Wavering, A.J., 1997. Stiffness Modeling of a Stewart Platform Based Milling Machine".

Courant, R., 1943. Variational methods for the solution of problems of equilibrium and vibrations. Bull. Am. Math. Soc. 49, 1–23.

Crane, C.D., III, Duffy, J., Correa, J.C., 2005. Static Analysis of Tensegrity Structures. J. Mech.

Des. 127, 257–268. https://doi.org/10.1115/1.1804194

D'Altri, A.M., Sarhosis, V., Milani, G., Rots, J., Cattari, S., Lagomarsino, S., Sacco, E., Tralli, A., Castellazzi, G., de Miranda, S., 2019. Chapter 1 - A review of numerical models for masonry structures, in: Ghiassi, B., Milani, Gabriele (Eds.), Numerical Modeling of Masonry and Historical Structures, Woodhead Publishing Series in Civil and Structural Engineering. Woodhead Publishing, pp. 3–53. https://doi.org/10.1016/B978-0-08-102439-3.00001-4

Deblaise, D., Hernot, X., Maurine, P., 2006. A systematic analytical method for PKM stiffness matrix calculation, in: Proceedings 2006 IEEE International Conference on Robotics and Automation, 2006. ICRA 2006. Presented at the Proceedings 2006 IEEE International Conference on Robotics and Automation, 2006. ICRA 2006., pp. 4213–4219. https://doi.org/10.1109/ROBOT.2006.1642350

Deng, H., Kwan, A.S.K., 2005. Unified classification of stability of pin-jointed bar assemblies. Int. J. Solids Struct. 42, 4393–4413. https://doi.org/10.1016/j.ijsolstr.2005.01.009

Fang, H.C., Ong, S.K., Nee, A.Y.C., 2013. Orientation planning of robot end-effector using augmented reality. Int. J. Adv. Manuf. Technol. 67, 2033–2049. https://doi.org/10.1007/s00170-012-4629-7

Fasquelle, B., Khanna, P., Chevallereau, C., Chablat, D., Creusot, D., Jolivet, S., Lemoine, P., Wenger, P., 2022. Identification and Control of a 3-X Cable-Driven Manipulator Inspired From the Bird's Neck. J. Mech. Robot. 14. https://doi.org/10.1115/1.4051521

Feng, X., Wu, Z., Wang, Z., Luo, J., Xu, X., Qiu, Z., 2021. Design and experiments of a bio-inspired tensegrity spine robot for active space debris capturing. J. Phys. Conf. Ser. 1885, 052024. https://doi.org/10.1088/1742-6596/1885/5/052024

Fraternali, F., Carpentieri, G., Modano, M., Fabbrocino, F., Skelton, R.E., 2015. A tensegrity approach to the optimal reinforcement of masonry domes and vaults through fiber-reinforced composite materials. Compos. Struct. 134, 247–254. https://doi.org/10.1016/j.compstruct.2015.08.087

Frecker, M.I., Ananthasuresh, G.K., Nishiwaki, S., Kikuchi, N., Kota, S., 1997. Topological Synthesis of Compliant Mechanisms Using Multi-Criteria Optimization. J. Mech. Des. 119, 238–245. https://doi.org/10.1115/1.2826242

Fu, F., 2005. Structural behavior and design methods of Tensegrity domes. J. Constr. Steel Res. 61, 23–35. https://doi.org/10.1016/j.jcsr.2004.06.004

Furet, M., Lettl, M., Wenger, P., 2019a. Kinematic Analysis of Planar Tensegrity 2-X Manipulators, in: Lenarcic, J., Parenti-Castelli, V. (Eds.), Advances in Robot Kinematics 2018.

Springer International Publishing, Cham, pp. 153–160. https://doi.org/10.1007/978-3-319-93188-3_18

Furet, M., van Riesen, A., Chevallereau, C., Wenger, P., 2019b. Optimal Design of Tensegrity Mechanisms Used in a Bird Neck Model, in: Corves, B., Wenger, P., Hüsing, M. (Eds.), EuCoMeS 2018. Springer International Publishing, Cham, pp. 365–375. https://doi.org/10.1007/978-3-319-98020-1_43

Furet, M., Wenger, P., 2019a. Kinetostatic Analysis and Actuation Strategy of a Planar Tensegrity 2-X Manipulator. J. Mech. Robot. 11, 060904. https://doi.org/10.1115/1.4044209

Furet, M., Wenger, P., 2019b. Workspace and Cuspidality Analysis of a 2-X Planar Manipulator, in: Gasparetto, A., Ceccarelli, M. (Eds.), Mechanism Design for Robotics. Springer International Publishing, Cham, pp. 110–117. https://doi.org/10.1007/978-3-030-00365-4_14

Furet, M., Wenger, P., n.d. Derivation of a polynomial equation for the boundaries of 2-X manipulators 7.

Gallagher, R.H., 2014. A Correlation Study of Methods of Matrix Structural Analysis: Report to the 14th Meeting, Structures and Materials Panel Advisory Group for Aeronautical Research and Development, NATO, Paris, France, July 6, 1962. Elsevier.

Ganguly, S., Garg, A., Pasricha, A., Dwivedy, S.K., 2012. Control of pneumatic artificial muscle system through experimental modelling. Mechatronics 22, 1135–1147. https://doi.org/10.1016/j.mechatronics.2012.09.010

Ghali, A., Neville, A.M., Brown, T.G., 2017. Structural Analysis: A unified classical and matrix approach 6th edition. CRC Press, London. https://doi.org/10.1201/9781315273006

Gilardi, G., Sharf, I., 2002. Literature survey of contact dynamics modelling. Mech. Mach. Theory 37, 1213–1239. https://doi.org/10.1016/S0094-114X(02)00045-9

Gordon, G., Tibshirani, R., n.d. Karush-Kuhn-Tucker conditions 26.

Gosselin, C., 1990. Stiffness Mapping for Parallel Manipulators. Robot. Autom. IEEE Trans. On 6, 377–382. https://doi.org/10.1109/70.56657

Goyal, R., Skelton, R.E., Peraza Hernandez, E.A., 2020. Efficient Design of Lightweight Reinforced Tensegrities Under Local and Global Failure Constraints. J. Appl. Mech. 87. https://doi.org/10.1115/1.4048049

Graells Rovira, A., Mirats Tur, J.M., 2009. Control and simulation of a tensegrity-based mobile robot. Robot. Auton. Syst. 57, 526–535. https://doi.org/10.1016/j.robot.2008.10.010

Gravagne, I.A., Rahn, C.D., Walker, I.D., 2003. Large deflection dynamics and control for planar continuum robots. IEEEASME Trans. Mechatron. 8, 299–307. https://doi.org/10.1109/TMECH.2003.812829

Gravagne, I.A., Walker, I.D., 2002. Uniform regulation of a multi-section continuum manipulator, in: Proceedings 2002 IEEE International Conference on Robotics and Automation (Cat. No.02CH37292). Presented at the Proceedings 2002 IEEE International Conference on Robotics and Automation (Cat. No.02CH37292), pp. 1519–1524 vol.2. https://doi.org/10.1109/ROBOT.2002.1014759

Gravagne, I.A., Walker, I.D., 2000a. On the kinematics of remotely-actuated continuum robots, in: Proceedings 2000 ICRA. Millennium Conference. IEEE International Conference on Robotics and Automation. Symposia Proceedings (Cat. No.00CH37065). Presented at the Proceedings 2000 ICRA. Millennium Conference. IEEE International Conference on Robotics and Automation. Symposia Proceedings (Cat. No.00CH37065), pp. 2544–2550 vol.3. https://doi.org/10.1109/ROBOT.2000.846411

Gravagne, I.A., Walker, I.D., 2000b. Kinematic transformations for remotely-actuated planar continuum robots, in: Proceedings 2000 ICRA. Millennium Conference. IEEE International Conference on Robotics and Automation. Symposia Proceedings (Cat. No.00CH37065). Presented at the Proceedings 2000 ICRA. Millennium Conference. IEEE International Conference on Robotics and Automation. Symposia Proceedings (Cat. No.00CH37065), pp. 19–26 vol.1. https://doi.org/10.1109/ROBOT.2000.844034

Gravish, N., Lauder, G.V., 2018. Robotics-inspired biology. J. Exp. Biol. 221. https://doi.org/10.1242/jeb.138438

Groppe, D., 2007. Precision feed end-effector composite fabric tape-laying apparatus and method. US20070277924A1.

Grzesiak, A., Becker, R., Verl, A., 2011. The Bionic Handling Assistant: a success story of additive manufacturing. Assem. Autom. 31, 329–333. https://doi.org/10.1108/01445151111172907

Guest, S.D., 2011. The stiffness of tensegrity structures. IMA J. Appl. Math. 76, 57–66. https://doi.org/10.1093/imamat/hxq065

Guo, Y., Dong, H., Ke, Y., 2015. Stiffness-oriented posture optimization in robotic machining applications. Robot. Comput.-Integr. Manuf. 35, 69–76. https://doi.org/10.1016/j.rcim.2015.02.006

Hannan, M.W., Walker, I.D., 2003. Kinematics and the Implementation of an Elephant's Trunk Manipulator and Other Continuum Style Robots. J. Robot. Syst. 20, 45–63.

https://doi.org/10.1002/rob.10070

Haugaløkken, B.O.A., Jørgensen, E.K., Schjølberg, I., 2018. Experimental validation of end-effector stabilization for underwater vehicle-manipulator systems in subsea operations. Robot. Auton. Syst. 109, 1–12. https://doi.org/10.1016/j.robot.2018.08.007

Howell, L.L., 2013. Compliant Mechanisms, in: McCarthy, J.M. (Ed.), 21st Century Kinematics. Springer, London, pp. 189–216. https://doi.org/10.1007/978-1-4471-4510-3_7

Hrennikoff, A., 2021. Solution of Problems of Elasticity by the Framework Method. J. Appl. Mech. 8, A169–A175. https://doi.org/10.1115/1.4009129

Huang, T., Zhao, X., Whitehouse, D.J., 2002. Stiffness estimation of a tripod-based parallel kinematic machine. IEEE Trans. Robot. Autom. 18, 50–58. https://doi.org/10.1109/70.988974

Huang, X., Liao, Q., Wei, S., 2010. Closed-form forward kinematics for a symmetrical 6-6 Stewart platform using algebraic elimination. Mech. Mach. Theory 45, 327–334. https://doi.org/10.1016/j.mechmachtheory.2009.09.008

Hughes, T.J.R., 2012. The Finite Element Method: Linear Static and Dynamic Finite Element Analysis. Courier Corporation.

Hughes, T.J.R., Hulbert, G.M., 1988. Space-time finite element methods for elastodynamics: Formulations and error estimates. Comput. Methods Appl. Mech. Eng. 66, 339–363. https://doi.org/10.1016/0045-7825(88)90006-0

Hustig-Schultz, D., SunSpiral, V., Teodorescu, M., 2016. Morphological design for controlled tensegrity quadruped locomotion, in: 2016 IEEE/RSJ International Conference on Intelligent Robots and Systems (IROS). Presented at the 2016 IEEE/RSJ International Conference on Intelligent Robots and Systems (IROS), pp. 4714–4719. https://doi.org/10.1109/IROS.2016.7759693

Izmailov, A.F., Solodov, M.V., 2003. Karush-Kuhn-Tucker systems: regularity conditions, error bounds and a class of Newton-type methods. Math. Program. 95, 631–650. https://doi.org/10.1007/s10107-002-0346-6

Jáuregui, V.G., 2020. Tensegrity Structures and their Application to Architecture. Ed. Universidad de Cantabria.

Jirouseka, J., Guex, L., 1986. The hybrid-Trefftz finite element model and its application to plate bending. Int. J. Numer. Methods Eng. 23, 651–693. https://doi.org/10.1002/nme.1620230410

Jones, R.M., 2006. Buckling of Bars, Plates, and Shells. Bull Ridge Corporation.

Kang, R., Branson, D.T., Zheng, T., Guglielmino, E., Caldwell, D.G., 2013. Design, modeling and control of a pneumatically actuated manipulator inspired by biological continuum structures. Bioinspir. Biomim. 8, 036008. https://doi.org/10.1088/1748-3182/8/3/036008

Kernbaum, A., Chiel, H., Quinn, R., 2009. Softworm: A Soft, Biologically Inspired Worm-Like Robot.

Khang, D.-Y., Rogers, J.A., Lee, H.H., 2009. Mechanical Buckling: Mechanics, Metrology, and Stretchable Electronics. Adv. Funct. Mater. 19, 1526–1536. https://doi.org/10.1002/adfm.200801065

Kim, C.-J., Pisano, A.P., Muller, R.S., Lim, M.G., 1992. Polysilicon microgripper. Sens. Actuators Phys. 33, 221–227. https://doi.org/10.1016/0924-4247(92)80169-4

Kim, N.H., Sankar, B.V., Kumar, A.V., 2018. Introduction to Finite Element Analysis and Design. John Wiley & Sons.

King, C.-H., Culjat, M.O., Franco, M.L., Lewis, C.E., Dutson, E.P., Grundfest, W.S., Bisley, J.W., 2009. Tactile Feedback Induces Reduced Grasping Force in Robot-Assisted Surgery. IEEE Trans. Haptics 2, 103–110. https://doi.org/10.1109/TOH.2009.4

Klimchik, Alexandr, Chablat, D., Pashkevich, A., 2019a. Advancement of MSA-Technique for Stiffness Modeling of Serial and Parallel Robotic Manipulators, in: Arakelian, V., Wenger, P. (Eds.), ROMANSY 22 – Robot Design, Dynamics and Control, CISM International Centre for Mechanical Sciences. Springer International Publishing, Cham, pp. 355–362. https://doi.org/10.1007/978-3-319-78963-7_45

Klimchik, A., Chablat, D., Pashkevich, A., 2014. Stiffness modeling for perfect and non-perfect parallel manipulators under internal and external loadings. Mech. Mach. Theory 79, 1–28. https://doi.org/10.1016/j.mechmachtheory.2014.04.002

Klimchik, Alexandr, Pashkevich, A., Caro, S., Chablat, D., 2012. Stiffness Matrix of Manipulators With Passive Joints: Computational Aspects. IEEE Trans. Robot. 28, 955–958. https://doi.org/10.1109/TRO.2012.2187395

Klimchik, Alexandr, Pashkevich, A., Chablat, D., 2019b. Fundamentals of manipulator stiffness modeling using matrix structural analysis. Mech. Mach. Theory 133, 365–394. https://doi.org/10.1016/j.mechmachtheory.2018.11.023

Klimchik, A., Pashkevich, A., Chablat, D., 2019. Stiffness modeling of NAVARO II transmission system. IFAC-Pap., 9th IFAC Conference on Manufacturing Modelling, Management and Control MIM 2019 52, 701–706. https://doi.org/10.1016/j.ifacol.2019.11.151

Klimchik, A., Pashkevich, A., Chablat, D., 2018. MSA-technique for stiffness modeling of manipulators with complex and hybrid structures. IFAC-Pap., 12th IFAC Symposium on Robot Control SYROCO 2018 51, 37–43. https://doi.org/10.1016/j.ifacol.2018.11.515

Klimchik, Alexandr, Pashkevich, A., Chablat, D., 2018a. Variable Actuation Modes in Parallel Manipulators: Impact on the Stiffness Behavior, in: 2018 23rd Conference of Open Innovations Association (FRUCT). Presented at the 2018 23rd Conference of Open Innovations Association (FRUCT), pp. 186–194. https://doi.org/10.23919/FRUCT.2018.8588031

Klimchik, Alexandr, Pashkevich, A., Chablat, D., 2018b. Stiffness Analysis of Parallel Manipulator NaVaRo with Dual Actuation Modes, in: 2018 International Russian Automation Conference (RusAutoCon). Presented at the 2018 International Russian Automation Conference (RusAutoCon), pp. 1–7. https://doi.org/10.1109/RUSAUTOCON.2018.8501754

Klimchik, A., Pashkevich, A., Chablat, D., 2012. Stiffness modeling of non-perfect parallel manipulators, in: 2012 IEEE/RSJ International Conference on Intelligent Robots and Systems. Presented at the 2012 IEEE/RSJ International Conference on Intelligent Robots and Systems, pp. 2781–2788. https://doi.org/10.1109/IROS.2012.6385513

Koizumi, Y., Shibata, M., Hirai, S., 2012. Rolling tensegrity driven by pneumatic soft actuators, in: 2012 IEEE International Conference on Robotics and Automation. Presented at the 2012 IEEE International Conference on Robotics and Automation, pp. 1988–1993. https://doi.org/10.1109/ICRA.2012.6224834

Konishi, S., Kawai, F., Cusin, P., 2001. Thin flexible end-effector using pneumatic balloon actuator. Sens. Actuators Phys., Special Issue: Micromechanics Section of Sensors and Actuators, based on contributions revised from the Technical Digest of the Thirteenth IEEE International Workshop on Micro Electro Mechanical Systems (MEMS-2000) 89, 28–35. https://doi.org/10.1016/S0924-4247(00)00533-1

Kordi, M.T., Husing, M., Corves, B., 2007. Development of a multifunctional robot end- effector system for automated manufacture of textile preforms, in: 2007 IEEE/ASME International Conference on Advanced Intelligent Mechatronics. Presented at the 2007 IEEE/ASME international conference on advanced intelligent mechatronics, pp. 1–6. https://doi.org/10.1109/AIM.2007.4412527

Kumar Hari Shankar Lal Das, G., Tondu, B., Forget, F., Manhes, J., Stasse, O., Souères, P., 2016. Performing Explosive motion using a multi-joint arm actuated by pneumatic muscles with quasi-DDP optimal control, in: MSC-2016 IEEE Multi-Conference on Systems and Control 2016. Buenos Aires, Argentina.

Kumar, K., Liu, J., Christianson, C., Ali, M., Tolley, M.T., Aizenberg, J., Ingber, D.E., Weaver, J.C., Bertoldi, K., 2017. A Biologically Inspired, Functionally Graded End Effector for Soft Robotics Applications. Soft Robot. 4, 317–323. https://doi.org/10.1089/soro.2017.0002

Lan, C.-C., Wang, J.-H., Chen, Y.-H., 2010. A compliant constant-force mechanism for adaptive robot end-effector operations, in: 2010 IEEE International Conference on Robotics and Automation. Presented at the 2010 IEEE International Conference on Robotics and Automation, pp. 2131–2136. https://doi.org/10.1109/ROBOT.2010.5509928

LANGEFORS, B., 1952. Analysis of Elastic Structures by Matrix Transformation with Special Regard to Semimonocoque Structures. J. Aeronaut. Sci. 19, 451–458. https://doi.org/10.2514/8.2339

Lee, K., 2001. Post-buckling of uniform cantilever column under a combined load. Int. J. Non-Linear Mech. 36, 813–816. https://doi.org/10.1016/S0020-7462(00)00047-0

Leidner, D.S., 2019. Cognitive Reasoning for Compliant Robot Manipulation, Springer Tracts in Advanced Robotics. Springer International Publishing, Cham. https://doi.org/10.1007/978-3-030-04858-7

Leipholz, H., 2013. Stability Theory: An Introduction to the Stability of Dynamic Systems and Rigid Bodies. Springer-Verlag.

Levin, S.M., 2002. The tensegrity-truss as a model for spine mechanics: biotensegrity. J. Mech. Med. Biol. 02, 375–388. https://doi.org/10.1142/S0219519402000472

Li, S., Ma, X., Liang, H., Görner, M., Ruppel, P., Fang, B., Sun, F., Zhang, J., 2019. Vision-based Teleoperation of Shadow Dexterous Hand using End-to-End Deep Neural Network, in: 2019 International Conference on Robotics and Automation (ICRA). Presented at the 2019 International Conference on Robotics and Automation (ICRA), pp. 416–422. https://doi.org/10.1109/ICRA.2019.8794277

Li, Y., Feng, X.-Q., Cao, Y.-P., Gao, H., 2010. Constructing tensegrity structures from one-bar elementary cells. Proc. R. Soc. Math. Phys. Eng. Sci. 466, 45–61. https://doi.org/10.1098/rspa.2009.0260

Li, Y.-W., Wang, J.-S., Wang, L.-P., 2002. Stiffness analysis of a Stewart platform-based parallel kinematic machine, in: Proceedings 2002 IEEE International Conference on Robotics and Automation (Cat. No.02CH37292). Presented at the Proceedings 2002 IEEE International Conference on Robotics and Automation (Cat. No.02CH37292), pp. 3672–3677 vol.4. https://doi.org/10.1109/ROBOT.2002.1014280

Liang, J., Bi, S., 2010. Design and experimental study of an end effector for robotic drilling. Int. J. Adv. Manuf. Technol. 50, 399–407. https://doi.org/10.1007/s00170-009-2494-9

Ma, K., Yang, G., 2016. Kinematic design of a 3-DOF force-controlled end-effector module, in: 2016 IEEE 11th Conference on Industrial Electronics and Applications (ICIEA). Presented at the 2016 IEEE 11th Conference on Industrial Electronics and Applications (ICIEA), pp. 1084–1089. https://doi.org/10.1109/ICIEA.2016.7603743

Ma, S., Chen, M., Skelton, R.E., 2020. Design of a new tensegrity cantilever structure. Compos. Struct. 243, 112188. https://doi.org/10.1016/j.compstruct.2020.112188

Majou, F., Gosselin, C., Wenger, P., Chablat, D., 2007. Parametric stiffness analysis of the Orthoglide. Mech. Mach. Theory 42, 296–311. https://doi.org/10.1016/j.mechmachtheory.2006.03.018

Marchese, A.D., Katzschmann, R.K., Rus, D., 2014a. Whole arm planning for a soft and highly compliant 2D robotic manipulator, in: 2014 IEEE/RSJ International Conference on Intelligent Robots and Systems. Presented at the 2014 IEEE/RSJ International Conference on Intelligent Robots and Systems, pp. 554–560. https://doi.org/10.1109/IROS.2014.6942614

Marchese, A.D., Onal, C.D., Rus, D., 2014b. Autonomous Soft Robotic Fish Capable of Escape Maneuvers Using Fluidic Elastomer Actuators. Soft Robot. 1, 75–87. https://doi.org/10.1089/soro.2013.0009

Marchese, A.D., Onal, C.D., Rus, D., 2013. Towards a Self-contained Soft Robotic Fish: On-Board Pressure Generation and Embedded Electro-permanent Magnet Valves, in: Desai, J.P., Dudek, G., Khatib, O., Kumar, V. (Eds.), Experimental Robotics: The 13th International Symposium on Experimental Robotics, Springer Tracts in Advanced Robotics. Springer International Publishing, Heidelberg, pp. 41–54. https://doi.org/10.1007/978-3-319-00065-7_4

Masic, M., Skelton, R.E., 2004. Open-loop control of class-2 tensegrity towers, in: Smart Structures and Materials 2004: Modeling, Signal Processing, and Control. Presented at the Smart Structures and Materials 2004: Modeling, Signal Processing, and Control, International Society for Optics and Photonics, pp. 298–308. https://doi.org/10.1117/12.540370

Masic, M., Skelton, R.E., Gill, P.E., 2006. Optimization of tensegrity structures. Int. J. Solids Struct. 43, 4687–4703. https://doi.org/10.1016/j.ijsolstr.2005.07.046

Masic, M., Skelton, R.E., Gill, P.E., 2005. Algebraic tensegrity form-finding. Int. J. Solids Struct. 42, 4833–4858. https://doi.org/10.1016/j.ijsolstr.2005.01.014

McGuire, W., Gallagher, R., Ziemian, R., 2000. Matrix Structural Analysis, 2nd Edition. Fac. Books.

McMahan, W., Chitrakaran, V., Csencsits, M., Dawson, D., Walker, I.D., Jones, B.A., Pritts, M., Dienno, D., Grissom, M., Rahn, C.D., 2006. Field trials and testing of the OctArm continuum manipulator, in: Proceedings 2006 IEEE International Conference on Robotics and Automation, 2006. ICRA 2006. Presented at the Proceedings 2006 IEEE International Conference on Robotics and Automation, 2006. ICRA 2006., pp. 2336–2341. https://doi.org/10.1109/ROBOT.2006.1642051

McMahan, W., Jones, B.A., Walker, I.D., 2005. Design and implementation of a multi-section continuum robot: Air-Octor, in: 2005 IEEE/RSJ International Conference on Intelligent Robots and Systems. Presented at the 2005 IEEE/RSJ International Conference on Intelligent Robots and Systems, pp. 2578–2585. https://doi.org/10.1109/IROS.2005.1545487

Melenk, J.M., Babuška, I., 1996. The partition of unity finite element method: Basic theory and applications. Comput. Methods Appl. Mech. Eng. 139, 289–314. https://doi.org/10.1016/S0045-7825(96)01087-0

Merlet, J.-P., Gosselin, C., Huang, T., 2016. Parallel Mechanisms, in: Siciliano, B., Khatib, O. (Eds.), Springer Handbook of Robotics, Springer Handbooks. Springer International Publishing, Cham, pp. 443–462. https://doi.org/10.1007/978-3-319-32552-1_18

Mintchev, S., Zappetti, D., Willemin, J., Floreano, D., 2018. A Soft Robot for Random Exploration of Terrestrial Environments, in: 2018 IEEE International Conference on Robotics and Automation (ICRA). Presented at the 2018 IEEE International Conference on Robotics and Automation (ICRA), pp. 7492–7497. https://doi.org/10.1109/ICRA.2018.8460667

Mirletz, B.T., Park, I.-W., Flemons, T.E., Agogino, A.K., Quinn, R.D., SunSpiral, V., n.d. Design and Control of Modular Spine-Like Tensegrity Structures 10.

Mirletz, B.T., Park, I.-W., Quinn, R.D., SunSpiral, V., 2015. Towards bridging the reality gap between tensegrity simulation and robotic hardware, in: 2015 IEEE/RSJ International Conference on Intelligent Robots and Systems (IROS). Presented at the 2015 IEEE/RSJ International Conference on Intelligent Robots and Systems (IROS), IEEE, Hamburg, Germany, pp. 5357–5363. https://doi.org/10.1109/IROS.2015.7354134

Mohammad, A.E.K., Hong, J., Wang, D., 2018. Design of a force-controlled end-effector with low-inertia effect for robotic polishing using macro-mini robot approach. Robot. Comput.-Integr. Manuf. 49. https://doi.org/10.1016/j.rcim.2017.05.011

Moored, K.W., Taylor, S.A., Bliss, T.K., Bart-Smith, H., 2006. Optimization of a tensegrity wing for biomimetic applications, in: Proceedings of the 45th IEEE Conference on Decision and Control. Presented at the Proceedings of the 45th IEEE Conference on Decision and Control, pp. 2288–2293. https://doi.org/10.1109/CDC.2006.377421

Morecki, A., Jaworek, K., Pogorzelski, W., Zielinska, T., Fraczek, J., Malczyk, G., 1988. Robotics System—Elephant Trunk Type Elastic Manipulator Combined with a Quadruped Walking Machine, in: Radharamanan, R. (Ed.), Robotics and Factories of the Future '87. Springer, Berlin, Heidelberg, pp. 649–656. https://doi.org/10.1007/978-3-642-73890-6_78

Mori, M., Suzumori, K., Takahashi, M., Hosoya, T., 2010. Very High Force Hydraulic McKibben Artificial Muscle with a p-Phenylene-2,6-benzobisoxazole Cord Sleeve. Adv. Robot. 24, 233–254. https://doi.org/10.1163/016918609X12586209967366

Motro, R., 1990. Tensegrity Systems and Geodesic Domes. Int. J. Space Struct. 5, 341–351. https://doi.org/10.1177/026635119000500315

Motro, R., Raducanu, V., 2003. Tensegrity Systems. Int. J. Space Struct. 18, 77–84. https://doi.org/10.1260/026635103769518198

Müller, D., Raisch, A., Hildebrandt, A., Sawodny, O., 2020. Nonlinear Model based Dynamic Control of Pneumatic driven Quasi Continuum Manipulators, in: 2020 IEEE/SICE International Symposium on System Integration (SII). Presented at the 2020 IEEE/SICE International Symposium on System Integration (SII), pp. 277–282. https://doi.org/10.1109/SII46433.2020.9026206

Murakami, H., 2001. Static and dynamic analyses of tensegrity structures. Part II. Quasi-static analysis. Int. J. Solids Struct. 38, 3615–3629. https://doi.org/10.1016/S0020-7683(00)00233-X

Muralidharan, V., Wenger, P., Furet, M., 2020. Static Analysis and Design Strategy of Two Antagonistically Actuated Joints, in: Pisla, D., Corves, B., Vaida, C. (Eds.), New Trends in Mechanism and Machine Science, Mechanisms and Machine Science. Springer International Publishing, Cham, pp. 459–469. https://doi.org/10.1007/978-3-030-55061-5_52

Muvdi, B.B., McNabb, J.W., 2012. Engineering Mechanics of Materials. Springer Science & Business Media.

Nagase, K., Skelton, R.E., 2014. Minimal Mass Tensegrity Structures. J. Int. Assoc. Shell Spat. Struct. 55, 37–48.

Nordin, M.H., Selvaraju, K., Fathullah, M., 2016. Increasing ABB FlexPicker Robot's Degree of Freedom (DOF) using Flexible End Effector. MATEC Web Conf. 78, 01056. https://doi.org/10.1051/matecconf/20167801056

Pan, Y., Wang, H., Li, X., Yu, H., 2018. Adaptive Command-Filtered Backstepping Control of Robot Arms With Compliant Actuators. IEEE Trans. Control Syst. Technol. 26, 1149–1156. https://doi.org/10.1109/TCST.2017.2695600

Papadrakakis, M., Sapountzakis, E.J., 2018. Chapter One - Introduction to Matrix Methods of Structural Analysis, in: Papadrakakis, M., Sapountzakis, E.J. (Eds.), Matrix Methods for Advanced Structural Analysis. Butterworth-Heinemann, pp. 1–15. https://doi.org/10.1016/B978-0-12-811708-8.00001-5

Pashkevich, A., Chablat, D., Wenger, P., 2009. Stiffness analysis of overconstrained parallel manipulators. Mech. Mach. Theory 44, 966–982. https://doi.org/10.1016/j.mechmachtheory.2008.05.017

Pashkevich, A., Klimchik, A., Caro, S., Chablat, D., 2011. Cartesian stiffness matrix of manipulators with passive joints: Analytical approach, in: 2011 IEEE/RSJ International Conference on Intelligent Robots and Systems. Presented at the 2011 IEEE/RSJ International Conference on Intelligent Robots and Systems, pp. 4034–4041. https://doi.org/10.1109/IROS.2011.6094419

Pashkevich, Anatol, Klimchik, A., Chablat, D., 2011. Enhanced stiffness modeling of manipulators with passive joints. Mech. Mach. Theory 46, 662–679. https://doi.org/10.1016/j.mechmachtheory.2010.12.008

Pashkevich, A., Klimchik, A., Chablat, D., 2010. Stiffness Analysis of Parallel Manipulators with Preloaded Passive Joints, in: Lenarcic, J., Stanisic, M.M. (Eds.), Advances in Robot Kinematics: Motion in Man and Machine. Springer Netherlands, Dordrecht, pp. 465–474. https://doi.org/10.1007/978-90-481-9262-5_50

Paul, C., Roberts, J.W., Lipson, H., Valero Cuevas, F.J., 2005. Gait production in a tensegrity based robot, in: ICAR ’05. Proceedings., 12th International Conference on Advanced Robotics, 2005. Presented at the ICAR ’05. Proceedings., 12th International Conference on Advanced Robotics, 2005., pp. 216–222. https://doi.org/10.1109/ICAR.2005.1507415

Pedersen, C.B.W., Fleck, N.A., Ananthasuresh, G.K., 2005. Design of a Compliant Mechanism to Modify an Actuator Characteristic to Deliver a Constant Output Force. J. Mech. Des. 128, 1101–1112. https://doi.org/10.1115/1.2218883

Pigoski, T., Griffis, M., Duffy, J., 1998. Stiffness mappings employing different frames of reference. Mech. Mach. Theory 33, 825–838. https://doi.org/10.1016/S0094-114X(97)00083-9

Pugh, A., 2020. An Introduction to Tensegrity, An Introduction to Tensegrity. University of California Press.

Quennouelle, C., Gosselin, C., 2009a. Stiffness Matrix of Compliant Parallel Mehanisms. Presented at the ASME 2008 International Design Engineering Technical Conferences and Computers and Information in Engineering Conference, American Society of Mechanical Engineers Digital Collection, pp. 151–161. https://doi.org/10.1115/DETC2008-49253

Quennouelle, C., Gosselin, C., 2009b. Instantaneous Kinemato-Static Model of Planar Compliant Parallel Mechanisms. Presented at the ASME 2008 International Design Engineering Technical Conferences and Computers and Information in Engineering Conference, American Society of Mechanical Engineers Digital Collection, pp. 163–173. https://doi.org/10.1115/DETC2008-49265

Ramm, E., Rank, E., Rannacher, R., Schweizerhof, K., Stein, E., Wendland, W., Wittum, G., Wriggers, P., Wunderlich, W., 2003. Error-controlled Adaptive Finite Elements in Solid Mechanics. John Wiley & Sons.

Rieffel, J., Mouret, J.-B., 2018. Adaptive and Resilient Soft Tensegrity Robots. Soft Robot. 5, 318–329. https://doi.org/10.1089/soro.2017.0066

Rimoli, J.J., 2018. A reduced-order model for the dynamic and post-buckling behavior of tensegrity structures. Mech. Mater., IUTAM Symposium on Dynamic Instabilities in Solids 116, 146–157. https://doi.org/10.1016/j.mechmat.2017.01.009

Rimoli, J.J., n.d. On the impact tolerance of tensegrity-based planetary landers, in: 57th AIAA/ASCE/AHS/ASC Structures, Structural Dynamics, and Materials Conference. American Institute of Aeronautics and Astronautics. https://doi.org/10.2514/6.2016-1511

Rimoli, J.J., Pal, R.K., 2017. Mechanical response of 3-dimensional tensegrity lattices. Compos. Part B Eng., Composite lattices and multiscale innovative materials and structures 115, 30–42. https://doi.org/10.1016/j.compositesb.2016.10.046

Robinson, G., Davies, J.B.C., 1999. Continuum robots - a state of the art, in: Proceedings 1999 IEEE International Conference on Robotics and Automation (Cat. No.99CH36288C). Presented at the Proceedings 1999 IEEE International Conference on Robotics and Automation (Cat. No.99CH36288C), pp. 2849–2854 vol.4. https://doi.org/10.1109/ROBOT.1999.774029

Rolf, M., Steil, J.J., 2014. Efficient Exploratory Learning of Inverse Kinematics on a Bionic Elephant Trunk. IEEE Trans. Neural Netw. Learn. Syst. 25, 1147–1160. https://doi.org/10.1109/TNNLS.2013.2287890

Rolf, M., Steil, J.J., 2012. Constant curvature continuum kinematics as fast approximate model for the Bionic Handling Assistant, in: 2012 IEEE/RSJ International Conference on Intelligent Robots and Systems. Presented at the 2012 IEEE/RSJ International Conference on Intelligent Robots and

Systems (IROS 2012), IEEE, Vilamoura-Algarve, Portugal, pp. 3440–3446. https://doi.org/10.1109/IROS.2012.6385596

Roper, D.T., Sharma, S., Sutton, R., Culverhouse, P., 2011. A review of developments towards biologically inspired propulsion systems for autonomous underwater vehicles. Proc. Inst. Mech. Eng. Part M J. Eng. Marit. Environ. 225, 77–96. https://doi.org/10.1177/1475090210397438

Sabelhaus, A.P., Bruce, J., Caluwaerts, K., Manovi, P., Firoozi, R.F., Dobi, S., Agogino, A.M., SunSpiral, V., 2015. System design and locomotion of SUPERball, an untethered tensegrity robot, in: 2015 IEEE International Conference on Robotics and Automation (ICRA). Presented at the 2015 IEEE International Conference on Robotics and Automation (ICRA), pp. 2867–2873. https://doi.org/10.1109/ICRA.2015.7139590

Salisbury, J., 1980. Active stiffness control of a manipulator in cartesian coordinates, in: 1980 19th IEEE Conference on Decision and Control Including the Symposium on Adaptive Processes. Presented at the 1980 19th IEEE Conference on Decision and Control including the Symposium on Adaptive Processes, IEEE, Albuquerque, NM, USA, pp. 95–100. https://doi.org/10.1109/CDC.1980.272026

Schellbach, K., 1851. Probleme der Variationsrechnung. 1851, 293–363. https://doi.org/10.1515/crll.1851.41.293

Schenk, M., Guest, S.D., Herder, J.L., 2007. Zero stiffness tensegrity structures. Int. J. Solids Struct. 44, 6569–6583. https://doi.org/10.1016/j.ijsolstr.2007.02.041

Sfakiotakis, M., Lane, D.M., Davies, J.B.C., 1999. Review of fish swimming modes for aquatic locomotion. IEEE J. Ocean. Eng. 24, 237–252. https://doi.org/10.1109/48.757275

Shekastehband, B., Abedi, K., Dianat, N., Chenaghlou, M.R., 2012. Experimental and numerical studies on the collapse behavior of tensegrity systems considering cable rupture and strut collapse with snap-through. Int. J. Non-Linear Mech. 47, 751–768. https://doi.org/10.1016/j.ijnonlinmec.2012.04.004

Shibata, M., Saijyo, F., Hirai, S., 2009. Crawling by body deformation of tensegrity structure robots, in: 2009 IEEE International Conference on Robotics and Automation. Presented at the 2009 IEEE International Conference on Robotics and Automation, pp. 4375–4380. https://doi.org/10.1109/ROBOT.2009.5152752

Simo, J.C., Rifai, M.S., 1990. A class of mixed assumed strain methods and the method of incompatible modes. Int. J. Numer. Methods Eng. 29, 1595–1638. https://doi.org/10.1002/nme.1620290802

Singh, P., Kumar, A., Vashisth, M., n.d. Design of a Robotic Arm with Gripper & End Effector for Spot Welding.

Skelton, R.E., Adhikari, R., Pinaud, J.-P., Chan, W., Helton, J.W., 2001. An introduction to the mechanics of tensegrity structures, in: Proceedings of the 40th IEEE Conference on Decision and Control (Cat. No.01CH37228). Presented at the Proceedings of the 40th IEEE Conference on Decision and Control (Cat. No.01CH37228), pp. 4254–4259 vol.5. https://doi.org/10.1109/CDC.2001.980861

Skelton, R.E., Fraternali, F., Carpentieri, G., Micheletti, A., 2014. Minimum mass design of tensegrity bridges with parametric architecture and multiscale complexity. Mech. Res. Commun., MULTI-SCALE MODELING AND CHARACTERIZATION OF INNOVATIVE MATERIALS AND STRUCTURES 58, 124–132. https://doi.org/10.1016/j.mechrescom.2013.10.017

Skelton, R.E., Helton, J.W., Adhikari, R., Pinaud, J.-P., Chan, W., 2002. An Introduction to the Mechanics of Tensegrity Structures 75.

Skelton, R.E., Montuori, R., Pecoraro, V., 2016. Globally stable minimal mass compressive tensegrity structures. Compos. Struct. 141, 346–354. https://doi.org/10.1016/j.compstruct.2016.01.105

Skelton, R.E., Oliveira, M.C. de, 2009. Tensegrity systems. Springer, Berlin.

Snelson, K., 2012. The Art of Tensegrity. Int. J. Space Struct. 27, 71–80. https://doi.org/10.1260/0266-3511.27.2-3.71

Soft Robotics mGrip Circular kit : données techniques et avis, n.d. . HumaRobotics. URL https://www.humarobotics.com/boutique/soft-robotics/soft-robotics-m-grip-circular-kit/ (accessed 7.23.21).

Stamenovic´, D., Coughlin, M.F., 1999. A Quantitative Model of Cellular Elasticity Based on Tensegrity. J. Biomech. Eng. 122, 39–43. https://doi.org/10.1115/1.429631

Stein, E., 2014. History of the Finite Element Method – Mathematics Meets Mechanics – Part I: Engineering Developments, in: Stein, E. (Ed.), The History of Theoretical, Material and Computational Mechanics - Mathematics Meets Mechanics and Engineering, Lecture Notes in Applied Mathematics and Mechanics. Springer, Berlin, Heidelberg, pp. 399–442. https://doi.org/10.1007/978-3-642-39905-3_22

Sun, J., Song, G., Chu, J., Ren, L., 2019. An Adaptive Bioinspired Foot Mechanism Based on Tensegrity Structures. Soft Robot. 6, 778–789. https://doi.org/10.1089/soro.2018.0168

Sun, T., Lian, B., Song, Y., 2016. Stiffness analysis of a 2-DoF over-constrained RPM with an articulated traveling platform. Mech. Mach. Theory 96, 165–178. https://doi.org/10.1016/j.mechmachtheory.2015.09.008

Taghvaeipour, A., Angeles, J., Lessard, L., 2012. On the elastostatic analysis of mechanical systems. Mech. Mach. Theory 58, 202–216. https://doi.org/10.1016/j.mechmachtheory.2012.07.011

Tanaka, M., Matsuno, F., 2014. Modeling and Control of Head Raising Snake Robots by Using Kinematic Redundancy. J. Intell. Robot. Syst. 75, 53–69. https://doi.org/10.1007/s10846-013-9866-y

Tavakoli, M., Patel, R.V., Moallem, M., 2005. Haptic interaction in robot-assisted endoscopic surgery: a sensorized end-effector. Int. J. Med. Robot. 1, 53–63. https://doi.org/10.1002/rcs.16

Tibert, A.G., Pellegrino, S., 2003. Review of Form-Finding Methods for Tensegrity Structures. Int. J. Space Struct. 18, 209–223. https://doi.org/10.1260/026635103322987940

Timoshenko, S.P., Gere, J.M., 2009a. Theory of Elastic Stability. Courier Corporation.

Timoshenko, S.P., Gere, J.M., 2009b. Theory of Elastic Stability. Courier Corporation.

Tondu, B., Boitier, V., Lopez, P., 1994. Naturally compliant robot-arms actuated by McKibben artificial muscles, in: Proceedings of IEEE International Conference on Systems, Man and Cybernetics. Presented at the Proceedings of IEEE International Conference on Systems, Man and Cybernetics, pp. 2635–2640 vol. 3. https://doi.org/10.1109/ICSMC.1994.400269

Tondu, B., Lopez, P., 2000. Modeling and control of McKibben artificial muscle robot actuators. IEEE Control Syst. Mag. 20, 15–38. https://doi.org/10.1109/37.833638

Trahair, N.S., 2019. Flexural-Torsional Buckling of Structures. CRC Press, Boca Raton. https://doi.org/10.1201/9780203755938

Tran, H.C., Lee, J., 2010. Advanced form-finding of tensegrity structures. Comput. Struct. 88, 237–246. https://doi.org/10.1016/j.compstruc.2009.10.006

Trivedi, D., Rahn, C.D., Kier, W.M., Walker, I.D., 2008. Soft robotics: Biological inspiration, state of the art, and future research. Appl. Bionics Biomech. 5, 99–117. https://doi.org/10.1080/11762320802557865

Tsui, K., Geisberger, A.A., Ellis, M., Skidmore, G.D., 2004. Micromachined end-effector and techniques for directed MEMS assembly. J. Micromechanics Microengineering 14, 542–549. https://doi.org/10.1088/0960-1317/14/4/015

Vassart, N., Motro, R., 1999. Multiparametered Formfinding Method: Application to Tensegrity

Systems. Int. J. Space Struct. 14, 147–154. https://doi.org/10.1260/0266351991494768

Venkateswaran, S., Chablat, D., Hamon, P., 2021. An Optimal Design of a Flexible Piping Inspection Robot. J. Mech. Robot. 13. https://doi.org/10.1115/1.4049948

Venkateswaran, S., Chablat, D., Hamon, P., 2020. Design of a Piping Inspection Robot by Optimization Approach. Presented at the ASME 2020 International Design Engineering Technical Conferences and Computers and Information in Engineering Conference, American Society of Mechanical Engineers Digital Collection. https://doi.org/10.1115/DETC2020-22021

Volokh, K.Yu., Vilnay, O., Belsky, M., 2000. Tensegrity architecture explains linear stiffening and predicts softening of living cells. J. Biomech. 33, 1543–1549. https://doi.org/10.1016/S0021-9290(00)00157-3

Wang, H., Chen, W., Yu, X., Deng, T., Wang, X., Pfeifer, R., 2013. Visual servo control of cable-driven soft robotic manipulator, in: 2013 IEEE/RSJ International Conference on Intelligent Robots and Systems. Presented at the 2013 IEEE/RSJ International Conference on Intelligent Robots and Systems, pp. 57–62. https://doi.org/10.1109/IROS.2013.6696332

Wang, H., Zhang, L., Chen, G., Huang, S., 2017. Parameter optimization of heavy-load parallel manipulator by introducing stiffness distribution evaluation index. Mech. Mach. Theory 108, 244–259. https://doi.org/10.1016/j.mechmachtheory.2016.10.011

Wang, M.Y., Chen, S., 2009. Compliant Mechanism Optimization: Analysis and Design with Intrinsic Characteristic Stiffness. Mech. Based Des. Struct. Mach. 37, 183–200. https://doi.org/10.1080/15397730902761932

Wang, Y., Xu, X., Luo, Y., 2020. Topology design of general tensegrity with rigid bodies. Int. J. Solids Struct. 202, 278–298. https://doi.org/10.1016/j.ijsolstr.2020.05.030

Webster, R.J., Jones, B.A., 2010. Design and Kinematic Modeling of Constant Curvature Continuum Robots: A Review. Int. J. Robot. Res. 29, 1661–1683. https://doi.org/10.1177/0278364910368147

Wen, L., Pan, F., Ding, X., 2020. Tensegrity metamaterials for soft robotics. Sci. Robot. 5. https://doi.org/10.1126/scirobotics.abd9158

Wenger, P., Chablat, D., 2019a. Kinetostatic analysis and solution classification of a class of planar tensegrity mechanisms. Robotica 37, 1214–1224. https://doi.org/10.1017/S026357471800070X

Wenger, P., Chablat, D., 2019b. Kinetostatic analysis and solution classification of a class of planar tensegrity mechanisms. Robotica 37, 1214–1224. https://doi.org/10.1017/S026357471800070X

Wenger, P., Chablat, D., 2019c. Kinetostatic analysis and solution classification of a class of planar tensegrity mechanisms. Robotica 37, 1214–1224. https://doi.org/10.1017/S026357471800070X

Wenger, P., Chablat, D., 2018. Kinetostatic Analysis and Solution Classification of a Planar Tensegrity Mechanism, in: Zeghloul, S., Romdhane, L., Laribi, M.A. (Eds.), Computational Kinematics, Mechanisms and Machine Science. Springer International Publishing, Cham, pp. 422–431. https://doi.org/10.1007/978-3-319-60867-9_48

Wenger, P., Furet, M., 2021. Kinematic Analysis of a Planar Manipulator with Anti-parallelogram Joints and Offsets, in: Lenarčič, J., Siciliano, B. (Eds.), Advances in Robot Kinematics 2020, Springer Proceedings in Advanced Robotics. Springer International Publishing, Cham, pp. 319–326. https://doi.org/10.1007/978-3-030-50975-0_39

Wickramatunge, K.C., Leephakpreeda, T., 2010. Study on mechanical behaviors of pneumatic artificial muscle. Int. J. Eng. Sci. 48, 188–198. https://doi.org/10.1016/j.ijengsci.2009.08.001

Wright, C., Buchan, A., Brown, B., Geist, J., Schwerin, M., Rollinson, D., Tesch, M., Choset, H., 2012. Design and architecture of the unified modular snake robot, in: 2012 IEEE International Conference on Robotics and Automation. Presented at the 2012 IEEE International Conference on Robotics and Automation, pp. 4347–4354. https://doi.org/10.1109/ICRA.2012.6225255

Xi, F., Zhang, D., Mechefske, C.M., Lang, S.Y.T., 2004. Global kinetostatic modelling of tripod-based parallel kinematic machine. Mech. Mach. Theory 39, 357–377. https://doi.org/10.1016/j.mechmachtheory.2003.09.007

Yang, J., Pitarch, E.P., Potratz, J., Beck, S., Abdel-Malek, K., 2006. Synthesis and analysis of a flexible elephant trunk robot. Adv. Robot. 20, 631–659. https://doi.org/10.1163/156855306777361631

Yang, K., Wang, Y., 2008. Design, drive and control of a novel SMA-actuated humanoid flexible gripper. J. Mech. Sci. Technol. 22, 895–904. https://doi.org/10.1007/s12206-008-0215-1

Yang, Y., Zhang, W., 2015. An elephant-trunk manipulator with twisting flexional rods, in: 2015 IEEE International Conference on Robotics and Biomimetics (ROBIO). Presented at the 2015 IEEE International Conference on Robotics and Biomimetics (ROBIO), IEEE, Zhuhai, pp. 13–18. https://doi.org/10.1109/ROBIO.2015.7407012

Yi, B.-J., Freeman, R.A., 1992. Synthesis of actively adjustable springs by antagonistic redundant actuation. ASME J. Dyn. Syst. Meas. Control B 114, 454–461.

Zahavi, Barlam, Eagle, 2001. Nonlinear Problems in Machine Design. Appl. Mech. Rev. 54, B86–B87. https://doi.org/10.1115/1.1399675

Zappetti, D., Jeong, S.H., Shintake, J., Floreano, D., 2020. Phase Changing Materials-Based Variable-Stiffness Tensegrity Structures. Soft Robot. 7, 362–369. https://doi.org/10.1089/soro.2019.0091

Zhang, D., 2005. On stiffness improvement of the Tricept machine tool. Robotica 23, 377–386. https://doi.org/10.1017/S0263574704000992

Zhang, D., Gosselin, C.M., 2002. Kinetostatic Analysis and Design Optimization of the Tricept Machine Tool Family. J. Manuf. Sci. Eng. 124, 725–733. https://doi.org/10.1115/1.1471529

Zhang, D., Xi, F., Mechefske, C.M., Lang, S.Y.T., 2004. Analysis of parallel kinematic machine with kinetostatic modelling method. Robot. Comput.-Integr. Manuf. 20, 151–165. https://doi.org/10.1016/j.rcim.2003.08.005

Zhang, H., Wang, J., Zhang, G., Gan, Z., Pan, Z., Cui, H., Zhu, Z., 2005. Machining with flexible manipulator: toward improving robotic machining performance, in: Proceedings, 2005 IEEE/ASME International Conference on Advanced Intelligent Mechatronics. Presented at the Proceedings, 2005 IEEE/ASME International Conference on Advanced Intelligent Mechatronics., pp. 1127–1132. https://doi.org/10.1109/AIM.2005.1511161

Zhang, J.Y., Ohsaki, M., 2006. Form-Finding of Tensegrity Structures Subjected to Geometrical Constraints. Int. J. Space Struct. 21, 183–195. https://doi.org/10.1260/026635106780866024

Zhang, J.Y., Ohsaki, M., n.d. Optimization Methods for Force and Shape Design of Tensegrity Structures 10.

Zhang, L.-Y., Li, Y., Cao, Y.-P., Feng, X.-Q., 2014. Stiffness matrix based form-finding method of tensegrity structures. Eng. Struct. 58, 36–48. https://doi.org/10.1016/j.engstruct.2013.10.014

Zhang, L.-Y., Li, Y., Cao, Y.-P., Feng, X.-Q., Gao, H., 2012. Self-equilibrium and super-stability of truncated regular polyhedral tensegrity structures: a unified analytical solution. Proc. R. Soc. Math. Phys. Eng. Sci. 468, 3323–3347. https://doi.org/10.1098/rspa.2012.0260

Zhang, P., Kawaguchi, K., Feng, J., 2014. Prismatic tensegrity structures with additional cables: Integral symmetric states of self-stress and cable-controlled reconfiguration procedure. Int. J. Solids Struct. 51, 4294–4306. https://doi.org/10.1016/j.ijsolstr.2014.08.014

Zhao, W., Xu, H., Jutamanee, A., Hu, M., Li, C., Zhu, L., 2018. Mixed phase activated artificial muscle 14.

Zhao, W., Xu, H., Ma, Y., Xu, Y., 2017. Design and experimental test of the contractive and elongate water hydraulic flexible manipulators, in: 2017 IEEE International Conference on Robotics and Biomimetics (ROBIO). Presented at the 2017 IEEE International Conference on Robotics and Biomimetics (ROBIO), pp. 1503–1508. https://doi.org/10.1109/ROBIO.2017.8324630

Zienkiewicz, O.C., Cheung, I.K., 1971. The Finite Element Method in Engineering Science. McGraw-Hill.

CENTRALE
NANTES

Titre : Conception d'un effecteur pour robots collaboratifs

Mots clés : Effecteur de robot, robot souple, mécanisme de tenségrité, analyse de la rigidité, contrôle cinématique.

Résumé : L'objectif de cette thèse est la conception de nouveaux effecteurs polyvalents et souples pour les robots collaboratifs, qui sont basés sur des mécanismes de tenségrité multi-segments à double-triangle qui peuvent être actionnés indépendamment pour obtenir la configuration désirée avec de bonne propriétés de rigidité. Contrairement aux effecteurs rigides conventionnels, l'analyse de la rigidité a démontré que ce type de mécanisme peut atteindre une grande flexibilité ; les concepteurs peuvent évaluer la sensibilité de la rigidité de ce mécanisme par rapport à une configuration initiale arbitraire pour différentes combinaisons de paramètres géométriques, de charge externes et de précontraintes des ressorts. Le phénomène de flambage et de quasi-flambage de ce mécanisme sous chargements a été étudié. Une méthode analytique permettant de calculer la force critique de flambage pour cette structure avec un nombre arbitraire de segments a été proposée. Elle est basée sur l'analyse des valeurs propres d'une matrice dépendant des paramètres géométriques et élastostatiques. Cela permet aux concepteurs de prédire ou d'éviter les états dangereux de ce mécanisme en modifiant correctement les paramètres géométriques et les entrées de la commande. De plus, les stratégies de contrôle cinématique basées sur l'optimisation ont été proposées dans cette thèse, ce qui permet à ce mécanisme multi-segment redondant d'atteindre l'emplacement d'une cible et d'éviter les collisions entre l'effecteur et le corps du robot et les obstacles de l'espace de travail. Les avantages de la technique développée sont confirmés par la simulation informatique, et les résultats montrent que ce mécanisme redondant en série a une capacité de changement de forme très flexible tout en traversant l'espace de travail.

Title : Design of Robot End-Effector for Collaborative Robot Works

Keywords: robot end-effector, compliant manipulator, tensegrity mechanism, stiffness analysis, kinematic control.

Abstract: This thesis focuses on the design of new versatile and compliant end-effectors for collaborative robot works, which are based on multi-segment dual-triangle tensegrity mechanisms that can be actuated independently to achieve the desired configuration with the required stiffness properties. Different with the conventional rigid robot end-effectors, it was demonstrated from the stiffness analysis that such type of mechanism can achieve high flexibility; designers can evaluate the stiffness sensitivity of this mechanism with respect to an arbitrary initial configuration for different combination of the geometric parameters, external loading and the spring's pre-stresses. Besides, the buckling and quasi-buckling phenomenon of this serial mechanism under the loading were detected. And an analytical method allowing to compute the critical force causing the buckling for this serial structure with an arbitrary number of segments was proposed, which is based on the eigenvalue analysis of the some special matrix depending on both geometric and elastostatic parameters. This allows designers to predict or avoid the dangerous states of this mechanism by properly changing the geometric parameters and control inputs. Furthermore, the optimization-based kinematic control strategies were proposed in this thesis, which allow this redundant multi-segment mechanism to achieve the target endpoint location and avoid collisions between not only the mechanism end-point but also the mechanism body and the workspace obstacles. The advantages of the developed technique are confirmed via the computing simulation, and the results show that this redundant serial mechanism has a very flexible shape changing capacity while passing through the task space.